Specific effects of organic and inorganic ions on soft interfaces

Leonor Pérez Fuentes

Universidad de Granada

Enero 2016

Directores:

Dra. Delfi Bastos González
Grupo de Física de Fluidos y Biocoloides
Departamento de Física Aplicada (Universidad de Granada)

Dr. Carlos Drummond
Centre de Recherche Paul Pascal (CNRS)
Pessac, France

Dr. Jordi Faraudo
Institut de Ciència de Materials de Barcelona (ICMAB-CSIC)
Barcelona

Programa de Doctorado en Física y Ciencias del Espacio

Editor: Universidad de Granada. Tesis Doctorales
Autora: Leonor Pérez Fuentes
ISBN: 978-84-9125-607-6
URI: http://hdl.handle.net/10481/43015

Derechos de propiedad intelectual

La doctoranda, Leonor Pérez Fuentes, y los directores de la tesis, Delfi Bastos González, profesora titular de universidad; Carlos Drummond, investigador titular del CNRS y Jordi Faraudo, científico titular del CSIC,

Garantizamos al firmar esta tesis doctoral, *Specific effects of organic and inorganic ions on soft interfaces*, que el trabajo ha sido realizado por la doctoranda bajo la dirección de los directores de la tesis y hasta donde nuestro conocimiento alcanza, en la realización del trabajo, se han respetado los derechos de otros autores a ser citados, cuando se han utilizado sus resultados o publicaciones.

Granada, 27 de Noviembre de 2015.

Directores de la tesis

Doctoranda

Fdo: Delfi Bastos González

Fdo: Leonor Pérez Fuentes

Fdo: Carlos Drummond

Fdo: Jordi Faraudo

A mis padres y a Migue por apoyarme siempre

Agradecimientos

La realización de esta tesis doctoral ha supuesto para mí un camino de aprendizaje en varios aspectos, tanto en el ámbito de la investigación como en el personal. He tenido tiempo de aprender, desaprender y volver a aprender, pero sobre todo me he sentido acompañada por muchas personas que han hecho que esta transición fuera más fácil y agradable, por ello a todas ellas me gustaría brindar mi gratitud en estas páginas.

En primer lugar me gustaría dar las gracias a mis directores de tesis.

Todo empezó en Oporto, en aquel RICI4, donde Delfi me habló de los efectos Hofmeister y me ofreció realizar la tesis doctoral con proteínas, iones y otros cachivaches. Más tarde, Carlos se unió a nuestra aventura, trajo consigo su conocimiento infinito sobre AFM y me enseñó lo importantes que son las manualidades en el laboratorio. Finalmente, Jordi se incorporó al equipo tesis y me ilustró en la parte de simulación que en mi opinión ha enriquecido en gran medida este trabajo. Desde el principio me hizo mucha ilusión poder trabajar en el laboratorio y también con el ordenador, ha sido realmente divertido poder manipular y observar las moléculas con las que también realizaba experimentos reales. Junto a vosotros me he sentido, en todo momento, parte de un gran equipo, sobre todo en esas reuniones donde resolvíamos grandes incógnitas y surgían nuevos retos. Muchas gracias por darme la oportunidad de trabajar con vosotros y por vuestra dedicación incansable.

También quiero agradecer al proyecto de excelencia de la Junta de Andalucía (P10-CTS-6270) que ha supuesto el apoyo económico sin el cual esta tesis no podría haberse realizado, y a las ayudas COST Action: Smart and green interfaces (MP1106) and Materials, Physics and Nanosciences (MP1303) que han financiado las estancias en Burdeos.

Me gustaría dar las gracias a todas las personas que me sirvieron de enlace entre mi etapa académica y mi etapa investigadora. Al grupo de Guillermo Rus donde pude iniciarme en la investigación. A Arturo Moncho, con el que pude realizar una beca de colaboración y que fue mi primer contacto en el mundo de los coloides. Gracias también a todos los profesores que me dieron clase durante el máster, donde considero que adquirí los conocimientos básicos en coloides e interfaces,

en especial a los del Grupo de Física de Fluidos y Biocoloides a los que siento más cercanos: Juan, Alberto, Julia, Pepe y Juan Luis.

También mencionar mi breve pero enriquecedora etapa desde el otro lado, como docente. Siento que he tenido mucha suerte al compartir docencia con Jorge, María, Artur, Fernando y Francisco; he aprendido y disfrutado mucho esta experiencia con vosotros. Quiero dar las gracias también a Irene Gallego que siempre tiene tantas ganas por aprender, gracias a ella pude entrever la experiencia de ser supervisora.

Y por supuesto quiero dar las gracias a todas las personas que constituyen el grupo de Física de Fluidos y Biocoloides, por hacer de este un grupo con integridad humana, en el que uno realmente se siente a gusto trabajando. En particular a sus pilares más visibles, Roque Hidalgo, Mª José Gálvez y Miguel Cabrerizo por preocuparos de la continuidad de este grupo de investigación. También quiero dar las gracias a Miguel Heredia, Belén y Conrado por mostrarse siempre serviciales cuando hay que resolver un problema burocrático. Muchas gracias a todos por vuestra calidez.

I would like to thank all the people that helped me during my stays at the Centre de Recherche Paul Pascal in Bordeaux. Thanks to Joanna Giermanska, who shared with me the QCM with absolute disponibility and thanks for the maintaining of the lab. To Hassan Saadaoui for his assistance with the AFM. To Kai Huang and Vincent Senechal for their help in the lab. To my office mates: George and Marie; and to Noelia, Miguel, Hanbin and Laura for their company at lunch time.

Y hablando de estancias, doy las gracias a Ana por esas fantásticas cenas en Burdeos. A Raquel por las veces que me recogió del aeropuerto de Barcelona y me invitó a comer. También a Elodia por abrirme su casa como si fuera la mía y por su deliciosa comida. Y a Cristina, en Granada, por interesarse siempre por como va todo.

No podían faltar en estas páginas las personas con las que comparto el día a día y que ya no sé discernir entre compañeros de trabajo y amigos. A los que dejaron atrás Granada pero que espero nos reencontremos pronto: a Amelia la chica que lo puede todo, a Paola la chica salvaje; a las dos me gustaría dedicaros un gracias especial, porque sin vuestra ayuda esta tesis no habría podido terminarse en el tiempo estipulado. Gracias también a Azahara porque es la persona más valiente que conozco, a Juan Pablo porque siempre está ahí si necesitas hablar, a Kasia por su dulzura de princesa polaca, a Laura por su eterna sonrisa, a Carmen que es el claro ejemplo de mujer fuerte, a Felipe por su sentido del humor y a Jesús Felipe que es un auténtico súper héroe. También a los que todavía seguís por aquí: a Álvaro por estar siempre ahí y preocuparse por todos (aunque no lo reconozca), a Germán por sus azarosos abrazos, a José Antonio porque juntos hemos sufrido y disfrutado los momentos tesis, a Irene a la que siempre puedo pedir opinión sobre si una gráfica es lo suficientemente bonita y con la que puedo hablar de todo, a Teresa porque siempre tiene palabras de ánimo y empatía, a Mª del Mar por su

capacidad innata de pegamento humano que tan necesaria es, a Paloma por su inigualable contacto humano que quita todas las preocupaciones, a Keshwad que no puede evitar ser divertido, a Elisa que poco a poco se está convirtiendo en un miembro indispensable entre nosotros, a José Rafael por su optimismo, a Inma por sus cálidos saludos y a Diego al que se le echa mucho de menos en la sala. También a los que no sois o habéis sido estrictamente del departamento, pero que habéis formado parte de mi vida durante la realización de mi tesis en mayor o menor medida, gracias a Esperanza por entenderme perfectamente, a Miki por nuestra conexión telepática, a Jordi por preocuparse por mí incluso a distancia, a Laura con la que he pasado muy buenos momentos y espero que sean más, a Juanpe porque cuando vuelve es como si no se hubiera ido, a Rafa por plantearnos siempre nuevas formas de ver la vida, a Fernando por su alegría permanente, a Alice por revolucionarnos a todas, a Ben por mantenernos cuerdos, a Pablo por su dedicación tan raccord, a José Alberto por hacerme ver que hay que aprovechar la vida aquí y ahora, a Javi Lizana por nuestros saludos especiales, a Virginia por los ratos divertidos, a Nico por nuestra complicidad y porque siempre me hace reír y a Adrián por ser tan noble y atento. Gracias por todos los momentos que hemos pasado juntos, y por todos los que nos quedan por compartir.

Gracias a mis padres, Leonor y Serafín, por darme una educación que me ha permitido llegar hasta este punto, pero sobre todo por apoyarme siempre y darme tanto cariño. Gracias a vosotros soy quien soy. Gracias a toda mi familia por brindarme una vida feliz, especialmente a mis abuelos Andrés y Ana, pero también a mis tíos y primos y a todos los que habéis estado siempre a mi alrededor. Además, quiero dar las gracias a mi familia más reciente que me hace sentir muy querida, me siento muy feliz de que forméis parte de mi vida. Gracias a Blanca, Pepe, Carmen, José David, Elisa y a mis sobrinos a los que adoro, Isabel y José.

Y por supuesto a Migue que siempre me ha animado a seguir hacia delante, recordándome en cada momento que yo podía conseguirlo. Gracias por entenderme, cuidarme y quererme siempre tanto sin pedir nada a cambio. Me siento muy agradecida de que nos cruzaramos en la vida y de que supiéramos agarrarnos. Estoy deseando continuar mi vida contigo y con todas las personas que nos quieren.

Contents

Abstract

Ionic specificity, also known as Hofmeister effects, is a widely studied phenomenon related with the ability of ions of the same valence to produce different effects over many interfaces. Anions and cations were arranged by Hofmeister in 1888 according to their capability of precipitating proteins. Ions are classified in these series as kosmotropes (strongly hydrated) or chaotropes (weakly hydrated). In addition, anions usually produce more intense effects than cations.

Many authors have developed different models to explain ion specific phenomena considering ion characteristics as size, polarizability or ion hydration; and ion-surface interactions by dispersion forces, chemical bindings or water hydration layers. Nevertheless, in spite of the performed advances in this area, a detailed microscopic theory to completely understand ionic specificity is still absent.

This thesis aims to elucidate the subjacent microscopic mechanisms in ionic specificity. For that, experiments, simulations and theoretical studies with different systems have been performed. We propose that ion accumulation or exclusion from interfaces is mediated by the interaction of the solvent with both, ions and surfaces. Special emphasis has been given to organic ions. The tetraphenyl ions are big hydrophobic ions recently added to the Hofmeister series as superchaotropes. These organic ions allow us to explore further in ion specific effects, since they have a deep impact on interfaces, in particular on hydrophobic soft systems as polymers or proteins. An attractive characteristic of the tetraphenyl ions is that the anion (Ph_4B^-) and the cation (Ph_4As^+) are nearly identical. We have demonstrated that the anion and the cation show different behaviors in solution and when they interact with other surfaces in spite of their similar chemical structure. Moreover, the anion always shows stronger specific effects than the cation. In addition, this difference is greater when ions interact with the thermoresponsive polymer PNIPAM (Poly (N-isopropylacrylamide)) instead of hard surfaces. This favorable interaction is mediated by the hydrophobic effect.

PNIPAM undergoes a sharp and reversible transition from a soluble to an insoluble state in aqueous solution. The transition temperature can be modified by the ionic conditions of the medium. We have studied this transition temperature with inorganic and organic ions. We have observed that the transition depends on

the capacity of the ions to compete with the water hydrating PNIPAM and also to the affinity of the poorly hydrated ions to accumulate on the hydrophobic moieties of the PNIPAM. The great ion accumulation in the insoluble state of PNIPAM produces important charge reversal of charged PNIPAM microparticles, when these last ions act as counterions.

On the other hand, several proteins of biotechnological interest and different degree of hydrophobicity were studied by physical adsorption of the different proteins onto hydrophobic surfaces. We have observed that the accumulation of the tetraphenyl ions is greater on increasingly hydrophobic interfaces. In addition, these large ions interact so strongly with the soft biomolecules that proteins undergo conformational changes. Proteins films, in water, are swollen when ions enhance their electrostatic charge, while these layers are compressed when ions screen the electrostatic repulsion between molecules. Nevertheless, the ionic concentration needed to achieve similar states of structuring protein is one order of magnitude lower for Ph_4B^- than for Ph_4As^+ corroborating that the anion causes more intense effects than the cation.

To carry out all this study we have used several experimental techniques, the most relevant of them have been: electrophoretic mobility, Atomic Force Microscopy (AFM), Quartz Crystal Microbalance (QCM), and Differential Scanning Calorimeter (DSC). In addition, Molecular Dynamics (MD) simulations were developed to analyze at microscopic level the interaction between ions and interfaces.

Resumen

La especificidad iónica, también conocida como efectos Hofmeister, es un fenómeno ampliamente estudiado relacionado con la habilidad de iones de la misma valencia para producir efectos diferentes sobre multitud de propiedades en interfaces. En 1888, Hofmeister ordenó los aniones y los cationes en función de su capacidad para precipitar proteínas. En estas series, los iones se clasifican en función de su grado de hidratación como kosmotrópicos (fuertemente hidratados) o caotrópicos (débilmente hidratados). Además, otra característica de la especificidad iónica es que los aniones suelen producir efectos más intensos que los cationes.

Existen en la bibliografía numerosos modelos que tratan de explicar los fenómenos de especificidad iónica. En dichos modelos, se han considerado diferentes características de los iones tales como tamaño, polarizabilidad o hidratación entre otras, así como, interacciones entre iones y superficies a través de fuerzas de dispersión, uniones químicas o capas de hidratación. Sin embargo, a pesar de los últimos avances realizados en este campo, aún no existe una teoría que sea capaz de explicar el origen de los fenómenos Hofmeister en su totalidad.

La presente tesis tiene como objetivo dilucidar los mecanismos microscópicos que dan lugar a la especificidad iónica. Para ello, se han realizado experimentos, simulaciones y estudios teóricos con diferentes sistemas. Se propone que la acumulación o exclusión de los iones en las interfaces está mediada por la interacción del solvente tanto con iones como con superficies. Se ha hecho especial hincapié en los iones orgánicos. Los iones tetrafenil son iones hidrófobos de gran tamaño que han sido recientemente añadidos a las series de Hofmeister como súper caotrópicos. Estos iones orgánicos nos permiten explorar la especificidad iónica desde otro punto de vista. Los iones orgánicos interaccionan mucho más fuerte con las interfaces que los iones inorgánicos, sobre todo en sistemas hidrófobos de tipo *soft* como polímeros o proteínas. Una característica muy relevante de los iones tetrafenil es que el anión (Ph_4B^-) y el catión (Ph_4As^+) son prácticamente idénticos. A pesar de su similar estructura química, hemos demostrado que el anión y el catión muestran comportamientos diferentes en solución y cuando interactúan con otras superficies. De hecho, el anión siempre muestra efectos específicos más acusados que el catión. Además, esta diferencia se hace mayor cuando estos iones

interactúan con el polímero termosensible PNIPAM (Poli (N-isopropilacrilamida)) en lugar de con superficies duras. El efecto hidrófobo es el responsable de esta interacción favorable.

El PNIPAM experimenta una transición reversible y abrupta desde un estado soluble a otro insoluble en solución acuosa. La temperatura de transición puede verse afectada por las condiciones iónicas del medio. Hemos estudiado esta temperatura de transición con iones inorgánicos y orgánicos, observándose que la transición depende de la capacidad de cada ion de competir por el agua que hidrata el PNIPAM, así como, de la afinidad de los iones pobremente hidratados de acumularse en las partes hidrófobas del PNIPAM. La gran acumulación de iones que se produce sobre el PNIPAM en su estado insoluble, causa importantes inversiones de carga de micropartículas de PNIPAM cuando los iones actúan como contraiones.

Por otro lado, hemos estudiado varias proteínas de interés biotecnológico y diferente grado de hidrofobicidad mediante adsorción física de las proteínas sobre superficies hidrófobas, observando que la acumulación de iones tetrafenil es mayor a medida que aumenta la hidrofobicidad de la interface. Además, estos iones de gran tamaño interactúan tan fuertemente con estas biomoléculas *soft* que las proteínas experimentan cambios conformacionales en su estructura. De esta manera, las películas de proteína inmersas en agua, se hinchan cuando los iones aumentan su carga electrostática, mientras que cuando los iones apantallan la repulsión electrostática entre las moléculas, las capas de proteína se comprimen. Sin embargo, la concentración iónica necesaria para obtener estados similares en la estructuración de proteínas, es un orden de magnitud menor para el Ph_4B^- que en el caso de Ph_4As^+, lo cual corrobora que el anión causa efectos más intensos que el catión.

Para llevar a cabo este estudio hemos usado diversas técnicas experimentales, las más relevantes han sido: movilidad electroforética, microscopía de fuerza atómica (AFM), microbalanza de cristal de cuarzo (QCM), y calorimetría diferencial de barrido (DSC). Este estudio se ha completado realizando simulaciones de dinámica molecular (MD) con el fin de analizar a nivel microscópico las interacciones entre iones e interfaces.

Introduction

1 Introduction

1.1 State of the art

1.1.1 Ionic solutions

Electrolyte solutions are present in most of the systems concerning to colloids and interfaces. In aqueous solutions, in particular, the existence of charged species is unavoidable and these ions provide electroneutrality to any dissolved charged solute [1, 2]. There is a wide diversity of ions that opens up a world of possibilities in the study of ionic solutions. It is not surprising that each ion shows a particular behavior in function of its characteristics, given the wide variety of sizes, shapes, polarizabilities, etc.

The consciousness of the ionic specificity arose from the experiences of Hofmeister in 1888, about protein solubility in several ionic media [3, 4]. In the last century, more and more researchers tried to elucidate why ions of the same valence are able to modify so differently the properties of any soft and solid/liquid interface in their proximities [5–8]. However, it seems that as deeper is the understanding of the ionic specificity, more interesting and unsolved issues arise.

It is important to keep in mind that the peculiar behavior of each ion is intimately linked to the nature of the solvent [9]. Bulk water forms a mobile network of hydrogen bonding that could be interrupted by the presence of ions to a greater or lesser extent [10]. In the proximities of the ions, water molecules are located at certain distance and with a particular orientation around them. The sign of the ion is one of the most noteworthy aspect, salts dissolved in water are dissociated in anions and cations. The special structure of water molecule, composed by one oxygen atom and two smaller hydrogen atoms, implicates that water molecules can approach closer to anions than to cations. In general, negatively charged species disturb the typical intermolecular forces between water molecules in a bigger extension than positive ions. For this reason, anions strongly change the properties of interfaces in comparison with cations [11–13].

Nevertheless, when the influence of anions and cations over interfaces is compared, it is not possible to exclusively attribute the differences to their unequal hydration, since commonly anions are bigger and more polarizable than cations. However, some recent simulation studies have demonstrated that in the hypothetical case of identical ions of opposite sign, anions show stronger specific effects than cations, such as larger adsorption at interfaces. It seems that this fact is directly related with the nonsymmetrical hydration of cations and anions [14].

It is worth noting that, although we cannot find atomic anions and cations of the same characteristics, some molecular ions enable to explore this possibility. For instance, organic ions like the tetraphenylarsonium cation and the tetraphenylborate anion (cf. Figure 1.1). These big hydrophobic ions possess nearly the same chemical structure and additionally, the tetraphenyl ions are monovalent. These characteristics bring the opportunity to investigate the water-mediated interactions of almost identical anions and cations with other interfaces. In the current dissertation we study ion effects over several kind of surfaces and in particular we focus on the behavior of these organic ions.

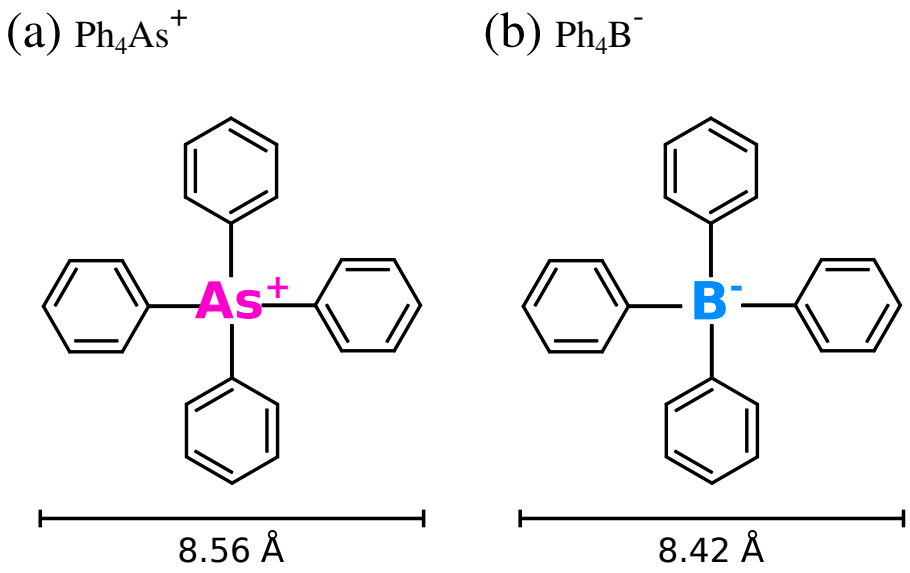

Figure 1.1: Chemical structure of (a) Ph_4As^+ and (b) Ph_4B^- ions. The van der Waals diameter is indicated [15].

1.1.2 Organic charged species: the tetraphenyl ions

The tetraphenyl ions (Ph_4B^- and Ph_4As^+) have been widely studied within the framework of single-ion solvation thermodynamics. The Ph_4AsPh_4B electrolyte assumption claims that the solvation of big organic anions or cations (with low

density of surface charge) will be almost identical to that for the corresponding (hypothetical) uncharged structure [16]. The direct implication leads to equal Gibbs free energies of transfer of these ions from one solvent to another; and even similar values of enthalpies and entropies at a given temperature [17].

This hypothesis seems to be plausible, since both ions have nearly the same size, shape and external groups. The only difference between the cation and anion underlies in the central atom, which is not in direct contact with the solvent. Nevertheless, simulation studies reveal that the free energies of transfer from water to nonpolar solvents are substantially different for the anion and the cation [18, 19]. Furthermore, recent spectroscopy results [20] have demonstrated that the arrangement of water molecules around these ions is strongly dependent on the anionic or cationic character. According to these results, the anion disrupts the water bulk structure to a greater extent in comparison with the cation.

As we have mentioned, the tetraphenyl ions show subtle differences in hydration, however, when the anion and cation interact with other systems, this difference is magnified. As direct consequence, we will see in the current dissertation that the anion always shows a more hydrophobic behavior than the cation.

Beyond the anion/cation asymmetry, both ions intensely interact with hydrophobic interfaces. The responsible driving force is the hydrophobic effect, which arises from the particular properties of water as solvent. Although the solvation of an hydrophobic molecule in water is energetically favorable, hydrophobic solutes tend to accumulate at interfaces [21, 22]. This leads to a dehydration of the surface and a decrease in the number of solvent molecules affected by these hydrophobic compounds. The ion adsorption to interfaces, although less marked, can be also experimented by small ions depending on their nature.

1.1.3 Hofmeister series: ion hydration

Commonly, inorganic ions are ordered according to the Hofmeister or lyotropic series. These sequences were established by Hofmeister as a function of the ion specific capability to enhance protein solubility [3]. The same series are followed by ions in numerous experimental systems: surface tension [23–25], protein stability [26], macromolecule solubility [27], colloidal aggregation [28, 29], among others.

Ions are arranged depending on their hydration degree in kosmotropic (well-hydrated) or chaotropic (poorly hydrated) ions. This character directly affects to ion-surface interaction mediated by the solvent. Although different parameters have been used trying to explain Hofmeister effects, it seems that the solvent structure around ions and surfaces is the main key under ionic specificity phenomena. Representative Hofmeister series for anions and cations are shown below:

Derjaguin–Landau–Verwey–Overbeek (DLVO) theory describes the interparticle interaction between colloids taking into account van der Waals and electrostatic

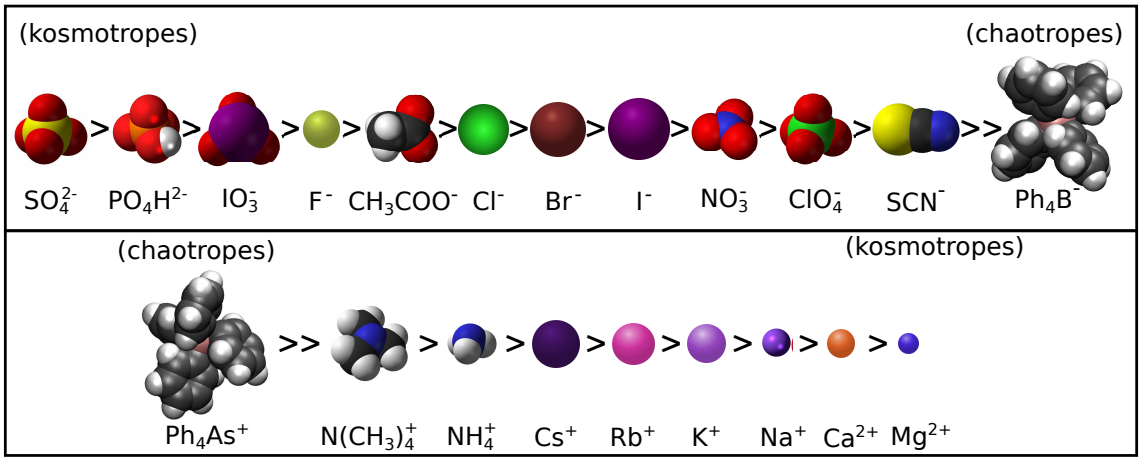

Figure 1.2: Representative Hofmeister series for anions and cations. Tetraphenyl ions are included as super-chaotropes.

interactions [30]. In the framework of this theory, water is treated as continuum dielectric and ions are modelled as point charges. In addition, nonelectrostatic forces of chemical origin are added to explain the specific adsorption of ions on surfaces, which cannot be justified by Coulombic interactions [31]. In this classical model, an adsorption isotherm is formulated for ions, whose parameters are experimentally determined. However, many authors have developed other models taking into account ion characteristics as size, polarizability or hydration to explore other possible explanations of ionic specificity [32–45]. Ninham and coworkers have widely contributed in this field. In many of their works [32–36], nonelectrostatic interactions are included in the Poisson-Boltzmann distribution. An additional term introduces the ion-surface and ion-ion dispersion forces related with the finite size of ions. On the other hand, from a qualitative point of view it is very well-accepted the "Law of matching water affinities" developed by Collins [37, 38]. According to this model, ion pairs are formed from opposite sign ions with similar solvation energies. Furthermore, Dos Santos and Levin developed a theory where the accumulation or exclusion of ions is completely dependent on the ion hydration. In the vicinity of a hydrophobic surface, kosmotropic ions maintain their strong hydration, while the chaotropic ones are adsorbed to the interface and lose their hydration shell [39, 40]. Nevertheless, a detailed and complete molecular understanding at microscopic level able to explain the specific adsorption or exclusion of ions from interfaces is still missing.

Ionic specificity is not exclusive of water, numerous works investigate this phenomenon in nonaqueous solvents [46–49]. The main conclusion is that the solvent structure results essential in the ion-interface interactions.

Regarding to organic ions, the tetraphenyl ions are not arranged in the classi-

cal Hofmeister series. However, the tetraphenyl anion has recently been included as an extension of the anionic Hofmeister series as super-chaotropes. This anion is referred as disruptor of soft-matter because they undergo stronger interactions with hydrophobic and soft matter systems in comparison to inorganic ions [50]. In addition, we have included the tetraphenyl cation in the cationic Hofmeister series. This cation is also classified as super-chaotrope due to the kind of interactions showing with interfaces [51, 52].

Nevertheless, we cannot ignore the role of the surface that, together with ion and water, provides the complete picture in these puzzling phenomena.

1.1.4 The role played by the nature of the surface

The established ionic sequence according to an determined experience is clearly influenced by the surface. The Hofmeister series are not unique, but instead the specific order depends on the characteristics of the surface and the medium conditions [6]. Direct, indirect or partially reversed series can be found by changing the positive/negative charge or the hydrophobic/hydrophilic nature of the surface [28, 39, 53–57].

Aside from the coion/counterion role, chaotropes and especially organic ions, are accumulated around hydrophobic interfaces, while they are excluded from hydrophilic ones. On the other hand, kosmotropes are attracted to hydrophilic surfaces, although not so intensely. The highly-structured water layers formed around kosmotropes and hydrophilic surfaces avoid a close approach like that in the case of chaotropes and hydrophobic surfaces (which are easily dehydrated). On the other hand, different water structures can explain why cations usually show less marked ionic specificity than anions. In general, the hydration layer formed around cations is more stable than that around anions. Therefore, anions usually disrupt the water bulk structure to a greater extent in comparison with cations. For this reason, anions can be easily dehydrated and they are more noticeable in ionic specificity.

In this way, we can establish a mechanism of ion accumulation/exclusion in the vicinity of interfaces according to chaotropic/kosmotropic ion character and hydrophobic/hydrophilic nature of surfaces. This mechanism is justified by entropic forces related with the attraction or repulsion between compounds with similar or disimilar microscopic hydration, respectively [12, 29, 56–58]. All of this can be summarized in the affinity to water of ions and interfaces.

In this dissertation, we provide a broad variety of studies with experimental systems and simulations, where this mechanism clearly comes out. Soft materials are very suitable to study ion effects, since it is possible to obtain different hydrophobic and hydrophilic degrees of the interfaces. In addition, this kind of systems are very sensitive to ion environment.

1.1.5 Soft systems

Polymers of type stimuli-response are interesting systems that show a soluble and insoluble state depending on the environmental conditions. The most studied system of this kind is, by far, the Poly (N-Isopropylacrylamide) (PNIPAM). PNIPAM is a thermoresponsive polymer used in many application fields [59–64]. In addition, it has shown very sensitive to ionic specificity. This polymer has both nature, hydrophilic and hydrophobic, and it can exist in a expanded or collapsed state as a function mainly of the temperature of the aqueous solution. The sharp transition temperature between both states is named lower critical solution temperature (T_{LCS}) and has a value around 32ºC [65]. Water is a good solvent for PNIPAM chains at temperatures below T_{LCS}, however chains become abruptly collapsed and form aggregates above this temperature. The coil-to-globule transition of the PNIPAM seems to be dominated by hydrogen bonding and hydrophobic forces in both intra- and inter-chains interactions, as some experimental and simulation studies have demonstrated [66–68].

PNIPAM chains are neutral, thus they are very useful to study ionic specificity irrespective of electrostatic interactions. However, it is possible to obtain reticulated polymeric particles formed by PNIPAM and other charged agents [69]. In this way, microgels with swelling-to-collapse transition are obtained. The stability of these colloidal particles is steric in the swollen state, while in the compact state appears electrostatic stabilization [70]. Both, positively or negatively charged particles can be synthesized, thus the role of the ions acting as coions or counterions can be explored.

Interestingly, the ionic enviroment has an important influence on the observed T_{LCS} [27]. In general, ions can help to dehydrate the polymer causing the transition at lower temperatures. This effect is very sensitive to ion concentration. Kosmotropic ions are more efficient in decreasing the T_{LCS} than the intermediate ions. Therefore, under conditions of equal concentrations, ions can be arranged according to the Hofmeister series as a function of the obtained T_{LCS}.

A striking result is observed in the case of the most chaotropic ions; they are able to slightly increase the value of the T_{LCS} at moderate ion concentrations [27, 71]. This behavior can be explained by the exclusion of these poorly solvated ions from the hydrophilic interface; the hydration around the polymer is enhanced because of unfavorable water-chaotrope interactions [72, 73]. Nevertheless, after the coil-to-globule transition, the ion interaction becomes more favorable and the ion adsorption to the PNIPAM is usually accompanied by a change in the electrokinetic charge of the system. This can result in charge reversal or overcharging of the particles depending on the counterion or coion role, respectively [73–75].

PNIPAM shows another highlighted characteristic; its chemical composition is very similar to an amino acid sequence, like in the case of proteins. Many works relate the similarities between the transition state of PNIPAM and cold denatura-

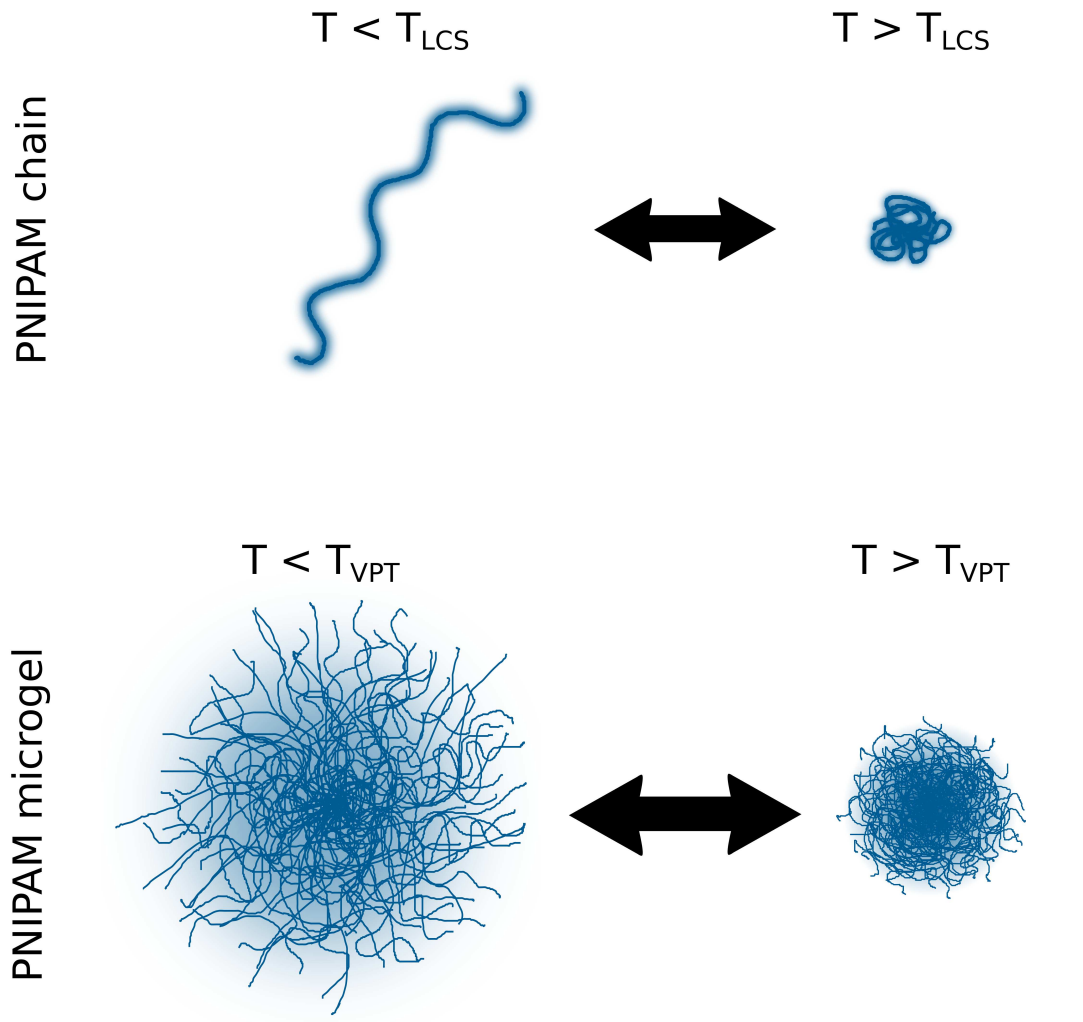

Figure 1.3: Reversible transition of PNIPAM from soluble to insoluble state according to temperature. The transition temperature is called lower critical solution temperature (T_{LCS}) for chains and volume phase transition temperature (T_{VPT}) for microgels (reticulated polymeric particles).

tion of proteins [76–80]. This polymer is a less complex system similar to proteins, thus is suitable to predict ion-protein interactions.

Protein folding and stability is determined by a balance of thermodynamic forces, such as electrostatic, van der Waals, conformational entropy, hydrogen bonding and hydrophobic interactions [81, 82]. Favorable (unfavorable) water-protein interaction is the key of the unfolding (folding) state of the proteins. This mechanism determines the degree of the hydrophobic interactions between residues, which maintain the native state of proteins. Changes in water structure

can come from thermodynamic conditions [83], as well as, the presence of ionic species. Numerous publications study protein stability and protein structure in presence of classical Hofmeister ions [26, 55, 84, 85]. Nevertheless, the interaction of organic ions with biomolecules is not very explored at date. We can found in the literature the effect of denaturing agents on proteins, for example organic surfactants [86, 87] or organic molecules such as, urea and guanidinium that interact strongly with proteins [88]. In contrast, organic osmolytes enhance the native state of proteins by osmolyte exclusion [89, 90]. Other compounds can act as protein-stabilizer or destabilizer depending on the medium conditions, as polyoxometalates (POMs) [91–93] or ionic liquids (ILs) [94–96], which are considered as super-chaotropes and are included as an extension in the Hofmeister series. Constantinescu *et al.*, dealing with ILs, found that the most chaotropic organic anions intensely interact and have a destabilizing effect on the native state of proteins, due to their weak hydration [97].

The tetraphenyl ions are big molecules in comparison with inorganic ions, but smaller than the typical organic compounds previously studied. In addition, their monovalent character makes them very adequate to investigate the hydrophobic interaction between ions and proteins. To the best of our knowledge, there are not studies in the literature about the interactions of tetraphenyl ions with proteins in relation with ionic specificity. In our opinion, the study of the tetraphenyl ions, also known as soft-matter disruptors [50], could contribute to a better understanding of the ionic specificity.

1.2 Objectives

The objective of this thesis is to investigate the underlying mechanisms to ionic specificity in aqueous systems. These universal phenomena are very relevant in the colloid and interface field since they are present in almost each ionic solution. In spite of the numerous advances in this area, today is an unsolved issue. In recent publications, many factors are taking into account: ion properties like size, shape or polarizability; hydration of chaotropic and kosmotropic ions; and non-electrostatic interactions between ions and surfaces. However, there are still some open questions: how water (or solvent) is affected at microscopic level by the presence of ions and interfaces; how the ion-surface interaction is related with the water structure around both; and, in general, why anions produce more marked effects than cations. This thesis aims to try to answer these questions.

This thesis is structured in three parts according to the system studied.

The first part is composed by three Chapters (4, 5 and 6) centered on the study of PNIPAM microgels and chains. The specific objectives of this part were:

1. To study the effect of organic ions on PNIPAM microgels with electrophoresis and Atomic Force Microscopy (AFM) techniques.

2. To identify the responsible underlying mechanisms of the strong interaction of PNIPAM and the organic ions by Molecular Dynamics (MD) simulations.

3. To investigate the collapsed-swollen transition of the microgels in presence of inorganic and organic ions with Quartz Crystal Microbalance (QCM).

4. To analyze the coil-to-globule transition of PNIPAM neutral chains in presence of inorganic and organic ions using Differential Scanning Microcalorimeter (DSC) technique.

The second part was focused on the study of allergenic proteins (Chapter 7 and 8). The main objectives are enumerated as follows:

1. To determine the structure and electrostatic charge of the proteins: β-casein, β-lactoglobulin and BSA in aqueous solution and at room temperature from the crystallographic known-structure by MD simulations.

2. To explore structural changes and molecule orientation in protein adsorption by MD simulations.

3. To study the protein adsorption onto hydrophobic flat substrates and hydrophobic polystyrene (PS) microspheres.

4. To characterize the protein-coated microparticles by electrophoretic mobility as a function of pH.

5. To analyze the possible effect of counterion condensation on protein-coated microparticles by comparison of theoretical models with electrokinetic measurements.

6. To stablish a sequence of hydrophobicity for the different proteins using thermodynamic calculations.

7. To study the extension of the interaction of organic ions with interfaces of different degree of hydrophobicity using electrokinetic and stability measurements.

8. To analyze the conformational changes of protein films in presence of organic ions by QCM.

The last part (Chapter 9) was aimed to study the interactions of organic ions with model surfaces by simulations and theoretical calculations. The specific objectives of this part were:

1. To quantify the interaction of organic ions on model surfaces of both nature, hydrophilic and hydrophobic by MD simulations.

2. To determine, by theoretical calculations, the ion-accumulation onto charged surfaces of opposite sign responsible for great charge inversions experimentally observed.

3. To study, using simulations, the hydration of the organic cation and anion in solution and when they are adsorbed onto a surface.

References

[1] Butt, H.-J.; Graf, K.; Kappl, M., *Physics and chemistry of interfaces*; John Wiley & Sons: 2006.

[2] Ricci, M.; Spijker, P.; Voïtchovsky, K. Water-induced correlation between single ions imaged at the solid–liquid interface. *Nat. Commun.* **2014**, *5*.

[3] Hofmeister, F. On the understanding of the effects of salts. *Arch. Exp. Pathol. Pharmakol.(Leipzig)* **1888**, *24*, 247–260.

[4] Kunz, W.; Henle, J.; Ninham, B. W. 'Zur Lehre von der Wirkung der Salze'(about the science of the effect of salts): Franz Hofmeister's historical papers. *Curr. Opin. Colloid Interface Sci.* **2004**, *9*, 19–37.

[5] Kunz, W., *Specific Ion Effects*; World Scientific Publishing Company: 2010.

[6] Lyklema, J. Simple Hofmeister series. *Chem. Phys. Lett.* **2009**, *467*, 217–222.

[7] Ninham, B. W.; Nostro, P. L., *Molecular forces and self assembly: in colloid, nano sciences and biology*; Cambridge University Press: 2010.

[8] Collins, K. D.; Washabaugh, M. W. The Hofmeister effect and the behaviour of water at interfaces. *Q. Rev. Biophys.* **1985**, *18*, 323–422.

[9] Robinson, R. A.; Stokes, R. H., *Electrolyte solutions*; Courier Corporation: 2002.

[10] Tielrooij, K.; Garcia-Araez, N.; Bonn, M.; Bakker, H. Cooperativity in ion hydration. *Science* **2010**, *328*, 1006–1009.

[11] Lyklema, J. Lyotropic sequences in colloid stability revisited. *Adv. Colloid Interface Sci.* **2003**, *100*, 1–12.

[12] López-León, T.; Jódar-Reyes, A.; Ortega-Vinuesa, J.; Bastos-González, D. Hofmeister effects on the colloidal stability of an IgG-coated polystyrene latex. *J. Colloid Interface Sci.* **2005**, *284*, 139–148.

[13] Morita, T.; Westh, P.; Nishikawa, K.; Koga, Y. How Much Weaker Are the Effects of Cations than Those of Anions? The Effects of K^+ and Cs^+ on the Molecular Organization of Liquid H_2O. *J. Phys. Chem. B* **2014**, *118*, 8744–8749.

[14] Yang, L.; Fan, Y.; Gao, Y. Q. Differences of cations and anions: Their hydration, surface adsorption, and impact on water dynamics. *J. Phys. Chem. B* **2011**, *115*, 12456–12465.

[15] Kim, J. Preferential solvation of single ions. A critical study of the Ph4AsPh4B assumption for single ion thermodynamics in amphiprotic and dipolar-aprotic solvents. *J. Phys. Chem.* **1978**, *82*, 191–199.

[16] Grunwald, E.; Baughman, G.; Kohnstam, G. The Solvation of Electrolytes in Dioxane-Water Mixtures, as Deduced from the Effect of Solvent Change on the Standard Partial Molar Free Energy. *J. Am. Chem. Soc.* **1960**, *82*, 5801–5811.

[17] Cox, B.; Parker, A. Solvation of ions. XVII. Free energies, heats, and entropies of transfer of single ions from protic to dipolar aprotic solvents. *J. Am. Chem. Soc.* **1973**, *95*, 402–407.

[18] Schurhammer, R.; Wipff, G. About the TATB hypothesis: solvation of the $As\varphi_4^+$ and $B\varphi_4^-$ ions and their tetrahedral and spherical analogues in aqueous/nonaqueous solvents and at a water–chloroform interface. *New J. Chem.* **1999**, *23*, 381–392.

[19] Schurhammer, R.; Wipff, G. Are the hydrophobic $AsPh_4^+$ and BPh_4^- ions equally solvated? A theoretical investigation in aqueous and nonaqueous solutions using different charge distributions. *J. Phys. Chem. A* **2000**, *104*, 11159–11168.

[20] Scheu, R.; Rankin, B. M.; Chen, Y.; Jena, K. C.; Ben-Amotz, D.; Roke, S. Charge asymmetry at aqueous hydrophobic interfaces and hydration shells. *Angew. Chem.* **2014**, *126*, 9714–9717.

[21] Sharp, K. A. The hydrophobic effect. *Curr. Opin. Struct. Biol.* **1991**, *1*, 171–174.

[22] Widom, B.; Bhimalapuram, P.; Koga, K. The hydrophobic effect. *Phys. Chem. Chem. Phys.* **2003**, *5*, 3085–3093.

[23] Boström, M.; Kunz, W.; Ninham, B. W. Hofmeister effects in surface tension of aqueous electrolyte solution. *Langmuir* **2005**, *21*, 2619–2623.

[24] Pegram, L. M.; Record, M. T. Hofmeister salt effects on surface tension arise from partitioning of anions and cations between bulk water and the air-water interface. *J. Phys. Chem. B* **2007**, *111*, 5411–5417.

[25] Dos Santos, A. P.; Diehl, A.; Levin, Y. Surface tensions, surface potentials, and the Hofmeister series of electrolyte solutions. *Langmuir* **2010**, *26*, 10778–10783.

[26] Baldwin, R. L. How Hofmeister ion interactions affect protein stability. *Biophys. J.* **1996**, *71*, 2056.

[27] Zhang, Y.; Furyk, S.; Bergbreiter, D. E.; Cremer, P. S. Specific ion effects on the water solubility of macromolecules: PNIPAM and the Hofmeister series. *J. Am. Chem. Soc.* **2005**, *127*, 14505–14510.

[28] Oncsik, T.; Trefalt, G.; Borkovec, M.; Szilagyi, I. Specific ion effects on particle aggregation induced by monovalent salts within the Hofmeister series. *Langmuir* **2015**, *31*, 3799–3807.

[29] López-León, T.; Ortega-Vinuesa, J. L.; Bastos-González, D. Ion-Specific Aggregation of Hydrophobic Particles. *ChemPhysChem* **2012**, *13*, 2382–2391.

[30] Israelachvili, J. N., *Intermolecular and surface forces: second edition*; Academic press: 1991.

[31] Lyklema, J., *Fundamentals of Interface and Colloid Science*; Fundamentals of Interface and Colloid Science; Academic Press: 1991.

[32] Parsons, D. F.; Deniz, V.; Ninham, B. W. Nonelectrostatic interactions between ions with anisotropic ab initio dynamic polarisabilities. *Colloids Surf. A* **2009**, *343*, 57–63.

[33] Parsons, D.; Bostrom, M.; Maceina, T.; Salis, A.; Ninham, B. W. Why direct or reversed Hofmeister series? Interplay of hydration, non-electrostatic potentials, and ion size. *Langmuir* **2009**, *26*, 3323–3328.

[34] Parsons, D. F.; Ninham, B. W. Charge reversal of surfaces in divalent electrolytes: The role of ionic dispersion interactions. *Langmuir* **2010**, *26*, 6430–6436.

[35] Parsons, D. F.; Boström, M.; Nostro, P. L.; Ninham, B. W. Hofmeister effects: interplay of hydration, nonelectrostatic potentials, and ion size. *Phys. Chem. Chem. Phys.* **2011**, *13*, 12352–12367.

[36] Kunz, W. Specific ion effects in colloidal and biological systems. *Curr. Opin. Colloid Interface Sci.* **2010**, *15*, 34–39.

[37] Collins, K. D. Ion hydration: Implications for cellular function, polyelectrolytes, and protein crystallization. *Biophys. Chem.* **2006**, *119*, 271–281.

[38] Collins, K. D.; Neilson, G. W.; Enderby, J. E. Ions in water: characterizing the forces that control chemical processes and biological structure. *Biophys. Chem.* **2007**, *128*, 95–104.

[39] Dos Santos, A. P.; Levin, Y. Ion specificity and the theory of stability of colloidal suspensions. *Phys. Rev. Lett.* **2011**, *106*, 167801.

[40] Levin, Y.; dos Santos, A. P. Ions at hydrophobic interfaces. *J. Phys. Condens. Matter.* **2014**, *26*, 203101.

[41] Quesada-Pérez, M.; Hidalgo-Álvarez, R.; Martín-Molina, A. Effect of ionic van der Waals forces on the diffuse potential of model colloids. *Colloid Polym. Sci.* **2010**, *288*, 151–158.

[42] Vereda, F.; Martín-Molina, A.; Hidalgo-Álvarez, R.; Quesada-Pérez, M. Specific ion effects on the electrokinetic properties of iron oxide nanoparticles: experiments and simulations. *Phys. Chem. Chem. Phys.* **2015**.

[43] Manciu, M.; Ruckenstein, E. Specific ion effects via ion hydration: I. Surface tension. *Adv. Colloid Interface Sci.* **2003**, *105*, 63–101.

[44] Jungwirth, P.; Tobias, D. J. Specific ion effects at the air/water interface. *Chem. Rev.* **2006**, *106*, 1259–1281.

[45] Lund, M.; Jungwirth, P.; Woodward, C. E. Ion specific protein assembly and hydrophobic surface forces. *Phys. Rev. Lett.* **2008**, *100*, 258105.

[46] Labban, A.-K. S.; Marcus, Y. The solubility and solvation of salts in mixed nonaqueous solvents. 2. Potassium halides in mixed protic solvents. *J. Solution Chem.* **1997**, *26*, 1–12.

[47] Freire, M. G.; Carvalho, P. J.; Silva, A. M.; Santos, L. M.; Rebelo, L. P.; Marrucho, I. M.; Coutinho, J. A. Ion specific effects on the mutual solubilities of water and hydrophobic ionic liquids. *J. Phys. Chem. B* **2008**, *113*, 202–211.

[48] Peruzzi, N.; Ninham, B. W.; Lo Nostro, P.; Baglioni, P. Hofmeister phenomena in nonaqueous media: the solubility of electrolytes in ethylene carbonate. *J. Phys. Chem. B* **2012**, *116*, 14398–14405.

[49] Peruzzi, N.; Nostro, P. L.; Ninham, B. W.; Baglioni, P. The Solvation of Anions in Propylene Carbonate. *J. Solution Chem.* 1–16.

[50] Leontidis, E.; Christoforou, M.; Georgiou, C.; Delclos, T. The ion–lipid battle for hydration water and interfacial sites at soft-matter interfaces. *Curr. Opin. Colloid Interface Sci.* **2014**, *19*, 2–8.

[51] Martín-Molina, A.; Calero, C.; Faraudo, J.; Quesada-Pérez, M.; Travesset, A.; Hidalgo-Álvarez, R. The hydrophobic effect as a driving force for charge inversion in colloids. *Soft Matter* **2009**, *5*, 1350–1353.

[52] Pérez-Fuentes, L.; Drummond, C.; Faraudo, J.; Bastos-González, D. Anions make the difference: insights from the interaction of big cations and anions with poly (N-isopropylacrylamide) chains and microgels. *Soft Matter* **2015**, *11*, 5077–5086.

[53] Schwierz, N.; Horinek, D.; Netz, R. R. Reversed anionic Hofmeister series: the interplay of surface charge and surface polarity. *Langmuir* **2010**, *26*, 7370–7379.

[54] Schwierz, N.; Horinek, D.; Netz, R. R. Anionic and cationic Hofmeister effects on hydrophobic and hydrophilic surfaces. *Langmuir* **2013**, *29*, 2602–2614.

[55] Boström, M.; Tavares, F.; Finet, S.; Skouri-Panet, F.; Tardieu, A.; Ninham, B. Why forces between proteins follow different Hofmeister series for pH above and below pI. *Biophys. Chem.* **2005**, *117*, 217–224.

[56] Peula-García, J. M.; Ortega-Vinuesa, J. L.; Bastos-González, D. Inversion of Hofmeister series by changing the surface of colloidal particles from hydrophobic to hydrophilic. *J. Phys. Chem. C* **2010**, *114*, 11133–11139.

[57] López-León, T.; Santander-Ortega, M. J.; Ortega-Vinuesa, J. L.; Bastos-González, D. Hofmeister effects in colloidal systems: influence of the surface nature. *J. Phys. Chem. C* **2008**, *112*, 16060–16069.

[58] Calero, C.; Faraudo, J.; Bastos-González, D. Interaction of monovalent ions with hydrophobic and hydrophilic colloids: Charge inversion and ionic specificity. *J. Am. Chem. Soc.* **2011**, *133*, 15025–15035.

[59] Okano, T.; Yamada, N.; Okuhara, M.; Sakai, H.; Sakurai, Y. Mechanism of cell detachment from temperature-modulated, hydrophilic-hydrophobic polymer surfaces. *Biomaterials* **1995**, *16*, 297–303.

[60] Von Recum, H.; Kikuchi, A.; Okuhara, M.; Sakurai, Y.; Okano, T.; Kim, S. W. Retinal pigmented epithelium cultures on thermally responsive polymer porous substrates. *J. Biomater. Sci.* **1998**, *9*, 1241–1253.

[61] Abbaspoor, S.; Abbasi, F.; Agbolaghi, S. A novel approach to prepare polymer mixed-brushes via single crystal surface patterning. *RSC Adv.* **2014**, *4*, 17071–17082.

[62] Park, Y. S.; Ito, Y.; Imanishi, Y. Permeation control through porous membranes immobilized with thermosensitive polymer. *Langmuir* **1998**, *14*, 910–914.

[63] Guan, Y.; Zhang, Y. PNIPAM microgels for biomedical applications: From dispersed particles to 3D assemblies. *Soft Matter* **2011**, *7*, 6375–6384.

[64] Go, H.; Sudo, Y.; Hosoya, K.; Ikegami, T.; Tanaka, N. Effects of mobile-phase composition and temperature on the selectivity of poly (N-isopropylacrylamide)-bonded silica gel in reversed-phase liquid chromatography. *Anal. Chem.* **1998**, *70*, 4086–4093.

[65] Schild, H. G. Poly (N-isopropylacrylamide): experiment, theory and application. *Prog. Polym. Sci.* **1992**, *17*, 163–249.

[66] Cho, E. C.; Lee, J.; Cho, K. Role of bound water and hydrophobic interaction in phase transition of poly (N-isopropylacrylamide) aqueous solution. *Macromolecules* **2003**, *36*, 9929–9934.

[67] Wu, C.; Wang, X. Globule-to-coil transition of a single homopolymer chain in solution. *Phys. Rev. Lett.* **1998**, *80*, 4092.

[68] Alaghemandi, M.; Spohr, E. Molecular Dynamics Investigation of the Thermo-Responsive Polymer Poly (N-isopropylacrylamide). *Macromol. Theory Simul.* **2012**, *21*, 106–112.

[69] Pelton, R.; Chibante, P. Preparation of aqueous latices with N-isopropylacrylamide. *Coll. Surf.* **1986**, *20*, 247–256.

[70] Tagit, O.; Tomczak, N.; Vancso, G. J. Probing the Morphology and Nanoscale Mechanics of Single Poly (N-isopropylacrylamide) Microgels Across the Lower-Critical-Solution Temperature by Atomic Force Microscopy. *Small* **2008**, *4*, 119–126.

[71] Shechter, I.; Ramon, O.; Portnaya, I.; Paz, Y.; Livney, Y. D. Microcalorimetric study of the effects of a chaotropic salt, KSCN, on the lower critical solution temperature (LCST) of aqueous poly (N-isopropylacrylamide)(PNIPA) solutions. *Macromolecules* **2009**, *43*, 480–487.

[72] Debeljuh, N. J.; Sutti, A.; Barrow, C. J.; Byrne, N. Phase Transition of Poly (N-isopropylacrylamide) in Aqueous Protic Ionic Liquids: Kosmotropic versus Chaotropic Anions and Their Interaction with Water. *J. Phys. Chem. B* **2013**, *117*, 8430–8435.

[73] López-León, T.; Ortega-Vinuesa, J. L.; Bastos-González, D.; Elaïssari, A. Thermally sensitive reversible microgels formed by poly (N-Isopropylacrylamide) charged chains: A Hofmeister effect study. *J. Colloid Interface Sci.* **2014**, *426*, 300–307.

[74] López-León, T.; Elaïssari, A.; Ortega-Vinuesa, J. L.; Bastos-González, D. Hofmeister effects on poly (NIPAM) microgel particles: macroscopic evidence of ion adsorption and changes in water structure. *ChemPhysChem* **2007**, *8*, 148–156.

[75] Moncho-Jordá, A.; Adroher-Benítez, I. Ion permeation inside microgel particles induced by specific interactions: from charge inversion to overcharging. *Soft matter* **2014**, *10*, 5810–5823.

[76] Ptitsyn, O. B. The molten globule state. *Protein folding* **1992**, 243–300.

[77] Tiktopulo, E. I.; Uversky, V. N.; Lushchik, V. B.; Klenin, S. I.; Bychkova, V. E.; Ptitsyn, O. B. " Domain" Coil-Globule Transition in Homopolymers. *Macromolecules* **1995**, *28*, 7519–7524.

[78] Kunugi, S.; Tanaka, N. Cold denaturation of proteins under high pressure. *Biochim. Biophys. Acta* **2002**, *1595*, 329–344.

[79] Kunugi, S.; Kameyama, K.; Tada, T.; Tanaka, N.; Shibayama, M.; Akashi, M. Differences in pressure and temperature transitions of proteins and polymer gels. *Braz. J. Med. Biol. Res.* **2005**, *38*, 1233–1238.

[80] Graziano, G. On the temperature-induced coil to globule transition of poly-N-isopropylacrylamide in dilute aqueous solutions. *Int. J. Biol. Macromol.* **2000**, *27*, 89–97.

[81] Kauzmann, W., *Some factors in the interpretation of protein denaturation. In Advances in Protein Chemistry, vol. 14, pp. 1-63*; Academic Press, NY: 1959.

[82] Dill, K. A. Dominant forces in protein folding. *Biochemistry* **1990**, *29*, 7133–7155.

[83] Bianco, V.; Franzese, G. Contribution of Water to Pressure and Cold Denaturation of Proteins. *Phys. Rev. Lett.* **2015**, *115*, 108101.

[84] Melander, W.; Horváth, C. Salt effects on hydrophobic interactions in precipitation and chromatography of proteins: an interpretation of the lyotropic series. *Archiv. Biochem. Biophys.* **1977**, *183*, 200–215.

[85] Pegram, L. M.; Record Jr, M. T. Thermodynamic origin of Hofmeister ion effects. *J. Phys. Chem. B* **2008**, *112*, 9428–9436.

[86] Lee, A.; Tang, S. K.; Mace, C. R.; Whitesides, G. M. Denaturation of proteins by SDS and tetraalkylammonium dodecyl sulfates. *Langmuir* **2011**, *27*, 11560–11574.

[87] Jain, S.; Ahluwalia, J. Differential scanning calorimetric studies on the effect of ammonium and tetraalkylammonium halides on the stability of lysozyme. *Biophys. Chem.* **1996**, *59*, 171–177.

[88] David, G. N. S. et al., *Biochemical Adaptation: Mechanism and Process in Physiological Evolution: Mechanism and Process in Physiological Evolution*; Oxford University Press: 2001.

[89] Clark, M. In *Transport processes, iono-and osmoregulation*; Springer: 1985, pp 412–423.

[90] Bolen, D.; Baskakov, I. V. The osmophobic effect: natural selection of a thermodynamic force in protein folding. *J. Mol. Biol.* **2001**, *310*, 955–963.

[91] Wu, Q.; Wang, J.; Zhang, L.; Hong, A.; Ren, J. Molecular recognition of basic fibroblast growth factor by polyoxometalates. *Angew. Chem.* **2005**, *117*, 4116–4120.

[92] Sun, L.; Wu, Q.; Liu, N.; Yang, C.; Liu, L.; Liu, Z.; Zhao, D. Effects of $K_5SiW_{11}O_{39}Co$ on mitogenic activity of basic fibroblast growth factor. *Chem. Lett.* **2004**, *33*, 298–299.

[93] Prudent, R.; Moucadel, V.; Laudet, B.; Barette, C.; Lafanechère, L.; Hasenknopf, B.; Li, J.; Bareyt, S.; Lacôte, E.; Thorimbert, S. et al. Identification of polyoxometalates as nanomolar noncompetitive inhibitors of protein kinase CK2. *Chem. Biol.* **2008**, *15*, 683–692.

[94] Fujita, K.; MacFarlane, D. R.; Forsyth, M. Protein solubilising and stabilising ionic liquids. *Chem. Commun.* **2005**, 4804–4806.

[95] Fujita, K.; Forsyth, M.; MacFarlane, D. R.; Reid, R. W.; Elliott, G. D. Unexpected improvement in stability and utility of cytochrome c by solution in biocompatible ionic liquids. *Biotech. Bioeng.* **2006**, *94*, 1209–1213.

[96] Rodrigues, J. V.; Prosinecki, V.; Marrucho, I.; Rebelo, L. P. N.; Gomes, C. M. Protein stability in an ionic liquid milieu: on the use of differential scanning fluorimetry. *Phys. Chem. Chem. Phys.* **2011**, *13*, 13614–13616.

[97] Constantinescu, D.; Weingärtner, H.; Herrmann, C. Protein denaturation by ionic liquids and the Hofmeister series: a case study of aqueous solutions of ribonuclease A. *Angew. Chem.* **2007**, *46*, 8887–8889.

III Materials and Methods

2 Experimental section

2.1 Materials

2.1.1 Reagents

All the products were of analytical grade and used as received. The salts used were purchased from Scharlau and Sigma Aldrich. The tetraphenyl salts were obtained from Sigma Aldrich: sodium tetraphenylborate (ref T25402) and tetraphenylarsonium chloride (ref T25305). Water used in all experiments was double distilled and deionized (DDI) with a Milli-Q Water Purification System (Millipore).

2.1.2 Proteins and buffered solutions

The proteins used were supplied by Sigma Aldrich: bovine serum albumin (BSA) (ref A7030), β-lactoglobulin (ref L3908) and β-casein (ref C6905). Several buffers of low ionic strength (lower than 2 mM) were used: pH 4 and 5 were buffered with acetic acid, pH 6 and 7 with monosodium phosphate and pH 8, 9 and 10 with boric acid. In each case, the pH was adjusted by adding NaOH. In addition, we used a buffered solution at pH 7 with Bis-Tris in order to dissolve the β-casein protein [1]. The pH of this solution was adjusted by adding HCl, the ionic strength of the solution was of 2.4 mM. Nonbuffered solution at pH 3 was prepared by adding dilute HCl to DDI water.

2.1.3 Polystyrene latex microspheres

Two kind of polystyrene (PS) microspheres were used: negatively and positively charged in all pH range studied (pH 3–10). The anionic latex was synthesized in our laboratories. Sulfonate groups provide the anionic nature, whose surface charge density is –9.6 μC/cm^2. This latex has a mean diameter of 138$\pm$7 nm with high monodispersity [2, 3]. The positive polystyrene latex has a surface charge

density of 17.4 μC/cm^2 and a mean diameter of 475$\pm$4 nm. Its positive charge is given by amine groups (IKERLAT polymers).

2.1.4 PNIPAM chains and microgels

Poly (N-isopropylacrylamide) (PNIPAM) (M_w=19000 – 30000 g/mol) was purchased from Sigma-Aldrich (ref 535311). The reagents needed for the preparation of the microgels: N-Isopropylacrylamide (NIPAM), N,N-Methylenebisacrylamide (MBA), aminoethyl methacrylate hydrochloride (AEMH) and 2-2'-Azobis-(amidinopropane) di-chloride (V50) were obtained from Acros. Potassium persulfate (KPS) was supplied by Sigma-Aldrich.

2.2 Synthesis of PNIPAM microgels

Crosslinked PNIPAM microgels were prepared using batch radical polymerization. During the synthesis, NIPAM monomers are copolymerized with crosslinker agents forming polymer chain networks [4]. The polymerization starts when the initiator is added, reacting with the monomers. The temperature of the process need to be well above the T_{LCS} of PNIPAM in order to enable the growth of particles. PNIPAM chains are very insoluble under these conditions, thus they collapse into growing aggregates until electrostatic repulsion is high enough to ensure the stability of the growing particles. The electrostatic charge of the microgels comes from the ionic initiator and other ionic compounds in some cases. When the synthesis process is completed, the stability of the particles below the T_{LCS} is ensured by the steric effect [5].

Characteristics of the microgels such as the morphology, size, density, molar mass and swelling ratio can be modified by the synthesis conditions [6]. The amount of the main monomer has influence in the size of the microgels. An erroneous quantity of crosslinked polymer may be responsible for structural inhomogeneities in the microgel particles. The most noteworthy factor is the concentration of the initiator modifying drastically the final product. The amount of initiator is directly related with the number of nucleus available to form particles. At fixed quantities of NIPAM monomer, the particles formed are smaller at higher amounts of initiator. The same effect occurs as the temperature rises, since the reaction velocity is increased. Another important factor is the stirring velocity during the synthesis process. Macrogels or polydisperse systems can be formed in non-stirring conditions, whereas the polymer can aggregate if the stirring is very fast. Therefore, optimum conditions are needed to ensure the homogeneity and monodispersity of the particles obtained.

The synthesis was performed in a 1000 ml thermostated reactor, round-bottomed four-necked flask (with an anchor-shaped stirrer, condenser, mercury

thermometer and nitrogen inlet). Anionic and cationic PNIPAM particles were prepared. The microgels were obtained following the protocol by Pelton and Chibante [7]. First, the main monomer (NIPAM) and the crosslinked monomers (MBA for the anionic particles or MBA/AEMH for the cationic ones) were dissolved in water and introduced into the reactor. Once the desired conditions of temperature (70ºC) and stirring (200 rpm) were reached, the initiator was added to start the polymerization (KPS for anionic particles or V50 for cationic particles). The solution turned from transparent to white color after few minutes and the reaction was allowed to proceed for 4 hours in both cases. The polymerization was carried out under a constant stream of nitrogen. The amounts used for each reactant are shown in Table 2.1 [5, 8, 9]. Negative charge on anionic microgels comes from sulfate groups supplied by KPS, while the positive charge on cationic ones comes from amine and amidine groups supplied by AEMH and V50.

After the synthesis, a purification process was carried out for removal of unreacted material. Anionic microgels underwent three cycles of centrifugation/decantation/redispersion at 38ºC at 14000 rpm (Kontron Instruments). In contrast, it was not possible to deposit cationic microgels by centrifugation; instead, serum replacement was used until the conductivity of the samples was constant and close to the conductivity of Milli-Q water [10].

	Water (ml)	NIPAM (g)	MBA (g)	KPS (g)	V50 (g)	AEMH (g)
Anionic	350	4.9	0.49	0.291	–	–
Cationic	500	13.656	0.233	–	0.157	0.374

Table 2.1: Amounts of each reactant used in the synthesis of the cationic and anionic PNIPAM microgels [5, 8, 9].

2.3 Transmission Electron Microscopy (TEM)

The morphology and monodispersity of the PNIPAM microgels were analyzed by transmission electron microscopy (TEM) (LIBRA 120 PLUS de Carl Zeiss SMT). For the sample preparation a small droplet of the solution was deposited onto a support grid. After that, the sample was dried in a furnace above the T_{LCS} until water was completely removed. The images corresponding to the anionic and the cationic microgels are shown in Figure 2.1. The sphericity and low polydispersity of the particles can be easily observed in the images for both samples. In addition, we can observe that the microgels form a hexagonal pattern, caused by the interparticle interactions of charged spherical microparticles of similar size during the drying process.

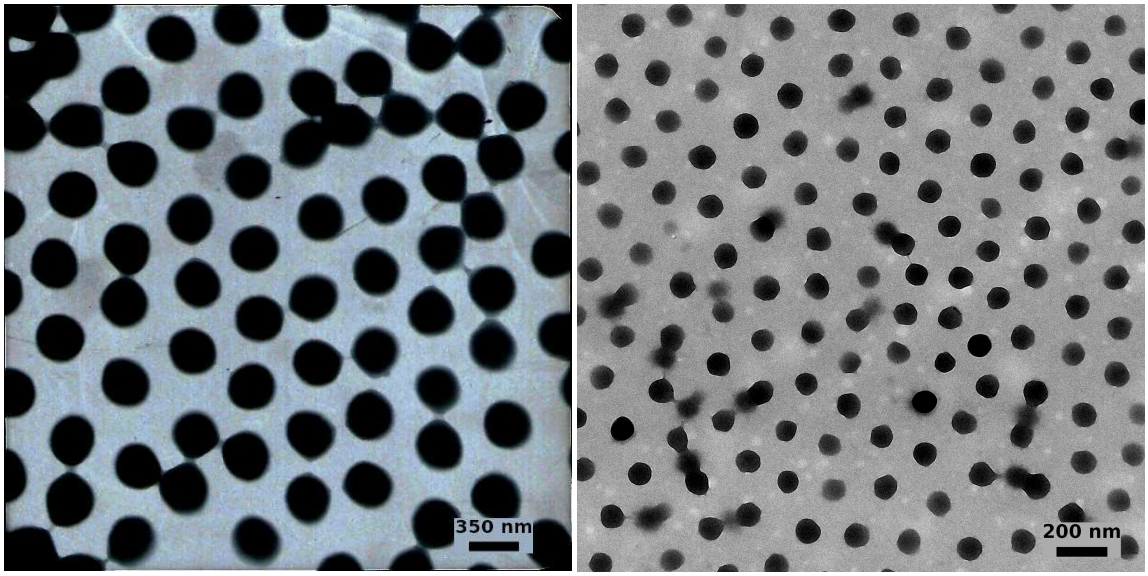

Figure 2.1: TEM images for anionic (left) and cationic (right) PNIPAM microgels.

2.4 Protein adsorption onto latex microspheres

Protein-coated PS microspheres were prepared by physical adsorption. First, the desired protein was dissolved in a buffered solution to get a concentration of around 1 mg/ml. Both, BSA and β-lactoglobulin were prepared in pH 6 buffer (monosodium phosphate), whereas β-casein was dissolved in pH 7 buffer (Bis-Tris) [1]. The β-casein concentration employed was always lower than the critical micelle concentration (CMC) [11, 12]. The solutions were stirred during 1 hour to ensure the complete solubilization of the proteins. The concentration of the protein solutions were determined by UV absorption. In general, proteins are able to absorb light in the ultraviolet range with a maximum in 280 nm. This fact is related with the particular composition in aromatic amino acids of each protein. The Beer-Lambert law relates the properties of the solution with the attenuation of light passing through the material:

$$A = \varepsilon\, c\, l \tag{2.1}$$

where A is the absorbance, ε the extinction coefficient (characteristic for each protein), c the protein concentration in solution and l the path length of the laser beam through the sample. The absorbance of our samples was measured at 280 nm in a Spectronic Genesys 5 device. The extinction coefficients of the proteins are shown in Table 2.2 [13–15].

The physical adsorption of the proteins onto the latex particles was carried out as follows: 2.4 ml of each protein solution (1 mg/ml) was added to a final volume

Protein	pI	ε (ml/mg·cm)
BSA	4.7	0.66
β-lactoglobulin	5.13	0.96
β-casein	4.83-5.07	0.46, 0.47

Table 2.2: Isoelectric point (pI) and extinction coefficient (ε) (280 nm) of the proteins studied [13–15].

of 8 ml of aqueous solution buffered at the same pH of the protein solution. The pH of the adsorption process was chosen close to the pI of the proteins in solution (Table 2.2) and of the complexes (as we will see later, Figure 7.11) to achieve a high degree of coverage onto the PS microspheres [16]. At this close-to-neutrality condition, the repulsion between the neighboring proteins is reduced. At the same time, the proteins remain stable in solution during the adsorption process.

Afterwards, an amount of latex microparticles corresponding to 0.3 m^2 of total area was added to the final solution. This ratio corresponds to 8 mg of protein for each m^2 of latex surface. Incubation was performed in a shaking water bath at 25ºC during 21 hours, as in a previous study [17]. After that, the solution with the complex (latex-protein) was centrifugated at 14000 rpm and 20ºC during 20 minutes (Hettich Mikro 220R) to remove the non-adsorbed proteins. The supernatant was discarded and the pellet was redispersed in the same pH buffer of the adsorption process. No desorption was found during one week after the incubation. Latex-protein complexes were discarded and no longer used after that period.

2.5 Malvern Zetasizer Nano Z

The measurements of size and electrophoretic mobility were carried out using a Zetasizer Nano Z device (Malvern Instruments). In every experience the microparticles were diluted in the desired solution using a concentration of 10^{10} particles/cm^3, a suitable concentration for measuring with this device. The data obtained was the average of three measurements and the standard deviation was always lower than 5%.

2.5.1 Size measurements

The Zetasizer device is based on the dynamic light scattering method (DLS) to obtain the size distribution profile of colloidal particles in a suspension. This technique works with typical characteristics of the colloidal samples: the Tyndall effect (scattering) and Brownian motion [18]. A laser beam illuminates the sample and the scattered light is collected at 173º by a detector. The light analysis at this

angle enables to measure in a wide range of particle concentration. A suitable concentration of the sample is crucial in order to obtain reliable measurements; a low concentration implies fluctuations of the number of particles inside the detection volume. On the other hand, multiple scattered phenomena are produced at high concentrations, and the interactions between particles in a very concentrated sample could affect to the Brownian diffusion.

The tool calculates the diffusion coefficient from the intensity of scattered light as a function of time. The diffusion coefficient (D) and the hydrodynamic diameter (D_h) of the particles are related by the Stokes-Einstein equation [19]:

$$D = \frac{k_B\, T}{3\,\pi\,\eta\, D_h} \tag{2.2}$$

where k_B is the Boltzmann's constant, T is the temperature and η is the solvent viscosity. In addition, the polydispersity index (PDI) can be obtained from the analysis of the size distribution. In Table 2.3 the relation between the PDI values and the degree of polydispersity of a dispersion of colloidal particles is shown.

PDI values	Degree of polydispersity
$<$0.05	Highly monodisperse standards
0.05-0.08	Nearly monodisperse sample
0.08-0.7	Mid-range value of polydispersity
$>$0.7	Very broad size distribution (not suitable for the DLS technique)

Table 2.3: Scale of the PDI values depending on the polydispersity of the sample.

2.5.2 Electrokinetic measurements

Electrophoresis is a technique used for measuring the motion of charged colloidal particles under an applied electric field. The force associated to the electric field is counteracted by the friction force caused by the viscosity of the solvent; in this way, the particles reach a constant velocity. The constant of proportionality between the applied electric field and the velocity of the particles is known as electrophoretic mobility (μ_e) [19]:

$$\vec{v} = \mu_e\, \vec{E} \tag{2.3}$$

This direct relation is strictly valid if the applied field is sufficiently low. The motion of the particles is monitored using the Doppler effect. A laser beam is shot into the sample; the scattered light undergoes a shift in frequency that is directly related with the velocity of the particles in suspension. The calculation of

the μ_e by the change in frequency is known as LDV (Laser Doppler Velocimetry). Nevertheless, the velocity of the particles could be affected by other effects like the Brownian motion, sedimentation or convection. For this reason, the device also used the PALS method (Phase Analysis Light Scattering) in order to obtain more accurate measurements. This technique is based on the change in phase between the scattered and the reference light as a funtion of the elapsed time. This mixed method, called M3-PALS, allows to acquire low values of mobility, since enhances the measurement of the particle position in small displacements [20].

Estimation of electrokinetic charge from mobility measurements

We calculated the electrokinetic charge density (σ_{ek}) for the PS latexes and the complexes (latex-protein) from their electrophoretic mobility, by using the Grahame equation [21]. σ_{ek} is an estimation of the electrostatic charge responsible for the electrophoretic motion of a particle. This amount depends on the intrinsic charge of the colloid, as well as on the ionic medium (kind of salt and ion concentration). The Grahame equation for a nonhomogeneous ionic solution is:

$$\sigma_{ek}^2 = 2\varepsilon_0\varepsilon_r RT \sum_j c_{0j} \left[e^{-z_j F\zeta/RT} - 1\right] \tag{2.4}$$

where c_{0j} is the bulk concentration of the ion j and z_j its valence; ε_0 is the vacuum permittivity and ε_r is the dielectric constant of water; R is the universal gas constant, T is the absolute temperature, F is the Faraday constant and ζ is the ζ-potential, which is related with μ_e by the Smoluchowski equation [22]:

$$\zeta = (\eta/\varepsilon_0\varepsilon_r)\mu_e \tag{2.5}$$

where η is the viscosity of water. The Grahame equation for a 1:1 electrolyte is:

$$\sigma_{ek} = \sqrt{8\varepsilon_0\varepsilon_r c_0 RT}\sinh\left(F\zeta/2RT\right) \tag{2.6}$$

where c_0 is the bulk concentration of 1:1 electrolyte. The Grahame equation is based on the Gouy-Chapman theory and assumes that the total charge in the whole double layer (sum of the surface charge plus the charge of the ions), must be zero (electroneutrality condition) [23].

2.6 Colloidal Stability

Inorganic and organic salts were used to modify the stability of several systems of microparticles. These colloidal particles are stable because of the charge repulsion between them (DLVO theory). When two particles undergo a collision, the probability of forming a dimer depends on the ionic concentration of the medium, related with the double layer electrostatic force. Counterions are able to screen

the surface charge of the particles decreasing the repulsive contribution between them. At this point, the attractive contribution (van der Waals forces) produces the aggregation of the system [24].

At the same time that the colloidal system aggregates (formation of dimers and bigger aggregates), the turbidity of the sample increases and the process can be followed by measuring the absorbance of the sample. The aggregation was monitored as a function of the elapsed time using a spectrophotometer (Spectronic Genesys 5). The optical absorbance of the sample was measured at 570 nm at 2-s intervals, during 120 seconds. The scattering cell was rectangular with a path length of 1 cm. Equal volumes (300 μl) of colloidal dispersion and salt solution were mixed into the cell at the time of measuring. In Figure 2.2 is shown an example of a typical stability experiment.

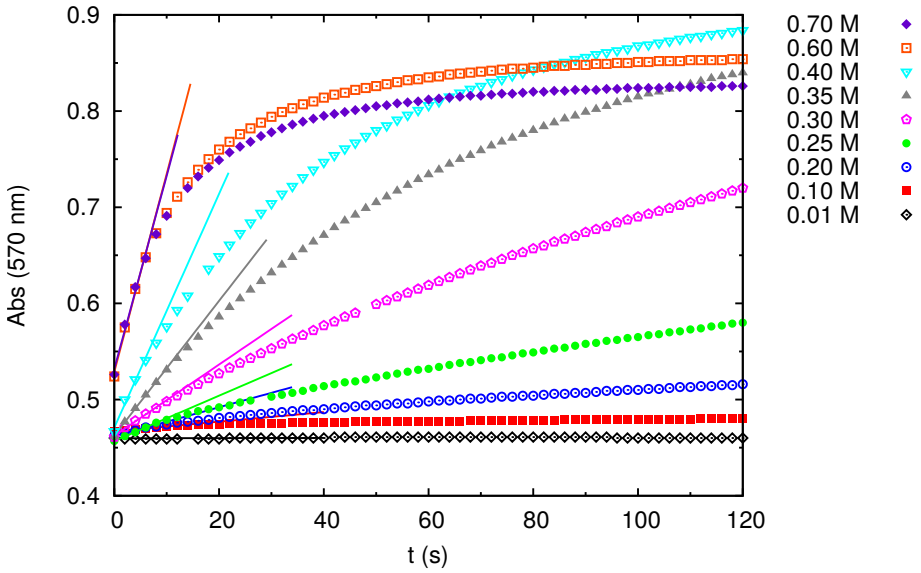

Figure 2.2: Optical absorbance (570 nm) of a dispersion of anionic PS microspheres as a function of the elapsed time at different ionic concentrations of NaCl. The velocity of particle aggregation increases at higher ionic strengths. The solid lines are linear fits of the first stage of the aggregation, the slopes are used to obtain the stability factor (W).

At the first stages of the aggregation process, the absorbance increases linearly against the time until reaches a plateau (see Figure 2.2). The aggregation velocity depends on the ionic strength, slower at low ionic concentration and faster when the concentration is increased. Hence, the velocity of aggregation is reflected in the absorbance/time ratio. The slopes of these ratios (at different ionic concentrations) are used to calculate the stability factor (W), also called the Fuchs factor [24]:

$$W = \frac{k_f}{k_s} = \frac{(dAbs/dt)_f}{(dAbs/dt)_s} \tag{2.7}$$

where k_f represents the fastest aggregation-kinetics constant, where each collision between the colloidal particles results in an aggregate (corresponding to 0.7 M in Figure 2.2) and k_s is referred to each one of the slower aggregations that occur at lower ionic concentrations. W is related with the number of collisions between two particles until they stick irreversibly [24]. The limit values of the parameter W take place when the system is stable ($k_s = 0$ and $W \longrightarrow \infty$); or when the system is completely unstable. In this latter case $k_s = k_f$ and $W = 1$.

The factor W is represented against the ionic strength in double logarithmic scale. In this kind of representation, W typically decreases linearly with the ionic strength when the colloidal particles are aggregating (see Figure 2.3). We can obtain the critical coagulation concentration (CCC) by a linear fit of the data. The CCC is the minimum ionic concentration needed to cause the complete destabilization of the system (W=1).

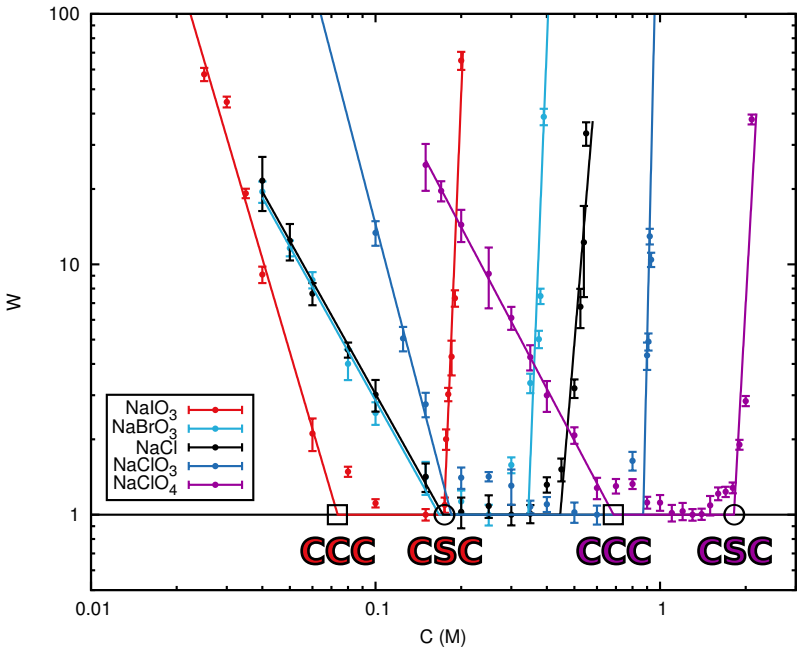

Figure 2.3: Representation of the stability of a cationic hidrophilic system (Chitosan microparticles). Double logarithmic plot of the stability factor (W) against the ionic concentration of different salts. The critical coagulation concentration (CCC) and the critical stabilization concentration (CSC) are obtained from a linear fit of the data. These values depend on the kind of salt used. Both, CCC and CSC values follow the Hofmeister series for anions.

The CCC value depends on the salt used as aggregating agent for a certain colloidal system. For instance, an important factor is the valency of the counterions. The amount of salt needed to aggregate anionic microparticles will be lower with a divalent cation as Ca^{2+} than with a monovalent cation as Na^{+}. Therefore, the CCC will have a smaller value for the $CaCl_2$ salt, whose cation is able to screen the electrostatic charge of the latex more efficiently than the NaCl. Another important factor is the kind of salt used, different monovalent ions can produce particular CCC values. This phenomenon is a clear example of ionic specificity. For instance, in Figure 2.3, the stability of cationic hydrophilic colloids (Chitosan microparticles) in presence of salts formed by different anions is represented. The salt needed to destabilize the hydrophilic system is lower with kosmotropic anions than with chaotropic anions. In contrast, for hydrophobic colloids the CCC values with kosmotropic ions are higher than with chaotropic ions.

Under certain experimental conditions, a re-stabilization of the colloidal particles is observed. This is, at ionic concentrations higher than the CCC, the colloidal system becomes stable again. Experimentally, this process is reflected in an increasing of W with the ionic concentration. The minimum concentration needed to re-stabilizes the system is known as the critical stabilization concentration (CSC). The re-estabilization can be produced by different mechanisms: hydration forces (only in the case of hydrophilic interfaces) [24] or great charge inversion [25]. We have also observed that this re-stabilization is ionic specific, depending on the hydrophilic degree of the colloidal surface and the chaotropic/kosmotropic character of the ions (see Figure 2.3 as example). In addition, we will see in Chapter 8 how the tetraphenyl ions, acting as counterions, can produce significant charge inversions of hydrophobic colloids and hence a re-stabilization by charge.

2.7 Atomic Force Microscopy (AFM)

The Atomic Force Microscopy (AFM) is a very useful tool for measuring the topography and other surface properties by using a nanometric probe [26]. This versatile apparatus allows us to perform the experiments in aqueous medium and at controlled temperature in real time. In addition, the samples are studied in their natural state, without any special preparation. These are some of the advantages of the AFM in comparison to other microscopy techniques.

The resolution of the images obtained by AFM depends on the shape and size of the tip or probe (4-60 nm). The tip is joined to a cantilever of a certain elastic constant. The relative movement between the tip and the sample is generated by piezoelectric materials. Thus, the quality of the images is also related with the accuracy of these materials that generally produce displacements around 0.1–1 nm in the horizontal and vertical directions.

The AFM works in different operating modes. In contact mode, the tip stays

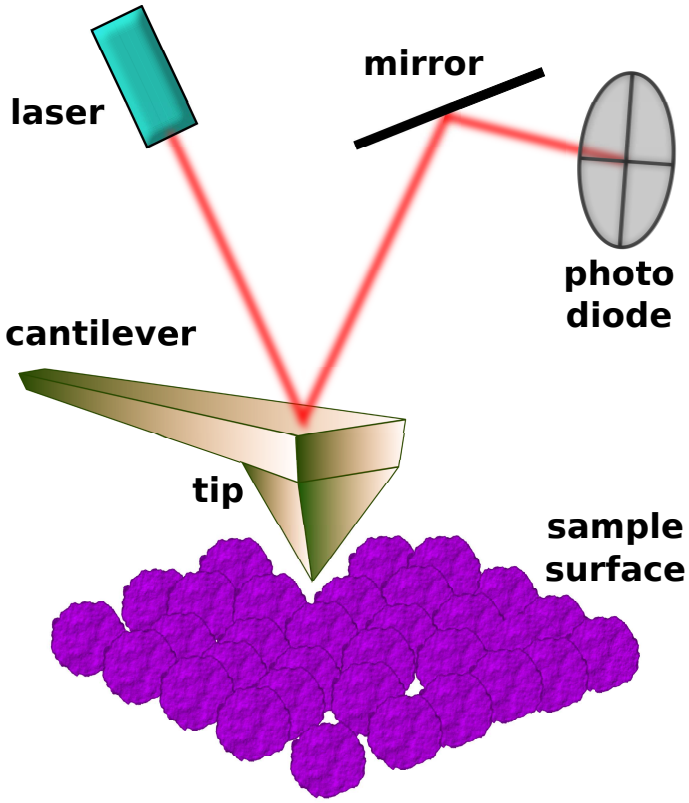

Figure 2.4: Schematic representation of the AFM device. The cantilever is deviated by the topography of the surface. These deviations are monitored by a laser beam reflected in the cantilever and collected in a photodiode. The sample is placed onto a piezoelectric actuator that provides the relative movement between the tip and the sample in all directions. [26].

in physical contact with the sample during the whole experiment, in a way that a constant force is applied over the surface. During the tip scanning, the cantilever is deviated by the differences in height of the sample. This deviation is detected in a four segment photodiode by the reflection of a laser beam on the cantilever. In this way, the AFM is able to generate images of the topography of a surface by coloring its differences in height. The interactions between the tip and the sample are of electrostatic (attraction or repulsion) and van der Waals kind, as well as, capillarity or friction forces. The contact mode is used with hard samples, non-damaged by the friction interactions between the tip and the surface during the scanning.

In contrast, the contact mode is less appropriate for soft materials, dynamic modes are used in order to reduce the interaction forces between the tip and the sample. One of the most used is the tapping mode. In these modes, the

cantilever is oscillated vertically close to its resonance frequency. The value of the resonance frequency depends on the material of the cantilever and the medium (50–500 kHz in air and 10–100 kHz in aqueous solution). When the AFM is operating in the tapping mode, the tip barely is in contact with the sample. The oscillation amplitude is significantly reduced in the proximities of the surface, and this reduction gives information about the topography. From this data, the image is generated.

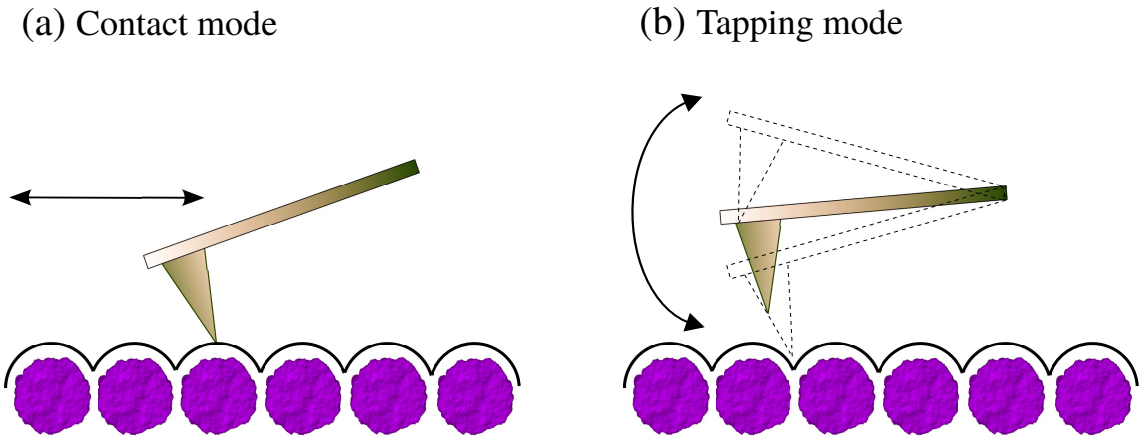

Figure 2.5: Operating modes of the AFM. (a) Contact mode (non-dynamic mode): a constant force is maintained between the tip in contact with the surface during the scanning. The topography is determined by the variations of the laser beam over the photodiode. (b) Tapping mode (dynamic mode): the cantilever oscillates close to the resonance frequency, thus the interactions between the tip and the sample are minimized. In this case, the image is generated by the variations in the oscillation amplitude. In the tapping mode the images show less resolution, however possible damages of the sample caused by the tip are prevented [26].

In the AFM images can appear artifacts. The most common artifacts are produced by defects in the tip. For instance, a blunt tip can produce blurred edges, while a broken tip can produce duplicated motives in the image. In this last case, if the tip shows multiple sharp ends, each element in the surface will be scanned once by each end, representing each element multiple times in the image.

2.7.1 AFM experiments in liquid media (PNIPAM microgels)

AFM experiments in liquid environment were carried out in tapping mode using SiO_2 tips on triangular Si_3N_4 cantilevers (NanoScope IV Multimode, Veeco Instruments, Santa Barbara, California, with a temperature control system Thermal Applications Controller). Freshly cleaved mica surfaces (Metafix, France)

were used as the substrate for microgel adsorption. Mica is a hydrophilic mineral ($KAl_2Si_3AlO_{10}(OH)_2$) distributed in layers (Figure 2.6). Each layer of this material is composed by Si and Al atoms bonded covanlently with oxygens. While the K atoms are bonded to oxygens by weaker interactions (electrostatic and van der Waals). For this reason, mica is easily exfoliated, which makes it a perfect material to obtain clean surfaces that are smooth at the atomic level (roughness ∼0.5 Å). When mica is submerged in water, K^+ cations are dissolved and the substrate becomes negatively charged, thus cationic components are readily adsorbed on it [27, 28].

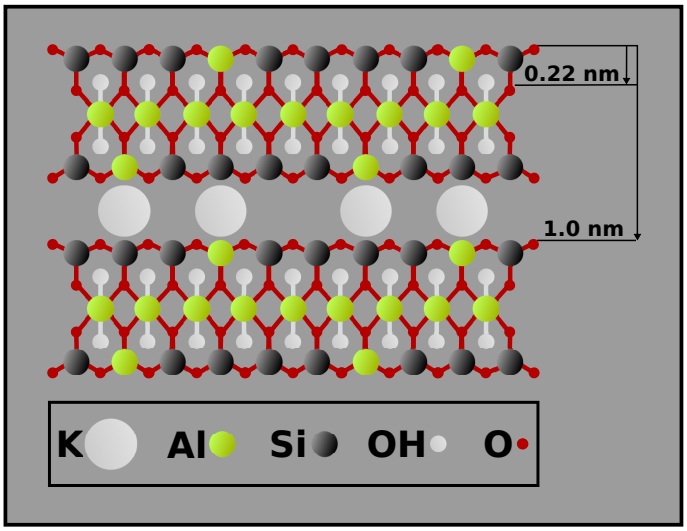

Figure 2.6: Schematic representation of the layered-structure and chemical composition of mica [29].

The following experimental protocol was carried out: the tips were irradiated with ultraviolet light in a UV/ozone cleaner for 15 minutes prior to use. Mica was glued on a steel disc and it was cleaved using adhesive tape just before being used. For the case of anionic microgels, mica was coated with the cationic polyelectrolyte polyethylenimine (PEI) previous microgel adsorption. In this way, the electrostatic charge of the substrate is reversed, favoring the adsorption of the anionic particles. For experiments in liquid environment we used a fluid cell sealed by a silicone O-ring, previously cleaned by rinsing with water and ethanol. Before adsorption, the device was heated at 38°C and a solution of diluted PNIPAM (previously heated at 40°C) was injected. In the case of the cationic (anionic) PNIPAM there is an electrostatic attraction between the mica (PEI-coated mica) surface and the microgel particles, which is enhanced when the microgel is in the collapsed state and its surface charge density is high. After one hour of adsorption, the liquid cell was rinsed with an unbuffered pH 4 solution (with HCl). After that, the desired salt

solution (always at pH 4) was injected, and several images were taken at different temperatures. The temperature was decreased in steps of 2ºC from 38ºC until the phase transition of the microgel from the collapsed to the swollen state was observed (the final temperature depended on the salt employed). After that, the temperature was increased in steps of 2ºC, until 37ºC where the microgels were again in a collapsed state. In this way the temperature range was completely covered with precision of ± 1ºC. The system was allowed to equilibrate for 15 minutes after each temperature change.

2.7.2 AFM experiments in air (sample preparation for protein adsorption)

Protein films in air were investigated by AFM. The proteins were adsorbed onto hydrophobic surfaces at buffered pH conditions as previously explained (section 2.1.2). The substrates were prepared following the next protocol. Ultraflat gold surfaces were obtained by gold deposition onto mica [30]. Afterwards, the mica was removed with tetrahydrofuran (Sigma-Aldrich). The substrate was rinsed generously with absolute ethanol (99.8% of purity) and gently dried with N_2 gas. Inmediately after, the gold surface was coated with CH_3 terminated self-assembled monolayers (SAM), by 4 hours exposure to a solution of 1 mM of 1-Octadecanethiol (Sigma Aldrich ref O1858) in absolute ethanol. Finally, the substrates were rinsed again with absolute ethanol and dried with N_2 gas. We obtained a hydrophobic surface for the protein adsorption at the same conditions that in the QCM experiments 2.8.2.

2.8 Quartz Crystal Microbalance (QCM)

The Quartz Crystal Microbalance with Dissipation monitoring (QCM-D) device (Q-sense E1 by Biolin Scientific) is a very sensitive tool commonly used to determine the thickness and viscoelastic properties of thin films adsorbed over flat substrates [31]. It is based on a piezoelectric system; an alternating voltage is applied over a quartz crystal, producing the mechanical deformation of the material. The frequency is chosen as the resonance frequency (f) of the crystal. Any small mass deposited over the crystal results in a change in the resonance frequency of the coated crystal, detectable by the device (see Figure 2.7). In addition, in the QCM-D, the voltage applied is intermittently switched on and off and the decay in time of the oscillation is monitored. In this way, we are able to obtain the "energy dissipation factor" D. That is the inverse of the quality factor (Q) of the resonance peak ($D = Q^{-1} = 2\Gamma/f$, where Γ is the half-band-half-width). The "dissipation" quantifies the damping in the system and provides information about the viscoelastic properties of the adsorbed film.

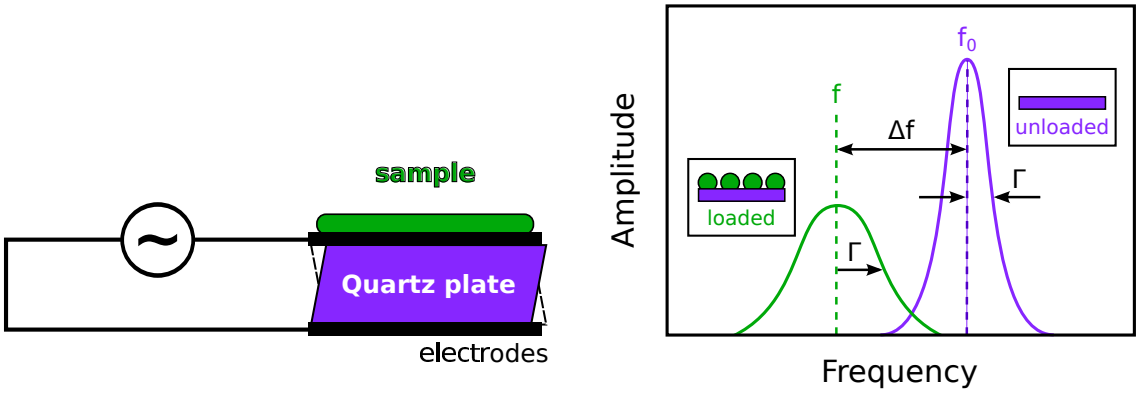

Figure 2.7: Quartz crystal deformation by an voltage applied (left). Change in resonance frequency (Δf) between the bare crystal (violet) and the loaded crystal (green) (right). Any mass adsorbed onto the crystal causes a decreasing in frequency. The Γ parameter is the half-band-half-width used to calculate the "dissipation factor" ($D = 2\Gamma/f$) [32].

For thin, rigidly attached films (small values of ΔD_n upon adsorption) the adsorbed mass can be calculated by using the Sauerbrey equation [33]. This equation relates the change in resonance frequency (Δf_n) with the mass adsorbed onto the substrate:

$$\Delta f_n = -\frac{n}{C} m_f = -\frac{n}{C} \rho_f h_f \tag{2.8}$$

where n is the overtone order (odd), C is a constant depending on the fundamental resonance frequency of the quartz crystal (in our case C=18 ng cm^{-2}Hz^{-1}, with a fundamental frequency of f_F=5 MHz), m_f is the areal mass density of the adsorbed film and ρ_f and h_f are the density and the thickness of the adsorbed film, respectively. The values of m_f calculated from eq. 2.8 may include solvent associated to the film. Hence, the Sauerbrey equation is strictly valid only when the film is homogeneously distributed and is rigid. This kind of film is characterized by small values of the dissipation ($\Delta D_n \approx 0$) and low dispersion in $\Delta f_n/n$ [31]. To obtain h_f, an assumption for the value of ρ_f is necessary; a typical value for soft systems is $\rho_f \approx 1$ g/cm^3 [31]. After its introduction, the QCM-D has been widely used to investigate the adsorption and viscoelastic properties of a number of different biomolecular films [34, 35]. In our case, we have investigated two kind of systems by QCM: proteins and PNIPAM microgels. On the one hand, the protein films studied in this work appear to meet the requirements needed to apply the Sauerbrey equation (rigid and homogeneous films). In contrast, the PNIPAM microgels form a thicker layer with high fraction of solvent inside the film. Therefore, the areal mass density calculated will include the mass of the mi-

crogels and the mass of water. The typical properties of the microgel films, such as softness and thick layers, are reflected in high values of the dissipation. In the case of $\Delta D_n > 0$, the data obtained by the device can be analyzed for studying the viscoelastic properties of the film [36].

2.8.1 Expansion of QCM data modeling

As mentioned above, the simple Sauerbrey description is not further valid if a large perturbation acts on the quartz crystal. Several methods have been developed to describe the response of the complex oscillator resulting from the coupling between the vibrating quartz crystal and different media; the influence of adsorbed layers of different properties (thickness and viscoelastic character) in presence or absence of an "infinite" media (solvent) has been described in the literature. One possible approach is to solve the equations of wave propagation through the stratified media (quartz, adsorbed layers and solvent) with the appropriate boundary conditions (e.g. continuity of stress and velocity or zero-stress in free boundaries). A second approach involves considering the QCM as an acoustical reflectometer, by calculating the reflectivity of the propagating shear wave at the different interfaces. This approach will be helpful to better understand the condition of "film resonance" described below. A third approach (probably the most extensively used in the literature) is to build equivalent electromechanical circuits to model the system response. The electromechanical analogy maps forces on voltages and velocities on currents, and uses combinations of resistors, inductor and capacitors to represent dashpots, masses and springs. By introducing the concept of mechanical impedance (the ratio of force and speed on a given surface) a powerful representation of the system can be built. A complete compilation of these methods was recently reported [37]. All the 3 methods outlined before produce analogous results. We briefly reproduce here some of the most relevant results, which are useful to better understand our experimental data. A more complete description of these models can be found in ref. [37].

A compact representation of the most important results can be expressed in terms of the complex resonance frequency ($\tilde{f}_r$) defined as:

$$\tilde{f}_r = f_r + i\Gamma \tag{2.9}$$

The shift in $\tilde{f}_r$ due to a load of the quartz crystal can be calculated by using the Small Load Approximation (SLA), as long as this shift is small compared with the resonance frequency [38]. The main consequence of this approximation can be expressed as:

$$\frac{\Delta \tilde{f}_r}{f_0} = \frac{i}{\pi Z_q} \tilde{Z}_L \tag{2.10}$$

where f_0 is the resonance frequency of the free crystal, Z_q the real part of the acoustic wave impedance of the quartz (a property of the materials, defined as $\tilde{Z}_q = (\rho\tilde{G}_q)^{1/2}$) and $\tilde{Z}_L$ the complex load impedance of the load layer (defined as the ratio between the tangential stress on the crystal surface and its tangential velocity). Additionally, $\tilde{G}$ is the complex shear modulus ($\tilde{G} = G' + iG''$), where the real part is the storage modulus (G'), while the imaginary part is the loss modulus (G''). G' is directly related with the average energy storage in a cycle of deformation by the shear wave. While G'' is directly proportional to the average dissipation or loss energy as heat in the same deformation process. The balance between both quantities determine the viscoelastic behavior of materials [39].

From the equation 2.10, several scenarios of increasing complexity can be considered. For modeling of elastic, viscous or viscoelastic loads, it is usually assumed that only variations in the direction perpendicular to the surface need to be considered. This implies that the loading layer(s) are laterally infinite and homogeneous. In addition, linear viscoelastic response (i.e. stresses are strictly proportional to strains) is considered. If these suppositions are valid, the following expressions are obtained:

1. Inertial loading. For a thin, purely elastic rigidly attached layer, the load impedance will be given by $\tilde{Z}_L = i\omega m_f$, with m_f the adsorbed mass per unit area on the quartz crystal. By inserting this value in eq. 2.10, Sauerbrey equation is readily obtained: the resonance frequency variation is proportional to the mass of the deposited layer.

2. Semi-infinite viscoelastic loading. The acoustic impedance is $(\rho i\omega\eta)^{1/2}$, where ω is the angular frequency and ρ and η are the density and complex viscosity of the media. Plugging this impedance in eq. 2.10, one obtains:

$$\frac{\Delta\tilde{f}_r}{f_0} = \frac{1}{\pi Z_q}\frac{-1+i}{\sqrt{2}}\sqrt{\rho\omega(\eta' - i\eta'')} \tag{2.11}$$

   It is important to understand that a shear wave has an evanescent character on a Newtonian liquid; it is strongly damped and has a finite depth of penetration. The depth of penetration or decay length (δ) of the shear wave in a viscoelastic media is related with the complex shear modulus ($\tilde{G}$) as:

$$\delta = -\frac{1}{\omega\sqrt{\rho}}\frac{|\tilde{G}|}{Im\left(\tilde{G}\right)} \tag{2.12}$$

3. Viscoelastic film in air. The evanescent shear wave will propagate through the viscoelastic media, and may be reflected in the stress free edge of the film

(neglecting the viscosity of the air, $\tilde{Z}_{air} \approx 0$). In this case the load impedance can be expressed as,

$$\tilde{Z}_L = i\tilde{Z}_f \tan(\tilde{k}_f d_f) \tag{2.13}$$

where $\tilde{Z}_f = (\rho_f \tilde{G}_f)^{1/2}$, $\tilde{G}_f$ the shear modulus, ρ_f the density, $\tilde{c}_f$ the speed of sound and $\tilde{k}_f = \omega/\tilde{c}_f$ is the wavenumber in the film. By plugging eq. 2.13 in the SLA equation (eq. 2.10), it is apparent that the shift in the complex resonance frequency is a non-monotonic function of the thickness of the film. A particular condition, the appearance of maxima in frequency shift is called "film resonance". It will appear for sufficiently thick films. A similar situation will arise for films immersed in a solvent (instead of air) as discussed below. As this concept will help understanding our experimental results, it will be discussed in more detail in the following paragraphs.

It can be shown that eq. 2.11 can be obtained from eq. 2.13 for Newtonian thick liquid films. In this case the shear wave is damped before it reaches the film-air interface, and no reflection is possible.

4. Viscoelastic film in a liquid. As in the previous case, the shear wave will be reflected on the film-liquid interface. The reflectivity will be given by

$$\tilde{r}_{f,liq} = (\tilde{Z}_f - \tilde{Z}_{liq})/(\tilde{Z}_f + \tilde{Z}_{liq}) \tag{2.14}$$

where $\tilde{Z}_{liq} = (i\omega\rho_{liq}\eta_{liq})^{1/2}$ is the shear wave impedance of the liquid. By considering the transmitted and reflected waves and applying the SLA (eq. 2.10), the following expression is obtained [40]:

$$\frac{\Delta\tilde{f}_r}{f_0} = \frac{-\tilde{Z}_f}{\pi Z_q} \frac{\tilde{Z}_f \tan(\tilde{k}_f d_f) - i\tilde{Z}_{liq}}{\tilde{Z}_f + i\tilde{Z}_{liq} \tan(\tilde{k}_f d_f)} \tag{2.15}$$

As for the previous case, "film resonance" will be observed if the film is thick enough. A short digression about this phenomenon will help understanding some of the experimental results described later. For this purpose, it is convenient to consider the QCM technique as an acoustical reflectometer. The shear wave produced by the electric stimuli of the quartz crystal propagates through the material, and is partially/totally reflected in presence of an impedance discontinuity, as mentioned above (e.g. the crystal surface). For certain excitation frequencies these waves interfere constructively; this is the situation of electromechanical resonance. The loading of the crystal modifies this resonance. Understanding this perturbation and employing its outcome to extract material properties is the base of the QCM technique. For instance, rigidly attached thin films shift the resonance frequency of the system as outlined above and the quartz crystal can be used as

the base for a film thickness monitor. As the film thickness increases, the system must be considered as a composed resonator; shear waves will reflect from all interfaces: quartz-film and film-air (or solvent). In addition, for viscous/viscoelastic films the shear waves will be seriously damped: the amplitude of the wave decreases exponentially with the travel distance. However, the phase of the wave will also be shifted; when a phase shift of $\pi/2$ rad through the film occurs, constructive interference between the waves will happen; the total phase shift between propagating and reflected wave will be 2π rad: $\pi/2$ rad on each direction plus a sign reversal upon reflection (eq. 2.14). This is the commonly termed "film resonance", which can be achieved either by changing the thickness or the viscoelastic properties of the film attached to the quartz crystal. It is important to realize that "film resonance" is not just a film property, but is related to the composed resonator. Thus, the highest overtone goes into resonance first because the corresponding wavelength is shorter than on n=3 or n=1.

Some examples of "film resonance" in QCM studies in liquid have been described in the literature. Johannsmann and coworkers studied the swelling of polystyrene in cyclohexane, using the temperature to change the thickness of a grafted polymer layer (by tuning solvency conditions) [40]. The growth of electrochemically deposited polymers has also been used to investigate this effect [41–43].

Although conceptually interesting, the condition of film resonance makes it more difficult to extract relevant physical parameters describing the film in contact with the quartz crystal from the measured data. However, as will be described later, it can be used as a clear indication of sudden film growth.

We performed QCM-D experiments with the quartz crystal in contact with air and pure water to test the performance of the device, in particular in conditions of varying temperature. Interestingly, we observed an important temperature dependence of the resonance frequency. On the contrary, no significant variation of the measured Γ (or D) was observed between 20 and 40ºC. Typical results for the measured variation in f and Γ (for the 7^{th} harmonic) are presented in Figure 2.8.

It can be expected that in presence of an ideal viscous loading (e.g. water), the shifts in $-\Delta f$ and $\Delta\Gamma$ will be similar, as the imaginary component of the viscosity (η'') vanishes (eq. 2.11). This condition was satisfied (purple data in Figure 2.8 (a)) if the variation in resonance frequency of the bare crystals in contact with air was taken into account, and subtracted from the measured raw data (red data in Figure 2.8 (a)). All the temperature dependent QCM-D data presented in this thesis were corrected by the observed shift in resonance frequencies of the bare crystal in air. No significant temperature dependence was observed for the values of Γ.

By applying equation 2.11, we calculated the product $\rho \cdot \eta'$ from the measured data; as can be observed in Figure 2.8 (b), we found an excellent agreement of the measured η' with the literature values (tabulated values for the density were used

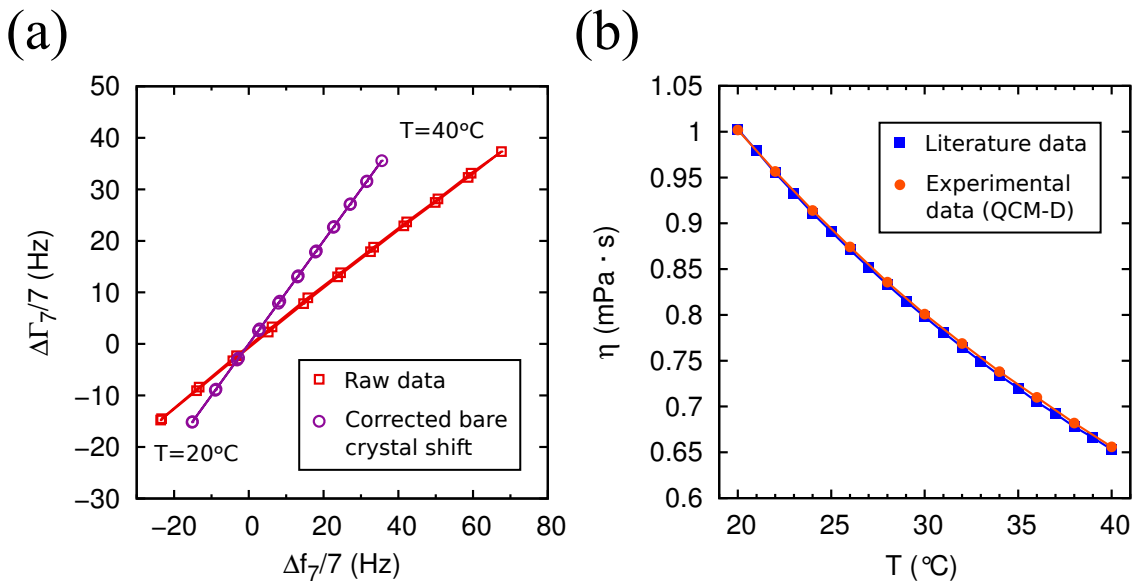

Figure 2.8: (a) Parametric plot of $-\Delta\Gamma$ vs. Δf for the 7^{th} harmonic, referred to the values measured between 20ºC and 40ºC. Similar results were observed for the different harmonics tested. (b) Water viscosity calculated from eq. 2.11, as described in the text. An excellent agreement with literature water viscosity data is observed [44].

to determine the viscosity from the experimental $\rho \cdot \eta$). As the viscosity of water is independent of frequency in the range of frequencies explored by the QCM (15-35 MHz in our experimental setup), by measuring f and Γ for 6 odd-harmonics (n=3–13), 12 data points are simultaneously determined for each temperature, improving the quality of the data.

2.8.2 QCM experiments: Protein adsorption

The experiments were performed using crystals with gold electrodes which were hydrophobically modified by following the next protocol. First, the crystal were cleaned with absolute ethanol (99.8% of purity) and gently dried with N_2 gas. Afterwards, they were irradiated with ultraviolet light in an UV/ozone cleaner for 30 minutes, and rinsed again with ethanol and dried with N_2 gas. After the cleaning process, the gold surfaces were coated with CH_3 terminated self-assembled monolayers, by 4 hours exposure to a solution of 1 mM of 1-Octadecanethiol (Sigma Aldrich ref O1858) in absolute ethanol. Finally, the surfaces were cleaned with ethanol to remove non-adsorbed material and dried with N_2 gas. The CH_3 groups form chemical bond with the gold surface. After that, the modified gold crystal were coated with polystyrene (250 kg/mol, ACROS Organics) solution in toluene

5% w/w by spin-coating (at 3500 rpm during 60 s) [45]. This technique enables to obtain uniform thin polymer films. The process is as follows: deposition of few drops of the PS solution onto the substrate; then the substrate is rotated at high angular velocities creating a thin film and evaporating the solvent; lastly the substrates are annealed at 95ºC for 12 h to remove the residual solvent and release any mechanical stress built up during the spin-coating process. Under these conditions, a 300 nm thick PS layer is obtained. In this way, we obtain a homogenous hydrophobic surface for the protein adsorption in order to replicate the experimental conditions with the PS latex nanoparticles. After each experience, the surface was rinsed with toluene removing the PS film and recovering the gold–CH_3 surface. Then, the crystal is ready for another polymer coating. We observed that the tetraphenyl ions modified the structure of the PS films [46], causing a slow response by the QCM. Therefore, in the experiments with tetraphenyl ions involved, the hydrophobic gold–CH_3 surface was directly used to adsorb the proteins. We tested that both surfaces had similar hydrophobic degree. The hydrophobicity of the surfaces was determined by water contact angle: 90º for the PS surface and 106º for the –CH_3 modified surface. In addition, the amount of adsorbed protein was the same in both surfaces: gold–CH_3–PS and gold–CH_3.

Once the quartz crystal was assembled in the cell of the QCM-D, the substrate was exposed to the desired buffer solution for enough time to reach a stable signal. At this point we take the reference ($\Delta f_n/n$=0 and ΔD_n=0). After that, the protein solution is injected in the same conditions that for the adsorption on latex: concentration 1 mg/ml at 25ºC, and pH 6 buffer (monosodium phosphate) for BSA and β-lactoglobulin, or pH 7 buffer (Bis-Tris) for the β-casein. After 30 minutes of adsorption, the cell was rinsed with the protein-free buffer solution in order to remove the non-adsorbed proteins, and then with buffer solutions at pH 3, 4 or 10 depending on the experience. After that, the protein film is exposed to different ionic concentrations of tetraphenyl salts, or sodium chloride.

2.8.3 QCM experiments: Microgel adsorption

The quartz crystals were cleaned following the same protocol previously mentioned (UV/ozone cleaner, ethanol rinsing and drying with N_2 gas). For cationic microgels, we used SiO_2 coated quartz crystals, whose surface is negatively charged at pH>3. In contrast, for anionic microgels, we used cystamine modified gold-coated crystals (cystamine SAM). The gold crystals were covered with a aqueous solution of 3 mM of cystamine dihydrochloride (Sigma-Aldrich ref 30050) during 4 hours. The cystamine-modified surface is positively charged at pH>3. In both cases, the adsorption was carried out at pH 4 and 40ºC (collapsed state). The cationic (anionic) microgels should readily adsorb on the SiO_2 (cystamine-modified) surface under these conditions by electrostatic attraction. Previous to the microgel injection, the zero ($\Delta f_n/n$=0 and ΔD_n=0) is taken as the bare crys-

tal in water at 40ºC. After adsorption, the QCM-D cell was rinsed with microgel-free aqueous solutions. For the study of collapsed-swollen transition of the adsorbed microgels and the effect of different ions on the transition temperature, the zero was set at conditions of bare crystal in water at 25ºC.

2.9 Differential Scanning Calorimeter (DSC)

The Differential Scanning Calorimeter (DSC) (TA Instruments Microcalorimeter Q2000) determines the temperature and heat flow associated with material transitions as a function of time and temperature [47–49]. The sample material is encapsulated in a pan (measuring cell) and an empty reference pan is placed on the thermoelectric disk surrounded by a furnace. When the temperature of the furnace is changed at a linear rate, heat is transferred to the sample and reference through the thermoelectric disk. The differential heat flow to the sample and reference is measured by area thermocouples using the thermal equivalent of Ohm's Law:

$$q = \Delta T / R \tag{2.16}$$

where q is the sample heat flow, ΔT is the temperature difference between the sample and the reference and R is the resistance of the thermoelectric disk. Additionally, ΔT depends on the heat capacity (C_p) of the sample. Usually, the heat capacity per unit mass is represented in function of the temperature in the thermograms.

2.9.1 DSC experiments: Sample preparation

Neutral PNIPAM chains were dissolved in cold water (4ºC) at 5.6% or 16.7% w/w depending on the experience. The samples were stirred during five hours at 4ºC until the solutions were completely transparent. On the other hand, the salt solutions were prepared at 10-fold the desired concentration for the experiments. Afterwards, salts and PNIPAM solutions were mixed at 1:9 proportion at room temperature. In this way, the final solution contains PNIPAM at 5% and 15% w/w, respectively. At high ionic concentrations the PNIPAM chains were dissolved directly in the salt solutions in a water-ice bath. In all the experiments, 9 μl of the final solution was enclosed in a pan. Each sample, in presence of different salts and concentrations, was equilibrated at 10ºC during 10 minutes. Then, the sample underwent a heating cycle from 10 to 50ºC, followed by an equilibrium time of 10 minutes and a cooling cycle (50–10ºC). The temperature rate in the cycles was of 1ºC/min.

The T_{LCS} was calculated from the onset temperature (T_{ons}) of the endothermic peak, determined as the intersection of the tangent of the endortherm's maximal

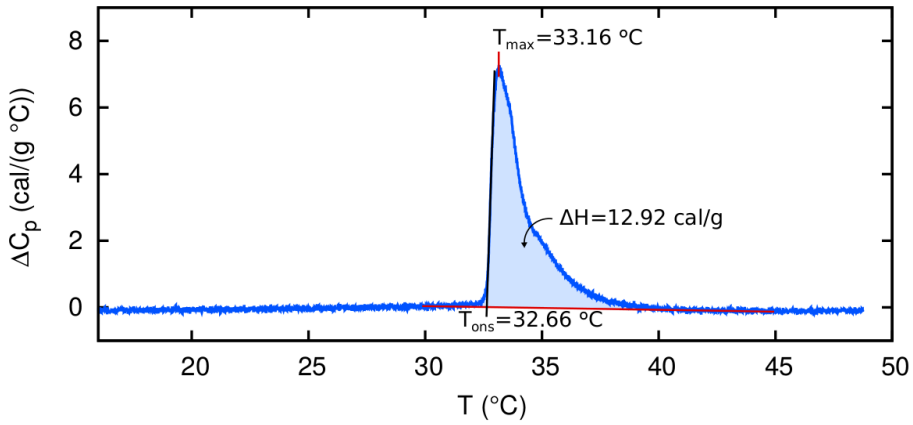

Figure 2.9: Analysis of the thermograms of PNIPAM. The parameters T_{ons}, T_{max} and ΔH are indicated.

slope and the baseline. T_{max} is the temperature at the maximum point of the endothermic peak. The change in enthalpy (ΔH), was calculated from the area under of the endothermic peak (see Figure 2.9).

References

[1] Maldonado-Valderrama, J.; Terriza, J. H.; Torcello-Gomez, A.; Cabrerizo-Vilchez, M. In vitro digestion of interfacial protein structures. *Soft Matter* **2013**, *9*, 1043–1053.

[2] López-León, T.; Jódar-Reyes, A. B.; Bastos-González, D.; Ortega-Vinuesa, J. L. Hofmeister effects in the stability and electrophoretic mobility of polystyrene latex particles. *J. Phys. Chem. B* **2003**, *107*, 5696–5708.

[3] López-León, T.; Santander-Ortega, M. J.; Ortega-Vinuesa, J. L.; Bastos-González, D. Hofmeister effects in colloidal systems: influence of the surface nature. *J. Phys. Chem. C* **2008**, *112*, 16060–16069.

[4] Acciaro, R.; Gilányi, T.; Varga, I. Preparation of monodisperse poly (N-isopropylacrylamide) microgel particles with homogenous cross-link density distribution. *Langmuir* **2011**, *27*, 7917–7925.

[5] Tagit, O.; Tomczak, N.; Vancso, G. J. Probing the Morphology and Nanoscale Mechanics of Single Poly (N-isopropylacrylamide) Microgels Across the Lower-Critical-Solution Temperature by Atomic Force Microscopy. *Small* **2008**, *4*, 119–126.

[6] Gao, J.; Frisken, B. J. Influence of reaction conditions on the synthesis of self-cross-linked N-isopropylacrylamide microgels. *Langmuir* **2003**, *19*, 5217–5222.

[7] Pelton, R.; Chibante, P. Preparation of aqueous latices with N-isopropylacrylamide. *Coll. Surf.* **1986**, *20*, 247–256.

[8] López-León, T.; Ortega-Vinuesa, J. L.; Bastos-González, D.; Elaïssari, A. Cationic and anionic poly (N-isopropylacrylamide) based submicron gel particles: Electrokinetic properties and colloidal stability. *J. Phys. Chem. B* **2006**, *110*, 4629–4636.

[9] López-León, T.; Elaïssari, A.; Ortega-Vinuesa, J. L.; Bastos-González, D. Hofmeister effects on poly (NIPAM) microgel particles: macroscopic evidence of ion adsorption and changes in water structure. *ChemPhysChem* **2007**, *8*, 148–156.

[10] Ahmed, S.; El-Aasser, M.; Pauli, G.; Poehlein, G.; Vanderhoff, J. Cleaning latexes for surface characterization by serum replacement. *J. Colloid Interface Sci.* **1980**, *73*, 388–405.

[11] Payens, T.; Brinkhuis, J.; Van Markwijk, B. Self-association in non-ideal systems. Combined light scattering and sedimentation measurements in β-casein solutions. *Biochim. Biophys. Acta* **1969**, *175*, 434–437.

[12] Portnaya, I.; Ben-Shoshan, E.; Cogan, U.; Khalfin, R.; Fass, D.; Ramon, O.; Danino, D. Self-assembly of bovine β-casein below the isoelectric pH. *J. Agric. Food Chem.* **2008**, *56*, 2192–2198.

[13] Demanèche, S.; Chapel, J.-P.; Monrozier, L. J.; Quiquampoix, H. Dissimilar pH-dependent adsorption features of bovine serum albumin and α-chymotrypsin on mica probed by AFM. *Colloid Surf. B* **2009**, *70*, 226–231.

[14] Pace, C. N.; Vajdos, F.; Fee, L.; Grimsley, G.; Gray, T. How to measure and predict the molar absorption coefficient of a protein. *Protein Sci.* **1995**, *4*, 2411.

[15] Farrell, H.; Jimenez-Flores, R.; Bleck, G.; Brown, E.; Butler, J.; Creamer, L.; Hicks, C.; Hollar, C.; Ng-Kwai-Hang, K.; Swaisgood, H. Nomenclature of the proteins of cows' milk—sixth revision. *J. Dairy Sci.* **2004**, *87*, 1641–1674.

[16] Elgersma, A. V.; Zsom, R. L.; Norde, W.; Lyklema, J. The adsorption of different types of monoclonal immunoglobulin on positively and negatively charged polystyrene latices. *Colloids Surf.* **1991**, *54*, 89–101.

[17] López-León, T.; Jódar-Reyes, A.; Ortega-Vinuesa, J.; Bastos-González, D. Hofmeister effects on the colloidal stability of an IgG-coated polystyrene latex. *J. Colloid Interface Sci.* **2005**, *284*, 139–148.

[18] Hassan, P. A.; Rana, S.; Verma, G. Making sense of brownian motion: colloid characterization by dynamic light scattering. *Langmuir* **2014**, *31*, 3–12.

[19] Hunter, R. J., *Foundations of colloid science*; Oxford University Press: 2001.

[20] Tscharnuter, W. W. Mobility measurements by phase analysis. *Appl. Opt.* **2001**, *40*, 3995–4003.

[21] Somasundaran, P., *Encyclopedia of surface and colloid science*; CRC press: 2006; Vol. 1.

[22] Ohshima, H. On the general expression for the electrophoretic mobility of a soft particle. *J. Colloid Interface Sci.* **2000**, *228*, 190–193.

[23] Butt, H.-J.; Graf, K.; Kappl, M., *Physics and chemistry of interfaces*; John Wiley & Sons: 2006.

[24] Peula-García, J. M.; Ortega-Vinuesa, J. L.; Bastos-González, D. Inversion of Hofmeister series by changing the surface of colloidal particles from hydrophobic to hydrophilic. *J. Phys. Chem. C* **2010**, *114*, 11133–11139.

[25] Pérez-Fuentes, L.; Bastos-González, D.; Drummond, C.; Faraudo, J. Re-estabilizing forces in colloids induced by hydrophobic ions. *Materials (in preparation)*,

[26] Jandt, K. D. Atomic force microscopy of biomaterials surfaces and interfaces. *Surf. Sci.* **2001**, *491*, 303–332.

[27] Israelachvili, J. N.; McGuiggan, P. M. Forces between surfaces in liquids. *Science* **1988**, *241*, 795–800.

[28] Israelachvili, J. N.; Adams, G. E. Measurement of forces between two mica surfaces in aqueous electrolyte solutions in the range 0–100 nm. *J. Chem. Soc., Faraday Trans.* **1978**, *74*, 975–1001.

[29] Helt, J. M.; Batteas, J. D. Wear of mica under aqueous environments: direct observation of defect nucleation by AFM. *Langmuir* **2005**, *21*, 633–639.

[30] Hegner, M.; Wagner, P.; Semenza, G. Ultralarge atomically flat template-stripped Au surfaces for scanning probe microscopy. *Surf. Sci.* **1993**, *291*, 39–46.

[31] Reviakine, I.; Johannsmann, D.; Richter, R. P. Hearing what you cannot see and visualizing what you hear: interpreting quartz crystal microbalance data from solvated interfaces. *Anal. Chem.* **2011**, *83*, 8838–8848.

[32] Burmistrova, A. Temperature-induced swelling/shrinking behavior of adsorbed PNIPAM microgels., 2011.

[33] Sauerbrey, G. Use of quartz vibration for weighing thin films on a microbalance. *J. Physik* **1959**, *155*, 206–212.

[34] Höök, F.; Rodahl, M.; Kasemo, B.; Brzezinski, P. Structural changes in hemoglobin during adsorption to solid surfaces: effects of pH, ionic strength, and ligand binding. *Proc. Natl. Acad. Sci. USA* **1998**, *95*, 12271–12276.

[35] Rodahl, M.; Höök, F.; Fredriksson, C.; Keller, C. A.; Krozer, A.; Brzezinski, P.; Voinova, M.; Kasemo, B. Simultaneous frequency and dissipation factor QCM measurements of biomolecular adsorption and cell adhesion. *Faraday Discuss.* **1997**, *107*, 229–246.

[36] Johannsmann, D. Viscoelastic, mechanical, and dielectric measurements on complex samples with the quartz crystal microbalance. *Phys. Chem. Chem. Phys.* **2008**, *10*, 4516–4534.

[37] Johannsmann, D., *The Quartz Crystal Microbalance in Soft Matter Research*; Springer: 2014.

[38] Johannsmann, D.; Mathauer, K.; Wegner, G.; Knoll, W. Viscoelastic properties of thin films probed with a quartz-crystal resonator. *Phys. Rev. B* **1992**, *46*, 7808–7815.

[39] Ferry, J. D., *Viscoelastic properties of polymers*; John Wiley & Sons: 1980.

[40] Domack, A.; Prucker, O.; Rühe, J.; Johannsmann, D. Swelling of a polymer brush probed with a quartz crystal resonator. *Phys. Rev. E* **1997**, *56*, 680–689.

[41] Mohamoud, M. A.; Hillman, A. R.; Efimov, I. Film mechanical resonance phenomenon during electrochemical deposition of polyaniline. *Electrochim. Acta* **2008**, *53*, 6235–6243.

[42] Saraswathi, R.; Hillman, A. R.; Martin, S. J. Mechanical resonance effects in electroactive polycarbazole films. *Electroanal. Chem.* **1999**, *460*, 267–272.

[43] Hillman, A. R.; Brown, M. J.; Martin, S. J. Resonance effects in electroactive poly (3-hexylthiophene) films. *J. Am. Chem. Soc.* **1998**, *120*, 12968–12969.

[44] Vanoni, V. A., *Sedimentation engineering. Appendix 2: Density and Viscosity of Water 0^o-40^o*, 2006, pp 407–409.

[45] Siretanu, I. Nanostructuration contrôlée de films de polymères., Ph.D. Thesis, Bordeaux 1, 2011.

[46] Siretanu, I.; Chapel, J.-P.; Bastos-González, D.; Drummond, C. Ions-Induced Nanostructuration: Effect of Specific Ionic Adsorption on Hydrophobic Polymer Surfaces. *J. Phys. Chem. B* **2013**, *117*, 6814–6822.

[47] Haines, P.; Wilburn, F. In *Thermal Methods of Analysis*; Springer: 1995, pp 63–122.

[48] Danley, R. L. New heat flux DSC measurement technique. *Thermochim. Acta* **2002**, *395*, 201–208.

[49] Gill, P.; Moghadam, T. T.; Ranjbar, B. Differential scanning calorimetry techniques: applications in biology and nanoscience. *J. Biomol. Tech.* **2010**, *21*, 167.

3 Simulation section

3.1 Molecular Dynamics simulations

3.1.1 Newtonian equations

Molecular Dynamics (MD) simulations allow us to obtain exact results of positions and velocities for a system with a large number of atoms by the Newtonian equations of motion. This is based on numerical solution of the equations under certain thermodynamic conditions [1, 2]. Computer simulations enable to model a physical system represented as a set of particles. This is very useful for a better understanding of the observed macroscopic behavior by investigating the system at microscopic level. For a system of N atoms, the Newtonian equations of motion are:

$$m_\alpha \ddot{\vec{r}}_\alpha = -\frac{\partial}{\partial \vec{r}_\alpha} U_{total}(\vec{r}_1, \vec{r}_2, ..., \vec{r}_N), \qquad \alpha = 1, 2, ..., N \tag{3.1}$$

where m_α is the mass of atom α, $\vec{r}_\alpha$ is its position and U_{total} is the total potential energy, which represents the interactions between all the atoms. In this kind of simulations, atoms are considered as classical entities. However the potential energy of the system (U_{total}) can be calculated by quantum mechanics (*ab initio* MD simulations) or classical mechanics (force fields). In the first case, the Schrödinger equation is solved in each time step. This method is used when quantum effects are important, this is, in chemical phenomena in which electrons play a role such as breaking or formation of covalent bonds or electron transfer, for example. While in the classical method, electrons are ignored and the interactions between atoms are calculated by approximated formulas obtained from theoretical or semiempirical methods, which are known with the generic name of Force Fields. This approach is appropriate for large and complex systems in solution (such as soft matter systems) which require long simulations as long as quantum

phenomena such as chemical reactions or electron transfer can be ignored. In this thesis, all simulations will be based on Force Fields.

The Newton's equations cannot be solved analytically by a computer. For the numerical solution, the time must be discretized in small intervals of size Δt. The discretization of the differential equations in time allows to get a system of nonlinear algebraic equations, which can be numerically solved.

There are several available numerical methods to solve the Newtonian equations (Euler, Leapfrog, Verlet, velocity Verlet...) [1]. The algorithm chosen should meet some requirements for a reliable resolution. An essential condition is the energy conservation, as expected for an isolated system. For instance, the Euler algorithm is not compatible with this condition, producing long-term energy drift problems. Therefore, this kind of algorithms are not adequate for MD simulations. Another noteworthy fact is the trajectory predictions. An exponential growth of the errors in the trajectory is unavoidable, however the algorithm will be more suitable if the errors are contained for longer time.

Although the true trajectories cannot be accurately predicted, we expect that the generated integration errors do not affect to the statistical properties of the system [1]. Our interest is the average behavior of the system, not the trajectory of every single atom.

One of the most used numerical methods is velocity Verlet [3]. This algorithm is based on a Taylor expansion of the coordinates of each atom. The position in each time step is calculated from the positions of the two earlier steps:

$$\vec{r}(t+\Delta t) \simeq 2\vec{r}(t) - \vec{r}(t-\Delta t) + \frac{f(t)}{m}\Delta t^2 \tag{3.2}$$

where $f(t)$ is the total interaction force exerted by all the elements of the system to each individual particle at instant t. Once the position is calculated in the current time step, the velocity is obtained as:

$$\vec{v}(t+\Delta t) = \vec{v}(t) + \frac{f(t+\Delta t) + f(t)}{2m}\Delta t \tag{3.3}$$

As the Newtonian equations, this process is completely reversible. The temporal reversibility of this algorithm implies energy conservation (Noether's theorem [4]), as is required for an algorithm useful in MD simulations.

On the other hand, the time step is chosen to be smaller than the typical time of the physical process that we observe. As an example the hydrogen bonding has a mean time of 2 ps ($2{\cdot}10^{-12}$ s) [5]. On the other hand, a very small Δt will require too much computational time. Standard time steps in MD simulations are shown in Table 3.1.

In our simulations we work with flexible molecules and rigid bonds. Hence, according to the table, an appropriate time step for us is 2 fs ($2{\cdot}10^{-15}$ s).

System	Types of motion	Time step (s)
Atoms	Translation	10^{-14}
Rigid molecules	Translation and rotation	$5{\cdot}10^{-15}$
Flexible molecules, rigid bonds	Translation, rotation and torsion	$2{\cdot}10^{-15}$
Flexible molecules, flexible bonds	Translation, rotation torsion and vibration	$5{\cdot}10^{-16}$–10^{-15}

Table 3.1: Standard time steps for atom or molecules motions in MD simulations.

Furthermore, Newton's laws require initial conditions to solve the equations. On the one hand, the positions of the atoms can be random or from known crystallographic structures of molecules. On the other hand, the system is initially at certain temperature, therefore the velocities follow a Maxwell–Boltzmann distribution. For this reason, the initial velocities of the atoms are randomly generated following a Maxwell–Boltzmann distribution.

3.1.2 Microcanonical ensemble (NVE)

The simulation system can be represented as an isolated system without applied external forces, only interactions between the internal atoms. The microcanonical ensemble (NVE) reproduces this kind of system, conserving the number of particles, volume and energy. Regarding the volume, we cannot simulate a macroscopic volume, instead of that we work with a small system where the density is maintained fixed. This means that the ratio between the number of particles and the volume is the same that in the real system. For that, periodic boundary conditions in all directions are used (see Figure 3.1).

The cell is infinitely replicated and translated in the space periodically. In this way, a particle that leaves the cell on one side is replaced by a copy entering the cell on the opposite side.

According to the statistical mechanics, we can obtain several physical magnitudes from the position and velocity data [1], such as, the kinetic energy, the potential energy, correlations, etc. In this way, the temperature in each instant is obtained using the Equipartition Theorem:

$$T_{inst} = \frac{2}{gk_B} E_{kin} \tag{3.4}$$

where g is the total number of degrees of freedom of the system, k_B the Boltzmann's constant and E_{kin} the kinetic energy. Both, potential and kinetic energy are usually provided as output of the simulation. On the other hand, pressure can be calculated using the Virial equation:

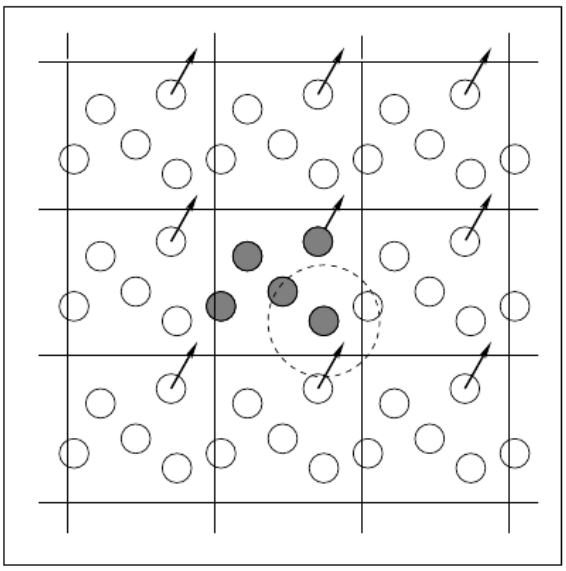

Figure 3.1: Representation of periodic boundary conditions implemented in a simulation box. The cell is infinitely replicated and translated in the space periodically. In this way, a particle that leaves the cell on one side is replaced by a copy entering the cell on the opposite side.

$$P = \rho k_B T + \frac{1}{3V} \left\langle \sum_{i<j} \vec{r}_{ij} \vec{F}(\vec{r}_{ij}) \right\rangle \tag{3.5}$$

where $\rho = N/V$ is the average number density and $\vec{F}(\vec{r}_{ij})$ represents the force applied by particle i^{th} on particle j^{th}, which are separated by a distance r_{ij}.

Nevertheless, these magnitudes can be fixed to implement the isothermal–isobaric ensemble (NPT). The microcanonical ensemble does not correspond to an experimentally realistic situation. In contrast, NPT ensemble is more appropriate.

3.1.3 Isothermal–isobaric ensemble (NPT)

The majority of our simulations are performed in the NPT ensemble. This means that the simulation is carried out under conditions of number of atoms, pressure and temperature at constant values. This ensemble plays an important role to be compared with experimental systems that usually work under these conditions. The system is not isolated, otherwise external energy can be added or removed from the system by a thermostat and barostat to maintain constant the temperature and pressure of the system, respectively.

The most intuitive idea to implement a thermostat is simulating a large system (at constant temperature) in contact with the system of interest. However, this is not possible because of involved computational cost. Therefore, an external force is applicated to vary the energy of the atoms. It is necessary using a thermostat that reproduces the properties of the NPT ensemble, since inadequate thermostats in this sense are available in the bibliography, for example the velocity scaling algorithm proposed by Evans [6, 7].

Mainly, there are two types of thermostats: stochastic (e.g. Langevin) and deterministic (e.g. Nosé-Hoover) [1]. In our simulations we have used the Langevin thermostat. As we have mentioned, the velocities of the atoms are set to follow the Maxwell–Boltzmann distribution with the thermodynamic temperature desired. After that, the temperature is maintained constant by the Langevin thermostat. This method is based on the Brownian motion of a particle in thermal contact with a large heat bath at the temperature required. Our simulation system is the Brownian particle immersed in an imaginarium fluid (the thermostat). The system is subjected to a friction force exerted by the thermostat plus a thermal noise [8, 9].

On the other hand, the pressure is maintained at the interest value by an applied external force, where the volume is adjusted. The Nosé-Hoover barostat was used for this purpose [1, 10]. For performing this scheme, an extra degree of freedom is added into the equations of motion. The extra parameter is known as the volume scaling factor, corresponding to a “piston” that allows changes in the volume of the simulation box.

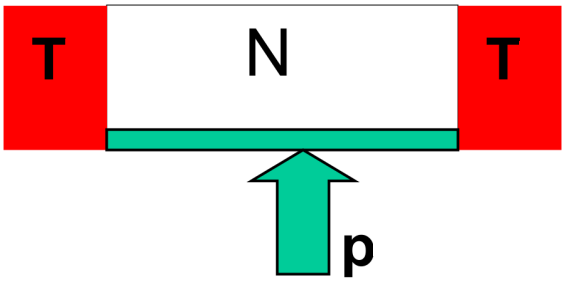

Figure 3.2: NPT ensemble. Thermodynamic state for a system defined by N particles. Temperature and pressure are determined by thermal and mechanical equilibrium with a thermal bath and a barostat, respectively.

Nowadays, we can found several open code programs for scientific usage to implement the resolution algorithms for MD simulations with the pertinent thermostats and barostats. In this dissertation we have used the programs: NAMD [10] and VMD [11] developed by the Theoretical and Computational Biophysics Group of the University of Illinois [12]. NAMD is used for solving the Newtonian

equations, while with VMD we can visualize and analyze the molecular systems. The combination of these two programs allows to obtain the instantaneous positions and velocities of all atoms, as well as, average properties of the model system. In addition, we have calculated some magnitudes not implemented in VMD, by homemade python scripts running in VMD, for example the radius of gyration of a polymer.

3.2 Modelling and force field for all–atomic simulations

3.2.1 CHARMM force field

Some common force fields are AMBER, GROMACS or OPLS [13–15]. In our simulations we used the standard CHARMM 2.7 force field (Chemistry at HARvard Molecular Mechanics) [16] implemented by NAMD. For this force field, the parameters of the intramolecular interactions are previously determined by quantum mechanics calculations (*ab initio*). The force field is tested to reproduce the properties of well-known molecules, as well as, the properties of the solvent. This force field is suitable for molecular systems such as, organic molecules, ions and surfaces in solution; and is widely used in simulations with polymers and proteins. Basically, we simulate this kind of systems.

The potential used is composed by intramolecular and intermolecular interactions [10]:

$$U_{total} = U_{bond} + U_{angle} + U_{dihedral} + U_{vdW} + U_{Coulomb} \tag{3.6}$$

The first three contributions form the intramolecular part. This is referred to interactions between atoms of the same molecule that includes covalent $bonds$, $angles$ between covalent bonds and $dihedral$ (angles formed by planes that contain atoms connected by three covalent bonds):

$$U_{bond} = \sum_{bonds} k_{ij}^{bond}(r_{ij} - r_0)^2 \tag{3.7}$$

$$U_{angle} = \sum_{angles} k_{ijk}^{angle}(\theta_{ijk} - \theta_0)^2 \tag{3.8}$$

$$U_{dihedral} = \sum_{dihedral} \begin{cases} k_{ijkl}^{dihedral}[1 + \cos(n\phi_{ijkl} - \phi_0)] & n \neq 0 \\ k_{ijkl}^{improper}(\psi_{ijkl} - \psi_0) & n = 0 \end{cases} \tag{3.9}$$

where r_{ij} represents the distance between atoms i and j bonded covalently, θ_{ijk} is the angle between two covalent bonds that connect atoms i, j and k, ϕ_{ijkl} is the dihedral angle, and ψ_{ijkl} is the so-called "improper" dihedral angle (see Figure 3.3). When four atoms i, j, k and l are linearly connected by three bonds, ϕ_{ijkl} is the angle formed by the plane containing atoms i, j, k and the plane containing atoms j, k, l. On the other hand, ψ_{ijkl} is the angle between the plane formed by atoms i, j, k and the plane formed by atoms j, k, l when atoms j, k, l are bonded separately to atom i.

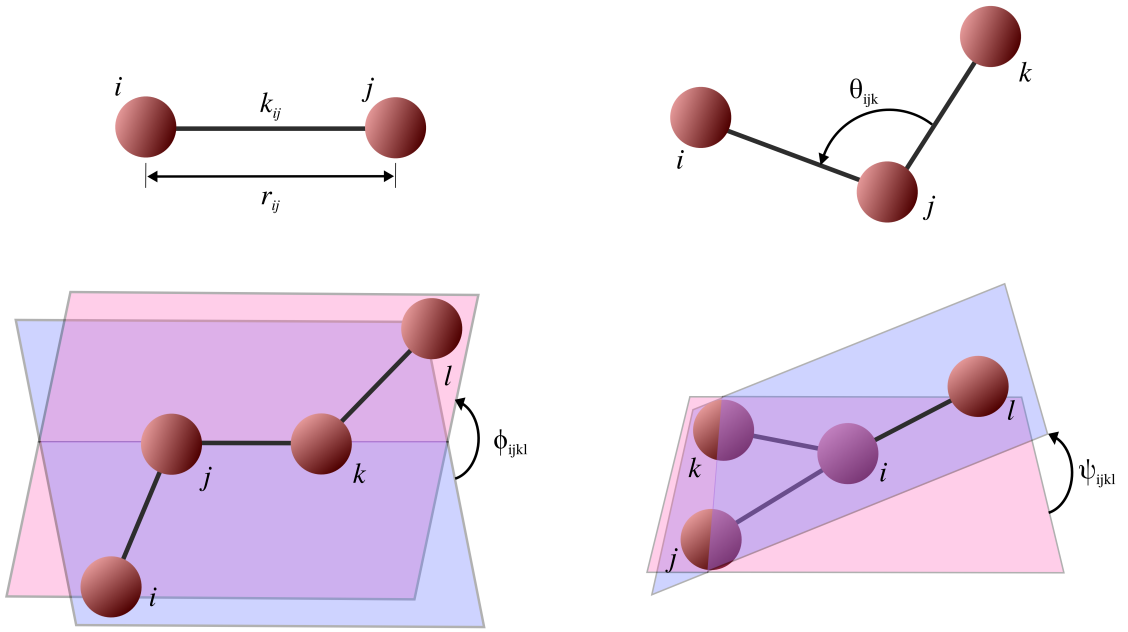

Figure 3.3: Coordinates for the intramolecular interactions between covalently bonded atoms.

Equation 3.7 represent the covalent bond between two atoms i, j as a harmonic potential by a Taylor approximation of elastic constant k_{ij}^{bond}. Hence, the real position of the atoms only undergoes small deviations from the equilibrium position r_0. The same is asumed for the angle between two bonds, subjected to a harmonic potential with a force constant of k_{ijk}^{angle} and reference value of θ_0 (eq. 3.8).

In contrast, for the dihedral angle, the potential harmonic approximation can fluctuate around several energy minima, which are found at the reference values ϕ_0. In equation 3.9, n indicates the number of energy minima and $k_{ijkl}^{dihedral}$ is the constant force. An example of various possible configurations for a molecule is the cis/trans isomerism.

In the case of the improper angle, the harmonic potential possesses only one energy minimum situated at ψ_0. This parameter is used for maintain planarity

in a molecular structure. Therefore, the value of ψ_{ijkl} suffers slight deviations from the reference value with a constant force of $k_{ijkl}^{improper}$ (3.9). A more extended explanation of the atom interactions can be consulted in ref. [17].

On the other hand, the interactions between non-bonded atoms (intermolecular), are represented by the other two contributions in equation 3.6. Atoms are modelled as hard spheres under a Lennard–Jones potential (van der Waals forces) and electrostatic interactions (Coulomb term):

$$U_{vdW} = \sum_i \sum_{j>i} 4\epsilon_{ij} \left[\left(\frac{\sigma_{ij}}{r_{ij}} \right)^{12} - \left(\frac{\sigma_{ij}}{r_{ij}} \right)^{6} \right] \tag{3.10}$$

$$U_{Coulomb} = \sum_i \sum_{j>i} \frac{q_i q_j}{4\pi\varepsilon_0 r_{ij}} \tag{3.11}$$

These interactions take into account characteristics of the individual atoms as size, electrostatic charge and polarizability.

The periodic boundary conditions introduce a problem related with the intermolecular interactions. Each atom is subject to the potential forces exerted by infinite number of particles, which is impossible to calculate. In order to solve this issue, the intermolecular interactions are truncated at certain distance. The potential associated to the van der Waals forces is quickly diminished with the distance ($U_{vdW} \propto r^{-6}$), thus a cutoff is establish for these interactions. In contrast, the electrostatic interactions can not be truncated in the same way. The long-range interactions are essential, since the potential is inversely proportional to the distance between particles ($U_{Coulomb} \propto r^{-1}$). For computing the Coulomb potential, the particle mesh Ewald summation method (PME) is employed. This method calculates the electrostatic contribution as a sum of screened charges instead of point charged, since the screened charges rapidly decay with the distance and can be easily computed [10].

3.2.2 Free energy calculation

Free Energy calculations require the use of specific methods, since a thermodynamic free energy cannot be obtained as a statistical average of positions and velocities for a single equilibrium MD simulation. In this thesis, we employ the adaptive biasing force (ABF) method [18] as implemented in NAMD. In the ABF method, a set of atoms (a given molecule for example) is constrained to follow a predefined path while the other atoms of the system are left to move without constraints, according to their equations of motion. This process needs to be conducted very slowly in order to the system will be capable of equilibrating under the effects of the thermostat and barostat. The force required to constraint the

trajectory of the atoms is computed in an adaptive fashion and in this way one obtains an approximation for the reversible work performed during the trajectory. As the process is performed in thermodynamic equilibrium in the NPT ensemble, the reversible work can be considered the Gibbs free energy. In simulation this is usually called potential of mean force (PMF).

3.2.3 Water model for CHARMM force field

In the CHARMM force field, water is modelled with the TIP3P model [19]. In this model water is treated as explicit solvent, this means that each water molecule is represented as an entity and is composed by an oxygen atom and two hydrogen atoms. The O–H covalent bonds are rigid and the angle H–O–H is maintained fixed at 104.52º. This means that intramolecular interactions are not calculated for the water molecule (eqs. 3.7–3.9). In fact, commonly, the interactions with the hydrogen atom are not considered. The lightest atom possesses very quick vibrations, which are not necessary for our simulations. Hence, only the intermolecular interactions among heavy atoms are calculated. This diminished the computing time.

On the other hand, the intermolecular interactions are specified by the parameters of van der Waals (Lennard–Jones) and electrostatic forces from atomic partial charges shown in Table 3.2. It deals with a non-polarizable model, since there is no internal redistribution of the electric charges. However, the model allows the free orientation of the molecules, as well as, the formation of hydrogen bondings among the different molecules. Although, other water models more complex are available in different force fields, the TIP3P model establish an agreement between the computational cost and its validity for liquid water.

Atom	ϵ_i (kcal/mol)	σ_i (Å)	q_i (e)
O	0.1521	3.5364	-0.834
H	0.0460	0.449	0.417

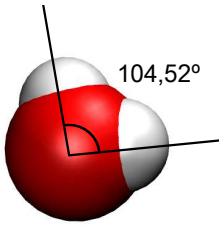

Table 3.2: Parameters for the intermolecular interactions (van der Waals and Coulomb forces) for water TIP3P model (see equations 3.10, 3.11).

3.2.4 Modelling of ions in CHARMM force field

We performed all-atomic MD simulations with the electrolytes $Na^+Ph_4B^-$ and $Ph_4As^+Cl^-$ in aqueous solution. The inorganic ions Na^+ and Cl^-, were simulated

as van der Waals spheres with electrostatic charge ± 1 and standard CHARMM 2.7 parameters. For the organic ions, we employed the force field parameters developed in ref. [20], obtained from *ab initio* calculations (partial charges for each atom are given in Table 3.3). In Figure 3.4, the electric charge distribution of the tetraphenyl ions is shown by a color scale. The most important difference between the two ions is the charge of the central atom (As or B), which is the most charged atom of each ion. In contrast, the external partial charges of both ions are very similar and they have low values.

Atom	q_i (Ph_4As^+)	q_i (Ph_4B^-)
X (central atom)	0.76	-0.48
C_1	-0.12	-0.29
C_2	-0.16	-0.15
C_3	-0.07	-0.24
C_4	-0.16	-0.15
C_5	-0.12	-0.29
C_6	-0.12	0.30
H_1	0.15	0.14
H_2	0.18	0.13
H_3	0.15	0.15
H_4	0.18	0.13
H_5	0.15	0.14

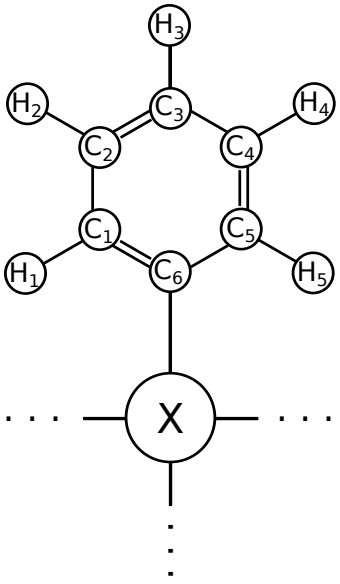

Table 3.3: Partial charges for each atom of the tetraphenyl ions (in units of electronic charge); the position of each atom is indicated in the diagram.

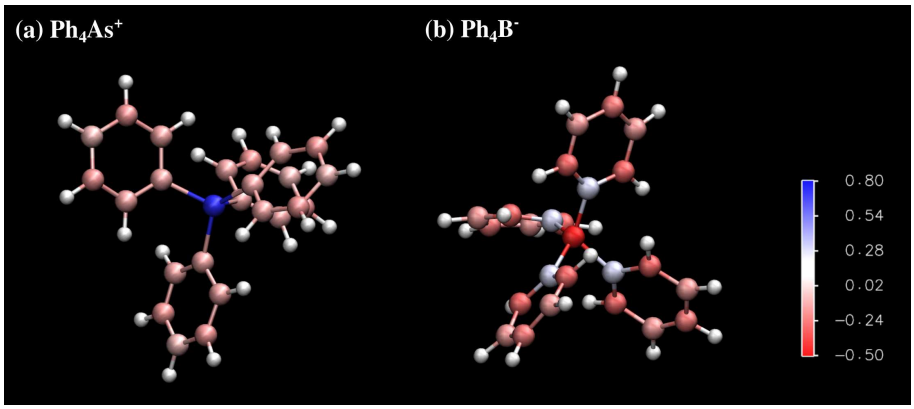

Figure 3.4: Electric charge distribution for the Ph_4As^+ cation (a) and the Ph_4B^- anion (b). The electrostatic charge is represented using a color scale, in this way the red color indicates a negative charge, whereas the blue color indicates a positive charge. The atoms are shown in CPK representation.

3.2.5 Modelling of PNIPAM chains in CHARMM force field

Neutral PNIPAM chains, with all-atomistic detail, were built replicating one monomer, formed by 19 atoms, with the VMD software (see Figure 3.5). Each PNIPAM chain has 20 monomers and the terminal molecules were capped with a $–CH_3$ group, as in previous work [21]. In Figure 3.6, one PNIPAM chain composed by 388 atoms is shown. In all our simulations, we have considered a system containing 5 PNIPAM chains in water electrolyte (a total of 1940 atoms of PNIPAM in the simulation box).

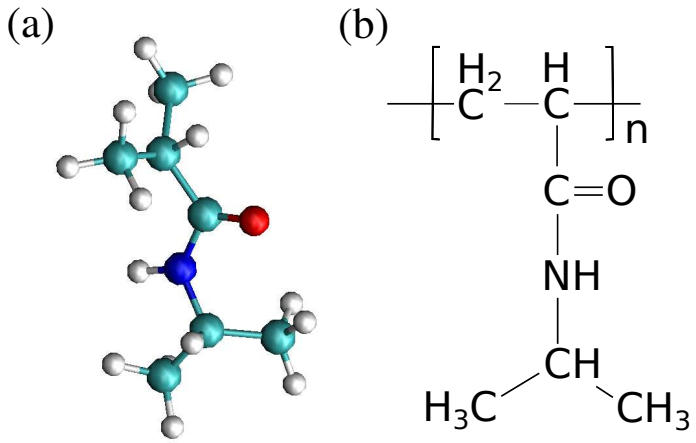

Figure 3.5: PNIPAM monomer: (a) all-atomic model (atoms are represented using standard colors (red=O, blue=N, white=H, cyan=C)) and (b) chemical structure.

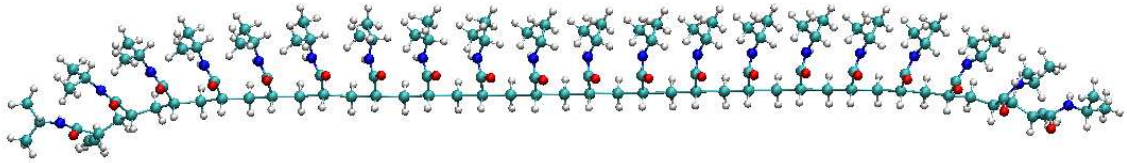

Figure 3.6: Model of one PNIPAM chain formed by 20 monomers in CPK representation.

3.3 Modelling and force field with implicit solvent: protein simulations

The proteins chosen, for this study, have been two proteins of the cow's milk: β-lactoglobulin and β-casein, as well as, the bovine serum albumin (BSA) as reference protein. Both, β-lactoglobulin and BSA are globular and well-structured proteins, whereas β-casein is a disorder and more flexible protein [22–25].

For the simulations, the structures of the globular proteins (BSA [26] and β-lactoglobulin [27]) were obtained from the Protein Data Bank [28]. This web holds the crystal structure of numerous proteins obtained mainly by X-ray diffraction. On the other hand, the crystalographic structure of the β-casein is not known, since is a disorder protein. Therefore, a 3D model developed by comparative modeling of known sequences was used for this protein [29]. According to these structures, each protein molecule is formed by 9207 atoms for BSA, 2584 atoms for β-lactoglobulin and 3124 atoms for β-casein.

We performed MD simulations of these proteins in aqueous solution at room temperature. The simulation of this system in all-atomistic detail would suppose a high computational cost. For this reason, the protein simulations were carried out in implicit water using the following model. Water is modelled by the Generalized Born Implicit Solvent (GBIS) as a dielectric continuum (polar solvent with water properties at 298 K and 1 atm). This model has been successfully used in MD simulations of macromolecules [30].

Therefore, the proteins are modelled with all-atomic detail and the potential (interaction) energy among the atoms is calculated by the force field CHARMM 2.7 plus interaction terms with the solvent. According to the GBIS model, the polar solvent (dielectric continuum) screens electrostatic interactions between solute atoms. The solute atoms are treated as van der Waals spheres of low protein dielectric constant immersed in a continuum of high solvent dielectric constant (ε=80, water). Therefore, the effective dielectric constant that affects each atom depends on the surrounding atoms to it. The total electrostatic energy for atoms is modeled as the sum of Coulomb and generalized Born energies:

$$E_{Elec} = E_{Coulomb} + E_{GBIS} \tag{3.12}$$

Only the protein area exposed is affected by the interactions with the solvent. In addition, each kind of atom (C,N,O,H...) has a particular interaction with the solvent.

Electrostatic charge

The protein simulation requires the knowledge of the protonation state of each residue as a function of pH. For this reason, the electrostatic charge of the proteins as a function of the pH was obtained by PropKa [31]. The computer program PropKa is an empirical method for fast protein pK_a prediction of structure-based proteins [32].

Proteins are formed by ionizable groups that intervene in intraprotein, protein-solvent and protein-ligand interactions, and they are directly related with protein solubility and folding. The pH dependency of the protein electrostatic charge is linked with the pK_a values of their ionizable residues.

In PropKa method the pK_a value of each amino acid is predicted by applying an environmental perturbation (pK_a shift), to the unperturbed intrinsic pK_a value of the group. The pK_a shift is calculated from the difference in electrostatic energy of a residue in its charged and neutral form. This method is based on numerical resolution of the Poisson-Boltzmann equation, taking into account this shift and the dielectric constant of the environs. The final pK_a values obtained by PropKa nearly match experimental results.

Hydrophobic degree of proteins

We calculated the hydrophobic degree of the investigated proteins. It is important to highlight that the structure of a protein strongly depends on the temperature. For this reason, the proteins were pre-equilibrated at 25°C and neutral pH by MD simulations. As we have mentioned, the simulations were carried out with the proteins immersed in a dielectric continuum with the water properties [30]. After an initial system minimization, MD simulations were carried out during 4 ns.

The last protein configuration was used to estimate its hydrophobicity. For that, we employed the Orientations of Proteins in Membranes (OPM) calculation, available in ref. [33]. A detail description of the method can be consulted in ref. [34]. This tool was developed for obtaining the arrangement of a protein in contact with a membrane. The protein is considered as a rigid body and the spatial orientation is determined by minimization of its transfer energy from water to a nonpolar liquid. The parameter set to define the nonpolar solvent corresponds to decadiene, which produces results in agreement with experimental data, in particular for transmembrane proteins in a lipid bilayer [35]. The transfer energy

of the proteins is an indicative of their degree of hydrophobicity, however this is variable depending on the nonpolar medium chosen. OPM is widely used, thus is a good method to stablish standard hydrophobicity values of proteins, which can be compared with other molecules reported in the literature.

3.4 Technical details and analysis of the MD simulations

As we previously mentioned, the MD simulation method is based on the numerical solution of the Newtonian equations of motion for all atoms of a molecular system constrained to the thermodynamic conditions (T, p). All the simulations were implemented in the standard version 2.9 of NAMD. The Newton's equations of motion were solved with a time step of 2 fs and electrostatic interactions were updated with a 4 fs time step. All bonds between heavy atoms and hydrogen atoms were maintained rigid. The nonbonding Lennard–Jones interactions were cut off at a distance of 1.2 nm employing a switching function starting at 1.0 nm. The particle Ewald summation method was employed with a 1 Å resolution. We employed periodic boundary conditions in all directions. The thermodynamic temperature was maintained constant (at 25ºC or 45ºC depending on the simulation) using a Langevin thermostat with a relaxation constant of 1 ps^{-1}. The pressure (1 atm) was maintained using the Nosé-Hoover piston as implemented in NAMD with an oscillation period of 100 fs and a decay time of 50 fs. In the case of the simulations with surfaces (Chapter 9), the pressure was maintained constant with the same barostat, but allowing changes of the simulation box only along the z axis (perpendicular to the surface).

In the particular case of protein simulations, the interaction with the solvent is conducted by an additional energy term that takes into account the properties of water at certain temperature and pressure. For this reason, periodic boundary conditions, thermostat and barostat are not used in these simulations.

In some simulations, we have used the software VMD to calculate the radial pair distribution function, g(r). This function characterize the local structure of set of atoms. g(r) is the ratio between the average number density at a distance from any given atom and the density at the same distance in an ideal gas at the same overall density [1]. In an ideal gas, g(r)=1, thus any deviation of g(r) from unity reflects correlations between the particles due to the intermolecular interactions (cf. Figure 3.7).

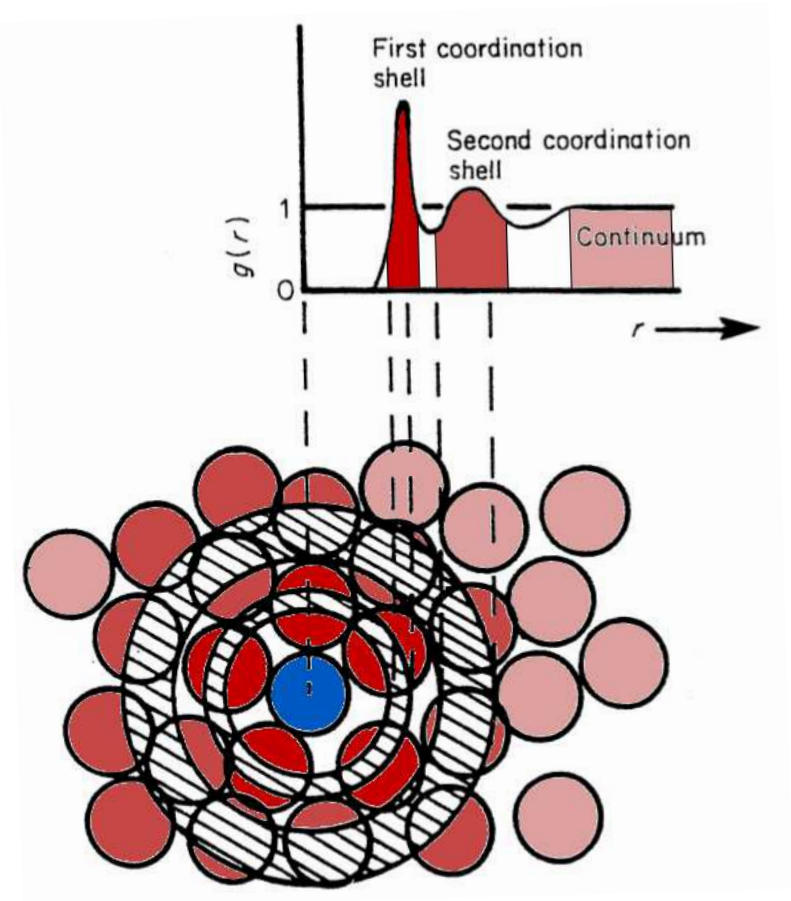

Figure 3.7: Radial pair distribution function, g(r). Average number density from a given atom as a function of the distance. The peaks indicate the existence of correlated atoms with respect to the reference atom. When there is no correlation, then g(r)=1. Image obtained from ref. [36].

References

[1] Frenkel, D.; Smit, B., *Understanding molecular simulation: from algorithms to applications*; Academic press: 2001; Vol. 1.

[2] Saiz-Poseu, J.; Martínez-Otero, A.; Roussel, T.; Hui, J. K.-H.; Montero, M. L.; Urcuyo, R.; MacLachlan, M. J.; Faraudo, J.; Ruiz-Molina, D. Self-assembly of a catechol-based macrocycle at the liquid–solid interface: experiments and molecular dynamics simulations. *Phys. Chem. Chem. Phys.* **2012**, *14*, 11937–11943.

[3] Swope, W. C.; Andersen, H. C.; Berens, P. H.; Wilson, K. R. A computer simulation method for the calculation of equilibrium constants for the formation of physical clusters of molecules: Application to small water clusters. *J. Chem. Phys.* **1982**, *76*, 637–649.

[4] Goldstein, H., *Classical Mechanics (2nd ed.)* Reading, MA: Addison-Wesley: 1980, pp 588–596.

[5] Jeffrey, G. A.; Jeffrey, G. A., *An introduction to hydrogen bonding*; Oxford university press New York: 1997; Vol. 12.

[6] Evans, D. J. Computer "experiment" for nonlinear thermodynamics of Couette flow. *J. Chem. Phys.* **1983**, *78*, 3297–3302.

[7] Evans, D. J.; Hoover, W. G.; Failor, B. H.; Moran, B.; Ladd, A. J. Nonequilibrium molecular dynamics via Gauss's principle of least constraint. *Phys. Rev. A* **1983**, *28*, 1016.

[8] Kubo, R. The fluctuation-dissipation theorem. *Rep. Prog. Phys.* **1966**, *29*, 255.

[9] Kohanoff, J.; Caro, A.; Finnis, M. W. An Isothermal–Isobaric Langevin Thermostat for Simulating Nanoparticles under Pressure: Application to Au Clusters. *ChemPhysChem* **2005**, *6*, 1848–1852.

[10] Phillips, J. C.; Braun, R.; Wang, W.; Gumbart, J.; Tajkhorshid, E.; Villa, E.; Chipot, C.; Skeel, R. D.; Kale, L.; Schulten, K. Scalable molecular dynamics with NAMD. *J. Comput. Chem.* **2005**, *26*, 1781–1802.

[11] Humphrey, W.; Dalke, A.; Schulten, K. VMD: visual molecular dynamics. *J. Mol. Graphics* **1996**, *14*, 33–38.

[12] Theoretical and Computational Biophysics Group. NAMD: Scalable Molecular Dynamics., http://www.ks.uiuc.edu/Research/namd, Accessed: 2015-11-27.

[13] Salomon-Ferrer, R.; Case, D. A.; Walker, R. C. An overview of the Amber biomolecular simulation package. *WIREs Comput. Mol. Sci.* **2013**, *3*, 198–210.

[14] Berendsen, H. J.; van der Spoel, D.; van Drunen, R. GROMACS: A message-passing parallel molecular dynamics implementation. *Comp. Phys. Comm.* **1995**, *91*, 43–56.

[15] Jorgensen, W. L.; Maxwell, D. S.; Tirado-Rives, J. Development and testing of the OPLS all-atom force field on conformational energetics and properties of organic liquids. *J. Am. Chem. Soc.* **1996**, *118*, 11225–11236.

[16] Brooks, B. R.; Brooks, C. L.; MacKerell, A. D.; Nilsson, L.; Petrella, R. J.; Roux, B.; Won, Y.; Archontis, G.; Bartels, C.; Boresch, S. et al. CHARMM: the biomolecular simulation program. *J. Comput. Chem.* **2009**, *30*, 1545–1614.

[17] PumMa. Atoms Interaction Potentials., http://cbio.bmt.tue.nl/pumma/index.php/Theory/Potentials, Accessed: 2015-11-27.

[18] Hénin, J.; Fiorin, G.; Chipot, C.; Klein, M. L. Exploring multidimensional free energy landscapes using time-dependent biases on collective variables. *J. Chem. Theory Comput.* **2009**, *6*, 35–47.

[19] Jorgensen, W. L.; Chandrasekhar, J.; Madura, J. D.; Impey, R. W.; Klein, M. L. Comparison of simple potential functions for simulating liquid water. *J. Chem. Phys.* **1983**, *79*, 926–935.

[20] Schurhammer, R.; Wipff, G. Are the hydrophobic $AsPh_4^+$ and BPh_4^- ions equally solvated? A theoretical investigation in aqueous and nonaqueous solutions using different charge distributions. *J. Phys. Chem. A* **2000**, *104*, 11159–11168.

[21] Du, H.; Wickramasinghe, R.; Qian, X. Effects of salt on the lower critical solution temperature of poly (N-isopropylacrylamide). *J. Phys. Chem. B* **2010**, *114*, 16594–16604.

[22] Caldwell, K. D.; Li, J.; Li, J.-T.; Dalgleish, D. G. Adsorption behavior of milk proteins on polystyrene latex: a study based on sedimentation field-flow fractionation and dynamic light scattering. *J. Chromatogr.* **1992**, *604*, 63–71.

[23] Maldonado-Valderrama, J.; Terriza, J. H.; Torcello-Gomez, A.; Cabrerizo-Vilchez, M. In vitro digestion of interfacial protein structures. *Soft Matter* **2013**, *9*, 1043–1053.

[24] Graham, D.; Phillips, M. Proteins at liquid interfaces. *J. Colloid Interface Sci.* **1979**, *70*, 403–439.

[25] Marinova, K. G.; Basheva, E. S.; Nenova, B.; Temelska, M.; Mirarefi, A. Y.; Campbell, B.; Ivanov, I. B. Physico-chemical factors controlling the foamability and foam stability of milk proteins: Sodium caseinate and whey protein concentrates. *Food Hydrocolloids* **2009**, *23*, 1864–1876.

[26] Bujacz, A.; Zielinski, K.; Sekula, B. Structural studies of bovine, equine, and leporine serum albumin complexes with naproxen. *Proteins* **2014**, *82*, 2199–2208.

[27] Loch, J.; Polit, A.; Gorecki, A.; Bonarek, P.; Kurpiewska, K.; Dziedzicka-Wasylewska, M.; Lewiński, K. Two modes of fatty acid binding to bovine β-lactoglobulin—crystallographic and spectroscopic studies. *J. Mol. Recognit.* **2011**, *24*, 341–349.

[28] Protein Data Bank: An Information Portal to Biological Macromolecular Structures., http://www.rcsb.org/, Accessed: 2015-11-27.

[29] Pieper, U.; Webb, B. M.; Dong, G. Q.; Schneidman-Duhovny, D.; Fan, H.; Kim, S. J.; Khuri, N.; Spill, Y. G.; Weinkam, P.; Hammel, M. et al. ModBase, a database of annotated comparative protein structure models and associated resources. *Nucl. Acids Res.* **2014**, *42*, D336–D346.

[30] Tanner, D. E.; Chan, K.-Y.; Phillips, J. C.; Schulten, K. Parallel generalized Born implicit solvent calculations with NAMD. *J. Chem. Theory Comput.* **2011**, *7*, 3635–3642.

[31] PropKa version 3.0., http://propka.org/, Accessed: 2015-11-27.

[32] Li, H.; Robertson, A. D.; Jensen, J. H. Very fast empirical prediction and rationalization of protein pKa values. *Proteins* **2005**, *61*, 704–721.

[33] OPM database: Orientations of Proteins in Membranes., http://opm.phar.umich.edu/, Accessed: 2015-11-27.

[34] Lomize, M. A.; Lomize, A. L.; Pogozheva, I. D.; Mosberg, H. I. OPM: orientations of proteins in membranes database. *Bioinformatics* **2006**, *22*, 623–625.

[35] Lomize, A. L.; Pogozheva, I. D.; Lomize, M. A.; Mosberg, H. I. Positioning of proteins in membranes: a computational approach. *Protein Sci.* **2006**, *15*, 1318–1333.

[36] Van de Ven, T. G., *Colloidal hydrodynamics*; Academic Press: 1989.

III Results and Discussion

4 Interaction of organic ions with PNIPAM chains and microgels

4.1 Background

It is well known that ions with the same valence induce different behavior in a wide range of phenomena such as the surface tension of water electrolyte/air interface, effect of salt in colloidal stability, protein precipitation by salt, etc [1, 2]. Although both cations and anions show these specific ionic effects, it has been known from long that anions show more pronounced specific ionic effects than cations [3–5]. This different behavior has been attributed to the fact that anions are bigger and more polarizable than cations and these two variables play a major role in specific ionic effects [6]. It is also clear that anions interact with water in a different way than cations. Anions and cations have very different hydrogen bonding capabilities, as recognized in experiments of transfer of ions from solvents with different tendency to form hydrogen bonds but similar dielectric constant [7]. A recent classification of the most common monovalent and divalent ions in a 2D map with hydrophilicity and hydrophobicity as coordinates shows that cations are found near the "neutral" point (no substantial hydrophobic/hydrophilic character) whereas anions are spread further out, particularly so for the more hydrophobic region of the map [8]. It is worth noting that the relative hydrophobic or hydrophilic character of ions and interfaces is essential in understanding specific ionic effects [9, 10].

Interestingly, MD simulations of hypothetical anions and cations identical in all respects except by the sign of the charge (i.e., equal size, charge, dispersion interactions) show that anions have more pronounced specific effects such as larger adsorption at the water/air interface [11] or larger adsorption at hydrophobic surfaces [12]. The simulations of these hypothetical ions also indicate that the ionic specific effects are directly linked to the ion-water interaction, which is different for cations and anions. The asymmetry between anions and cations of the same size arises because water molecules can approach closer to anions (due to the small size of the hydrogen atom) as compared with the cations (which interact

with the larger oxygen atoms of water). Recent spectroscopy experiments clearly demonstrate the existence of this solvation asymmetry between anions and cations [13].

All these studies suggest that substantial insight in the difference between cations and anions could be obtained by considering real (instead of hypothetical) ions with (almost) identical size, valency and chemistry but differing only in their anionic or cationic character. This is precisely our objective in this chapter, by considering the interaction of the tetraphenyl ions Ph_4B^- and Ph_4As^+ (Figure 4.1) with a particular soft matter system (PNIPAM microgels). Both ions are large (their radius is about 0.5 nm [14, 15]) and their external chemical and electronic structure is identical, with four phenyl rings responsible for the direct interaction of the ions with water, surfaces or interfaces. The anionic or cationic nature of the ions is due to the central atom (B or As), which does not interact directly with the environment (solvent or interfaces). Minute concentrations of these big hydrophobic ions have the ability to induce substantial effects in soft matter systems. For example, they can induce novel phases in lipid layers [16], giant charge inversion in colloids [10, 17] or induce nanostructuration in polymer surfaces in contact with water [18]. The effects are so strong that Leontidis *et al.* [16] coined the term "soft matter disruptors" to describe their deep impact on surfaces, which goes beyond what is observed for the classical ions considered in lyotropic (Hofmeister) sequences. It seems clear that in these effects, water structure [13] and solvation thermodynamics [10] play a fundamental role.

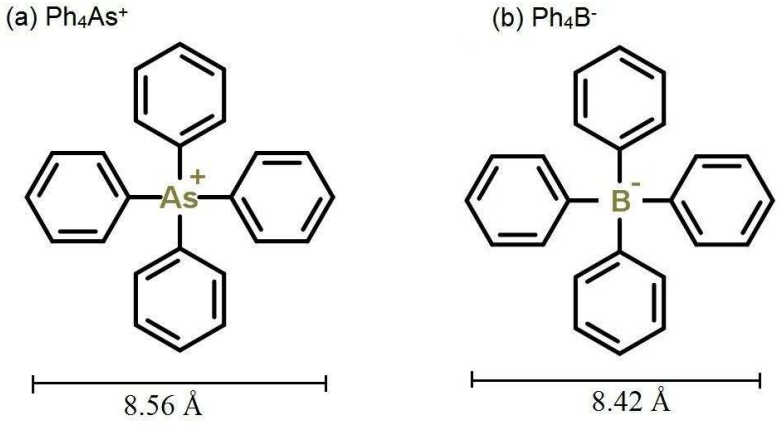

Figure 4.1: Chemical structures of Ph_4As^+ and Ph_4B^- ions. The van der Waals diameter [15] is indicated.

We will consider here the interaction of these ions with a thermoresponsive polymer, PNIPAM (Figure 4.2 (a)). This polymer undergoes a transition from extended coil to compact globule (or from swollen to collapsed states in the case

of microgels) when the temperature is increased over a critical value –usually called lower critical solution temperature (T_{LCS})– which is around 31–34ºC for PNIPAM [19]. According to previous studies with PNIPAM microgels [20] and PNIPAM charged chains [21], this system is particularly well suited for the study of specific ionic effects, due to its capacity to adsorb ions and its sensibility to the hydration state of ions. In addition, PNIPAM particles can be prepared with both cationic or anionic character, which allows the study of the behavior of ions Ph_4B^- and Ph_4As^+ as either counterions or coions.

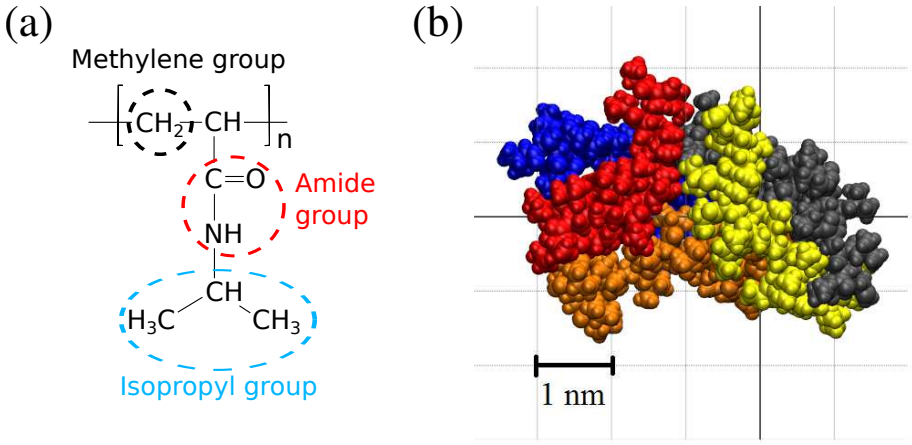

Figure 4.2: (a) Chemical structure of PNIPAM. (b) Simulation snapshot of an aggregate made by the self-assembly of 5 PNIPAM chains at 45ºC in the presence of NaCl (simulation S2 in Table 4.1). Each PNIPAM chain is shown in a different color. Atoms are shown as spheres with their van der Waals radius. Water and ions are not shown for clarity.

In this chapter, we show evidence from MD simulations, electrokinetic measurements and AFM imaging demonstrating dramatic differences between the specific effects due to the Ph_4B^- anion and the Ph_4As^+ cation. The effects of Ph_4B^- on neutral PNIPAM chains and in cationic or anionic PNIPAM microgels are always much stronger than the effects of Ph_4As^+. We argue that the evidences provided here strongly support the view that even for big ions solvation of anions is essentially different than the solvation of cations and, more importantly, the affinity of anions and cations for interfaces is intrinsically different.

4.2 Simulation results

4.2.1 Description of simulations

MD simulations with PNIPAM chains were performed in different ionic compositions. The size of the system and other details considered in our simulations are summarized in Table 4.1. In each simulation, we randomly place the 5 PNIPAM chains, the ions and water. After energy minimization, we performed a NPT run between 80 and 90 ns, to ensure that slow magnitudes such as the polymer radius of gyration equilibrate. The radius of gyration was obtained by a home-made python script running in VMD. In the case of Ph_4B^- and Ph_4As^+, we have computed the Gibbs free energy characterizing the ion adsorption by performing additional simulations (S5 and S6 in Table 4.1).

	T (K)	Number of ions	Number of water molecules	PNIPAM monomers	Total atoms	Size simulation box (Å)
S1 (MD)	298	15 Na^+, 15 Cl^-	22248	100	68714	87.78
S2 (MD)	318	15 Na^+, 15 Cl^-	22248	100	68714	87.78
S3 (MD)	318	15 Na^+, 15 Ph_4B^-	21779	100	67967	87.98
S4 (MD)	318	15 Ph_4As^+, 15 Cl^-	22126	100	69008	88.47
S5 (ABF-MD)	318	1 Na^+, 1 Ph_4B^-	22365	100	69081	88.45
S6 (ABF-MD)	318	1 Ph_4As^+, 1 Cl^-	22367	100	69087	88.46

Table 4.1: Summary of parameters for MD and ABF-MD computer simulations.

The adaptive biasing force (ABF) methodology [22] (see section 3.2.2 of Materials and Methods) is implemented in NAMD for the calculation of free energies along collective coordinates (the potential of mean force) in MD simulations. The biased simulations S5 and S6 employing the ABF simulations were performed in order to obtain the potential of mean force (PMF) corresponding to the ion-PNIPAM interaction. The initial configuration for the calculation was obtained as follows. We started from the results of simulations S3 and S4 in Table 4.1 and removed all ions except one adsorbed ion and one counter-ion. We added more water, and performed further NPT runs (of about 30 ns). The final configuration of the NPT run was employed as the initial configuration for the ABF calculation. The initial configuration is illustrated in Figure 4.3.

The first choice to be made in the ABF calculation is the selection of the collective variable or "reaction coordinate". We use the separation between the PNIPAM chains and the adsorbed ion. The separation between PNIPAM and the ion is computed using the central atom of the ion (B or As depending on the tetraphenyl ion) and a few reference atoms of the PNIPAM molecule which are located near the initial position of the ion. These atoms are indicated in Figure 4.3. Concerning the parameters of the technique, we tried different values for the force constant employed in the calculation and selected those which produced the better (less

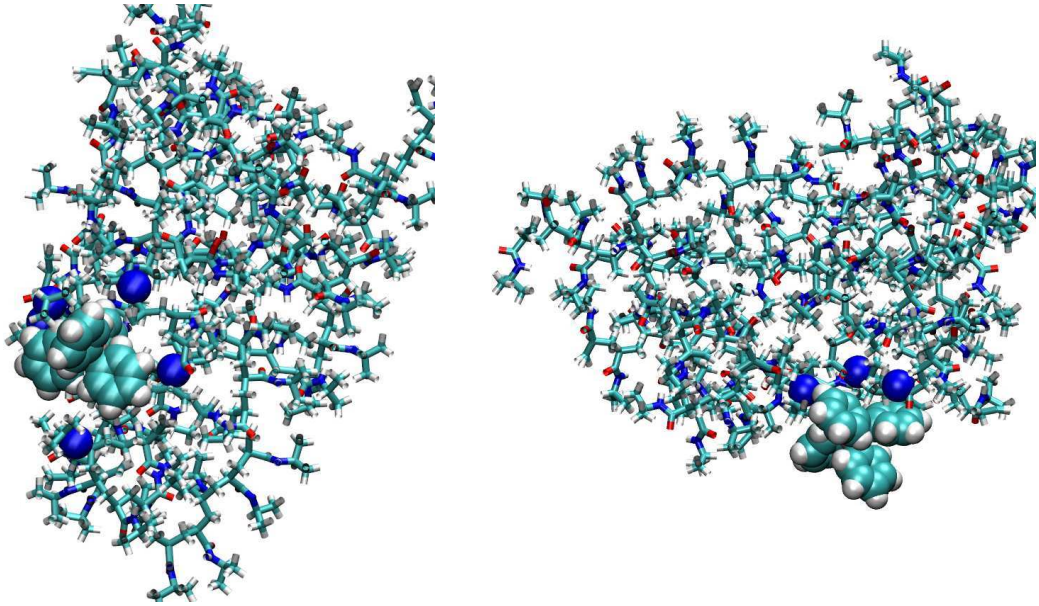

Figure 4.3: Snapshots of the initial configurations for the ABF-MD simulations. Left: Simulation S5 in Table 4.1 (adsorbed Ph_4B^- ion). Right: Simulation S6 in Table 4.1 (adsorbed Ph_4As^+ ion). The Ph_4B^- and Ph_4As^+ ions are shown in van der Waals representation. PNIPAM atoms are shown in bonds representation, except the reference atoms for the distance calculation which are shown with their van der Waals radius. Water molecules and the counter-ion of each adsorbed ion (Na^+ or Cl^-) are not shown for clarity. Figure made with VMD (Ref. [23]).

noisy) PMF curves. Our final choice was 5.0 kcal/(mol $\cdot$ Å^2) in simulation S5 (adsorbed Ph_4B^- ion) and 3.0 kcal/(mol $\cdot$ Å^2) in simulation S6 (adsorbed Ph_4As^+ ion). During the calculation, we avoid the displacement of the PNIPAM particle by applying an harmonic constraint with k=5.0 kcal/(mol $\cdot$ Å^2) to the positions of the heavy atoms (C,N,O) of PNIPAM (as equilibrium positions we select their initial positions). The potential of mean force of each ion was obtained with a 0.1 Å resolution in a simulation run with 2.5×10^6 steps. In each bin, the average of the PMF was calculated discarding the first 400 configurations.

4.2.2 Self-assembly of chains in presence of NaCl

Previous MD simulation studies about the temperature-induced transition of several PNIPAM chains are scarce [24]. In general, this transition is only studied at the single chain level [25–28]. This means that in these studies only the transition between coil and globule in a single PNIPAM chain was investigated, but the expanded/compressed state of PNIPAM particles was not simulated.

In principle, the interaction of ions with a single chain may differ with the inter-

action with aggregates containing several chains. For this reason, in this chater we will consider the interaction with a PNIPAM nanoparticle or aggregate (described in full atomistic detail), made by the self-assembly of several PNIPAM chains (see Methods section 3.2.5). Let us consider first simulations S1 and S2 in Table 4.1, which correspond to a system with 5 PNIPAM chains of 20 monomers each in presence of NaCl at two different temperatures (below and above the experimental transition temperature). A snapshot of a typical aggregate is shown in Figure 4.2 (b). In both simulations, we observe aggregation of the PNIPAM chains after a few ns of simulation. However, the nature of the aggregates is very different at each temperature. In simulation S1 (25ºC, below the transition temperature) the assembly is less stable, in the sense that partial disaggregation is sometimes found (i.e. a chain leaves the particle) and the size of the aggregate shows large fluctuations: the average radius of gyration of the self-assembled nanoparticle is $R_g \simeq$2.5 nm but the system explores configurations with larger radius ($\sim$3 nm or more) or configurations with groups of smaller aggregates ($\sim$2 nm) during time intervals of the order of tens of ns. In contrast, in simulation S2 (45ºC, above the experimental transition temperature) we observe self-assembly of the chains onto a single aggregate or particle (cf. Figure 4.2 (b)) with a radius of gyration $R_g =$1.5 nm (with no significant fluctuations), consistent with a collapsed state. The expanded state obtained in simulation S1 is also more hydrated than the collapsed state obtained in S2, as expected. In Figure 4.4, we show the total number of hydration molecules obtained for the PNIPAM particle at 25ºC and 45ºC.

We can also obtain the hydration of the different groups of the PNIPAM monomer at 25ºC and 45ºC. The results are summarized in Table 4.2. According to our results, the hydration of the PNIPAM chains at 25ºC is larger than at 45ºC, consistent with the experimentally observed transition of PNIPAM from a swollen state to a collapsed state with temperature (see Figure 4.8). The largest change in hydration occurs in the isopropyl group, as has been discussed previously both in the experimental and simulation [19–21, 25–28].

System	Monomer	Methylene	Amide	Isopropyl
S1 (25ºC)	8.38	1.25	1.31	8.32
S2 (45ºC)	7.05	1.02	1.23	7.02

Table 4.2: Number of water molecules in the first coordination shell of PNIPAM. “Monomer” corresponds to the hydration per monomer (excluding the capping of the chains), and Methylene, Amide and Isoporpyl correspond to the hydration of the different functional groups indicated in Figure 4.2 (a). Note that hydration water is shared between functional groups, so the sum of columns 3, 4 and 5 is greater than the value reported in column 2.

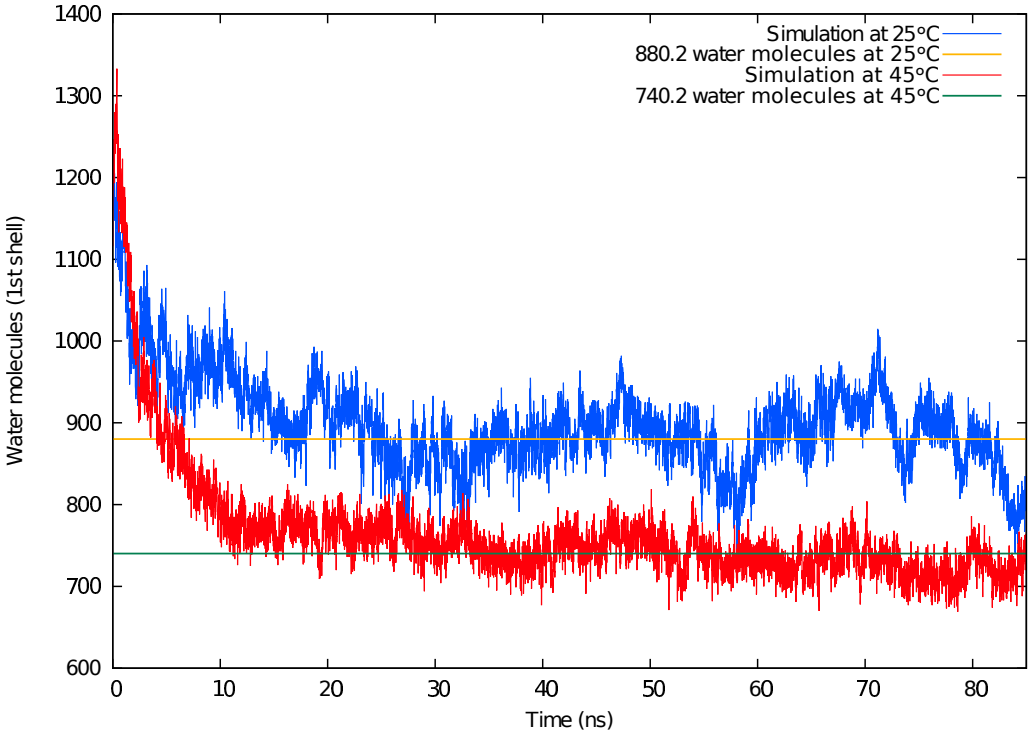

Figure 4.4: Time evolution of the number of water molecules in the first coordination shell of PNIPAM in simulations S1 at T=25ºC (blue) and S2 at T=45ºC (red) in presence of NaCl. The equilibrium values, computed discarding the first 30 ns of simulation, are shown as lines.

In both cases, the PNIPAM nanoparticle shows no adsorption of Na^+ or Cl^-. The analysis of the radial distribution functions g(r) presented in Figure 4.5 shows that the Na^+ cation interacts with PNIPAM through the oxygen atom of the amide group, in agreement with previous results obtained for a single chain [26], although the interaction is not strong enough to lead to adsorption of Na^+. Concerning the anion, we did not observe significant interaction of Cl^- with PNIPAM.

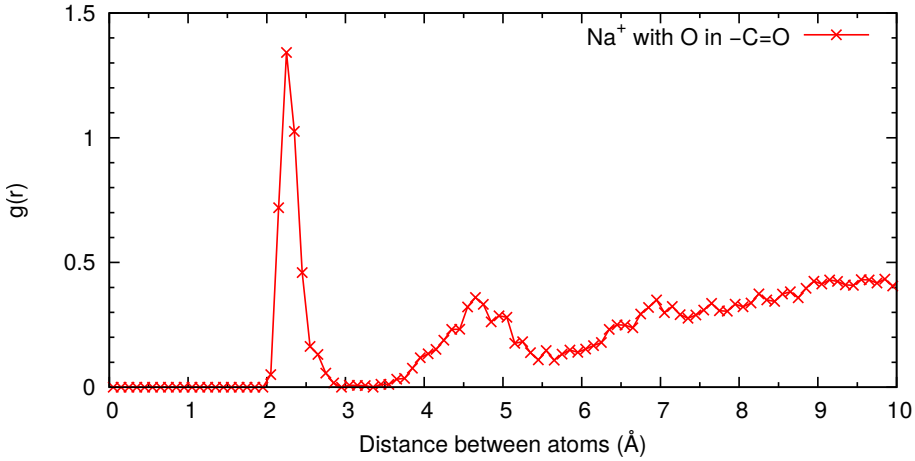

Figure 4.5: Radial distribution function between Na^+ ions and oxygen atoms from amide groups in PNIPAM obtained in simulation S1 (25ºC).

4.2.3 Interaction of big hydrophobic ions with a PNIPAM hydrophobic nanoparticle: MD simulations

Now, let us focus on the results for the interaction of the big hydrophobic ions of Figure 4.1 with a PNIPAM nanoparticle in the collapsed state (simulations S3 and S4 in Table 4.1). In analysing the results, it is important to keep in mind that the main difference between the two ions in the employed models is their anionic or cationic character due to the charge of the central atom (see model details in the Methods section 3.2.4). The analysis of pair distribution functions (Figure 4.6) shows several remarkable features. First of all, it can be observed that both ions interact with the hydrophobic isopropyl group. In previous works [25], it was observed that poorly solvated anions (I^- and to a less extend Br^-) interact weakly with these groups. Here we see that this interaction is not exclusive to anions since both Ph_4B^- and Ph_4As^+ interact strongly with the isopropyl group. The driving force for this interaction can be clearly attributed to the hydrophobic effect. However, there are significant differences between g(r) obtained for each ion (compare Figures 4.6 (a) and 4.6 (b)). The first peak for the anion is more pronounced than the peak for the cation: the relative height is higher for the anion

and it is broader for the cation, indicating that the anion-isopropyl interaction is stronger than the cation-isopropyl interaction. Interestingly, there is a clear secondary peak for the anion which is barely visible for the cation. This can be interpreted with the help of the snapshots shown in Figures 4.6 (c) and 4.6 (d). As seen in Figure 4.6 (d), the cation tends to be adsorbed at the surface of the side chains of the PNIPAM aggregate, at distances around 5.16 Å–5.65 Å of the different $–CH_3$ groups of the isopropyl moieties, giving rise to a peak in g(r) in Figure 4.6 (b). In contrast, the anion tends to be engulfed by the PNIPAM chains, in contact with backbone methylene $–CH_2–$ groups (at distances about 5.71 Å–5.87 Å in Figure 4.6 (c)) and $–CH_3$ groups of the lateral chains of PNIPAM. In this internal location, the anion cannot be in contact with both $–CH_3$ groups of a given isopropyl moiety, being only in contact with the $–CH_3$ group nearest to the backbone $–CH_2–$ group. The direct contact with one of the $–CH_3$ of the isopropyl moieties gives the first peak in Figure 4.6 (a). The second peak in Figure 4.6 (a), located at about 7.75 Å, is due to the other $–CH_3$ group of the same isopropyl moiety, which is not in direct contact with the anion.

As we said, the engulfment of the Ph_4B^- anion by PNIPAM chains allows significant interaction of the ion with the methylene $–CH_2–$ groups located in the chain backbone, as clearly seen in the g(r) shown in Figure 4.6 (a). A strong candidate for the driving force for this interaction is again the hydrophobic effect, which appears to be more important in the case of the Ph_4B^- anion than in the case of the Ph_4As^+ cation. Also, we note that in previous studies [25, 26] no interaction was found between the backbone of single PNIPAM chains and inorganic anions such as I^- and Br^-.

In Figure 4.6 (d) we also see that the Ph_4As^+ cation interacts with the oxygen atoms of the amide groups (cation hydrogen–PNIPAM oxygen distance 2.75 Å). The g(r) function between hydrogen atoms of Ph_4As^+ and amide oxygen atoms (Figure 4.6 (b)) shows a clear peak corresponding to this ion–amide interaction. Previous works [26] show that the interaction of inorganic cations with PNIPAM amide groups is significant for small cations (such as Li^+) but it is weak for the largest cations (Cs^+) and it is also weak for hydrated divalent cations (Mg^{2+}, Ca^{2+}). We see here that the interaction is also present for this big hydrophobic cation. Therefore, the PNIPAM amide–cation interaction is not simply determined by the size of the cation. The important factor is the ability to make bonds with oxygen atoms, which can be done either by a small cation (Li^+) with a large surface charge density or by a big molecular ion such as Ph_4As^+ which has many small hydrogen atoms able to interact with an interfacial oxygen atom. Therefore, our results in Figure 4.6 show that, although the hydrophobic effect plays a fundamental role in the interaction of both Ph_4B^- and Ph_4As^+ with PNIPAM, the structural details of the cation–PNIPAM or anion–PNIPAM interactions are different. The Ph_4As^+ cation interacts with isopropyl and amide groups located in the side chains of PNIPAM and adsorbs onto the surface of the PNIPAM nanoparticle.

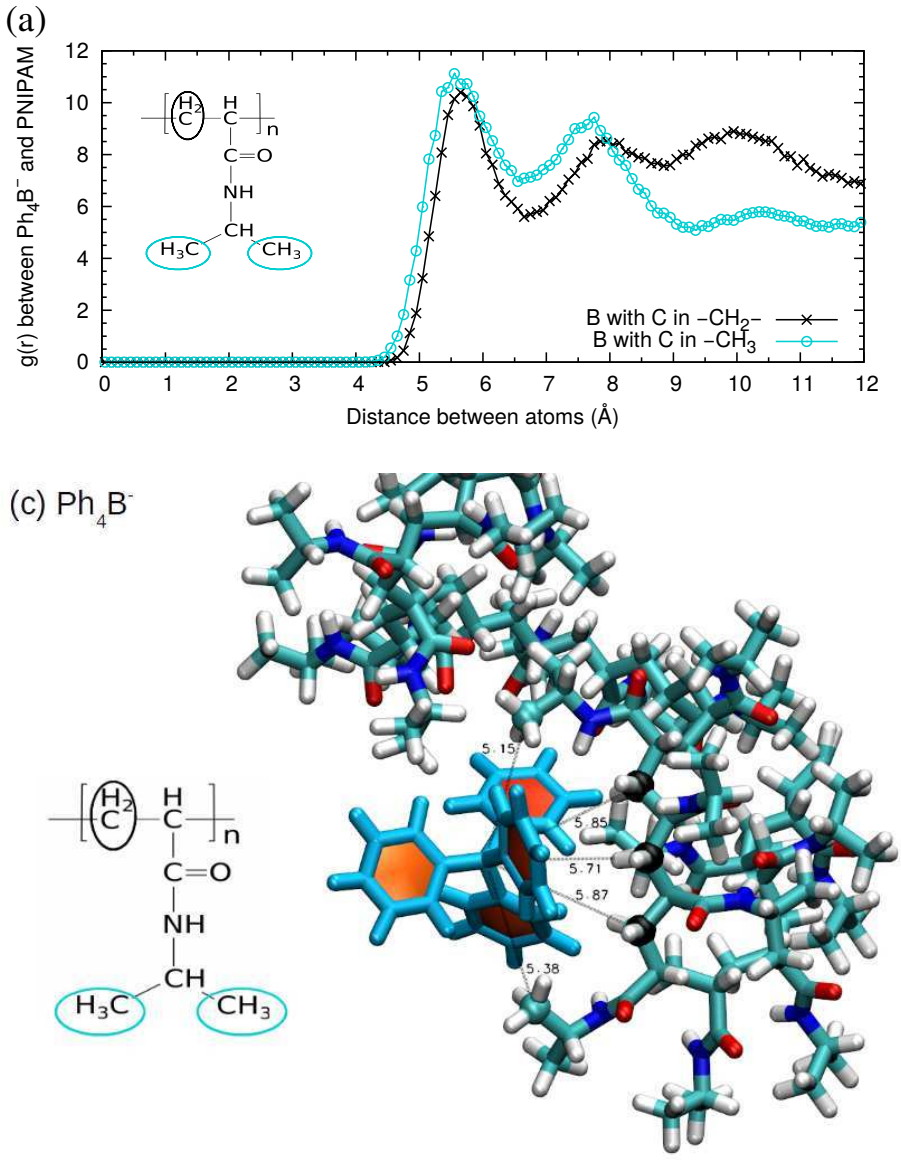

Figure 4.6: Simulation results for the adsorption of ions on PNIPAM: atomic radial distribution functions g(r) and simulation snapshots indicating typical ion–PNIPAM distances contributing to the peaks of the g(r) functions. In all panels, the structure of the PNIPAM monomer is shown with an indication of the chemical groups involved in the interaction. (a) g(r) between the central B atom in Ph_4B^- and carbon atoms in $–CH_2–$ and $–CH_3$ groups of PNIPAM. (b) g(r) between the central As atom in Ph_4As^+ and carbon atoms in $–CH_3$ groups of PNIPAM and $\longrightarrow$

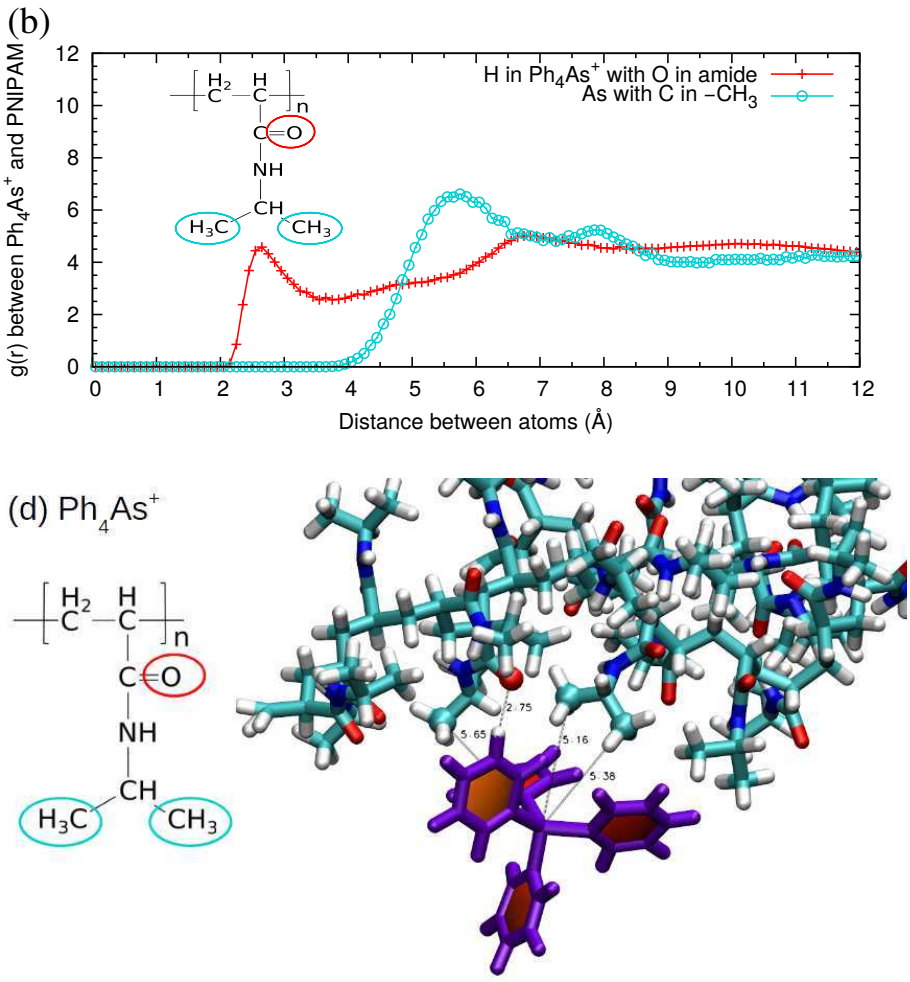

between hydrogen atoms in Ph_4As^+ and oxygen atoms in amide groups in PNIPAM. (c) Snapshot of a simulation of PNIPAM with Ph_4B^- and (d) snapshot of a simulation of PNIPAM with Ph_4As^+. All atoms are shown as bond representations and water molecules are not shown for clarity. Ph_4B^- is shown in blue, Ph_4As^+ in purple and atoms in PNIPAM are colored using standard colors (red=O, blue=N, white=H, cyan=C) except C atoms in $–CH_2–$ groups interacting with ions, which are shown in black.

In contrast, the Ph_4B^- anion is able not only to adsorb onto the surface of the PNIPAM nanoparticle but it is also able to penetrate inside the PNIPAM nanoparticle.

We have also evaluated the strength of the interaction between PNIPAM chains and the Ph_4As^+ and Ph_4B^- ions using the MD-ABF simulations described in the Methods section 3.2.2 (simulations S5 and S6 in Table 4.1). The results are shown in Figure 4.7. In the case of Ph_4B^- anion, the attractive interaction extends over a distance of about 1 nm and the minimum of the free energy shows the impressive value of –37.7 kcal/mol (expressed in units of thermal energy, this is –63.6 k_BT). In the case of the Ph_4As^+ cation, the attractive interaction has a range of about 0.5 nm and the adsorption free energy is estimated to be –8.5 kcal/mol (–14.3 k_BT). The first important conclusion from these results is that the difference in the free energy of adsorption between the cation and the anion is very large, being the adsorption of Ph_4B^- more favorable than that of Ph_4As^+ by about 29 kcal/mol (i.e. by about 49 k_BT). Interestingly, simulation results for the free energy of transfer of these ions from water to organic solvents [29] predict that transfer of Ph_4B^- is more favorable than transfer of Ph_4As^+ by a similar amount (between 24–40 kcal/mol depending on the models employed in the calculations). It is also interesting to note that in previous works it was observed that the energy of adsorption of Ph_4B^- onto cationic hydrophobic latex colloids was estimated to be larger than that for the case of Ph_4As^+ onto similar anionic latex colloids. The difference in free energy in that case was smaller [10, 17], between 2–3 k_BT. We believe that the fact that the PNIPAM system is a soft, self-assembled particle plays a decisive role. In this case, the water surrounding the hydrophobic ions can be more efficiently removed and replaced by chemical groups of the polymer than in the case of adsorption onto a solid non deformable surface, in which at least two of the phenyl rings are completely immersed in water. Simulations performed in the case of a hydrophobic solid surface (Chapter 9), show that adsorption of Ph_4B^- is preferred over adsorption of Ph_4As^+ by about 2.5 k_BT. It is also remarkable that the interaction free energies obtained for the interaction of Ph_4B^- and Ph_4As^+ are much larger than the typical interaction energies of ions with interfaces. In the case of monovalent ions typical adsorption free energies [4] are of the order of a few k_BT and in the case divalent and trivalent ions with strongly charged interfaces (such as ionic lipid layers or membranes) we typically found [30, 31] values of the order of 8–10 k_BT. The strong interaction between Ph_4B^- and Ph_4As^+ with PNIPAM and the dramatic difference between both ions have substantial implications that can be experimentally observed, as will be explored in the next section.

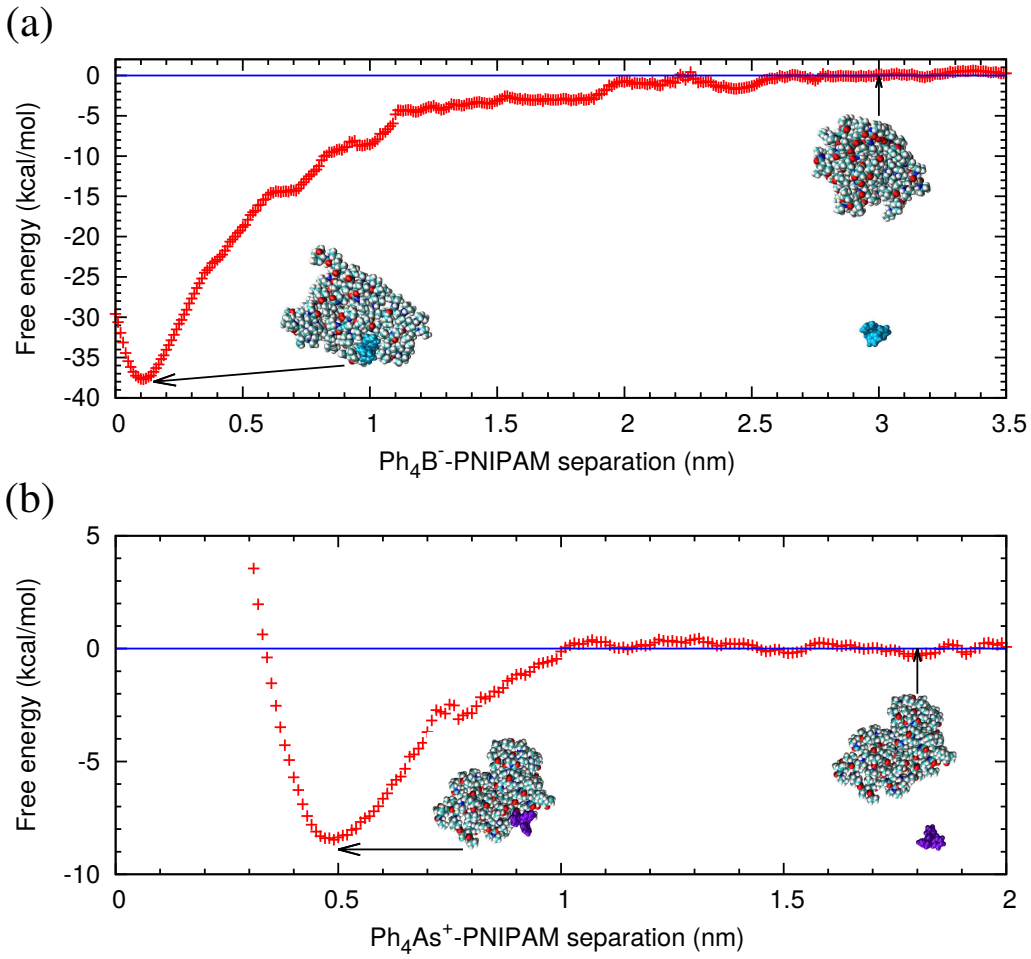

Figure 4.7: Free energy (potential of mean force) corresponding to the interaction of (a) Ph_4B^- and (b) Ph_4As^+ with PNIPAM computed from ABF simulations S5 and S6 in Table 4.1.

4.3 Experimental results

4.3.1 Characterization for PNIPAM microgels

Cationic and anionic PNIPAM microgels were produced as described in the Methods section 2.2. Once the microgels were purified, their main physicochemical properties were analyzed. First, the samples were studied by TEM to verify the monodispersity and sphericity of the particles (results shown in Figure 2.1).Then the microgels were characterized in solution by DLS. The temperature dependence of the diameter and the electrophoretic mobility of the particles at pH 4 are shown in Figure 4.8. The diameters of both microgels progressively diminish around the volume phase transition temperature (T_{VPT}) when they transit from swollen to collapsed states. In contrast, electrophoretic mobility values, μ_e, are very low when the particles are in the swollen state, due to high frictional forces [32], and progressively increase as the temperature surpasses the T_{VPT}. In addition, as the microgel shrinks its surface charge density increases, and this is reflected in higher mobility values.

The negative sign in μ_e confirms the nature of the anionic microgel (Figure 4.8 (a)) while the μ_e positive values confirm the nature of the cationic one (Figure 4.8 (b)). Table 4.3 shows the main data extracted from these figures. Anionic particles were bigger than the cationic ones. This can be justified by the presence of the charged AEMH co-monomer, besides the initiator, in the positive particles. During the polymerization reaction the presence of AEMH enhances the charge of the forming particles and for this reason the final particle size needed to stabilize the colloid is reduced. The low polydispersity index (PDI) obtained reflects a high monodispersity of both samples. The particle swelling ratios (S_w) were calculated from hydrodynamic volumes at 25ºC and 51ºC. Cationic particles showed a higher capacity of swelling than the anionic although the differences were not very significant. Table 4.3 also shows the transition temperature of the microgels obtained from the diameters (T_{VPT}) and the electrophoretic mobility (T_{ET}) calculated from the maximum of dD_h/dT and $d\mu_e/dT$ as a function of T, using a sigmoidal fit. The T_{VPT} differences between both microgels can be explained taking into account that the cationic microgel incorporates the more hydrophilic co-monomer AEMH. As a consequence the temperature to transit from the swollen state to the collapsed one increases. In contrast, the anionic microgel with NIPAM as unique monomer shows a lower T_{VPT} which is similar to that of PNIPAM chains [19].

4.3.2 Interaction of big hydrophobic ions with PNIPAM microgels: Electrophoresis

The next set of experiments was aimed to analyse the role of the different salts on the electrophoretic mobility of the microgels. These results will allow us to com-

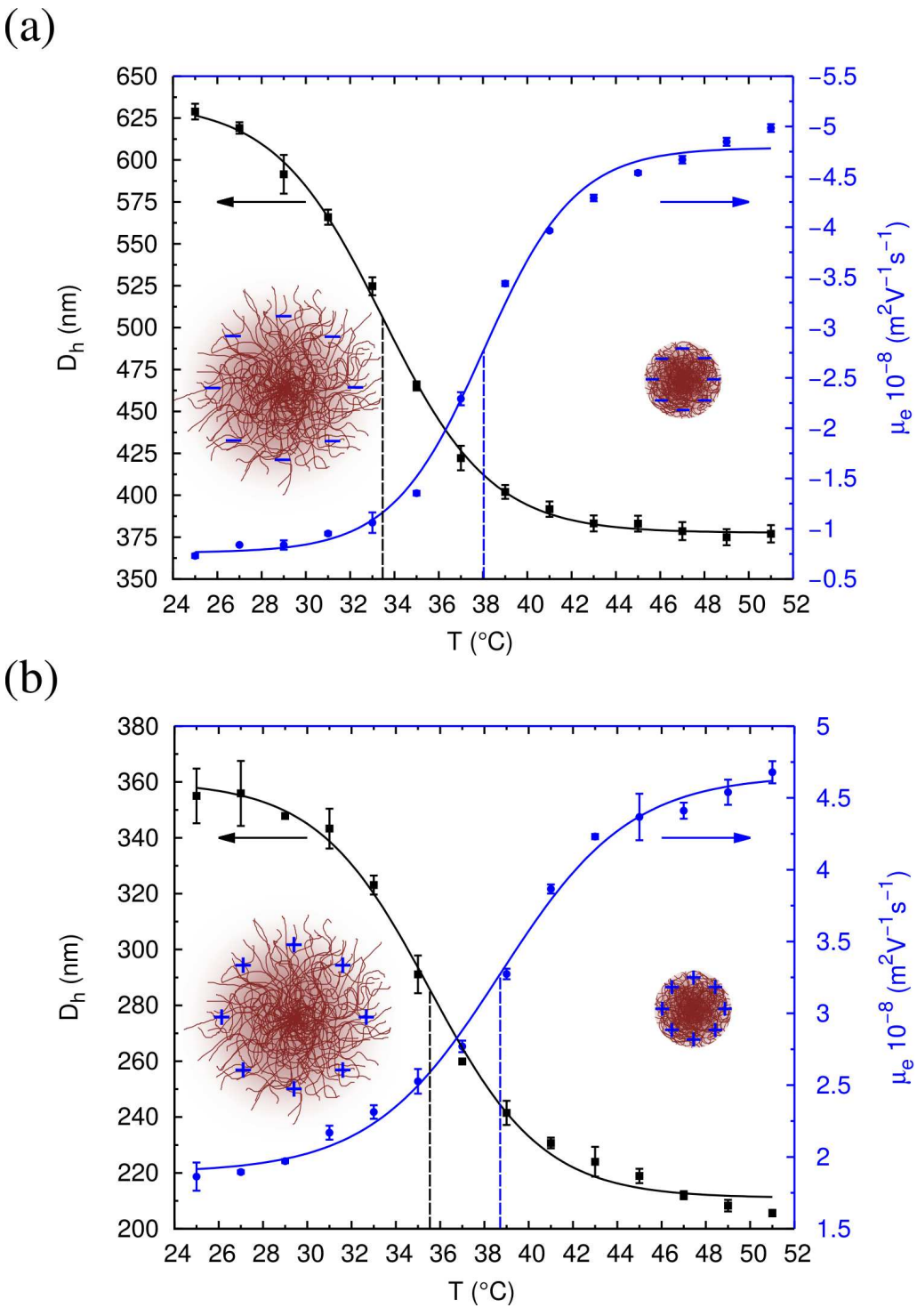

Figure 4.8: Hydrodynamic diameter (■) and electrophoretic mobility (μ_e) (●) of the (a) anionic and (b) cationic PNIPAM microgels as a function of temperature at pH 4.

	D_h (25ºC) (nm)	D_h (51ºC) (nm)	PDI (51ºC)	S_w	T_{VPT} (ºC)	T_{ET} (ºC)
Cationic	355 ± 10	206 ± 1	0.07 ± 0.01	5.1 ± 0.4	35.5 ± 0.2	38.7 ± 0.3
Anionic	629 ± 5	377 ± 5	0.06 ± 0.07	4.6 ± 0.2	33.5 ± 0.1	38.1 ± 0.2

Table 4.3: Microgel characterization, hydrodynamic diameters (D_h) at 25ºC and 51ºC, polydispersity index (PDI), swelling ratios (S_w), volume phase transition temperature (T_{VPT}) and electrokinetic transition temperature (T_{ET}).

pare how the electric state of the PNIPAM interface is changed depending on the nature of the ions present in solution. We have studied the two hydrophobic monovalent ions considered in the theoretical section, $Ph_4B^-(Na^+)$ and $Ph_4As^+(Cl^-)$ (see Figure 4.1). In addition, NaCl was used as reference salt, since according to our calculations previously described; we do not expect a significant interaction between NaCl ions and PNIPAM. The differences in the electrophoretic mobility observed in presence of the different salts can be ascribed to the hydrophobic ions. All the experiments were performed in unbuffered pH 4 solutions. The results are presented in Figure 4.9.

For the case of the anionic microgel (Figure 4.9 (a)), Ph_4B^- anion acts as coion while Ph_4As^+ cation acts as counterion. The ion specific influence of these two ions in comparison with NaCl becomes evident when we compare the electrophoretic mobility curves. These results reveal the accumulation of both ions at the PNIPAM–water interface, in agreement with the results of MD simulations for the uncharged PNIPAM chains. For the Ph_4B^- anion acting as coion, this accumulation is reflected in a substantial increase of the electrophoretic mobility in relation to NaCl at 1 mM, which is more evident as the microgel collapses and the surface becomes more hydrophobic. Note that the Ph_4B^- anion is electrostatically repelled from the anionic particle surface, but according to the calculations shown from results in Figure 4.7 (a), the free energy of interaction with PNIPAM is so strong ($\sim$–64 k_BT) that we expect a strong accumulation of Ph_4B^- onto the microgel even as a coion at very low concentrations (1 mM). For the Ph_4As^+ cation, acting as counterion, the electrophoretic mobility almost vanishes at 1 mM of Ph_4As^+, and mobility inversion is readily observed when the concentration of cation is 10 mM. This mobility inversion is due to a charge reversal in the system: the Ph_4As^+ is being accumulated on the anionic microgel and the positive charge due to the adsorbed cation surpasses the anionic charge of the microgel; once again, this accumulation is more evident when the PNIPAM interface becomes more hydrophobic (i.e. at higher T).

Figure 4.9 (b) shows the results for the cationic microgel. In this case, Ph_4B^- anion acts as counterion while Ph_4As^+ cation acts as coion. The most striking result is the important inversion of the electrophoretic mobility observed with the

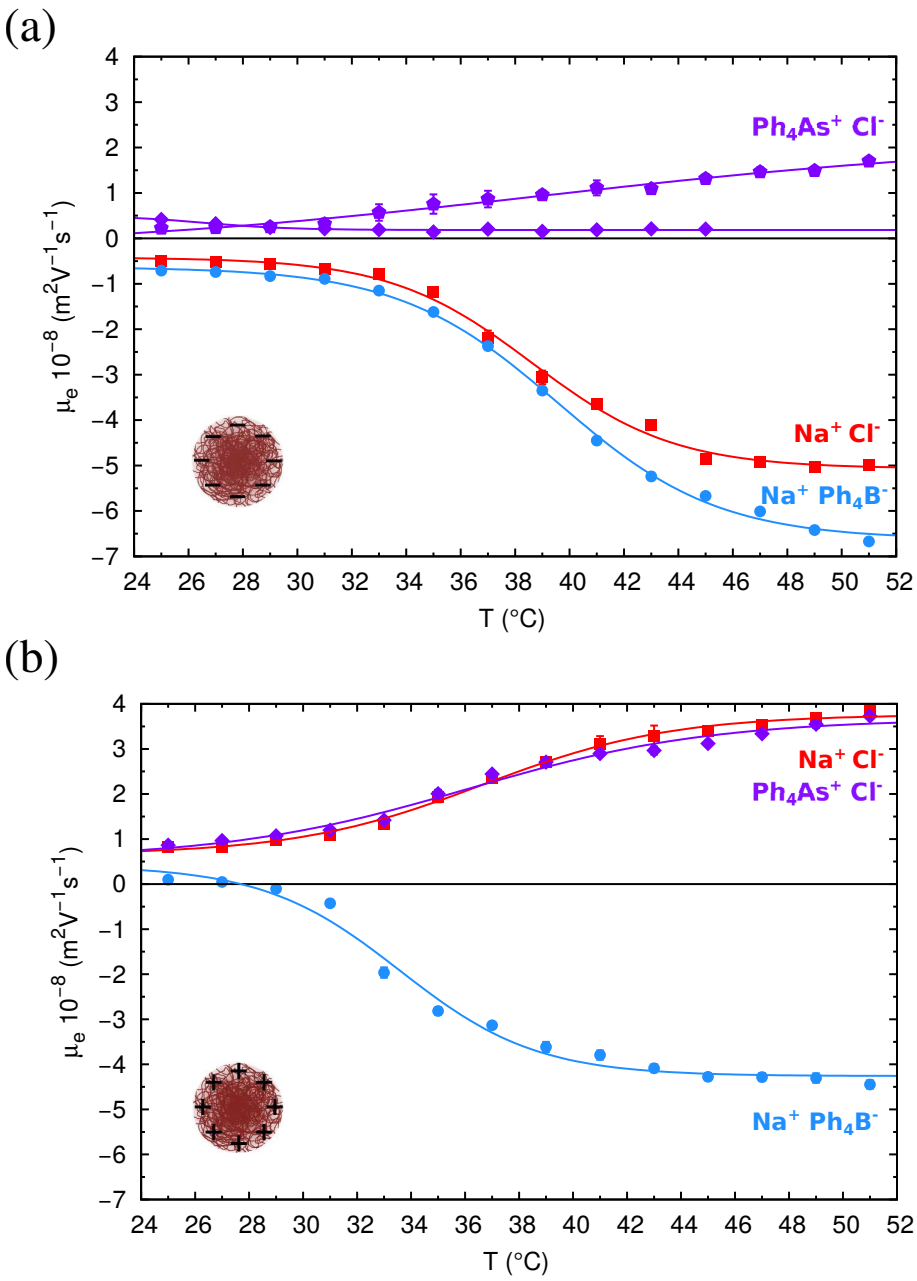

Figure 4.9: Electrophoretic mobility (μ_e) of the (a) anionic and (b) cationic PNIPAM microgels as a function of temperature in the presence of different salts and concentrations. (■) NaCl 1 mM; (●) $NaPh_4B$ 1 mM; (◆) Ph_4AsCl 1 mM; and (⬟) Ph_4AsCl 10 mM.

Ph_4B^- at concentrations as low as 1 mM. The negative electrokinetic charge in presence of Ph_4B^- increases as the microgel collapse and it is even higher than the positive charge reached with the NaCl at 1 mM, (see Figure 4.9 (b)). Hence, the charge reversal of the cationic PNIPAM is higher than 100%, which is an impressive figure. These results demonstrate an extremely large adsorption of Ph_4B^- onto hydrophobic PNIPAM particles in the collapsed state, in agreement with the strong adsorption of Ph_4B^- predicted in the previous calculations (Figure 4.7 (a)). Figure 4.9 (b) also shows the effect of Ph_4As^+ on the electrophoretic mobility of cationic microgels. In this case, the Ph_4As^+ acts as coion, and it is electrostatically repelled form the particle surface. However, according to previous calculations (Figure 4.7 (b)), the free energy of interaction with PNIPAM ($\sim$–14 k_BT) is strong enough to overcome electrostatic repulsion and we expect an important accumulation of Ph_4As^+ onto the microgel. This predicted adsorption of Ph_4As^+ onto the cationic microgel is not reflected in the electrophoretic mobility reported in Figure 4.9 (b). There is almost no difference between the electrophoretic mobility in presence of $Ph_4As^+Cl^-$ or NaCl. As a plausible explanation we propose that the sum of the surface charge resulting from the accumulation of Ph_4As^+ and the cationic charge of the microgel is large enough to induce substantial condensation of the Cl^- counterions. This hypothesis is supported by AFM measurements reported in the next subsection.

As a summary of this subsection, the results shown in Figure 4.9 (a) and 4.9 (b) demonstrate that both hydrophobic ions (Ph_4B^- and Ph_4As^+) acting as counterions produce a large charge inversion in the microgels. This inversion is much more notable when the anion is acting as counterion. This stronger accumulation is reflected in higher electrophoretic mobility and lower concentration values at which the reversed charge is observed with Ph_4B^-. Therefore, we have provided a clear experimental demonstration that the two ions Ph_4B^- and Ph_4As^+ (which have the same size, shape and valence) have different interactions with an interface, being the anion the most active species, as predicted by our theoretical calculations (Figure 4.6).

4.3.3 Interaction of big hydrophobic ions with PNIPAM microgels: AFM

The behavior of the adsorbed microgels was studied by tapping mode AFM using the procedure described in Methods section 2.7.1. AFM micrographs were taken at several temperatures above and below the T_{VPT} of the microgels to analyze the effects produced by the accumulation of the hydrophobic ions on PNIPAM microgel particles. In order to simplify the discussion of the results only micrographs and height profiles for two temperatures, one above and one below the T_{VPT}, will be shown here.

Figure 4.10 shows the results obtained for the cationic and anionic microgels

in presence of 1 mM of NaCl and with no added salt, respectively. For both microgels, it can be observed that when the particles are in the collapsed state they behave as hard particles; the individual particles can be clearly distinguished, as the edges of the particles are well defined. In contrast, in the swollen state the particles are softer; as the AFM tip can penetrate them easily more blurred images are obtained, even though large tapping amplitudes were chosen in order to minimize the tip-substrate interaction. These differences can also be observed in the height profiles. At temperature above the T_{VPT} the individuality of the particles are reflected by well-defined, narrow peaks, while in the swollen state these peaks are wider, shorter and can even disappear reflecting the softer structure of the particles.

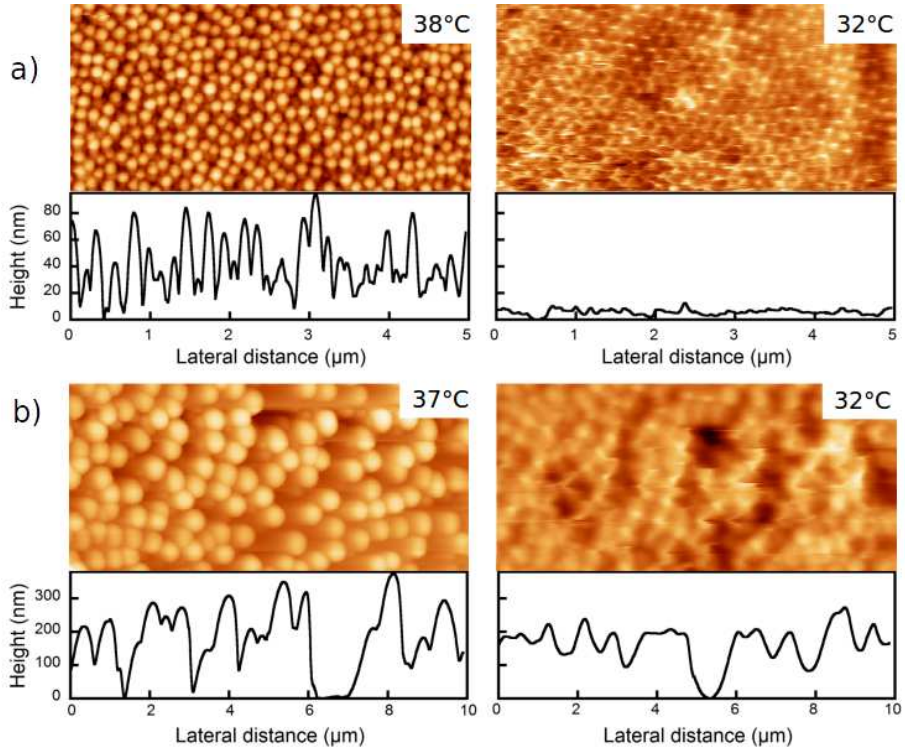

Figure 4.10: Height tapping mode AFM micrographs of the adsorbed PNIPAM microgels at two temperatures above and below T_{VPT}: (a) cationic microgel; 1 mM of NaCl; and (b) anionic microgel at pH 4. A typical height profile for each sample is presented. The size of the images corresponds to the values shown in the horizontal axis.

Figure 4.11 shows the results obtained for the cationic microgel in presence of the two hydrophobic ions. As mentioned in Methods section 2.7.1, the PNIPAM particles were adsorbed on the mica surface from a solution of pH 4 before

injection of the salts. In Figure 4.11 (a) the micrographs obtained in presence of the anion Ph_4B^- at 1 mM are presented. Electrophoretic mobility measurements showed an important charge inversion when Ph_4B^- acts as counterion at this concentration. The ionic adsorption is also reflected in the AFM results. As the effective charge of the PNIPAM particles becomes negative they are not further attracted to the negatively charged mica surface. Therefore, as the tip scanned the surface, the particles were dragged along. The effect is more dramatic at low temperatures, when the pre-adsorbed hydrophilic particles are essentially removed from the surface by the rastering AFM tip. Figure 4.11 (b) shows the results for the Ph_4As^+ cation at 1 mM. In this case, because the cation is acting as coion, the accumulation on the surface of the PNIPAM increases the positive particle charge. Thus, the electrostatic interaction with the negatively charged mica is enhanced and the particles stay well fixed.

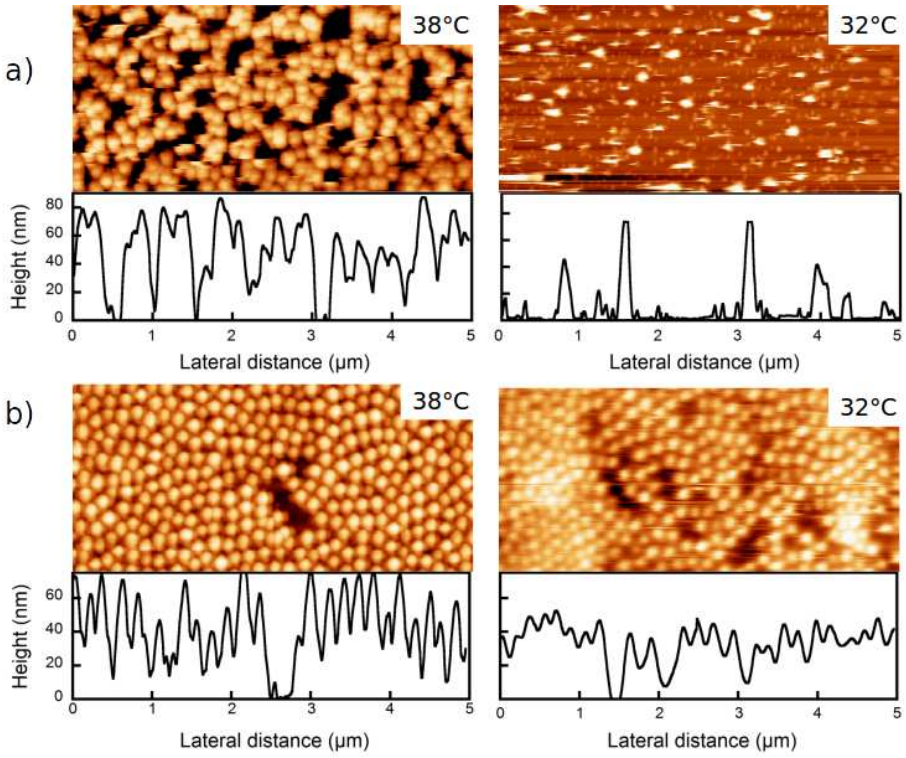

Figure 4.11: Height tapping mode AFM micrographs of the adsorbed cationic microgel at 1 mM of the (a) Ph_4B^- anion and (b) Ph_4As^+ cation at two temperatures. A typical height profile for each sample is presented. The size of the images is shown in the horizontal axis of the profiles. The images at high temperature were taken few minutes after salt injection.

This is clearly reflected in the AFM images, which demonstrate the strong ac-

cumulation of this cation even acting as coion. From these data, our previous hypothesis to explain why we observed almost no differences on μ_e between this salt and NaCl appears more plausible (Figure 4.9 (b)). In order to further verify this accumulation we performed another experiment, by replacing the Ph_4B^- anion by the Ph_4As^+ cation both at 1 mM, as shown in Figure 4.12. First, we scanned the surface in presence of the Ph_4B^- anion at 1 mM at different temperatures. We observed that many particles detached from the surface or formed aggregates (Figure 4.12 (a), (b)). Then, we washed the surface with pH 4 solution and after that we injected the Ph_4As^+ cation at 1 mM and 38ºC. As a result, the remained particles adhered again to the mica surface (Figure 4.12 (c); the images were taken in different areas of the sample).

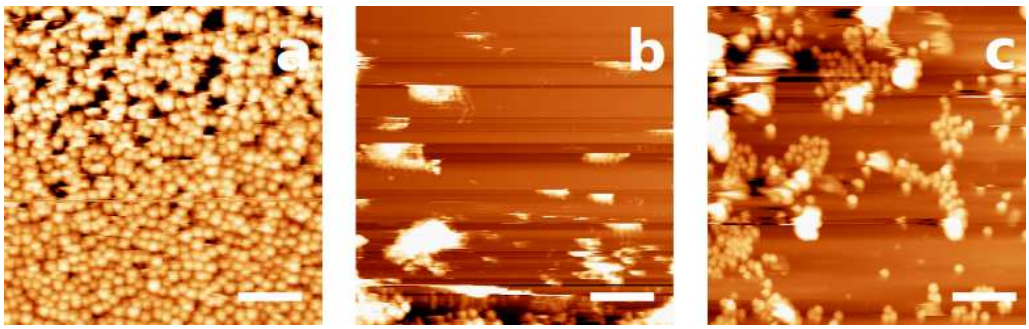

Figure 4.12: 5 μm $\times$ 5 μm height tapping mode AFM micrographs of the adsorbed cationic microgel. (a) Scan right after injection of Ph_4B^- at 1 mM; a different ordering of the particles can be observed between the beginning (lower section) and the end (upper section) of the image; (b) image measured 4 hours after injection of Ph_4B^-; and (c) height image measured 1 hour after injection of Ph_4As^+ at 1 mM. The scale bars correspond to 1 μm.

These results clearly evidence the accumulation of these two hydrophobic ions acting as counter or coions. The experiments with the anionic microgel confirm these conclusions. Figure 4.13 (a) shows the results in presence of Ph_4B^- anion at 1 mM. For this case, μ_e values showed an increase in the surface charge of the microgel due to the accumulation of Ph_4B^- acting as coion. AFM images show that even at 32ºC particles are better attached to the surface than those corresponding at pH 4 (Figure 4.10 (b)); the microgel particles appear better defined in presence of Ph_4B^-.

In contrast, for the Ph_4As^+ cation at 1 mM, Figure 4.13 (b), AFM images show scanning-induced detachment of the particles at 32ºC: only a section of some particles appear in the image. These results corroborate the charge inversion observed by μ_e with this cation acting as counterion. In addition, if we compare the images of Figure 4.11 (a) and 4.13 (b), we can see that the detachment and the aggregation of the particles is higher when Ph_4B^- is acting as counterion than when

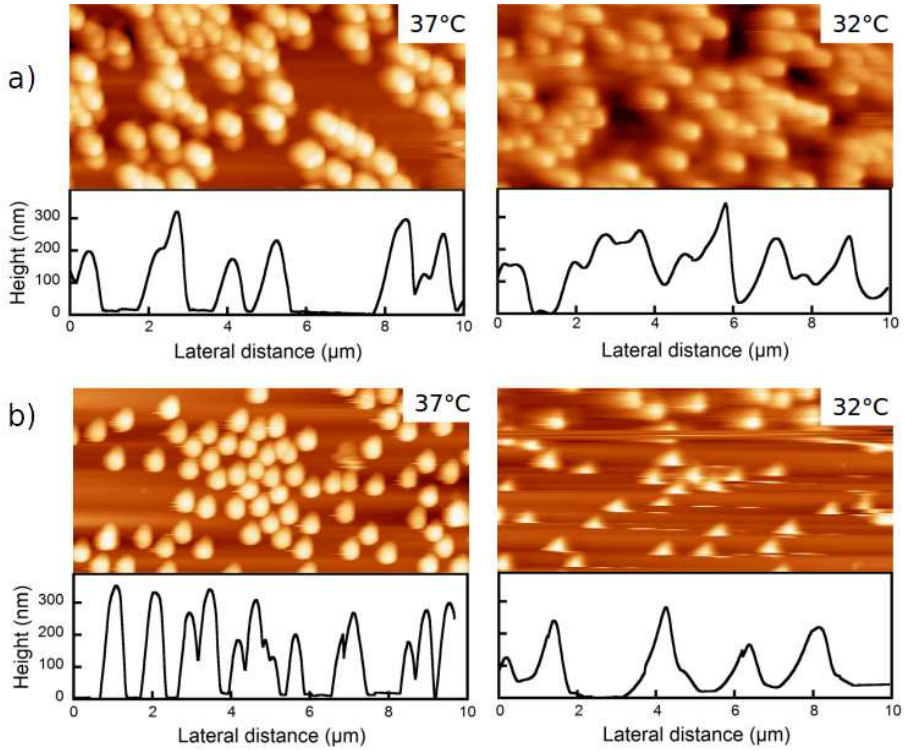

Figure 4.13: Height tapping mode AFM micrographs of the adsorbed anionic microgel at 1 mM of (a) Ph_4B^- anion and (b) Ph_4As^+ cation at two temperatures. A typical height profile for each sample is presented. The size of the images is shown in the horizontal axis of the profiles.

Ph_4As^+ plays that role. This is also in agreement with the μ_e results, where we observed that the charge inversion was higher when Ph_4B^- anion was acting as counterion. It is also consistent with the MD results (Figure 4.7) in which we found higher affinity of PNIPAM for Ph_4B^- than for Ph_4As^+. In the broader context of specific ionic effects, our results could also have important implications in understanding why cations and anions play a different role in Hofmeister effects.

4.4 Conclusions

In this chapter, we show evidence from MD simulations, electrokinetic measurements and AFM imaging demonstrating dramatic differences between the specific effects on a soft matter system (PNIPAM chains and microgels) of Ph_4B^- anion and the Ph_4As^+ cation. Both molecular ions are almost identical in all relevant ion properties (size, surface groups interacting with materials, polarizability...) differing only in their anionic or cationic character. However, the effects of Ph_4B^- on

neutral PNIPAM chains and in charged (cationic and anionic) PNIPAM microgels are always much stronger than the effects of Ph_4As^+.

The obvious question arising from these results is why apparently identical hydrophobic anions and cations have different interactions with soft interfaces in water. Correlation functions obtained from the MD simulations provide interesting clues. In previous works [11], it has been shown that in the case of identical anions and cations water molecules approach closer to anions due to the small size of the positively charged H atoms of water, leading to a higher disruption of water hydrogen bonding network by anions. The asymmetry in the anion-water hydrogen *versus* cation-water oxygen makes anions more hydrophobic than cations of equal size [8, 11, 12]. Here, we observe a similar effect in the interaction of Ph_4B^- and Ph_4As^+ with interfaces, in this case PNIPAM chains. Both ions interact with the hydrophobic side chain $–CH_3$ groups (belonging to the isopropyl group) but according to the radial correlation functions obtained in our simulations (Figure 4.6) the Ph_4B^- anions are closer and interact more strongly than Ph_4As^+. Another difference observed in our simulations (Figure 4.6) is that Ph_4As^+ weakly interacts with amide groups in the side chains, whereas Ph_4B^- has a substantial interaction with $–CH_2–$ groups present in the polymer chain backbone. All these evidences provided here strongly supports the view that even for big ions solvation of anions is essentially different than the solvation of cations and, more importantly, the affinity of anions and cations for interfaces is intrinsically different.

References

[1] Kunz, W., *Specific Ion Effects*; World Scientific Publishing Company: 2010.

[2] Kunz, W. Specific ion effects in colloidal and biological systems. *Curr. Opin. Colloid Interface Sci.* **2010**, *15*, 34–39.

[3] Lyklema, J., *Fundamentals of Interface and Colloid Science*; Fundamentals of Interface and Colloid Science; Academic Press: 1991.

[4] Lyklema, J. Lyotropic sequences in colloid stability revisited. *Adv. Colloid Interface Sci.* **2003**, *100*, 1–12.

[5] Lyklema, J. Simple Hofmeister series. *Chem. Phys. Lett.* **2009**, *467*, 217–222.

[6] Tobias, D. J.; Stern, A. C.; Baer, M. D.; Levin, Y.; Mundy, C. J. Simulation and theory of ions at atmospherically relevant aqueous liquid-air interfaces. *Annu. Rev. Phys. Chem.* **2013**, *64*, 339–359.

[7] Marcus, Y. Effect of ions on the structure of water: structure making and breaking. *Chem. Rev.* **2009**, *109*, 1346–1370.

[8] Morita, T.; Westh, P.; Nishikawa, K.; Koga, Y. How Much Weaker Are the Effects of Cations than Those of Anions? The Effects of K^+ and Cs^+ on the Molecular Organization of Liquid H_2O. *J. Phys. Chem. B* **2014**, *118*, 8744–8749.

[9] López-León, T.; Santander-Ortega, M. J.; Ortega-Vinuesa, J. L.; Bastos-González, D. Hofmeister effects in colloidal systems: influence of the surface nature. *J. Phys. Chem. C* **2008**, *112*, 16060–16069.

[10] Calero, C.; Faraudo, J.; Bastos-González, D. Interaction of monovalent ions with hydrophobic and hydrophilic colloids: Charge inversion and ionic specificity. *J. Am. Chem. Soc.* **2011**, *133*, 15025–15035.

[11] Yang, L.; Fan, Y.; Gao, Y. Q. Differences of cations and anions: Their hydration, surface adsorption, and impact on water dynamics. *J. Phys. Chem. B* **2011**, *115*, 12456–12465.

[12] Zangi, R. Can salting-in/salting-out ions be classified as chaotropes/kosmotropes? *J. Phys. Chem. B* **2009**, *114*, 643–650.

[13] Scheu, R.; Rankin, B. M.; Chen, Y.; Jena, K. C.; Ben-Amotz, D.; Roke, S. Charge asymmetry at aqueous hydrophobic interfaces and hydration shells. *Angew. Chem.* **2014**, *126*, 9714–9717.

[14] Marcus, Y. Gibbs energies of transfer of anions from water to mixed aqueous organic solvents. *Chem. Rev.* **2007**, *107*, 3880–3897.

[15] Kim, J. Preferential solvation of single ions. A critical study of the Ph4AsPh4B assumption for single ion thermodynamics in amphiprotic and dipolar-aprotic solvents. *J. Phys. Chem.* **1978**, *82*, 191–199.

[16] Leontidis, E.; Christoforou, M.; Georgiou, C.; Delclos, T. The ion–lipid battle for hydration water and interfacial sites at soft-matter interfaces. *Curr. Opin. Colloid Interface Sci.* **2014**, *19*, 2–8.

[17] Martín-Molina, A.; Calero, C.; Faraudo, J.; Quesada-Pérez, M.; Travesset, A.; Hidalgo-Álvarez, R. The hydrophobic effect as a driving force for charge inversion in colloids. *Soft Matter* **2009**, *5*, 1350–1353.

[18] Siretanu, I.; Chapel, J.-P.; Bastos-González, D.; Drummond, C. Ions-Induced Nanostructuration: Effect of Specific Ionic Adsorption on Hydrophobic Polymer Surfaces. *J. Phys. Chem. B* **2013**, *117*, 6814–6822.

[19] Schild, H. G. Poly (N-isopropylacrylamide): experiment, theory and application. *Prog. Polym. Sci.* **1992**, *17*, 163–249.

[20] López-León, T.; Elaïssari, A.; Ortega-Vinuesa, J. L.; Bastos-González, D. Hofmeister effects on poly (NIPAM) microgel particles: macroscopic evidence of ion adsorption and changes in water structure. *ChemPhysChem* **2007**, *8*, 148–156.

[21] López-León, T.; Ortega-Vinuesa, J. L.; Bastos-González, D.; Elaïssari, A. Thermally sensitive reversible microgels formed by poly (N-Isopropylacrylamide) charged chains: A Hofmeister effect study. *J. Colloid Interface Sci.* **2014**, *426*, 300–307.

[22] Hénin, J.; Fiorin, G.; Chipot, C.; Klein, M. L. Exploring multidimensional free energy landscapes using time-dependent biases on collective variables. *J. Chem. Theory Comput.* **2009**, *6*, 35–47.

[23] Humphrey, W.; Dalke, A.; Schulten, K. VMD: visual molecular dynamics. *J. Mol. Graphics* **1996**, *14*, 33–38.

[24] Alaghemandi, M.; Spohr, E. Molecular Dynamics Investigation of the Thermo-Responsive Polymer Poly (N-isopropylacrylamide). *Macromol. Theory Simul.* **2012**, *21*, 106–112.

[25] Du, H.; Wickramasinghe, R.; Qian, X. Effects of salt on the lower critical solution temperature of poly (N-isopropylacrylamide). *J. Phys. Chem. B* **2010**, *114*, 16594–16604.

[26] Du, H.; Wickramasinghe, S. R.; Qian, X. Specificity in cationic interaction with poly (N-isopropylacrylamide). *J. Phys. Chem. B* **2013**, *117*, 5090–5101.

[27] Deshmukh, S. A.; Sankaranarayanan, S. K.; Suthar, K.; Mancini, D. C. Role of solvation dynamics and local ordering of water in inducing conformational transitions in poly (N-isopropylacrylamide) oligomers through the LCST. *J. Phys. Chem. B* **2012**, *116*, 2651–2663.

[28] Deshmukh, S. A.; Kamath, G.; Suthar, K. J.; Mancini, D. C.; Sankaranarayanan, S. K. Non-equilibrium effects evidenced by vibrational spectra during the coil-to-globule transition in poly (N-isopropylacrylamide) subjected to an ultrafast heating–cooling cycle. *Soft matter* **2014**, *10*, 1462–1480.

[29] Schurhammer, R.; Wipff, G. Are the hydrophobic $AsPh_4^+$ and BPh_4^- ions equally solvated? A theoretical investigation in aqueous and nonaqueous solutions using different charge distributions. *J. Phys. Chem. A* **2000**, *104*, 11159–11168.

[30] Martín-Molina, A.; Rodríguez-Beas, C.; Faraudo, J. Charge reversal in anionic liposomes: experimental demonstration and molecular origin. *Phys. Rev. Lett.* **2010**, *104*, 168103.

[31] Martín-Molina, A.; Rodríguez-Beas, C.; Faraudo, J. Effect of calcium and magnesium on phosphatidylserine membranes: experiments and all-atomic simulations. *Biophys. J.* **2012**, *102*, 2095–2103.

[32] López-León, T.; Ortega-Vinuesa, J. L.; Bastos-González, D.; Elaïssari, A. Cationic and anionic poly (N-isopropylacrylamide) based submicron gel particles: Electrokinetic properties and colloidal stability. *J. Phys. Chem. B* **2006**, *110*, 4629–4636.

5 Effects of inorganic and organic ions on PNIPAM microgels: a QCM study

5.1 Background

Previous electrokinetic studies with PNIPAM and inorganic anions [1, 2] and those shown in the previous chapter with organic ions, together with the MD simulations, have demonstrated the key role that water solvation and hydrophobic effect play in the interaction of ions and interfaces. In order to complement these studies in ionic specific effects on the volume phase transitions, we have carried out QCM measurements. As described in the Materials and Methods part (section 2.8) QCM allows to determine the thickness and the viscoelastic properties of the films which we expect depend on the type of ions present in the medium. As far as we know, a work research with PNIPAM microgels and ionic specificity studied by QCM does not exist in the literature.

5.2 Results and discussion

5.2.1 Adsorption: cationic microgel

Cationic microgels were absorbed on SiO_2 coated quartz crystals at 40ºC. Electrostatic interaction between the negatively charged silica surfaces and the cationic spheres promotes microgel adsorption; the adsorbed amount was controlled by the concentration of microgel particles in solution. Typical QCM-D signals (frequency and dissipation shifts) measured during microgel adsorption are presented in Figure 5.1. For the results presented in this subsection, the zero of f and D was set at conditions of the bare crystal in water, at 40ºC (right before adsorption started).

As can be observed in Figure 5.1, a decrease in resonance frequency accompanied by the increase in D appears quickly after microgel injection. As described before (section 2.8 of Materials and Methods), the reduction in resonance frequency can be understood as a consequence of the increase of the effective mass

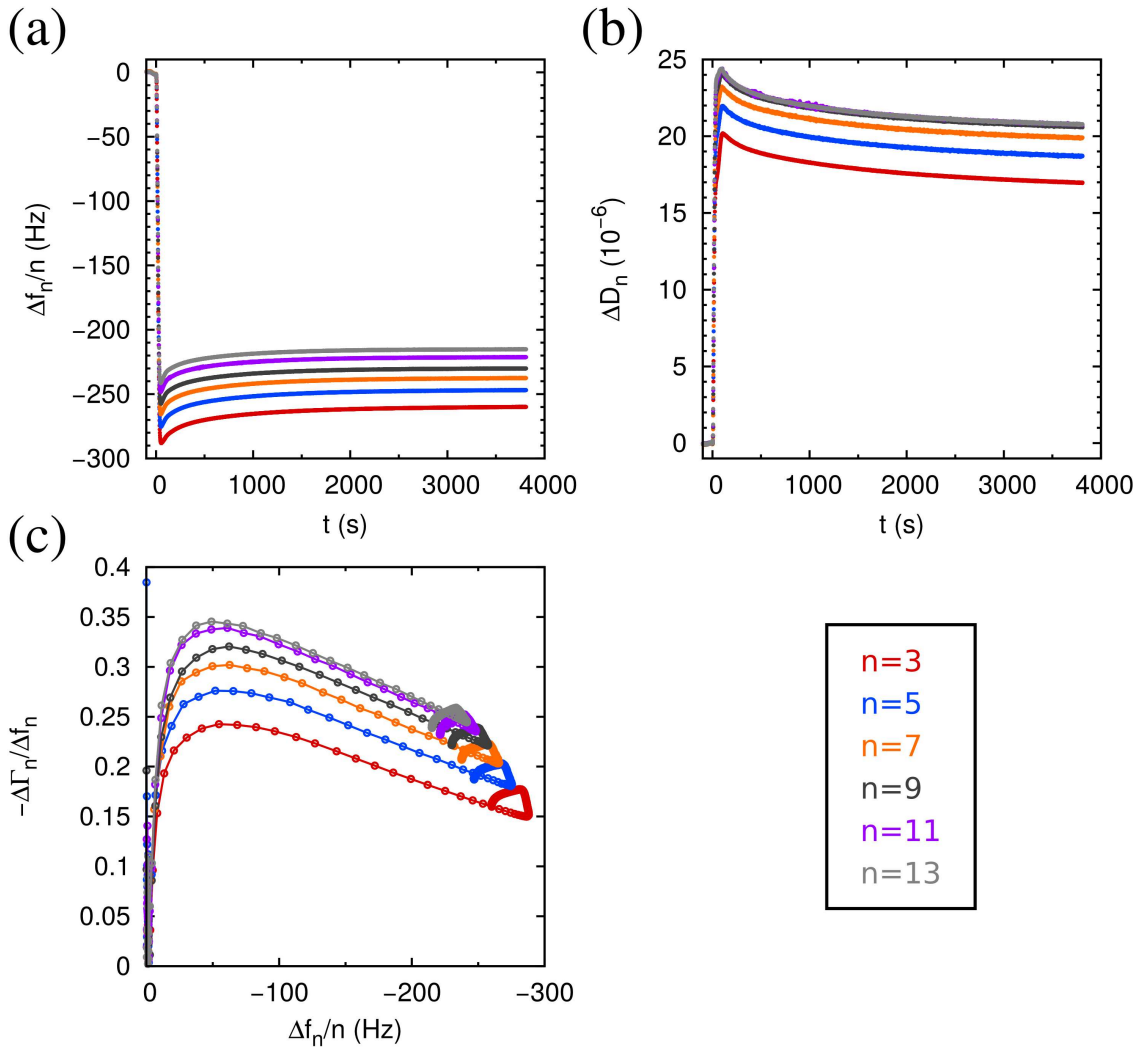

Figure 5.1: Cationic microgel adsorption. Temporal evolution of (a) Δf and (b) ΔD, and (c) $-\Delta\Gamma/\Delta f$ *vs.* Δf measured by QCM-D. The concentration of PNIPAM microgel was 0.14 g/l. $T = 40$ºC. Odd harmonics n=3–13 are shown.

of the quartz crystals, due to microgel adsorption. Similarly, the increase in dissipation indicates that the adsorbed layer is not rigidly attached to the crystal and that its viscoelastic properties need to be considered in the data analysis. However, marked maxima (minima) in the dissipation (resonance frequency) are observed about 45 seconds after microgel adsorption. This behavior is commonly associated to the rearrangement accompanied by thickness reduction of an adsorbed film (e.g. vesicles conversion in bilayer). We believe this scenario is unlikely in the present case, as the peaks are much less marked (and appear at longer times) at lower microgel concentration. In addition, no minima (maxima) in frequency (dissipation) were observed when the adsorption of the larger anionic microgel was investigated (see below 5.2.2).

It has been reported in previous publications that a plot of $-\Delta\Gamma/\Delta f$ *vs.* Δf often shows a linear behavior, which can be used to estimate the particle size by extrapolating the linear region of $\Delta\Gamma/\Delta f$ equal to zero (Tellechea *et al.* assumption [3]), even though no solid theoretical basis for this behavior has been described. In agreement with these reports, we observe a linear response for a limited range of adsorption time, as can be observed in Figure 5.1 (c). If the extrapolation to zero of $\Delta\Gamma/\Delta f$ is attempted, a value of Δf coherent with the particle size measured by DLS can be estimated ($\sim$100–200 nm, Table 4.3) by using Sauerbrey equation, eq. 2.8. However, the temporal range of the linear response is quite limited: it is obviously lost after reaching the peaks in the measured signals. Moreover, no linear response is observed for lower microgel concentrations, or larger particle size (see Figure 5.2 and 5.5).

Lower shifts in resonance frequency and dissipation were measured for lower concentration of microgels, as can be observed in Figure 5.2. In this case, the transient maxima in D are clearly observed; on the contrary, the peaks are less pronounced (or absent) in f. In addition, these peaks appear at longer times (2 minutes after injection) compared with the more concentrated case. In general, we observed a good correlation between the times of appearance of the peaks (and its size) measured QCM-D signals and the concentration of microgel: more marked peaks showing at shorter times were observed for larger microgel concentrations.

For the case of lower microgel concentration, the $-\Delta\Gamma/\Delta f$ *vs.* Δf representation did not show a linearly decreasing response; thus, the assumption of Tellechea and coworkers [3] outlined above is not fulfilled.

We have measured ex-situ AFM micrographs of the microgel coated QCM-D crystals, to explore the morphology of the adsorbed microgel layer. Some examples are shown in Figures 5.3 and 5.4. As can be observed in Figure 5.3, a fairly complete coverage of the quartz crystal seems to be obtained for high microgel concentrations (the image is obtained in dry conditions). Assuming that particle size measured by DLS is correct (Table 4.3), coverage of 50% can be estimated; close to random close packing. On the contrary, a less significant coverage is observed for lower microgel concentrations during adsorption (see Figure 5.4). In

this last case, coverage of about 10% can be estimated if the particle size measured by DLS is assumed. In addition, the particle distribution is not uniform: some aggregates in the surface can be observed. As discussed below, this tendency to aggregate may be related to the peaks observed in the QCM-D signals upon adsorption.

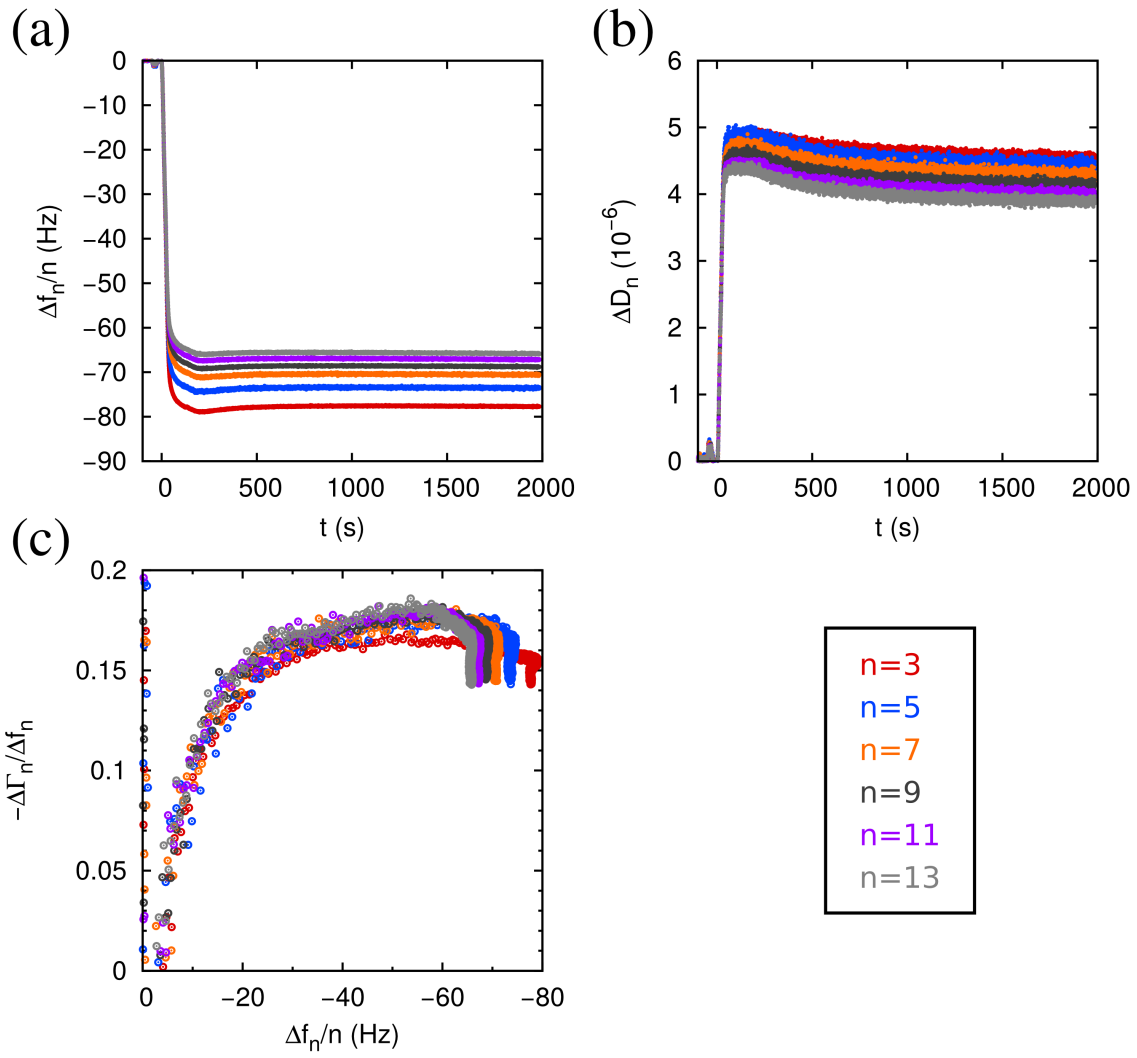

Figure 5.2: Cationic microgel adsorption. Temporal evolution of (a) Δf and (b) ΔD, and (c) $-\Delta\Gamma/\Delta f$ *vs.* Δf measured by QCM-D. The concentration of PNIPAM microgel was 0.014 g/l. $T = 40$ºC. Odd harmonics n=3–13 are shown.

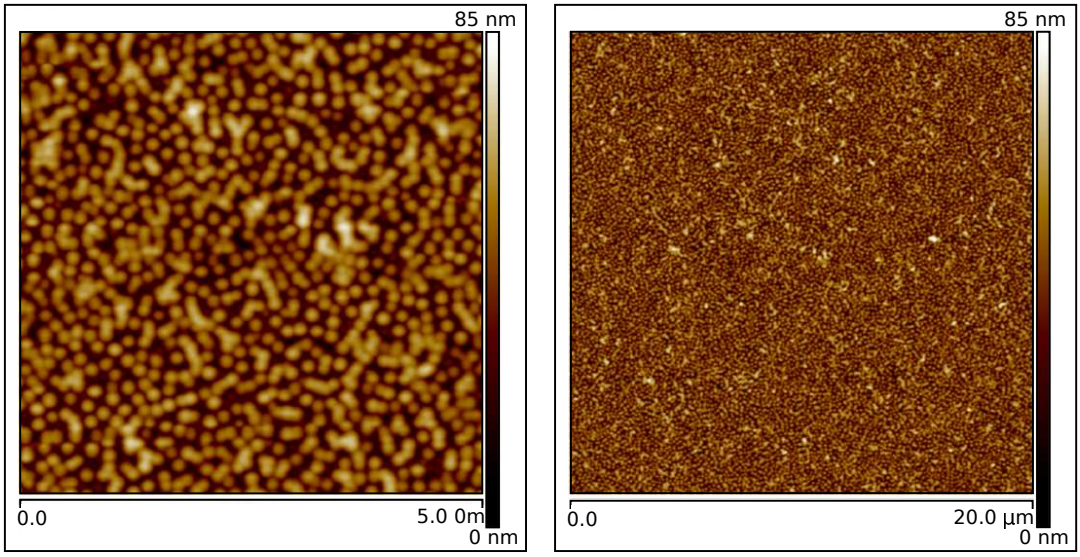

Figure 5.3: 5×5 (left) and 20×20 μm^2 (right) height AFM micrographs taken in tapping mode of a QCM-D crystal coated with cationic microgel after surface drying. The images correspond to the crystal used to obtain the results presented in Figure 5.1.

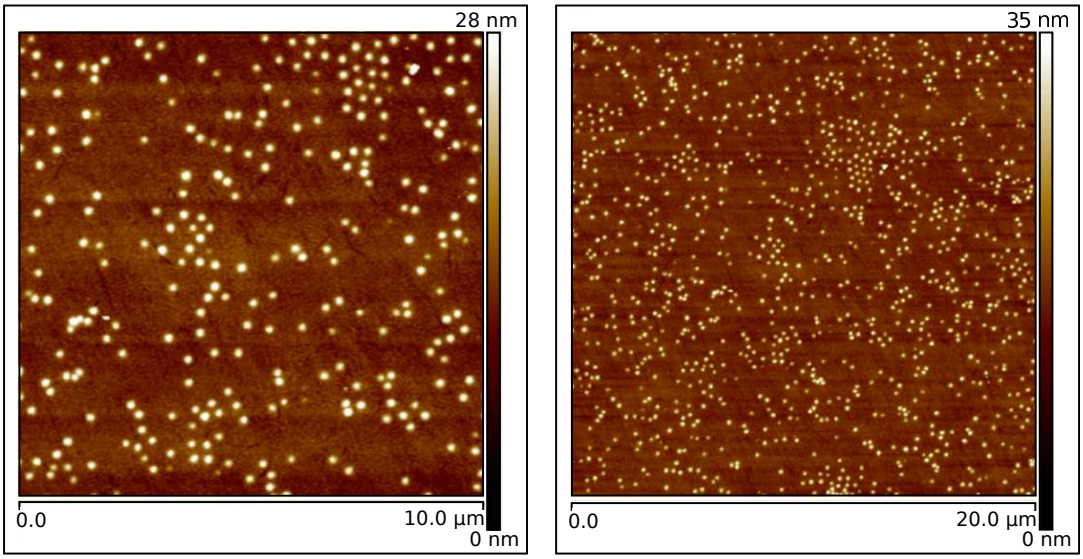

Figure 5.4: 10×10 (left) and 20×20 μm^2 (right) height AFM micrographs taken in tapping mode of a QCM-D crystal coated with cationic microgel after surface drying. The images correspond to the crystal used to obtain the results presented in Figure 5.2.

5.2.2 Adsorption: anionic microgel

As described in the experimental section 2.8.3, we prepared self-assembled monolayers (SAMs) of cystamine on gold-coated quartz crystals for the study of anionic microgels. The PNIPAM anionic microspheres readily adsorb on these SAMs, as the cystamine-modified surfaces are positively charged at pH>3. Typical QCM-D results during adsorption are shown in Figure 5.5.

For the case of the bigger anionic microgel, we observe again a pronounced reduction in f, accompanied by a marked increase in D upon microgel injection. However, the signal evolution was much slower, and no peak in the signals was ever observed. A monotonic reduction (increase) in resonance frequency (dissipation) was observed. A linearly decreasing response was observed in a $-\Delta\Gamma/\Delta f$ *vs.* Δf representation. However, the Δf value obtained by extrapolation of $\Delta\Gamma/\Delta f$ equal to zero does not agree with the values that could be expected for the size of the adsorbed microgel particles. Thus, our results on adsorbed microgel particles do not seem to support the hypothesis of Tellechea and coworkers [3] outlined above. Ex-situ AFM imaging of the coated QCM crystal showed uniform coverage of the surface by the anionic microgel (Figure 5.6), with a less marked tendency to form aggregates compared with the case of the cationic microgel.

We believe the aggregation tendency of the microgels on the surface may be directly related to peaks observed in the QCM-D signal. As the particles adsorb, the mass influencing the quartz crystal movement will also include water associated with the particles. As they aggregate, the amount of water associated to the motion (par particle) may get reduced, causing this counterintuitive tendency reversal on the QCM-D signals. This problem was less significant for the larger anionic particles, which seems to adhere better to the surface (vide infra).

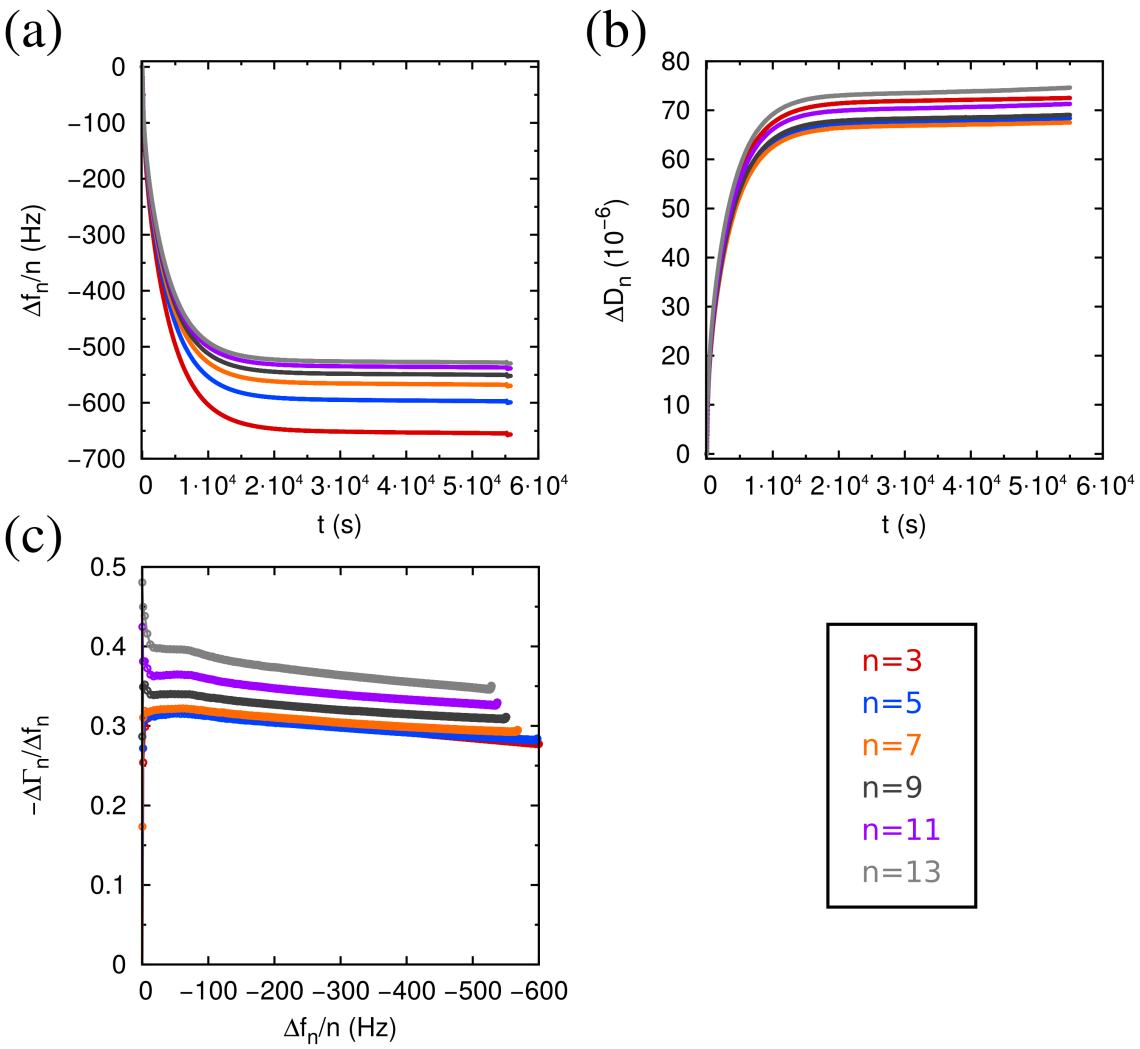

Figure 5.5: Temporal evolution of (a) Δf and (b) ΔD, and (c) $-\Delta\Gamma/\Delta f$ *vs.* Δf for adsorption of anionic microgel from a solution of intermediate concentration. $T = 40$°C. Odd harmonics n=3–13 are shown.

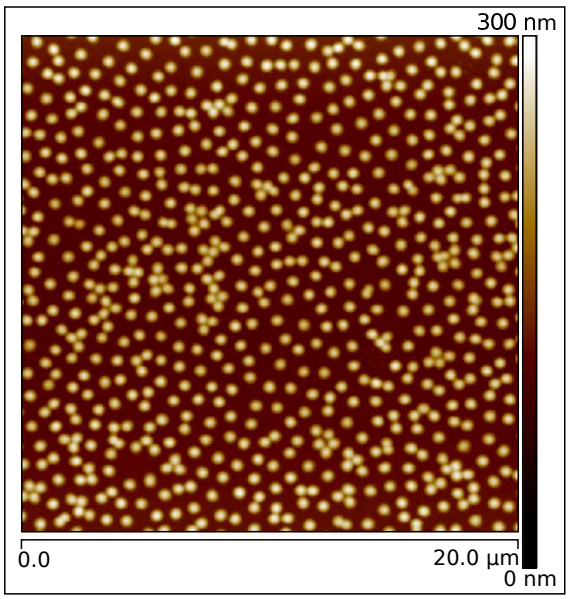

Figure 5.6: 20×20 μm^2 height AFM micrographs taken in tapping mode of a QCM-D crystal coated with anionic microgel. Particle coverage of about 20% can be estimated from the particle size measured by DLS (Table 4.3).

5.2.3 Anionic microgel collapsed-swollen transition

General observations

After microgel adsorption was finished, the QCM-D cell was rinsed with water at pH 4 to remove the excess (non-adsorbed) particles. In general, no (or very small) changes were observed on frequency or dissipation signals upon rinsing, evidencing that the microgel particles were well adsorbed to the substrates. Similar results were observed for the cationic microgel. However, as we will discuss below, the adsorption strength is reduced for the cationic microgel in presence of particular salts as a consequence of the change of the particles charge, an effect discussed in Chapter 4. After rinsing, the temperature of the QCM-D cell was cycled between temperatures above and below the T_{LCS} (typically between 40ºC and 26ºC) to investigate the volume transition of the adsorbed microgels. For the results presented in this subsection, the zero was set at conditions of bare crystals in water at 25ºC. Typical results for the anionic microgel are presented in Figure 5.7. A complete cooling-heating cycle is included. As can be observed, the process was entirely reversible; no particle desorption appears to be occurring during the process. As can be noted in the figure, a non-monotonic behavior of f and D was observed when the temperature was cycled. Cooling-down from $T = 40$ºC, a reduction in f accompanied by an increase in D was initially observed. This

evolution is to be expected, as the microgel particles are progressively swollen with water as the temperature is reduced. However, at a particular temperature (different for each harmonic) f started to increase; the opposite is true for D.

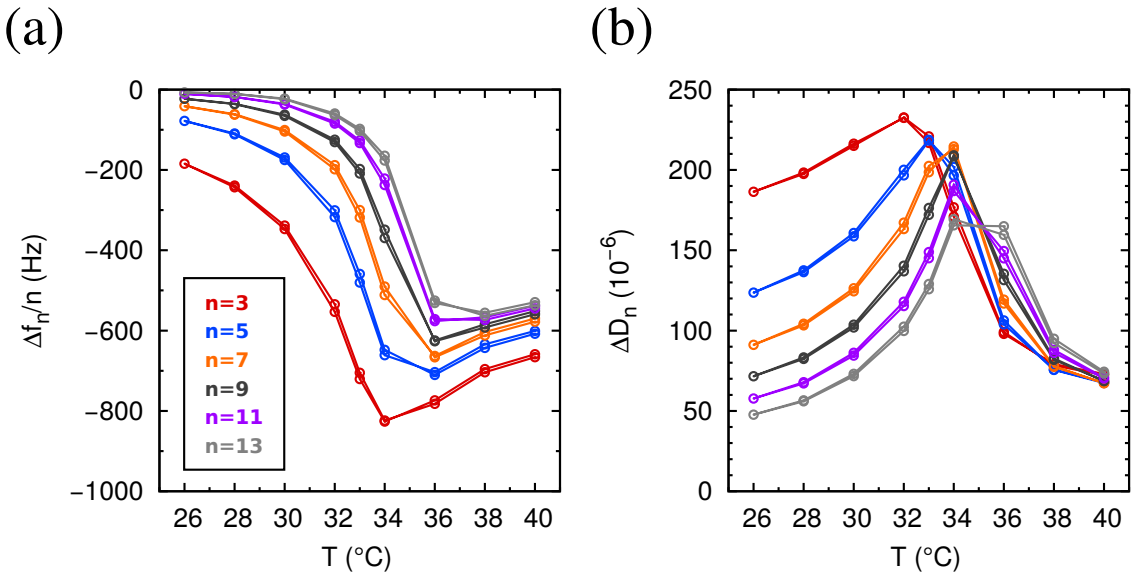

Figure 5.7: Swollen-collapsed transition for anionic microgel in contact with water at pH 4. (a) Δf and (b) ΔD for different harmonics are shown. Raw data was corrected by subtracting Δf and ΔD values measured at the different temperatures in bare water (before microgel adsorption).

The general behavior observed in Figure 5.7 appears to be compatible with the transition of the adsorbed film through a condition of "film resonance", as described in subsection 2.8.1 of Materials and Methods. When cooling down from $T = 40$ºC the microgel particles swell and the thickness of the film increases. This is compatible with the reduction in f and the increment in D observed. However, as the film gets thicker, the resonance condition is achieved: the characteristic frequency of the film matches the resonance frequency of the crystal; at this point the acoustic shear wave propagating from the crystal to the microgel film interferes constructively with the wave reflected at the microgel/water interface, and dissipation is maximized. As the condition of "film resonance" is frequency dependent, it is not purely a material property; it is determined by the physical properties of the composed film-quartz system. It is for this reason that the peak in dissipation (Figure 5.7) appears at different temperatures for different harmonics. As the characteristic wavelength of the harmonic decreases with n, the "film resonance" conditions are fulfilled for thinner films (higher temperatures) for higher n values. As we described before (Figure 4.8), DLS results evidence that the swollen-collapse transition of the microgels occurs in a rather wide range of temperatures;

the condition of "film resonance" is progressively achieved for lower order harmonics when the temperature is reduced. Thus, from the raw QCM-D results we cannot assign a particular temperature to the T_{LCS}, as we did from DLS or electrokinetic results using the inflexion point of the measured curves (Chapter 4). However, we can identify the relative effect of a particular salt by comparing the behavior of a particular harmonic, as will be discussed below.

The resonance condition can be clearly identified if the $\Delta\Gamma$–Δf representation is chosen, as can be observed in Figure 5.8 (the frequency of resonance corresponds to the maximum value of $\Delta\Gamma$ for the different harmonics). As will be shown below, this representation allows an easy identification of changes in the response of the film when exploring the scenario of resonance.

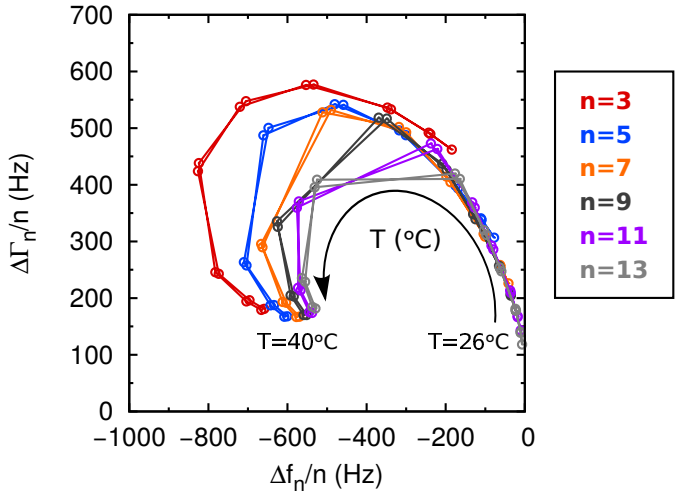

Figure 5.8: Swollen-collapsed transition for anionic microgel in contact with water at pH 4. $\Delta\Gamma$ *vs.* Δf for different harmonics is shown.

Quantitative analysis

The mechanical response of the composed resonator-film system changes abruptly during "film resonance" conditions, making it involved to univocally extract the viscoelastic properties of the film. On the contrary, when the film thickness is sufficiently large compared with the decay length of the acoustic wave, the microgel film can be considered as a semi-infinite viscoelastic media, and the complex shear moduli of the film can be obtained by using eq. 2.11 (assuming the density of the viscoelastic media to be 1 g/cm^3). This quantity often depends on the shear rate, so it will be harmonic dependent. Typical results for the anionic microgel at pH 4 are presented in Figure 5.9. As can be observed in the figure, the measured moduli increases sublinearly with harmonic number (increasing frequency), i.e.

the adsorbed film has a shear thinning behavior. More interestingly, it is apparent that the shear modulus can be accurately determined for different temperatures. It shows an increment of five times in the available temperature range for the different harmonics.

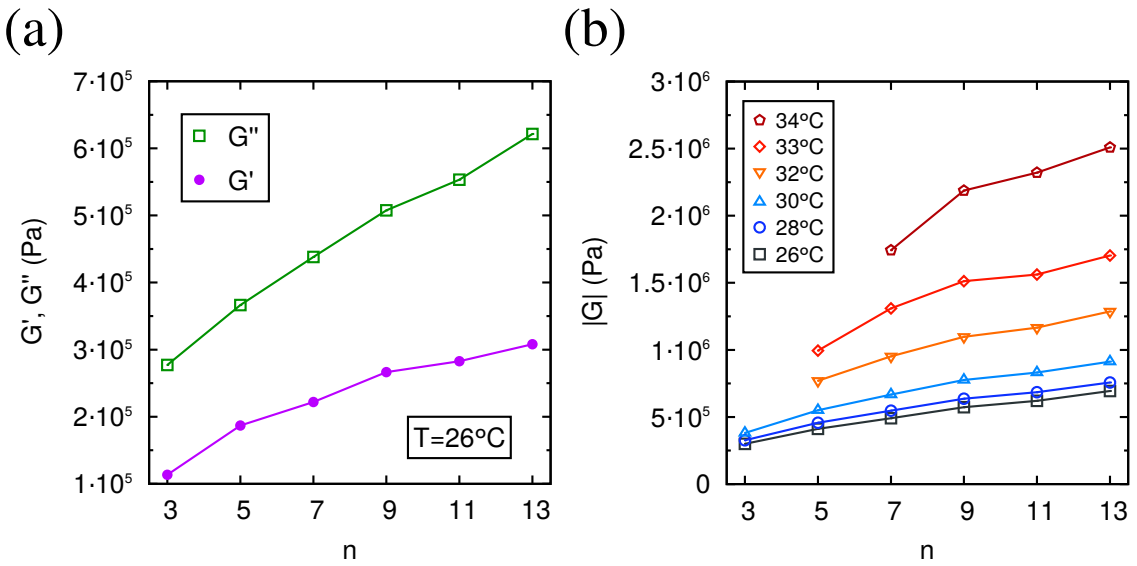

Figure 5.9: Shear moduli of the adsorbed anionic microgel layer. (a) storage (G') and loss (G") modulus for the different harmonics. Shear thinning behavior is observed. (b) Measured shear modulus at different temperatures. The increasing shear modulus allows a reliable determination of the T_{LCS}.

The simple analysis described can only be applied for thick enough films. Otherwise, the assumption of a semi-infinite viscoelastic media breaks down. For this reason high temperature data in Figure 5.9 (b) is missing for the low harmonics; as explained before, the decay length of the propagation wave (δ) decreases with harmonic order. When δ is not small compared with the thickness of the microgel layer the simple assumption of a semi-infinte media cannot be applied. Nevertheless, this situation is easily identified; the results of the analysis of the measured data using eq. 2.11, brings unphysical negative values for the storage moduli.

δ can be calculated from the measured shear modulus, as described in the equation 2.12 of the Materials and Methods part; the data for different harmonics are presented in Figure 5.10 (a), in the range of validity of the assumption of a semi-infinite viscoelastic media. It can be observed in Figure 5.10 (a) that δ increases rapidly with temperature, as a consequence of the increasing shear modulus of the collapsing microgel. The shrinking particle size together with the increasing δ is responsible for the abrupt appearance of the condition of film resonance. We are presenting in the same plot the hydrodynamic diameter of the particles measured

by DLS (shifting the scale by 200 nm). As can be expected, the range of validity (in n) of the assumption of a semi-infinite media growths with the hydrodynamic particle size, which determines the thickness of the adsorbed layer.

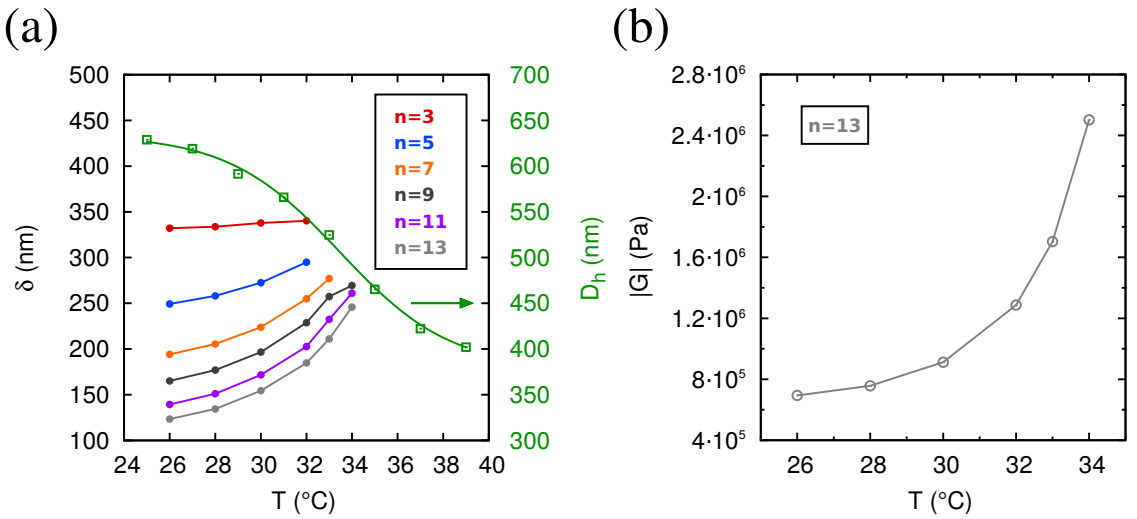

Figure 5.10: Swollen-collapsed transition of an adsorbed layer of anionic microgel. (a) Decay length of the shear wave δ as a function of temperature for the different harmonics. The progressive change of viscoelastic properties of the PNIPAM microgel determines δ. The hydrodynamic diameter of the microgel (determined by DLS) is presented in a shifted scale (right axis). (b) Shear modulus calculated from the 13^{th} harmonic data. The onset of the rapid modulus increase can be reliably used to define the T_{LCS}.

Figure 5.10 (b) shows the shear modulus G calculated from the 13^{th} harmonic data; $|G|$ increases continuously with T, but a marked increase starts at a temperature that can be identified with the T_{LCS}. As can be observed in Figure 5.9, a similar trend is present for all the harmonics investigated. However, we have chosen to focus on the higher order harmonic, because it has the shortest δ, widening the temperature range accessible. There are only few reports of rheological studies of PNIPAM microgel particles. To the best of our knowledge, no quantitative determination of the loss and storage shear moduli of PNIPAM microgels (Figure 5.9 (a)) has been reported before. Hashmi and Dufresne used atomic force microscopy to measure the Young's modulus of individual PNIPAM microgel particles; no values of shear modulus were reported [4]. Voudouris and coworkers [5] studied the full elastic response (Young and Shear moduli) of PNIPAM microgels by using capillary micromechanics. In agreement with our results, they observed around a three times increment in G changing from the swollen to the collapse state of the microgel. However, the G values observed by us are about 250 times larger,

even though our microgels have similar cross-linker-to-monomer ratios (1/15 (this work) *vs.* 1/14 (Voudourias and coworkers)). We believe the difference in G is likely to be related to the vastly different shear rates used in both studies.

5.2.4 Anionic microgel collapsed-swollen transition: ion specificity

As discussed several times during this thesis, the ionic environment has an important influence on the observed T_{LCS}. This can also be observed by QCM-D. As has been reported before, the relative influence of different anions on the T_{LCS} follows the Hofmeister series: chaotropic ions increase the value of T_{LCS}; the opposite is true for kosmotropic ions. We measured temperature cycles similar to the one described in the previous section for different sodium salt, and observed a similar behavior. The values of Δf and ΔD for the 3^{th} and 13^{th} harmonics for the different salts investigated are presented in Figure 5.11. As can be observed in the figures, thiocyanate, a chaotropic ion, increased the collapsed-swollen transition temperature; the opposite was true for the case of sulfate, a kosmotropic ion. Addition of 100 mM of NaCl decreased T_{LCS} compared with the case of pH 4 in absence of salt. We can make calculations similar to the one described above to determine the shear modulus of the microgel layer for the different salts. As can be observed in Figure 5.12, these data allows a clear determination of the influence of the different ions on the T_{LCS}.

Interestingly, no significant effect is appreciated for the two hydrophobic salts: sodium tetraphenylborate ($NaPh_4B$) and tetraphenylarsonium chloride (Ph_4AsCl); the hydrophobic tetraphenyl salts do not seem to affect the observed transition at the low concentrations investigated (1 and 10 mM for the anionic and cationic hydrophobic ions). As discussed before (Figure 4.9), the charge of the anionic microgel was reversed in presence of 10 mM tetraphenylarsonium chloride; however, this change does not appear to be large enough to affect PNIPAM T_{LCS} or the adhesion of the microgel to the cystamine-coated gold substrate. The T_{LCS} changes observed by QCM-D for the different salts correlates very well with the changes observed by DSC for PNIPAM chains. These results will be discussed in Chapter 6.

A $\Delta\Gamma$–Δf representation (analogous to the one used in Figure 5.8) allows a quick comparison of the behavior of the microgels before and after adding the hydrophobic salts. As can be observed in Figure 5.13, the results obtained in the absence of salt or in the presence of the two hydrophobic ions at low concentrations are very close. Once again, no significant effect of these salts on the viscoelastic properties of the microgels or on the adhesion with the substrate can be observed.

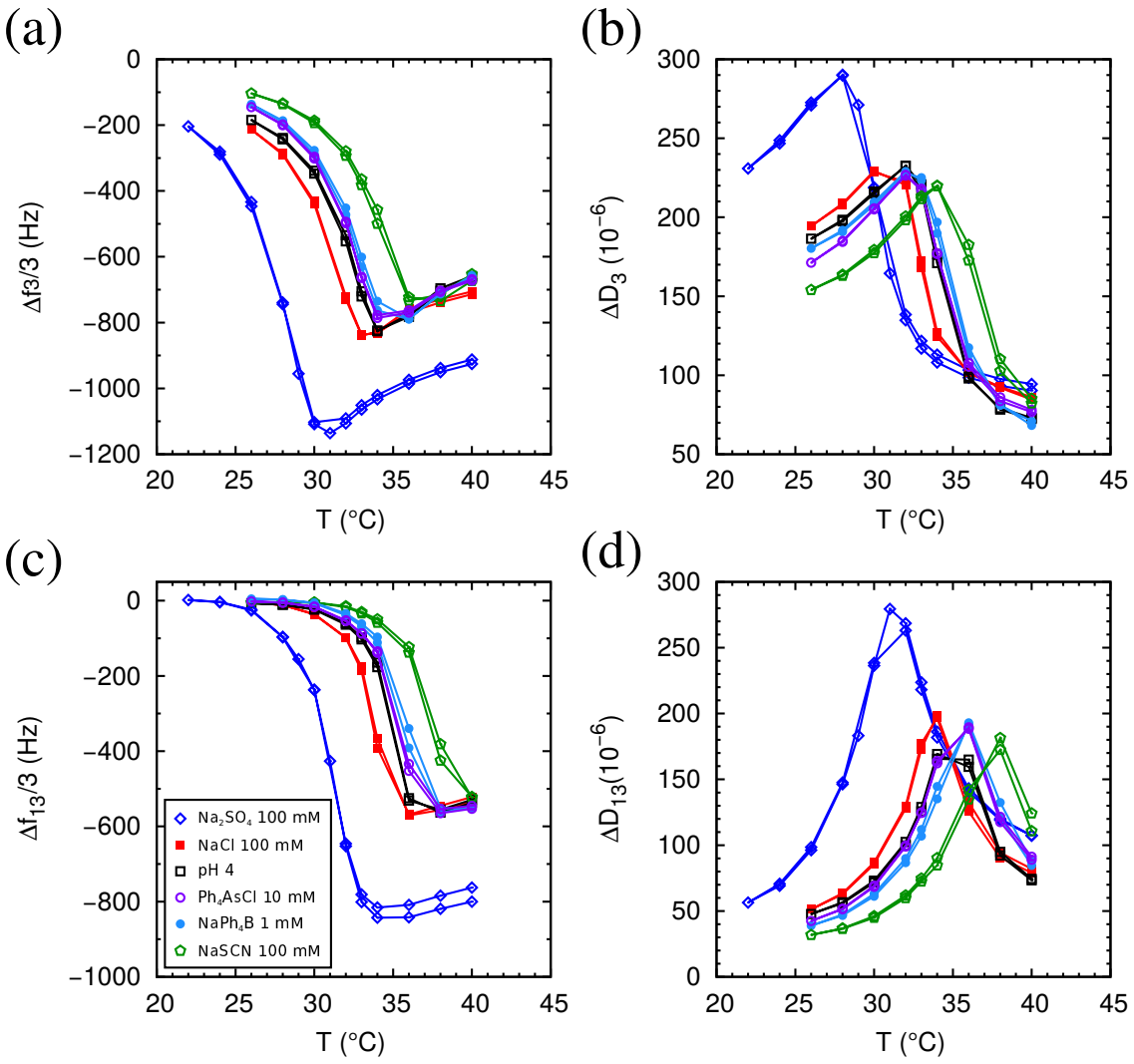

Figure 5.11: (a) Δf and (b) ΔD for n=3, in presence of different salts. (c) Δf and (d) ΔD for n=13, in presence of different salts. Quartz crystal previously coated with anionic microgel. Reference: bare crystal in water at 25°C. The large signal intensity observed for Na_2SO_4 is due to a larger amount of adsorbed microgel particles in this experiment, which does not seem to affect the measured shear modulus (see Figure 5.12).

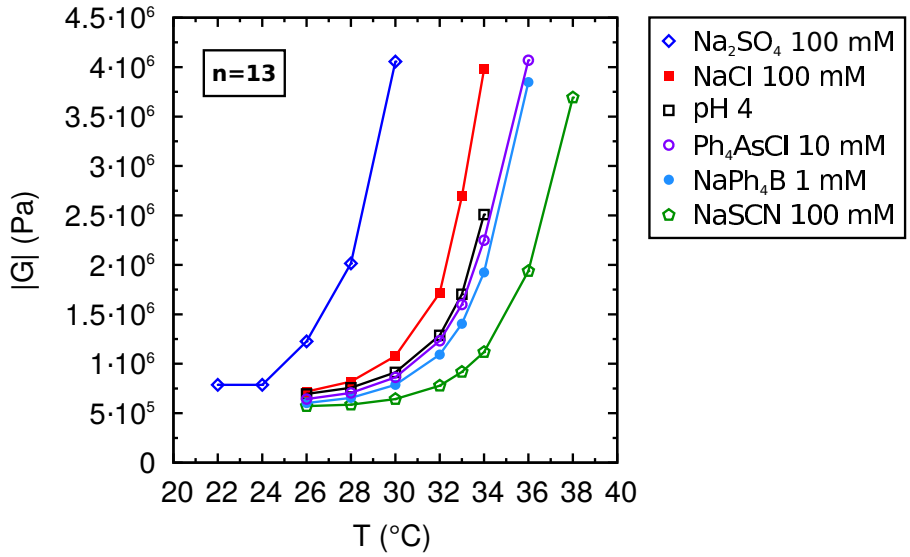

Figure 5.12: Shear modulus of a preadsorbed anionic microgel layer rinsed with different salt solutions (as indicated) calculated from the 13^{th} harmonic data. The onset of the rapid modulus increase can be reliably used to define the T_{LCS}.

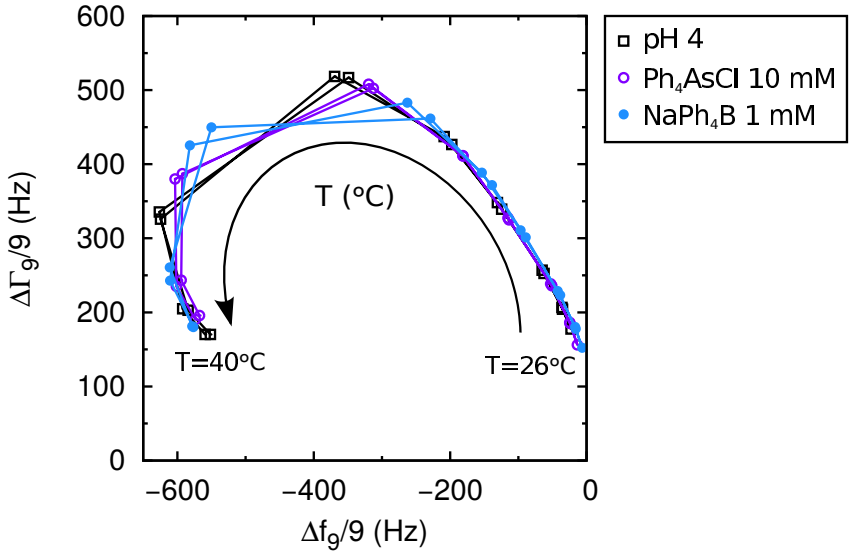

Figure 5.13: $\Delta\Gamma$–Δf for n=9, measured for a preadsorbed layer of anionic microgel in presence of different hydrophobic ions. Reference: bare crystal in water at 25°C.

5.2.5 Cationic microgel collapsed-swollen transition: ion specificity

The adsorbed cationic microgel layers showed a similar response to temperature and inorganic salts that the one described in the two previous subsections for the anionic microgel. However, some irreversibility in a cooling-heating cycle was sometimes observed, in particular in the presence of the hydrophobic tetraphenyl anion. This indicates irreversible modification of the adsorbed layer during the measurement. This effect can already be observed in the raw QCM-D data. As can be observed in Figure 5.14, reversible and reproducible QCM-D data is obtained while rinsing a preadsorbed layer of cationic microgel with solutions of different NaCl concentration. On the contrary, substantial modifications on the layer seem to occur when rinsing with the anionic tetraphenyl salt. Indeed, no steady state seems to be reached 1 hour after rinsing with 10 mM $NaPh_4B$. This is probably due to the continuous rearrangement of the microgel particles, as described below. If a similar experiment is performed using the cationic tetraphenyl salt (Ph_4AsCl) a different behavior is observed, as shown in Figure 5.15. The system appears to quickly reach steady state after each salt injection. In addition, no major changes can be observed in the measured f and D signals after rinsing with Ph_4AsCl solutions of different concentrations.

We believe this distinctive behavior of the cationic microgel layer in presence of the anionic ion is due to weakening of the adhesion between the cationic particles and the substrate, due to the charge reversal discussed in Chapter 4. We measured ex-situ AFM micrographs of the quartz crystals after the QCM-D experiments, and we found a very heterogeneous distribution of particles on the substrate after the experiment performed with the anionic tetraphenyl ion (data in Figure 5.14). On the contrary, homogeneous particle adsorption was observed on the quartz crystals exposed to NaCl or the cationic tetraphenyl salt (data in Figure 5.15). The presence of tetraphenyl ions seems to modify the interaction between the microgel particles and the SiO_2 substrate, in agreement with the in-situ AFM results of cationic microgel in mica discussed in Chapter 4. Ex-situ AFM images of the quartz crystals taken after the QCM-D experiments corroborate this hypothesis. A heterogeneous coverage was observed for the crystal rinsed with $NaPh_4B$ solutions (Figure 5.16). Some zones with large particle coverage were observed, while almost complete depletion of microgel was found in different regions. On the contrary, much more homogeneous particle coverage was observed for the crystal exposed to Ph_4AsCl solutions (Figure 5.17).

The influence of the hydrophobic ions on the cationic microgel can be evidenced by the $\Delta\Gamma$–Δf representation described before, as shown in Figure 5.18. As can be clearly observed in the figure, a different response is observed for the different hydrophobic salts with respect to the no changes observed with the anionic microgel (cf. Figure 5.13). In presence of the cation Ph_4As^+ the resonant behavior is

more marked: positive frequency shifts are observed at the lowest temperatures. We read this result as a consequence of a more solidly attached microgel layer, increasing the reflectivity at the particle-liquid boundary. On the contrary, in presence of the anion Ph_4B^- substantial hysteresis (together with apparent coverage reduction, Figure 5.14) is observed. We believe charge reversal of the microgel spheres is responsible for this effect.

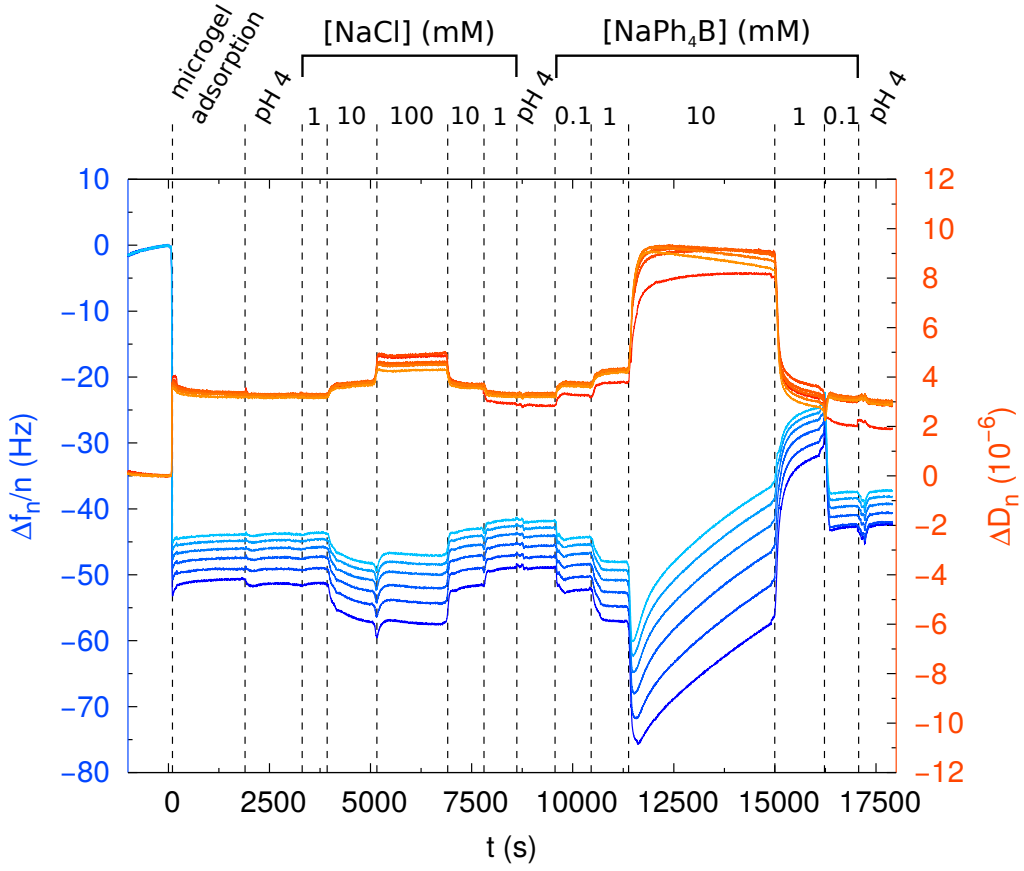

Figure 5.14: Raw QCM-D data. Δf (left axis in blue) and ΔD (right axis in orange) for the different harmonics between n=3 (dark tonalities) and n=13 (pale tonalities), measured during adsorption of the cationic microgel and rinsing with different salt solutions as indicated. T = 40ºC. Microgel concentration during adsorption 0.028 g/l.

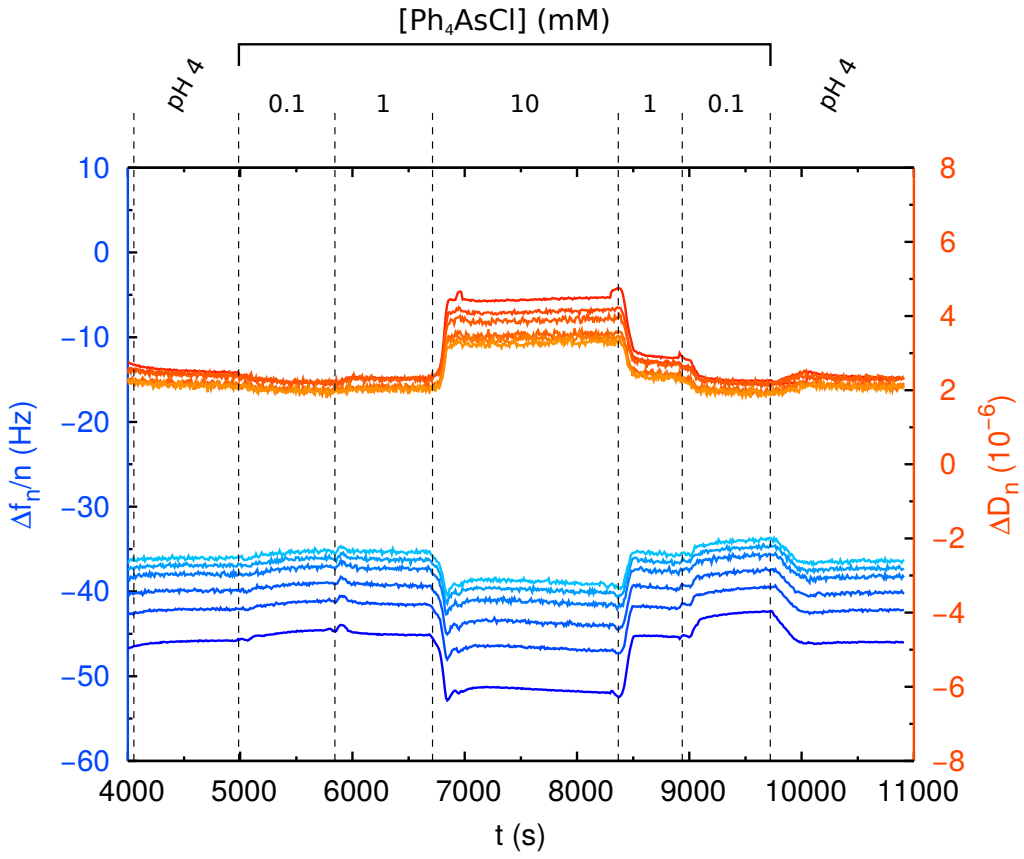

Figure 5.15: Raw QCM-D data. Δf (left axis in blue) and ΔD (right axis in orange) for the different harmonics between n=3 (dark tonalities) and n=13 (pale tonalities), measured during adsorption of the cationic microgel and rinsing with solutions of Ph_4AsCl at different concentrations as indicated. $T = 40$ºC. Microgel concentration during adsorption (not shown) 0.028 g/l.

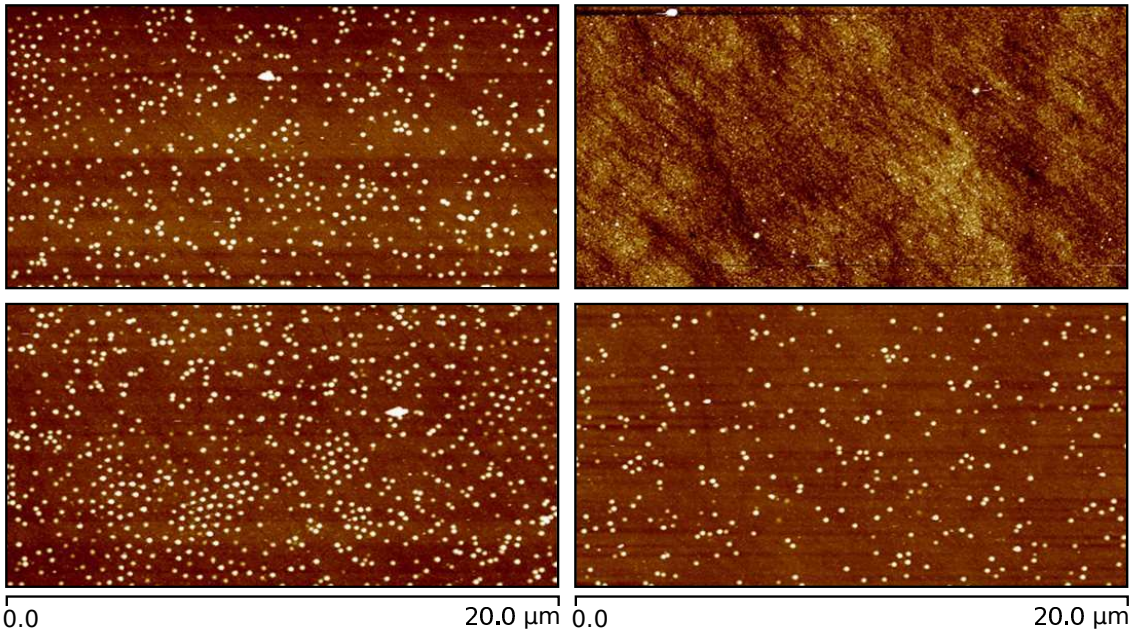

Figure 5.16: 20 μm (horizontal size) height AFM micrographs taken in tapping mode of a QCM-D crystal coated with cationic microgel after surface drying. The images correspond to the crystal used to obtain the results presented in Figure 5.14.

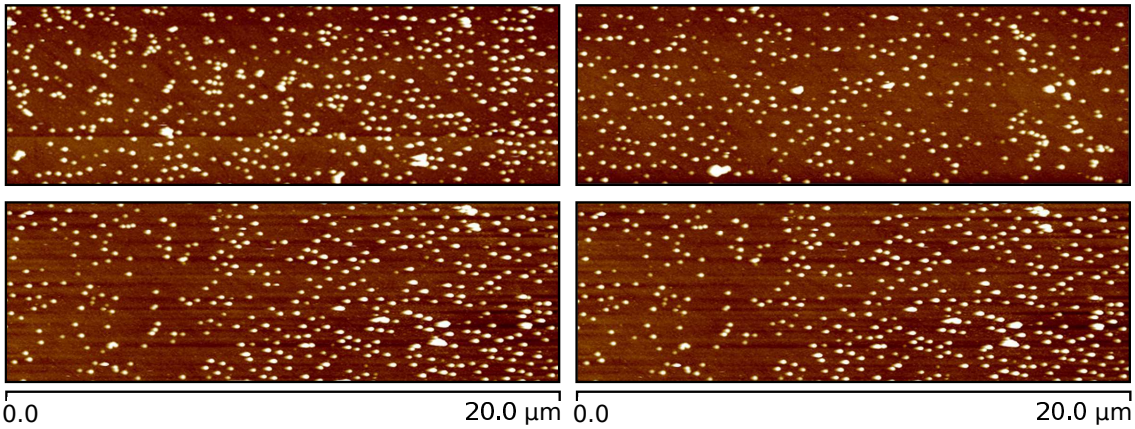

Figure 5.17: 20 μm (horizontal size) height AFM micrographs taken in tapping mode of a QCM-D crystal coated with cationic microgel after surface drying. The images correspond to the crystal used to obtain the results presented in Figure 5.15.

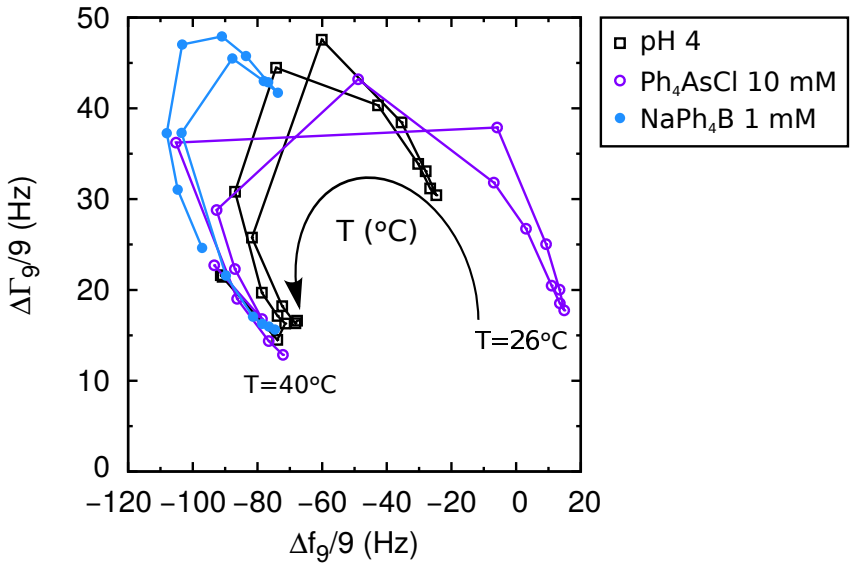

Figure 5.18: $\Delta\Gamma$–Δf for n=9, measured for a preadsorbed layer of cationic microgel in presence of different hydrophobic ions. Reference: bare crystal in water at 25°C.

5.3 Conclusions

In this chapter, the volume phase transition of anionic and cationic PNIPAM microgels in aqueous medium has been studied by the QCM technique. A complete cooling-heating cycle produces the swollen-collapsed transition of the microgel particles. At certain temperature, the thickness of the adsorbed layer reaches the condition of "film resonance". At this point the dissipation is maximized and the viscoelastic properties of the film can be easily obtained. The QCM technique has shown to be a powerful tool to characterize the viscoelastic properties of PNIPAM microgels. In addition, the shear modulus of the layer has been accurately determined for different temperatures. At the same time, the shear modulus allows a reliable determination of the T_{LCS}, which is very sensitive to the ionic environment. We have observed that the T_{LCS} values in presence of different inorganic anions, follow the Hofmeister series, as it has been previously reported. Kosmotropic ions decrease the value of T_{LCS}, whereas chaotropic ions produce the opposite effect. On the other hand, no significant effect of the tetraphenyl salts on the T_{LCS} or the viscoelastic properties of the microgels were observed. However, as we have seen in the previous chapter, the tetraphenyl ions feel a great attraction to the PNIPAM interface, especially in the collapsed state resulting in important charge reversal of the microgels. In the QCM experiments we have observed in the case of the

cationic microgel that its adsorption onto negatively charged surfaces is weakening in presence of the Ph_4B^- which should be a direct consequence of the charge reversal. Similar results were also obtained by AFM in Chapter 4. In contrast, no major changes were observed in presence of Ph_4As^+. This agrees that the interaction of the tetraphenyl anion with PNIPAM is more intense than that caused by the tetraphenyl cation.

References

[1] López-León, T.; Elaïssari, A.; Ortega-Vinuesa, J. L.; Bastos-González, D. Hofmeister effects on poly (NIPAM) microgel particles: macroscopic evidence of ion adsorption and changes in water structure. *ChemPhysChem* **2007**, *8*, 148–156.

[2] López-León, T.; Ortega-Vinuesa, J. L.; Bastos-González, D.; Elaïssari, A. Thermally sensitive reversible microgels formed by poly (N-Isopropylacrylamide) charged chains: A Hofmeister effect study. *J. Colloid Interface Sci.* **2014**, *426*, 300–307.

[3] Tellechea, E.; Johannsmann, D.; Steinmetz, N. F.; Richter, R. P.; Reviakine, I. Model-independent analysis of QCM data on colloidal particle adsorption. *Langmuir* **2009**, *25*, 5177–5184.

[4] Hashmi, S. M.; Dufresne, E. R. Mechanical properties of individual microgel particles through the deswelling transition. *Soft Matter* **2009**, *5*, 3682–3688.

[5] Voudouris, P.; Florea, D.; van der Schoot, P.; Wyss, H. M. Micromechanics of temperature sensitive microgels: dip in the Poisson ratio near the LCST. *Soft Matter* **2013**, *9*, 7158–7166.

6 Effects of inorganic and organic ions on PNIPAM chains: a DSC study

6.1 Background

Poly (N-isopropylacrylamide) (PNIPAM) is a thermoresponsive polymer, containing hydrophilic and hydrophobic moieties. Its dissolution in water is favored by the possibility of hydrogen bonding between the amide groups in the polymer and water, which lowers the free energy of the binary system. However, this bonding implies an entropic penalty to the mixing process due to its orientational nature. In addition, the presence of hydrophobic groups on the polymer also reduces the orientational freedom of nearby water molecules. As temperature is raised the contribution of the entropic free-energy components augments, decreasing the quality of water as PNIPAM solvent; at a particular temperature the entropic penalty dominates over the exothermic hydrogen bonding, and phase separation occurs. Interestingly, this temperature is largely independent of polymer concentration; for this reason it is commonly termed lower critical solution temperature (T_{LCS}), a term which strictly applies to the minimum of the coexistence curve.

When $T > T_{LCS}$, several scenarios can be considered, depending on polymer concentration. The competition between intrachain contraction and interchain association (driven by hydrogen bonding and hydrophobic interaction between a single or independent polymer chains) will determine the resulting state. Single chain coil-to-globule transition has only been observed at extremely low PNIPAM concentration [1, 2]. At concentrations well below the overlapping concentration (dilute regime) microscopic phase separation has been reported: aggregation of colloidal particles of narrow size distribution has been observed by few research groups [3, 4]. The size of the aggregates varied with heating history (rate and temperature) and polymer concentration, evidencing the out-of-equilibrium state of the colloidal system. It appears that the aggregates are stabilized by charges in the end-groups [5], although other stabilization mechanisms have also been suggested [4, 6]. Colloidal stability has also been achieved by adding surfactants (e.g. SDS) to the water-PNIPAM mixture [7, 8]. Finally, at sufficiently large

polymer concentrations (in the semidilute or concentrated regimes) the interchain interaction largely dominates and macroscopic phase separation (precipitation) is observed. Most of the results presented in this chapter correspond to the semidilute polymer concentration regime.

The balance between stabilizing and destabilizing factors is delicate; for instance, if any salt is added to the solution of the PNIPAM chains, it is expected that the hydrated ions compete with the water around the hydrophobic and hydrophilic groups of the PNIPAM causing the collapse of the chains at temperatures lowers than the T_{LCS} [9]. These effects are the core of the study reported in this chapter.

6.2 Results and discussion

We studied the thermally induced phase transition of PNIPAM by differential scanning calorimetry (DSC) and dynamic light scattering (DLS). DSC allows to study the thermodynamic parameters of the heat-induced phase transition. The polymer used in this work was obtained from Aldrich; its molecular weight (M_w) was between 19 and 30 kDa, which is too small to measure its size by DLS. However, we can estimate its gyration radii R_g in good solvent conditions by extrapolation the results reported by Kubota and coworkers [10] as $R_g = 0.022 \cdot M_w^{0.54}$ (nm), where M_w is expressed in Da. Using this expression, we calculate a value of R_g between 4.5 and 5.8 nm. We can then estimate the polymer overlapping concentration in good solvent condition (C^*) as:

$$C^* = \frac{3M_w}{4\pi N_A R_g^3} \tag{6.1}$$

Thus, for the PNIPAM used in this study C^* varies between 6.1 and 8.3% w/w. Most of the results presented in this study were obtained at semidilute conditions ($C > C^*$). Some tests in dilute conditions ($C < C^*$) were also performed as indicated.

In Figure 6.1, we present the measured relative specific heat for a solution of PNIPAM 15% w/w in pure water. One typical heating-cooling cycle obtained at a scan rate of 1°C/min is presented in the figure. The heat exchange in the transition (ΔH), the T_{LCS} and the temperature at the peak of specific heat can be easily determined from the thermogram. As described above, the process is the result of the intrachain collapse of the PNIPAM chains around the T_{LCS} of the polymer and the interchain aggregation due to the high concentration of PNIPAM chains in the solution. The whole process is endothermic: heat must be added to the system to complete the transition. Early studies associated this fact to the rupture of polymer-solvent hydrogen bonds [11, 12], other groups attributed more importance to the hydrophobic effect [13]. Although there is still some controversy

about the exact mechanism controlling the transition, it is likely that the interplay of both effects determines the overall behavior of the system. We will come back to this point below.

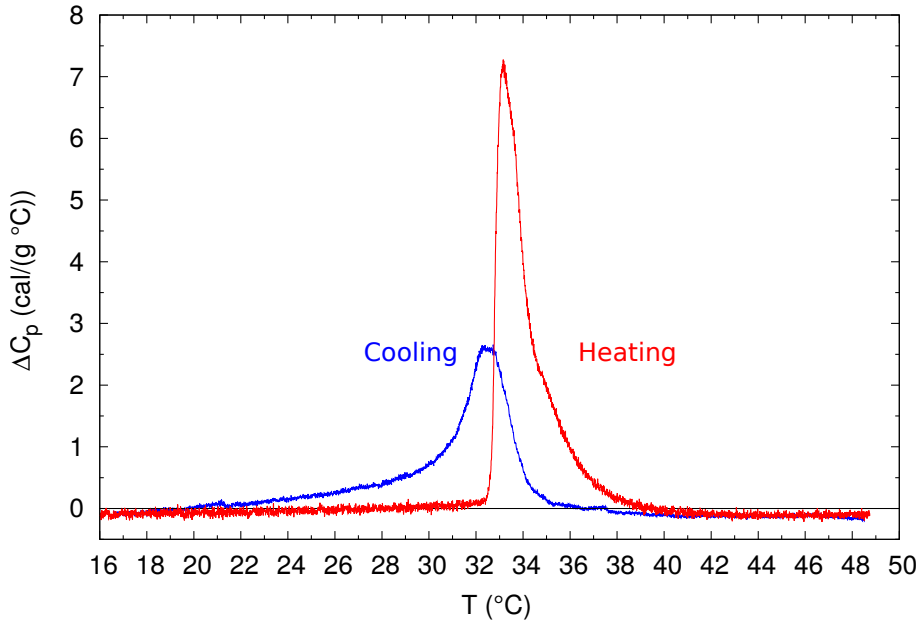

Figure 6.1: Thermogram of PNIPAM at 15% in pure water for one heating and cooling cycle.

In the cooling process, the temperature of the maximum is lower than in the heating process, $\Delta T_{max} = 0.5$ºC, indicating hysteresis. This hysteresis has been previously observed and it is attributed to some additional hydrogen bonding on PNIPAM chains formed in the collapsed states [1, 14, 15]. It is not an equilibrium phenomenon but a kinetic effect that can be undone if the heating and cooling processes could be carried out at zero scanning rate. However, when the temperature is decreased enough the system comes back to its original state [14, 15]. We performed three different thermograms (heating-cooling cycles) in pure water (for 5% and 15% of PNIPAM) by reloading the measuring cell (pan) with fresh solution and these repeated measurements were used to calculate the standard deviations of the measured quantities. We have assumed that these values also represent the uncertainties measured with the rest of the salts.

Next, we measured thermograms for the reference salt, NaCl, and for the most chaotropic inorganic salt used; NaSCN. Results are presented in Figure 6.2. In the case of NaCl, increasing salt concentration results in a decrease of the T_{LCS}. At 10 mM the amount of salt is not enough to induce any significant effect on T_{LCS} in comparison with pure water, but at 100 mM and 1 M the displacement of T_{LCS} at lower temperatures is clearly observed. On the contrary, in presence of NaSCN

the T_{LCS} increases at 100 mM and at 1 M slightly decreases. Because both salts share the same cation, Na^+, these differences must be attributed to the effect of the anions. The NaCl behaves as expected. This salt shows more affinity for water than PNIPAM. As the concentration of Cl^- increases the polymer dehydrates more easily, reducing the T_{LCS}. On the contrary, water prefers to hydrate PNIPAM than SCN^-, a poorly hydrated anion. Thus, in presence of moderate SCN^- concentrations T_{LCS} increases. It is necessary to add a high concentration of SCN^- to observe a T_{LCS} slightly lower than the value obtained in pure water.

We have also observed that the endothermic curve of PNIPAM changes depending on salt concentrations. For NaCl this change is readily observed at 1 M: the heat capacity curve is broader and its height is clearly reduced in comparison with lower NaCl concentrations (Figure 6.2 (a)). On the other hand, for the NaSCN, the curve clearly changes at 100 mM, becoming broader and wider; this effect is even more pronounced at 1 M (Figure 6.2 (b)). The changes in the curves indicate that the balance collapse/aggregation of the PNIPAM chains is being affected by the type and concentration of salt. Similar results were reported by Shechter *et al.* in a study of PNIPAM in presence of KSCN [16]. They argued that in pure water the PNIPAM collapse occurs in a sharp transition due to the cooperative collapse of long segments and probably of the entire polymer chains [11]. However, when salt is present the collapse is a less cooperative process because the SCN^- bound to PNIPAM reduces the length of unperturbed segments of the chains. Hence, the size distribution heterogeneity of the chains increases, resulting in decreasing the peak heights and increasing the widths. We will return to this point later.

We measured thermograms for a number of salts belonging to the Hofmeister series. We have chosen different anions in order to cover a representative range from kosmotropic to chaotropic anions. We also investigated the behavior of the big hydrophobic ions described in previous chapters, tetraphenylarsonium (Ph_4As^+) and tetraphenylborate (Ph_4B^-). Table 6.1 shows the results obtained with the inorganic ions. As expected, the T_{LCS} and T_{max} values depend on the salt and the concentration employed. Figure 6.3 shows the thermograms for the different salts at 100 mM. Ordering the values of the T_{LCS} for each anion in a sequence we find:

$$SO_4^{2-} < IO_3^- < Cl^- < Br^- < I^- < SCN^-$$

which corresponds to the reversed Hofmeister series. Thus, more hydrated salts show lower T_{LCS} values because of their higher affinity for water compared with PNIPAM. On the contrary, in presence of more chaotropic anions water prefers to hydrate the polymer, so an increase in T_{LCS} is observed in presence of I^- or for the poorly hydrated SCN^- anion.

The reduction of T_{LCS} by highly and moderate hydrated anions and the opposite effect by poorly hydrated anions have been previously observed by other authors working with neutral PNIPAM chains [17] and charged PNIPAM chains and

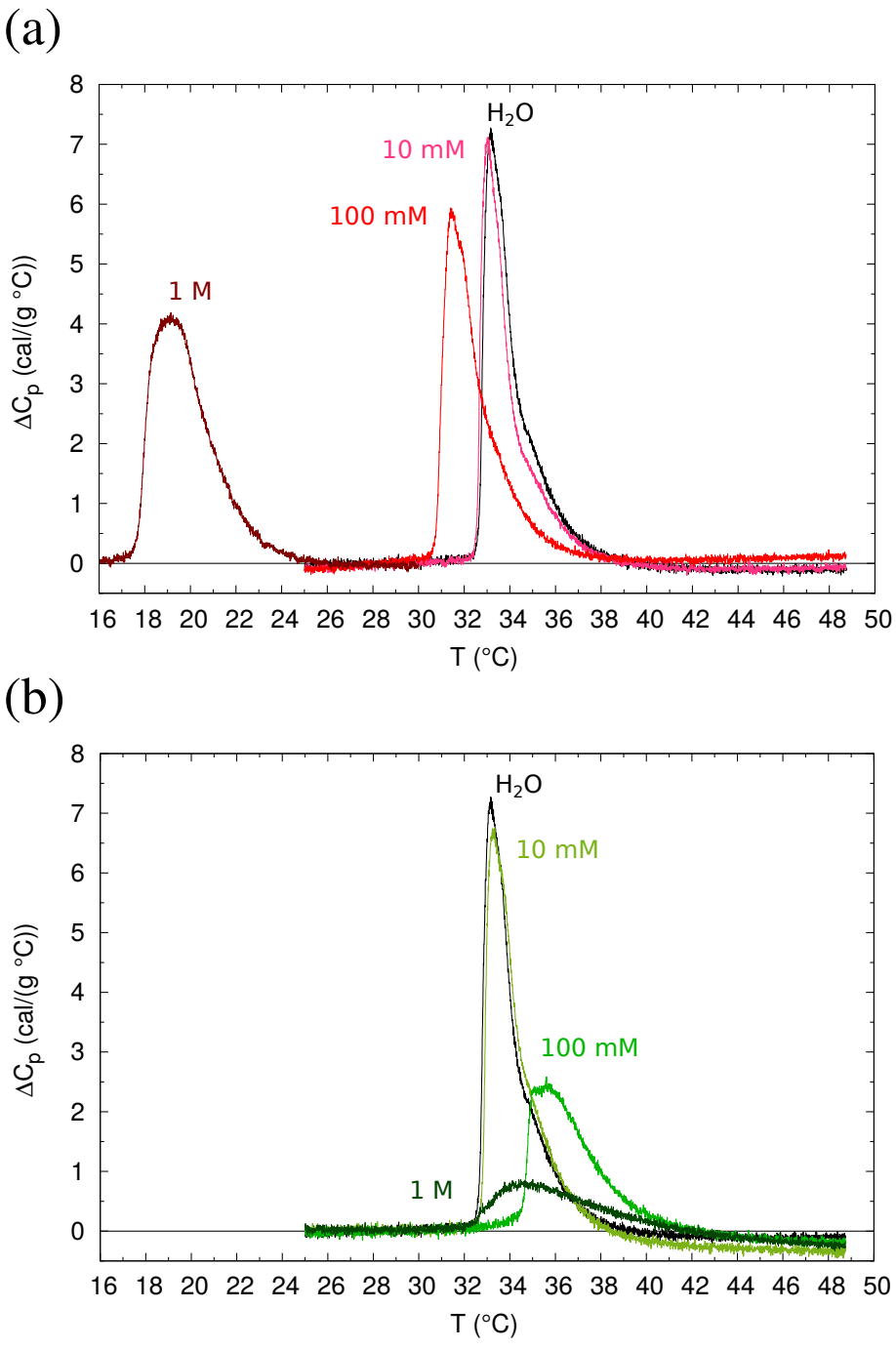

Figure 6.2: Thermograms of PNIPAM at 15% at different concentrations of (a) NaCl and (b) NaSCN salts. The thermogram in pure water is also shown.

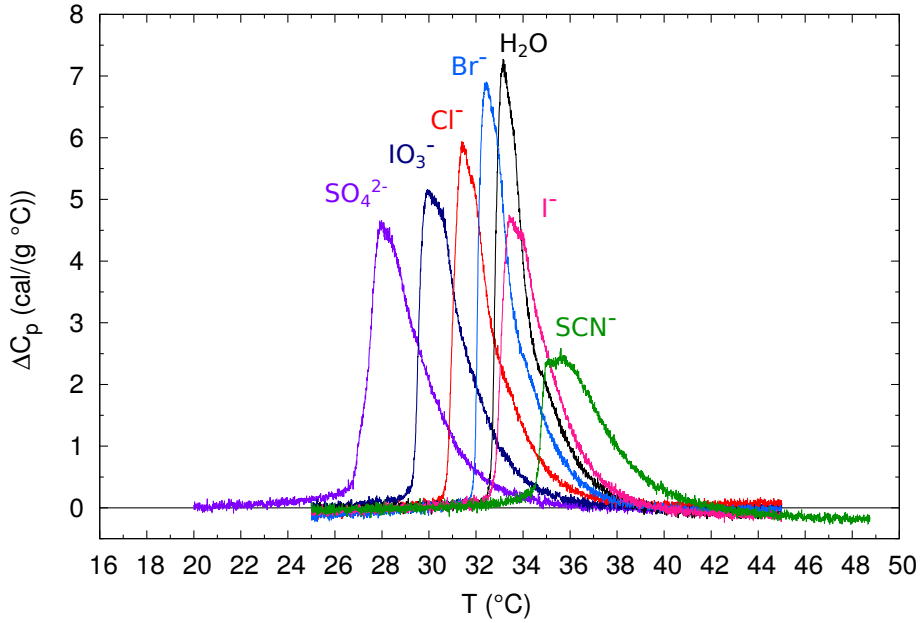

Figure 6.3: Thermograms of PNIPAM at 15% for different salts belonging to Hofmesiter series at 100 mM. The thermogram in pure water is also shown.

Salt	Water	$NaSO_4$	KIO_3	NaCl	NaBr	NaI	NaSCN
$T_{LCS} \pm 0.3$ (ºC) [10 mM]	32.7	32.0	31.9	32.6	32.6	32.7	32.8
$T_{max} \pm 0.3$ (ºC) [10 mM]	33.2	32.6	32.6	33.1	33.1	33.3	33.3
$T_{LCS} \pm 0.3$ (ºC) [100 mM]		27.0	29.4	30.8	32.0	32.8	34.5
$T_{max} \pm 0.3$ (ºC) [100 mM]		28.0	29.9	31.4	32.4	33.4	35.6
$T_{LCS} \pm 0.3$ (ºC) [1 M]		–	–	17.7	–	–	32.0
$T_{max} \pm 0.3$ (ºC) [1 M]		–	–	19.2	–	–	35.0

Table 6.1: T_{LCS} and T_{max} of PNIPAM at 15% for water and the different salts belonging to Hofmeister series at several concentrations.

microgels [18, 19]. In a series of papers leaded by Cremer, the increase on the T_{LCS} for most chaotropic anions was attributed to anionic binding to the amide moieties (NH group) of PNIPAM, which would cause the charge of the polymer surfaces [20]. However, in a more recent study of poly (N,N-diethylacrylamide) (PDEA) Cremer and co-authors have found that the NH group is not required for the interactions between weakly hydrated anions and polymer chains in aqueous solutions. On the contrary, they found that the backbone CH groups provide a binding site for the weakly hydrated anions [21]. Similarly, it has been observed that poly (propylene oxide) (PPO), which has no amide groups in its structure, also increased its phase separation temperature in comparison to pure water in presence of KSCN [22].

It can also be observed in Figure 6.3 that height and width of the peaks depend on the type of salt employed. On one hand, the height decreases and the width increases as the anion is more kosmotropic. On the other hand, SCN^-, the most chaotropic anion, shows the lowest peak and highest width observed for all the salts. Schild and Tirrell observed very similar tendencies with PNIPAM chains and Na_2SO_4, NaSCN and NaBr; they pointed out that the physical origin of the T_{LCS} changes must differ for each salt [11]. We propose that these discrepancies are a consequence of the different interaction of these ions with hydrophobic surfaces. Although PNIPAM chains contain both hydrophilic and hydrophobic moieties, it seems that when T_{LCS} is surpassed PNIPAM globules and aggregates could contain significantly more hydrophobic internal environments [23]. It is well known that kosmotropic anions are excluded from hydrophobic interfaces while chaotropic ones are accumulated on them [24, 25]. Hence, at temperatures lower than the T_{LCS} kosmotropic anions weakened the interaction between water hydrating PNIPAM possibly turning the cooperative collapse of the PNIPAM chains more heterogeneous, which would imply wider peak transitions. Once the T_{LCS} is surpassed, kosmotropic anions tend to be excluded from the interface and the final state reached for the collapsed/aggregated PNIPAM chains should be similar to the one reached in pure water. On the contrary, at T> T_{LCS} chaotropic anions feel a strong attraction for the more hydrophobic PNIPAM interface and will tend to accumulate on it. This effect is especially relevant for the most chaotropic anion, SCN^-, which has been previously shown to be able to reverse the surface charge of PNIPAM microgels and PNIPAM charged chains at low concentrations [18, 19]. Hence, as the temperature is closer to the T_{LCS}, the SCN^- increasingly interacts with the PNIPAM chains globules and aggregates which in turn would also change the peak of the PNIPAM transition. In this case the final state of the globules and aggregates should differ in some extension from that of pure water because of the accumulation of the poorly hydrated anions.

We have also analyzed the change of enthalpy (ΔH) for each salt. ΔH was found from the integration of the endothermic peak, and it is related with the change in the hydration that PNIPAM suffers in the transition from globule to col-

lapsed state. We can see in Table 6.2 that ΔH remains almost constant for all the inorganic salts except for the SCN^-. This means that the way of PNIPAM changes its hydration is independent of the nature of the salt present in the medium. However, for the SCN^- we observe a ΔH reduction as salt concentration increases, indicating that SCN^- interacts in a different or more extensive way than the other anions with PNIPAM, and that it is able to significantly alter the dehydration of the polymer. In an analogous study with poly (propylene oxide) (PPO), Thormann [22] also observed that ΔH only was significantly reduced with increasing salt concentration for KSCN while for the rest for the salts it remained unaffected. He ascribed this result to a decrease of the hydrophobic hydration of PPO by the KSCN, which would agree with the mechanism proposed by us. In summary, the thermograms for the SCN^- seem to reflect that the increase of T_{LCS} comes from the poor competition of SCN^- to water hydrating PNIPAM, but also from the accumulation of SCN^- close to hydrophobic moieties of PNIPAM.

Salt	Water	$NaSO_4$	KIO_3	NaCl	NaBr	NaI	NaSCN
$\Delta H \pm 1$ (cal/g) [10 mM]	13	13	13	12	11	13	13
$\Delta H \pm 1$ (cal/g) [100 mM]		13	13	12	13	11	8
$\Delta H \pm 1$ (cal/g) [1 M]		–	–	14	–	–	6

Table 6.2: Change of enthalpy (ΔH) of PNIPAM at 15% for water and the different salts belonging to Hofmeister series at several concentrations.

Next, we are going to present the thermograms for the tetraphenyl ions. Because of their hydrophobic character, we would expect a behavior similar to that observed with the most poorly hydrated inorganic anions for both the Ph_4B^- and the Ph_4As^+. These hydrophobic ions should not compete with the water hydrating PNIPAM and should experience a strong attraction for hydrophobic interfaces. Results are shown in Figures 6.4 and 6.5 and Tables 6.3 and 6.4 for PNIPAM chains solutions of 15% and 5%, respectively.

Figure 6.4 (a) shows the thermogram for the Ph_4B^- at three different salt concentrations. We can see that in spite of the lower salt concentrations used, T_{LCS} clearly diminishes (cf. Table 6.3) as the concentration increases, while the height of the peaks decreases and the curves becomes wider. This behavior would not be in accordance with that observed for poorly hydrated inorganic anions (a slightly increase of T_{LCS} at low or moderate concentration of salt). A plausible explanation is that Ph_4B^- anion feels such a strong interaction for PNIPAM hydrophobic interface that very low concentrations of Ph_4B^- are enough to strongly interact with it. Hence, instead of helping to solubilize the PNIPAM, Ph_4B^- induces the destabilization of the polymer at temperatures lower than the T_{LCS}. This strong interaction between PNIPAM interface and Ph_4B^- was discussed in previous chapters [26]; we will see further implications of it. By contrast, the results with Ph_4As^+ (Figure

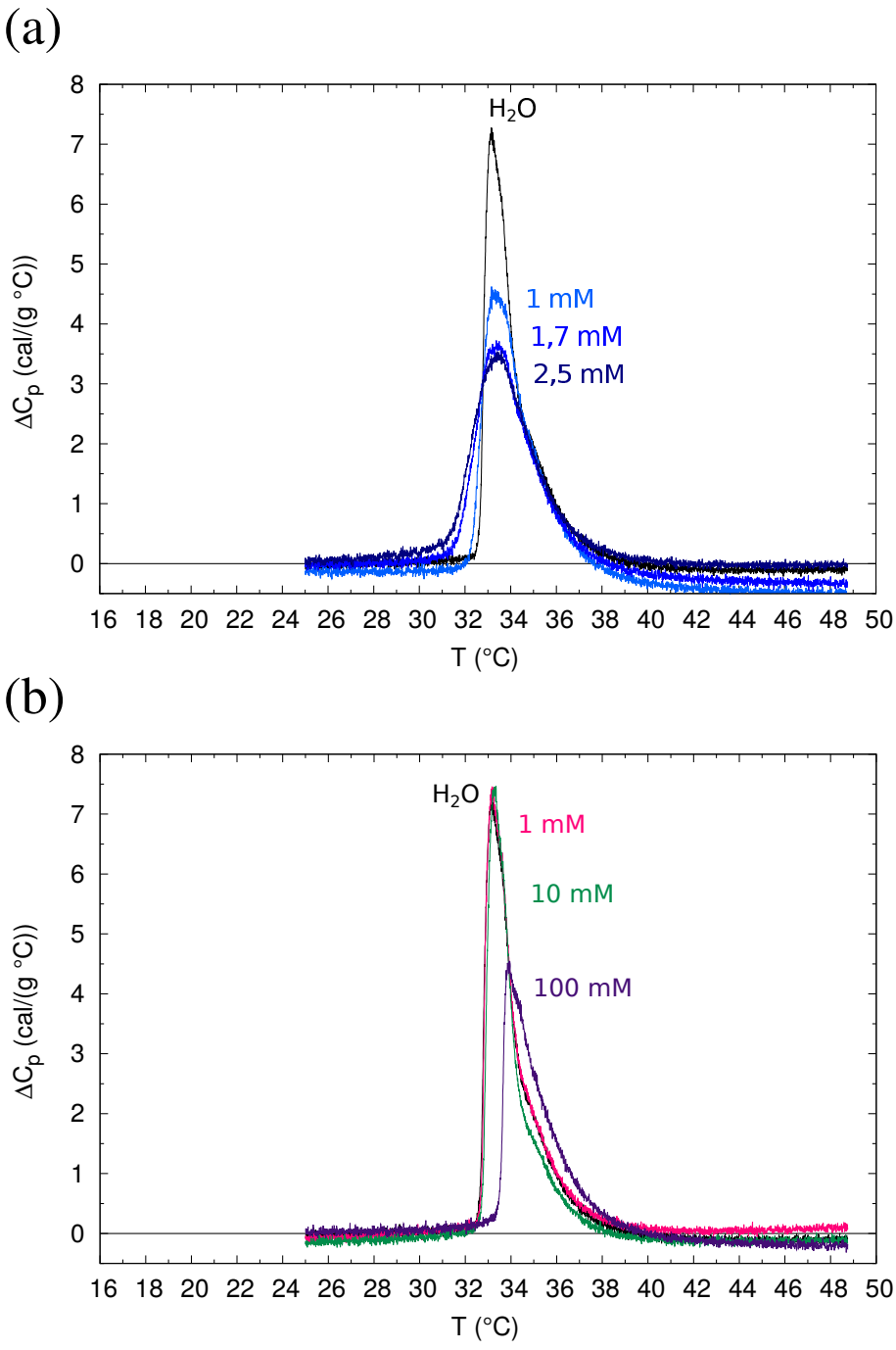

Figure 6.4: Thermograms of PNIPAM at 15% for the tetraphenyl ions at different concentrations (a) Ph_4B^- (b) Ph_4As^+. The thermogram in pure water is also shown.

6.4 (b)) shows that the T_{LCS} tends to increase in the concentration range studied, in accordance with the results found for the most chaotropic inorganic anions. We have to limit our study to a maximum value of Ph_4As^+ concentration of 100 mM because of its limited solubility. For this reason we did not observe the subsequent fall in T_{LCS} as for the inorganic anions. It is interesting to notice that at 100 mM the T_{LCS} of Ph_4As^+ is 33.5ºC, while for the SCN^- we found 34.5ºC. This seems to indicate that the effect of the poorly hydrated inorganic anion was stronger than that of the Ph_4As^+. However, the big cation is clearly hydrophobic and we have previously shown that it strongly interacts with PNIPAM (although in a lesser extension that Ph_4B^-). This apparent contradiction can be explained by the competition between the water hydrating PNIPAM interface and the big tendency of this cation to interact with PNIPAM as the interface become more hydrophobic. The first effect would augment T_{LCS} while the second would reduce it (like in the Ph_4B^- but to a lesser extent). Subsequent results will show that the interaction of Ph_4As^+ with PNIPAM is stronger than that of SCN^-).

	PNIPAM 15%						
Salt	Water	$NaPh_4B$ [1 mM]	$NaPh_4B$ [1.7 mM]	$NaPh_4B$ [2.5 mM]	Ph_4AsCl [1 mM]	Ph_4AsCl [10 mM]	Ph_4AsCl [100 mM]
$T_{LCS} \pm 0.3$ (ºC)	32.7	32.3	31.6	31.3	32.7	32.8	33.5
$T_{max} \pm 0.3$ (ºC)	33.2	33.2	33.4	33.6	33.2	33.3	33.9

Table 6.3: T_{LCS} and T_{max} of PNIPAM at 15% for water and the tetraphenyl ions at different concentrations.

Because of the novelty of these last results we also performed the thermograms at a lower PNIPAM solution of 5%, and different salts concentrations. The thermograms presented in Figure 6.5 confirm the tendencies observed at 15%. At 0.07 mM of Ph_4B^- the T_{LCS} remains almost constant (data in Table 6.4) but the height and the width of the curve have clearly changed, as a consequence of interaction between Ph_4B^- and PNIPAM. For larger salt concentrations the decrease of T_{LCS} is clearly observed, the height of the curves is reduced and they become wider. At 7 mM the decrease on the T_{LCS} is around 5ºC (note that at this concentration none of the other anions, including the hydrophobic Ph_4As^+, showed any variation in relation to the T_{LCS} of the pure water, cf. Tables 6.1 and 6.3). These changes suggest a less homogeneous collapse of the PNIPAM chains as the interaction with Ph_4B^- acquires more relevance. These results support the above explanation for SCN^- anion and also the previous findings [26]; the interaction of Ph_4B^- with PNIPAM interface is so strong that it disturbs the PNIPAM structure, acting as a real disruptor of soft matter.

The Ph_4As^+ results on Figure 6.5 (b) and Table 6.4 also confirm the tendency observed at 15% of PNIPAM. We observe a slight increment on T_{LCS} for larger salt concentrations, in marked contrast with the results obtained with Ph_4B^-.

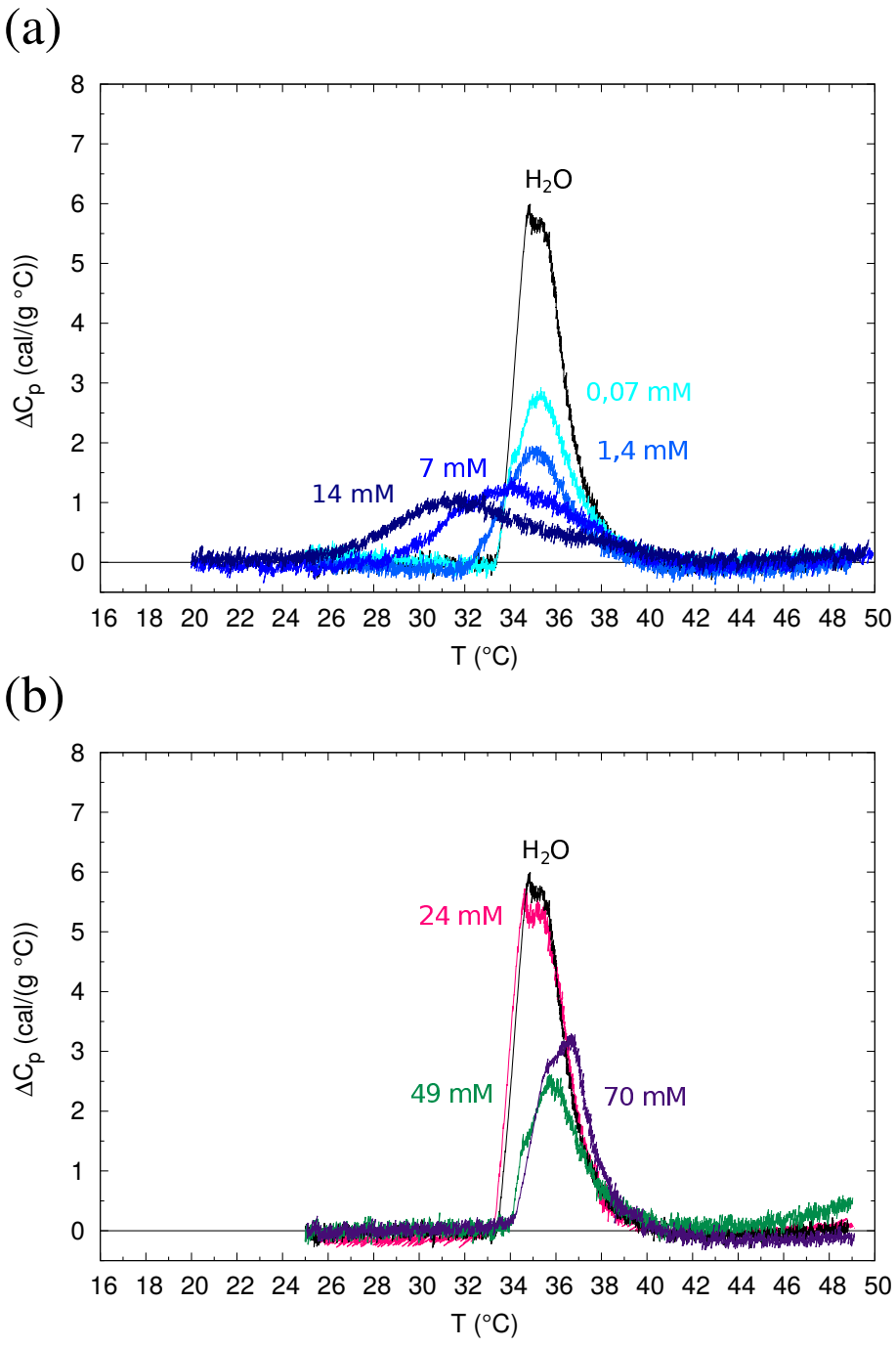

Figure 6.5: Thermograms of PNIPAM at 5% for the tetraphenyl ions at different concentrations (a) Ph_4B^- (b) Ph_4As^+. The thermogram in pure water is also shown.

PNIPAM 5%								
Salt	Water	$NaPh_4B$ [0.07 mM]	$NaPh_4B$ [1.4 mM]	$NaPh_4B$ [7 mM]	$NaPh_4B$ [14 mM]	Ph_4AsCl [24 mM]	Ph_4AsCl [49 mM]	Ph_4AsCl [70 mM]
$T_{LCS} \pm 0.2$ (ºC)	33.5	33.4	32.5	29.1	26.7	33.4	33.9	34.0
$T_{max} \pm 0.2$ (ºC)	33.9	34.9	34.7	32.8	31.1	33.8	35.3	35.3

Table 6.4: T_{LCS} and T_{max} of PNIPAM at 15% for water and the tetraphenyl ions at different concentrations.

Even though both ions are almost identical in size and polarizability, the way they interact with PNIPAM is clearly different. MD simulations described in Chapter 4 showed that although both ions interact with isopropyl groups of PNIPAM (Ph_4B^- in a higher extension), only Ph_4As^+ interact with the amide group, while Ph_4B^- interact with the CH_2 located at the backbone of the PNIPAM chains [26]. Calorimetric data confirm that these differences are also reflected in the thermograms of each salt.

We have also measured ΔH for the PNIPAM volume phase transition in presence of the hydrophobic ions. Results are shown in Tables 6.5 and 6.6. A significant ΔH reduction was observed for both salts. This reduction seems to be largely independent of salt concentration for the case of Ph_4B^-: the ΔH loss is observed at very low salt concentration, (0.07 mM) and it remains constant until the maximum value tested (14 mM). On the contrary, the ΔH value seems to decrease as the concentration of Ph_4As^+ increases. Similar results were observed for the case of SCN^-. The difference of ΔH between heating and cooling processes is very significant (cf. Figure 6.1). Ding *et al.* reported that the enthalpy change upon cooling is always smaller than in the heating process [14]. We observed a similar effect for all the conditions investigated. For instance, comparing heating *vs.* cooling processes for 5% PNIPAM solutions, we found a 25% reduction in ΔH in water or in presence of Ph_4As^+. Interestingly, we found a significantly smaller reduction for the case of Ph_4B^- (between 2 and 8%). This substantial difference points to the possibility of significant changes in the coil-globule transition in the latter case. I will come back to this point below.

PNIPAM 15%							
Salt	Water	$NaPh_4B$ [1 mM]	$NaPh_4B$ [1.7 mM]	$NaPh_4B$ [2.5 mM]	Ph_4AsCl [1 mM]	Ph_4AsCl [10 mM]	Ph_4AsCl [100 mM]
$\Delta H \pm 1$ (cal/g)	13	11	11	10	12	11	8

Table 6.5: Change of enthalpy (ΔH) of PNIPAM at 15% for water and the tetraphenyl ions at several concentrations.

PNIPAM 5%								
Salt	Water	$NaPh_4B$ [0.07 mM]	$NaPh_4B$ [1.4 mM]	$NaPh_4B$ [7 mM]	$NaPh_4B$ [14 mM]	Ph_4AsCl [24 mM]	Ph_4AsCl [49 mM]	Ph_4AsCl [70 mM]
$\Delta H \pm 1$ (cal/g)	15	9	8	9	8	13	8	9

Table 6.6: Change of enthalpy (ΔH) of PNIPAM at 5% for water and the tetraphenyl ions at several concentrations.

The aggregation state of the PNIPAM solution in presence of the different salts is very revealing. As can be appreciated in the following photos (taken after the samples were aged at T=45ºC for 30 minutes), the turbidity of the system was clearly salt dependent.

As shown in Figure 6.6 (a), solution in presence of Ph_4B^- a clear (bluish) appearance was observed. On the contrary, in presence of NaCl or NaSCN the PNIPAM solution became milky as soon as the T_{LCS} was surpassed. The 100 mM SCN^- sample shows clear phase separation. Figure 6.6 (b) shows similar results for lower PNIPAM concentration. While highly turbid solutions were observed in presence of NaCl or NaSCN, by adding the hydrophobic salts PNIPAM aggregation was clearly stopped in an earlier stage, suggesting the formation of submicrometric particles.

We performed DLS measurements of the different samples at temperatures above the T_{LCS}. Multiple scattering was observed in all cases for the polymer concentrations used in the DSC experiments. For this reason we reduced PNIPAM concentration to 0.5%. As it can be inferred from the photos in Figure 6.6, large particle size (and multiple scattering) was observed for NaCl or NaSCN. On the contrary, we observed the formation of long-lasting small particles with very narrow size distributions in presence of Ph_4B^-. The average particle radius varied from 20 to 100 nm depending on the Ph_4B^- concentration used. For the case of Ph_4As^+ we observed particle formation at 0.005% of PNIPAM and 10 mM of salt, with diameter between 350 and 1500 nm. With the other two salts, NaSCN and NaCl, we were not able to obtain particles at any combination of PNIPAM and salt concentration tested. These results evidence that the interaction of the big tetraphenyl ions with the PNIPAM hydrophobic interface is stronger than that of the poorly hydrated inorganic anion SCN^-, and, once again, that the interaction of Ph_4B^- with PNIPAM is much stronger than for the case of Ph_4As^+.

The particle formation in the presence of strongly adsorbing salts can be associated with the globules formation in presence of surfactant discussed at the beginning of the chapter, as represented in Figure 6.7. The ions probably adhere to the polymer due to a hydrophobic interaction, preventing aggregation due to electrostatic stabilization. This process was fully reversible. After cooling, the particles disappeared; independent PNIPAM chains were identified at $T < T_{LCS}$. In

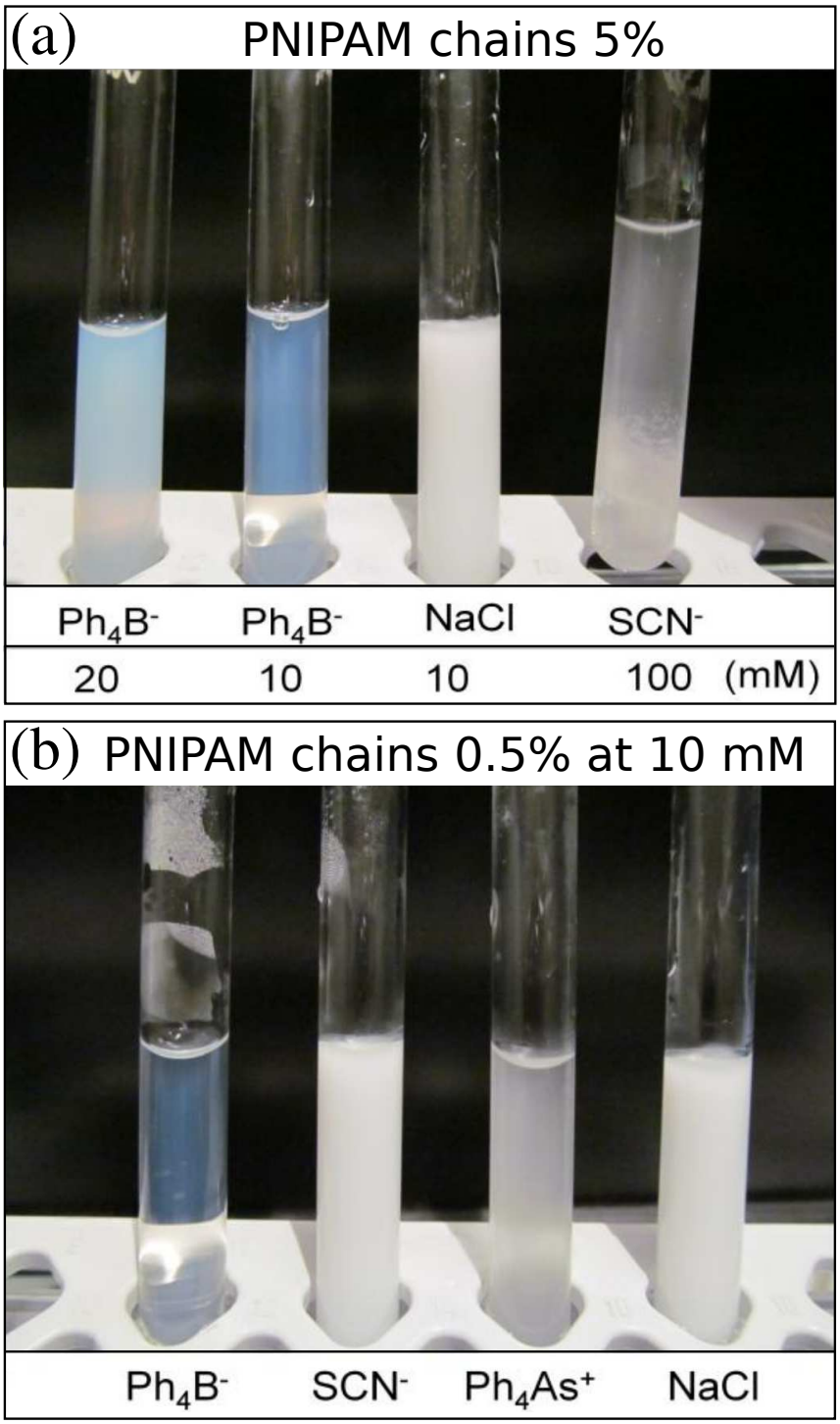

Figure 6.6: Photographs of PNIPAM solutions in presence of different salts and polymer concentrations. (a) 5% of PNIPAM at several ionic concentrations and (b) 0.5% of PNIPAM at 10 mM of salt concentration.

addition, the limited PNIPAM aggregation at $T > T_{LCS}$ may be the reason of the reduced ΔH observed in presence of the hydrophobic or chaotropic salts. Particle formation limits the contribution of the hydrophobic interaction of the collapsed polymer chains, reducing the enthalpy change measured during the transition. Limited aggregation (particle formation) in presence of Ph_4B^- is further reflected in the reduced loss of ΔH when heating and cooling processes are compared. The fact that PNIPAM remains in a fairly divided state at temperatures above T_{LCS} accelerates the re-hydration of the chains upon cooling. In that sense, the observed strong difference in ΔH between heating and cooling has an out-of-equilibrium (kinetic) component that is substantially reduced in presence of Ph_4B^-.

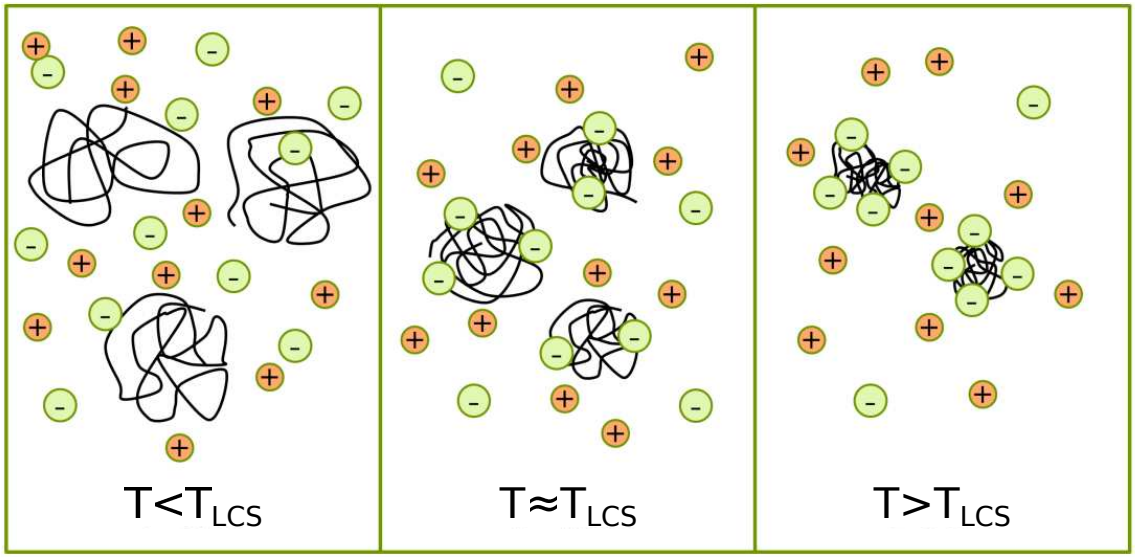

Figure 6.7: Anionic adsorption on PNIPAM chains limits the aggregation of polymer at $T > T_{LCS}$.

6.3 Conclusions

Calorimetric data confirm that the tetraphenyl anion feels a stronger interaction to hydrophobic PNIPAM interface than the tetraphenyl cation. This difference has been reflected in the displacement of T_{LCS} for both salts: while Ph_4B^- significantly reduced the T_{LCS} at low concentrations, Ph_4As^+ slightly increased the T_{LCS} in the range of concentrations studied. In addition, the shapes of the endothermic peaks obtained were also different, being those of the Ph_4B^- much shorter and wider than those of the Ph_4As^+. More importantly, the formation of long-lasting small particles with very narrow size distributions at temperatures higher than T_{LCS} was observed for the Ph_4B^- anion, but not for the Ph_4As^+ cation.

Calorimetric results with inorganic anions reveal the importance of considering the structure of water in ionic specificity. T_{LCS} obtained for the different salts varied according to the Hofmeister series. This indicates that more hydrated anions can easily dehydrated PNIPAM chains reducing the T_{LCS} in a higher extension than less hydrated anions. On the other hand, the data obtained with the SCN^- point out that, in addition to water competition, this chaotropic anion should interact with the hydrophobic moieties of PNIPAM chains further increasing the T_{LCS} of the PNIPAM. The shape of the endothermic peak and the reduction of ΔH compared with the rest of the inorganic salts confirm this last observation.

Finally, the results obtained for the most chaotropic anion SCN^- and those obtained for the organic ions showed similar tendencies, which reinforces the conclusion that the origin of Hofmeister effects or ionic specificity are intimately linked to the hydration properties of the ions and the surfaces.

References

[1] Wu, C.; Wang, X. Globule-to-coil transition of a single homopolymer chain in solution. *Phys. Rev. Lett.* **1998**, *80*, 4092.

[2] Wang, X.; Qiu, X.; Wu, C. Comparison of the coil-to-globule and the globule-to-coil transitions of a single poly (N-isopropylacrylamide) homopolymer chain in water. *Macromolecules* **1998**, *31*, 2972–2976.

[3] Siu, M.; Liu, H.; Zhu, X.; Wu, C. Formation of mesoglobular phase of amphiphilic copolymer chains in dilute solution: effect of comonomer composition. *Macromolecules* **2003**, *36*, 2103–2107.

[4] Wu, C.; Li, W.; Zhu, X. X. Viscoelastic effect on the formation of mesoglobular phase in dilute solutions. *Macromolecules* **2004**, *37*, 4989–4992.

[5] Chan, K.; Pelton, R.; Zhang, J. On the formation of colloidally dispersed phase-separated poly (N-isopropylacrylamide). *Langmuir* **1999**, *15*, 4018–4020.

[6] Aseyev, V.; Hietala, S.; Laukkanen, A.; Nuopponen, M.; Confortini, O.; Du Prez, F. E.; Tenhu, H. Mesoglobules of thermoresponsive polymers in dilute aqueous solutions above the LCST. *Polymer* **2005**, *46*, 7118–7131.

[7] Schild, H. G.; Tirrell, D. A. Interaction of poly (N-isopropylacrylamide) with sodium n-alkyl sulfates in aqueous solution. *Langmuir* **1991**, *7*, 665–671.

[8] Meewes, M.; Ricka, J.; De Silva, M.; Nyffenegger, R.; Binkert, T. Coil-globule transition of poly (N-isopropylacrylamide): a study of surfactant effects by light scattering. *Macromolecules* **1991**, *24*, 5811–5816.

[9] López-León, T.; Ortega-Vinuesa, J. L.; Bastos-González, D.; Elaïssari, A. Cationic and anionic poly (N-isopropylacrylamide) based submicron gel particles: Electrokinetic properties and colloidal stability. *J. Phys. Chem. B* **2006**, *110*, 4629–4636.

[10] Kubota, K.; Fujishige, S.; Ando, I. Solution properties of poly (N-isopropylacrylamide) in water. *Polym. J.* **1990**, *22*, 15–20.

[11] Schild, H. G.; Tirrell, D. A. Microcalorimetric detection of lower critical solution temperatures in aqueous polymer solutions. *J. Phys. Chem.* **1990**, *94*, 4352–4356.

[12] Heskins, M.; Guillet, J. E. Solution properties of poly (N-isopropylacrylamide). *J. Macromol. Sci. Chem.* **1968**, *2*, 1441–1455.

[13] Otake, K.; Inomata, H.; Konno, M.; Saito, S. Thermal analysis of the volume phase transition with N-isopropylacrylamide gels. *Macromolecules* **1990**, *23*, 283–289.

[14] Ding, Y.; Ye, X.; Zhang, G. Microcalorimetric investigation on aggregation and dissolution of poly (N-isopropylacrylamide) chains in water. *Macromolecules* **2005**, *38*, 904–908.

[15] Cheng, H.; Shen, L.; Wu, C. LLS and FTIR studies on the hysteresis in association and dissociation of poly (N-isopropylacrylamide) chains in water. *Macromolecules* **2006**, *39*, 2325–2329.

[16] Shechter, I.; Ramon, O.; Portnaya, I.; Paz, Y.; Livney, Y. D. Microcalorimetric study of the effects of a chaotropic salt, KSCN, on the lower critical solution temperature (LCST) of aqueous poly (N-isopropylacrylamide)(PNIPA) solutions. *Macromolecules* **2009**, *43*, 480–487.

[17] Zhang, Y.; Cremer, P. S. Chemistry of Hofmeister anions and osmolytes. *Annu. Rev. Phys. Chem.* **2010**, *61*, 63–83.

[18] López-León, T.; Elaïssari, A.; Ortega-Vinuesa, J. L.; Bastos-González, D. Hofmeister effects on poly (NIPAM) microgel particles: macroscopic evidence of ion adsorption and changes in water structure. *ChemPhysChem* **2007**, *8*, 148–156.

[19] López-León, T.; Ortega-Vinuesa, J. L.; Bastos-González, D.; Elaïssari, A. Thermally sensitive reversible microgels formed by poly (N-Isopropylacrylamide) charged chains: A Hofmeister effect study. *J. Colloid Interface Sci.* **2014**, *426*, 300–307.

[20] Zhang, Y.; Furyk, S.; Bergbreiter, D. E.; Cremer, P. S. Specific ion effects on the water solubility of macromolecules: PNIPAM and the Hofmeister series. *J. Am. Chem. Soc.* **2005**, *127*, 14505–14510.

[21] Rembert, K. B.; Okur, H. I.; Hilty, C.; Cremer, P. S. An NH Moiety Is Not Required for Anion Binding to Amides in Aqueous Solution. *Langmuir* **2015**, *31*, 3459–3464.

[22] Thormann, E. On understanding of the Hofmeister effect: how addition of salt alters the stability of temperature responsive polymers in aqueous solutions. *RSC Adv.* **2012**, *2*, 8297–8305.

[23] Hoare, T.; Pelton, R. Impact of microgel morphology on functionalized microgel-drug interactions. *Langmuir* **2008**, *24*, 1005–1012.

[24] López-León, T.; Santander-Ortega, M. J.; Ortega-Vinuesa, J. L.; Bastos-González, D. Hofmeister effects in colloidal systems: influence of the surface nature. *J. Phys. Chem. C* **2008**, *112*, 16060–16069.

[25] López-León, T.; López-López, J. M.; Odriozola, G.; Bastos-González, D.; Ortega-Vinuesa, J. L. Ion-induced reversibility in the aggregation of hydrophobic colloids. *Soft Matter* **2010**, *6*, 1114–1116.

[26] Pérez-Fuentes, L.; Drummond, C.; Faraudo, J.; Bastos-González, D. Anions make the difference: insights from the interaction of big cations and anions with poly (N-isopropylacrylamide) chains and microgels. *Soft Matter* **2015**, *11*, 5077–5086.

7 Films of allergenic proteins: characterization and modelling

7.1 Background

Proteins are macromolecules that tend to accumulate at interfaces [1]. Protein adsorption has an important interest in many research areas, such as drug delivery [2], disease detection [3, 4] or enhancing [5, 6] or avoiding [7, 8] protein adsorption in biomedical implant development. In spite of the recent progress in this area, protein adsorption is a complicated phenomenon to understand. A great variety of factors dominate the adsorption process: the chemistry, the surface charge and the topography of the material surface, as well as, protein orientation, molecule rearrangements and conformational changes caused by the medium conditions, among others [9, 10].

The main driving force in many protein adsorption processes is the entropic force, which contributes to a decrease of the Gibbs free energy of the system, especially for hydrophobic surfaces [11]. Other important contributions in the protein adsorption are perturbations in the protein structure or electrostatic interactions. Overall, the hydrophobic interactions between the protein residues and the sorbent are much more dominant than the electrostatic interactions [12]. Proteins tend to maximize their area in contact with the surface, since a gain in free energy is produced [10].

In this chapter, we have studied the adsorption process of three proteins. We have chosen well-known proteins of biotechnological interest, as β-casein and β-lactoglobulin, which are the major allergenic proteins of the cow's milk, especially in children [13, 14]. Additionally, we have used in our experiments, Bovine Serum Albumin (BSA) that has been extensively studied in the bibliography [15–18]. The structure of each protein is shown in Figure 7.1.

β-lactoglobulin is the main component of the whey [20] and it is a globular and well-structured protein, like BSA [21]. In contrast, β-casein is a disordered and structureless protein. Each kind of protein adopts a particular arrangement in contact with a surface. For instance, globular proteins, as BSA or β-lactoglobulin,

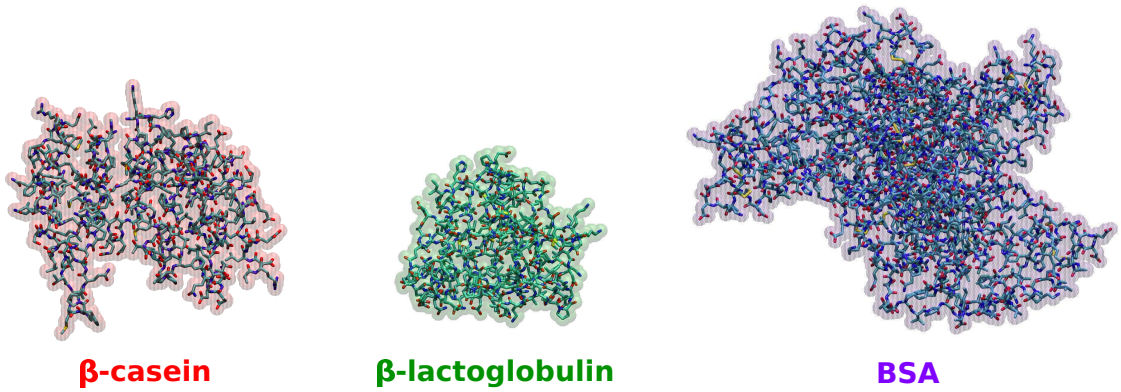

Figure 7.1: Protein 3D structures for β-casein, β-lactoglobulin and BSA. Images made with VMD [19].

keep their compact structure when are adsorbed onto a surface, although they flatten slightly [20, 21]. On the other hand, proteins like β-casein are flexible and have a random coil conformation in solution. β-casein adopts a more compact conformation when is in contact with a surface. The majority of their residues stay close to the sorbent, but the other part is extended to the water. Once adsorbed, β-casein remains flexible and structureless onto the substrate [12, 21].

Apart from the interest in the protein arrangement onto surfaces, the protein adsorption is a good way to investigate the particular characteristics of proteins. Proteins are very small molecules for a direct characterization by experimental techniques, which normally work at the colloidal size range. A common way for the protein study is its physical adsorption onto colloidal particles. This allows to obtain relevant information about the protein properties by a physico-chemical characterization of the complexes.

In this chapter, we have studied the proteins mentioned when are adsorbed onto hydrophobic substrates. In addition, we have investigated the electrostatic charge of the proteins and how is affected by the medium conditions.

7.2 Results from computer simulations

7.2.1 Crystallographic structures and proteins in solution

In this section, we present the main characteristics of the proteins by MD simulations from their 3D structures. The information obtained will be useful to analyze the experimental results in the next sections.

The proteins chosen have been: β-casein, β-lactoglobulin and BSA, as we mentioned above. Both, β-lactoglobulin and BSA are globular and well-structured

proteins, whereas β-casein is a disordered and more flexible protein [20–23]. Therefore, in the simulation part, we have used the crystallographic structures of the globular proteins obtained by X-ray diffraction [18, 24] from Protein Data Bank [25]. In contrast, for β-casein, we have employed a 3D model generated from well-known amino acids sequences, since the crystal structure is not available [26]. The 3D structures for the three proteins are shown in Figure 7.1.

In Figure 7.2, we can see the electrostatic charge of an individual protein as a function of pH obtained by a computational calculation (PropKa [27]). The β-casein and β-lactoglobulin have similar charges because of they are composed by a similar number of amino acids (see Table 7.2). In contrast, the BSA is much bigger than the other two, and this is reflected in its electrostatic charge, mostly at extreme pHs. Each amino acid has an electrostatic charge of -1, 0 or +1e depending on its protonation state, thus the total charge of one protein is the sum of the charges of all its amino acids. Additionally, the isoelectric points (pI) of the proteins are summarized in Table 7.1. By comparing the theoretical and the experimental pI [16, 28, 29], we note that they are very similar and between 5 and 6 for the three proteins.

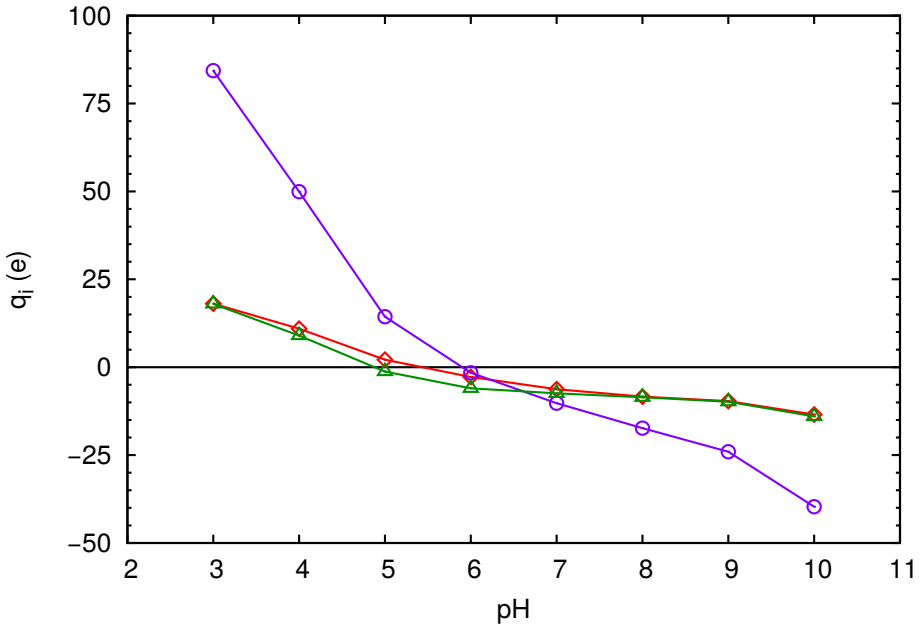

Figure 7.2: Partial charges (in units of electronic charge) for a protein molecule: BSA (○), β-lactoglobulin (△) and β-casein (◇) as a function of pH. The electrostatic charge of the proteins (β-casein, BSA and β-lactoglobulin) has been calculated from the 3D structures with PropKa [27].

It is important to highlight that the properties of the proteins are intrinsically linked to the environmental conditions. The crystallographic structures are ob-

Protein	pI (experimental)	pI (theoretical)
β-casein	4.83-5.07	5.36
BSA	4.7	5.85
β-lactoglobulin	5.13	4.85

Table 7.1: Experimental and theoretical isoelectric point (pI) of the proteins studied [16, 28, 29].

tained at very low temperature, therefore the characteristics of the proteins can vary with respect to a more natural medium as aqueous solution at neutral pH and room temperature. The same occurs for the model generated of β-casein, whose structure can be far from the equilibrated structure under these conditions. For this reason, we have performed a MD simulation for each protein at neutral pH and 25ºC during 4 ns. After that, we have used two tools to analyze structural changes of the studied proteins. On the one hand, the root mean squared deviation (RMSD) is the average distance between the heavy atoms belonging to two different aligned states of a biomolecule. It is a measurement about how much the atoms are displaced from the original structure. On the other hand, we have calculated the solvent-accessible surface area (SASA) in the initial state and the final state (equilibrated structure). SASA is the surface area of a biomolecule that is accessible to a solvent. In addition, from the SASA data, we have estimated the radius of gyration (R_g) in the equilibrated state. These parameters, together with the number of amino acids of each protein, are shown in Table 7.2.

Protein	Number of amino acids	RMSD (nm)	$SASA_{i-f}$ (nm^2)	R_g (nm)
β-casein	195	0.99	118–124	3.1
β-lactoglobulin	162	0.27	87–96	2.8
BSA	582	0.37	284–317	5.0

Table 7.2: Number of amino acids; RMSD between the initial state (crystallographic structure or 3D model for β-casein) and the final state (equilibrated structure after 4 ns of MD simulation in water at neutral pH and 25ºC); SASA in both states; and radius of gyration (R_g) in the final state for the three proteins.

On one hand, the solvent-accessible area increases for the equilibrated structure of the three proteins, thus the proteins show more area accessible to water at 25ºC with respect to the crystal structure. On the other hand, the RMSD values show an important difference between the globular proteins and β-casein. As we have mentioned, this data is related with the conformational changes experimented

by the proteins. For BSA and β-lactoglobulin, we obtain low values of RMSD, indicating that the 3D protein structure is very similar between the initial and final state. However, according to the RMSD value obtained for β-casein, it seems that the amino acids are very mobile, as we expected for a flexible protein. Actually, between 0.5 and 1.5 ns of MD simulation, this protein explores a configuration with a RMSD of 0.66 nm, then the value of 0.99 is reached from 2 ns to 4 ns (at the end of the simulation).

In the light of these results, we have studied how the properties of β-casein change when it is adsorbed onto a planar surface.

7.2.2 Protein adsorption: β-casein

Three different situations were explored: protein adsorption onto neutral and charged surfaces; pH change on an adsorbed protein and multiple adsorption. For the adsorption processes, the most hydrophobic part of the protein (evaluated by OPM [30]) was oriented to the surface to enhance the protein interaction with hydrophobic surfaces. During the MD simulation we could observed that the proteins were quickly adsorbed onto the surface.

The force field employed for the hydrophobic surface was based on a generic model developed previously [31]. The hydrophobic nature of the surface is determined by a contact angle of 140º with a water droplet on the surface (measured in MD simulations [31, 32]). The surface was made of 1600 atoms arranged in four equal layers of 400 atoms each one (67.48 Å $\times$ 67.48 Å). The layers were aligned one above another one forming a primitive cubic structure. The atoms of the surface were maintained fixed during the whole simulation, as in previous studies [31, 33]. The Lennard–Jones parameters of the spheres are σ=3.374 Å and ϵ=0.164 kcal/mol. For the negatively charged surface, the total electrostatic charge was of -10 μC/cm^2 (0.62 e/nm^2), homogeneously distributed over all atoms.

At first place, from the equilibrated structure, one molecule of β-casein was adsorbed onto a hydrophobic neutral surface and a hydrophobic surface with negative charge (see Figure 7.3). We can observe that the most hydrophobic residues (white spheres) are in contact with the surface. In addition, in Figure 7.4, we represent the RMSD as a function of the elapsed time between the protein in solution (0 ns) and the protein adsorbed onto the surface (4 ns). We can observe that there is no difference between the adsorption on a neutral or charged hydrophobic surface. The SASA results indicate that the solvent-accessible area diminish slightly in both cases, since the protein part adsorbed loses its contact with the solvent (Figure not shown). Therefore, in both cases, the orientation and structure of the protein is essentially the same due to the protein-surface interaction is driven by hydrophobic forces. Only few amino acids are adsorbed or desadsorbed from the charged surface depending on the own charge of the amino acids.

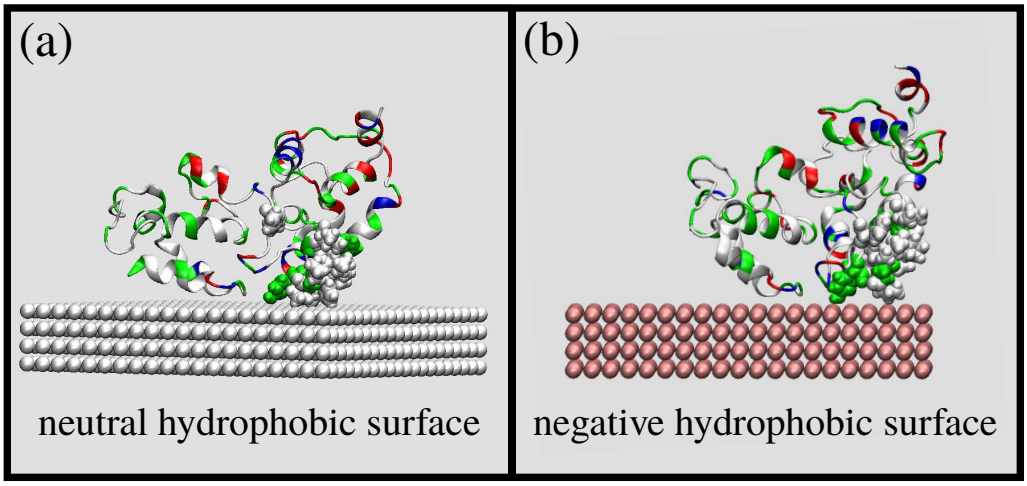

Figure 7.3: Representative snapshots of the adsorption of a β-casein molecule onto a neutral hydrophobic surface (a) and a negative hydrophobic surface (b). The protein residues are colored depending on their nature: hydrophobic (white), hydrophilic (green), positively charged (blue) and negatively charged (red). The most hydrophobic part of the protein is represented as van der Waals spheres.

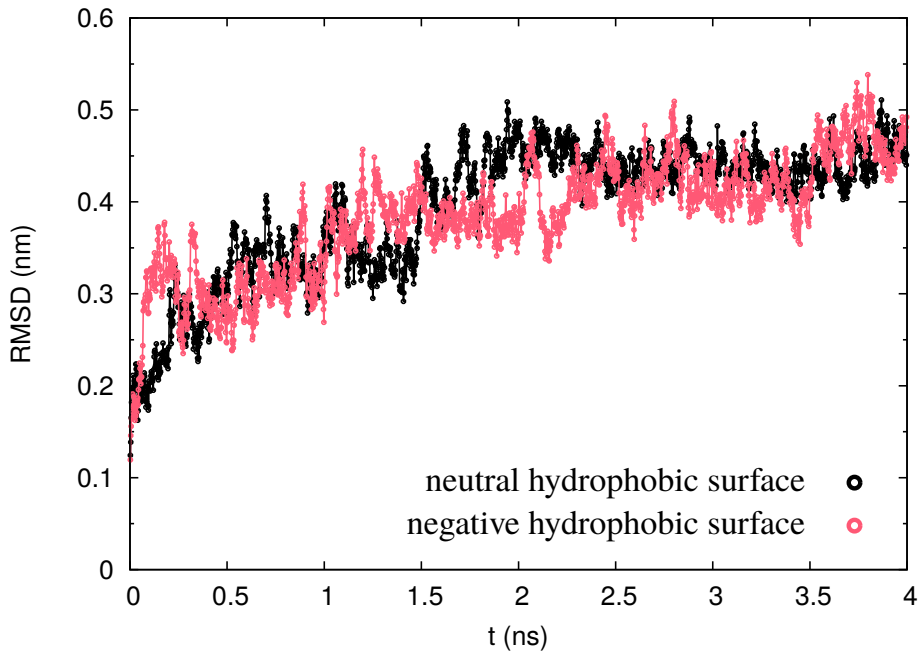

Figure 7.4: Root mean squared deviation (RMSD) between the structures of β-casein in solution and the protein adsorbed onto neutral hydrophobic surface (●) and negative hydrophobic surface (●).

Another experience was performed in order to inquire into the structural changes caused by changing the pH of the medium, as it is usual in experiments with proteins. Once the β-casein protein was adsorbed onto the negative surface, the pH was changed from 7 to 4. This replacement affects to 14 amino acids in each molecule. The total charge of one molecule passes from –6e to +8e, some of the protonated residues are marked in purple in Figure 7.5. In addition, this change in pH affects to the conformational structure of the protein, as is shown in Figure 7.6. We can see that the protein increases the area in contact with the adsorbent due to the electrostatic interaction with the surface becomes favorable.

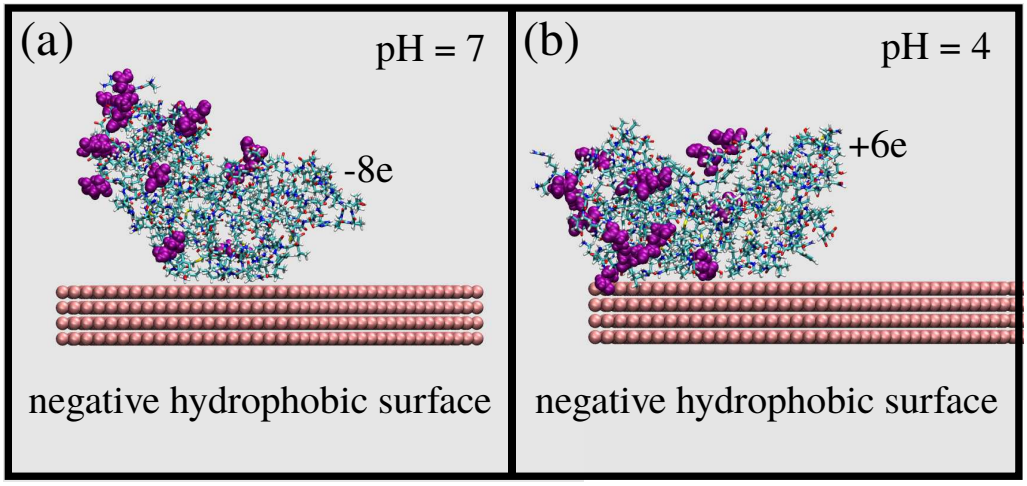

Figure 7.5: Representative snapshots of the configuration of a β-casein molecule adsorbed onto a negative hydrophobic surface at pH 7 (a) and pH 4 (b). The protonated amino acids are represented as purple van der Waals spheres. The total charge of the molecule passes from –6e to +8e.

In Figure 7.6, we represent the RMSD experimented by the protein due to the pH replacement from 7 to 4. As we can observe in the figure, the change in the average separation among both structures when the pH is changed is around 0.5 nm. In contrast, no significant changes were observed in SASA results (Figure not shown).

Finally, a progressive adsorption of 1, 2 and 3 protein molecules was carried out to study the final arrangement of a film of proteins onto a planar surface. This adsorption process was performed onto the hydrophobic surface with negative charge and at neutral pH, as in Figure 7.3. After one protein was added, the system was allowed to equilibrated during 4 ns. When the three β-caseins were adsorbed, the simulation were performed for 8 ns. The total simulation time was of 16 ns. A Representative snapshot of the final configuration is shown in Figure 7.7 (two views), the most hydrophobic residues in the protein film are indicated as van der Waals spheres.

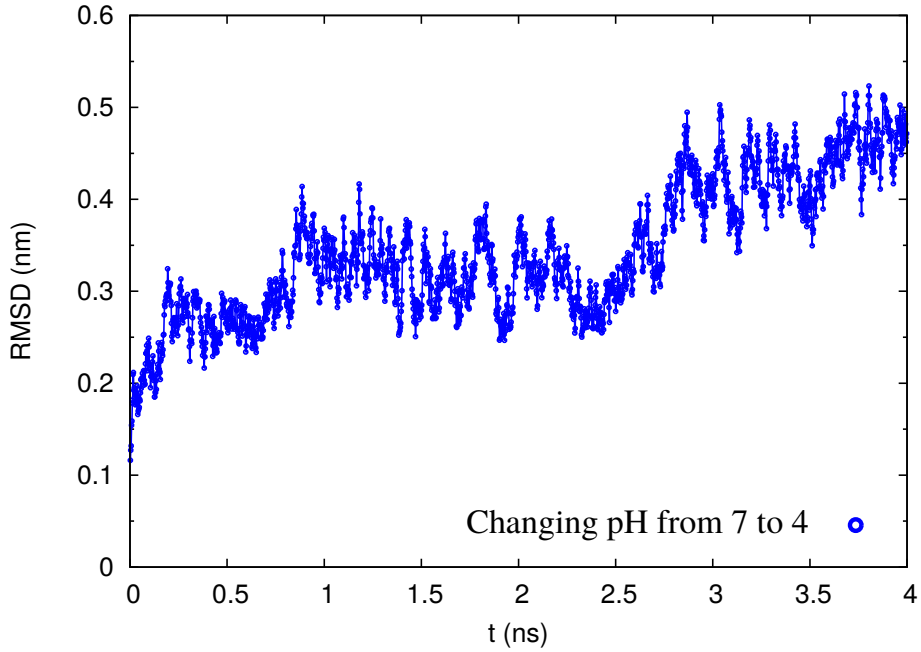

Figure 7.6: Root mean squared deviation (RMSD) of the β-casein structure adsorbed onto neutral hydrophobic surface changing the pH from 7 to 4.

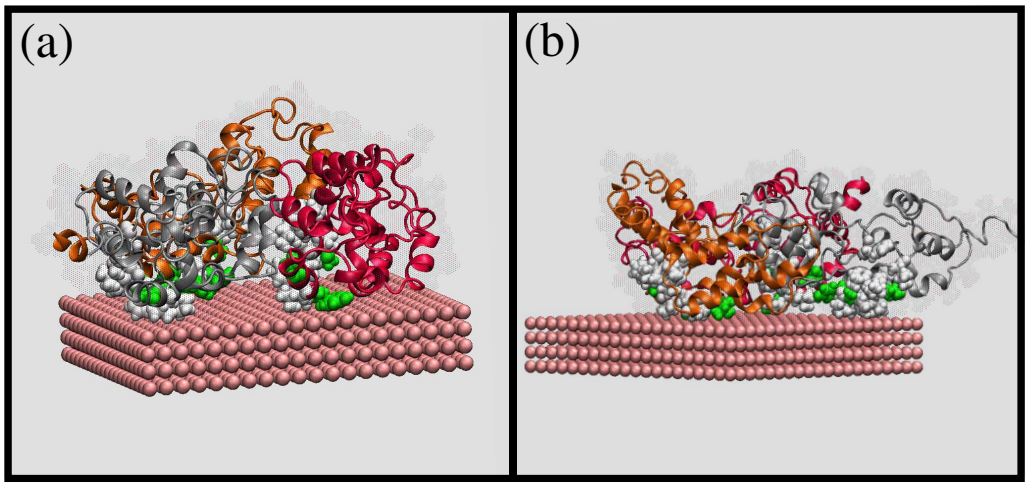

Figure 7.7: Representative snapshots of a β-casein film formed by 3 molecules onto a hydrophobic and negative surface (adsorption at neutral pH) from two views (a) and (b). The most hydrophobic residues of the protein film are marked as van der Waals spheres.

The thickness of the layer formed was calculated in every step from the MD simulations using "density profile tool" of VMD [34]. This tool computes 1-D projections of various atomic densities. We calculated the atomic density, over the equilibrated configurations, of the heavy atoms (carbon atoms of the proteins) in function of the z axis (vertical direction to the surface). These results provide us information about the thickness of a monolayer of β-casein and the variation of the thickness with the elapsed time. As we can see in Figure 7.8, at first (1 molecule) the thickness is about 3.6 nm. However, as the molecules are added to the simulation and the time elapses, the protein layer is reorganized and the thickness decreases. The final state of the simulation ($\sim$2.9 nm) tends to the typical thickness of a β-casein monolayer (2–3 nm) [12].

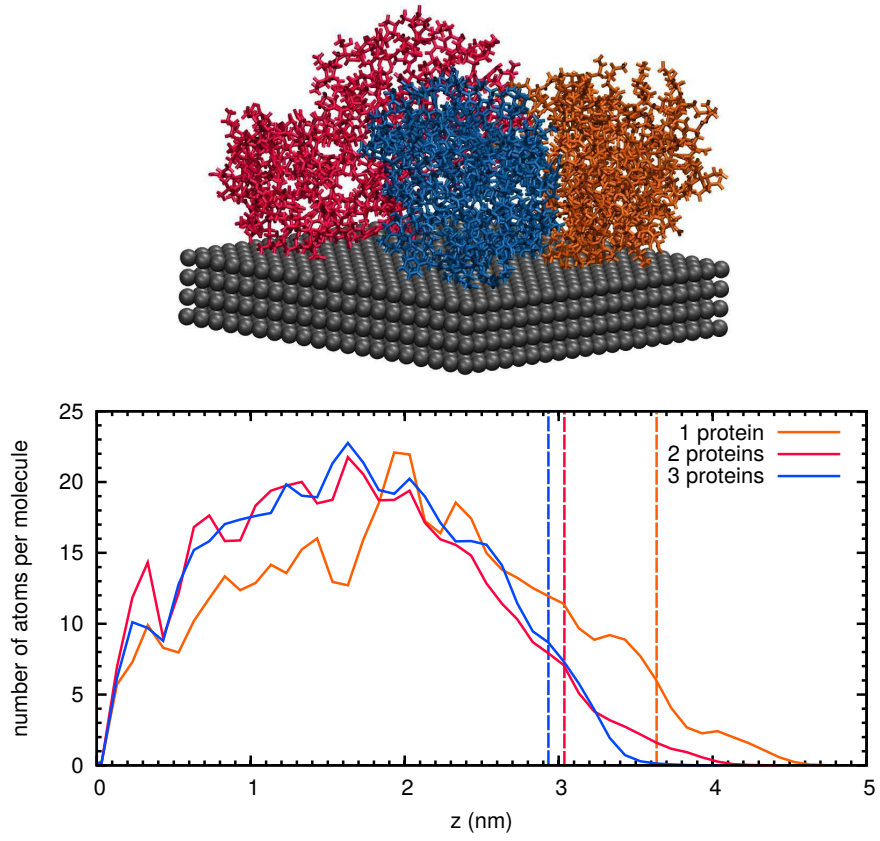

Figure 7.8: MD simulation results for the density of carbon atoms of adsorbed β-caseins (number of atoms per molecule) in the vertical direction (z) to the surface. The thickness of the protein layer decreases as the protein molecules are reorganized onto the surface. The final value ($\sim$2.9 nm) agrees with the typical thickness for a β-casein monolayer (2–3 nm).

7.3 Protein adsorption onto flat surfaces: QCM results

7.3.1 Direct adsorption

Protein adsorption kinetic has been studied by Quartz Crystal Microbalance (QCM). This novel tool allows us to obtain physical information about nanofilms adsorbed onto planar substrates. Properties like the amount of adsorbed mass and the viscoelasticity are measured as the protein molecules are deposited onto the surface in real time. As described in the experimental section 2.8.2 of Materials and Methods, a protein solution of 10^{-3} g/cm^3 was injected over a polystyrene (PS) hydrophobic surface. The PS surface is negatively charged at neutral pH [35]. The different proteins were adsorbed at pH values close but above the pI to maximize protein adsorption (by decreasing the intermolecular electrostatic repulsion) yet avoiding protein aggregation in solution. As can be observed in Figure 7.9, rapid variations in frequency (f) and dissipation (D) were observed upon protein injection. Some qualitative differences can be established between the adsorption of the globular BSA and β-lactoglobulin, and the more disordered β-casein. In the first case, f and D acquire their steady-state values within few minutes after protein injection. On the contrary, an overshoot in f and D before reaching the equilibrium value was commonly observed for the case of β-casein adsorption. This overshoot can be identified with protein reorganization after adsorption. The experimentally observed rearrangement of the β-casein is in concordance with the simulation results obtained in the previous section (7.2.2). In Figure 7.8 we can see the time evolution of the thickness of a β-casein film by MD simulations, which is stabilized around $\sim$ 2.9 nm (typical thickness of a β-casein monolayer, 2–3 nm [12]).

On one hand, the amount of BSA or β-lactoglobulin on the quartz crystal remained unchanged after rinsing few times the protein coated quartz crystals. However, we observed a substantial reduction on the adsorbed mass of β-casein after several rinsing cycles; only the protein molecules strongly attached to the surface, remains adsorbed.

The areal mass adsorbed has been calculated from the changes in frequency by the Sauerbrey equation 2.8. This equation is strictly valid only when the film is homogeneously distributed and rigid. These protein films seem to follow this criteria. Small values of ΔD_n were measured upon protein adsorption and neutral buffer rinsing for the 3 proteins. This fact, together with the low dispersion in $\Delta f_n/n$ for the different harmonics, validates the analysis of the adsorption data using Sauerbrey equation (eq. 2.8). Table 7.3 shows the adsorbed mass per unit area of the adsorbed protein films and their thickness after adsorption and subsequent rinsing. A value of 1 g/cm^3 has been used for the density of the film, a

reasonable value for this kind of systems [36].

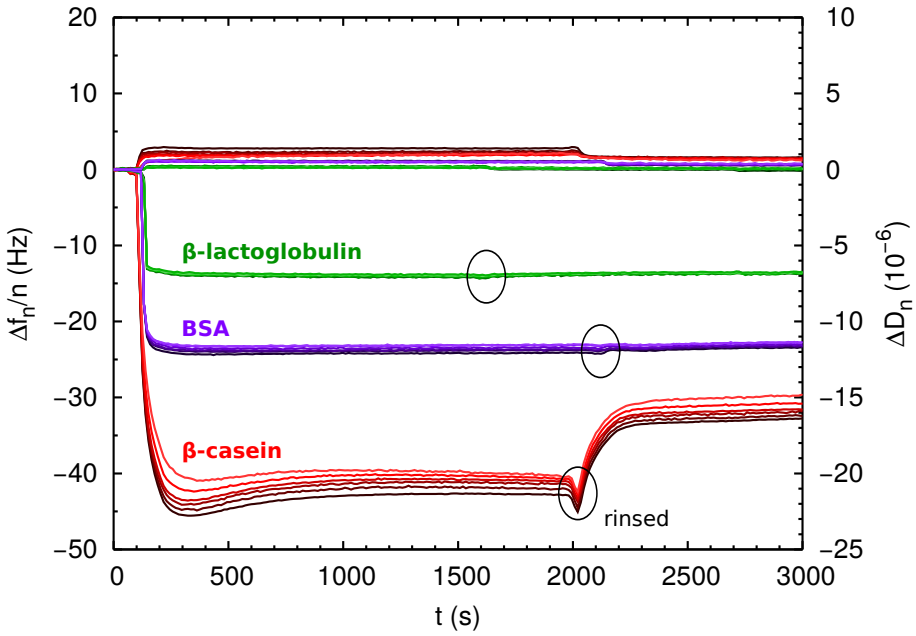

Figure 7.9: Changes in frequency (negative part) and energy dissipation (positive part) caused by the protein adsorption onto PS hydrophobic surfaces. The overtones (n=3–13) are represented in different tonalities from dark to pale. Rapid variations in f were observed upon protein injection. The small values in dissipation ($\Delta D_n \approx 0$) and low dispersion in $\Delta f_n/n$, indicate rigid and homogeneously distributed layers. An overshoot in the frequency data is observed for the β-casein adsorption few seconds upon the injection of the solution. The area marked indicates the rinsed with protein-free buffer solution. For the globular proteins, no protein desorption was observed (constant values of Δf and ΔD). In contrast, a significant increase in f indicates desorption of β-casein molecules.

Protein	Dimensions (nm^3)	Areal mass (mg/m^2)	Thickness (nm)
BSA	$14 \times 4 \times 4$	3.8 ± 0.4	3.8 ± 0.4
β-lactoglobulin	$3.6 \times 3.6 \times 3.6$	2.1 ± 0.2	2.1 ± 0.2
β-casein	–*	6.1 ± 0.7	6.1 ± 0.7

Table 7.3: Dimensions of the proteins studied [9], as well as, the areal mass and the thickness of the protein film adsorbed onto a PS hydrophobic substrate. The areal mass and the thickness of the film have been determined by the Sauerbrey equation (eq. 2.8), using the overtones n=3–13. Assuming an homogeneous film and full coverage of the substrate and $\rho_f = 1$ g/cm^3. The data obtained was the average of four different experiments. *The size of the β-casein is not well-determined, since is a disordered protein.

The values of adsorption mass obtained, are in good agreement with previous studies for the 3 proteins investigated. The amount of adsorbed protein for globular BSA and β-lactoglobulin suggests a full coverage of the substrate and it indicates the adsorption of a protein monolayer. Similar results have been reported in theoretical and experimental studies for BSA [9, 23, 37] and β-lactoglobulin [9, 38, 39]. On the contrary, the larger mass of β-casein layer measured by us suggests the adsorption of a protein multilayer. A larger scatter in reported adsorption of this protein can be found in the bibliography. Earlier β-casein QCM-D studies are in agreement with our results [40, 41]. In contrast, previous experimental works based on depletion [12, 42] or ellipsometry [43] reported values of 2-3 mg/m^2 for a full-coverage monolayer of β-casein [12, 23, 38]. In addition, the mass measured by QCM includes the water associated with the protein film and is larger than the net amount of adsorbed protein. The apparent difference between the net mass of adsorbed protein and coating layer can be detected by other methods. For instance, Brooksbank and coworkers [42] reported a thickness of the adsorbed β-casein layer (measured by dynamic light scattering) incompatible with the measured adsorbed mass of protein if a solvent-free protein layer was considered.

In our case, the thickness of the protein films was measured in air with the AFM device (Table 7.4). The values obtained were similar to those with the QCM technique. Therefore, the usage of the Sauerbrey equation provides us a good estimation of the adsorbed mass for these proteins. The AFM micrographs (not shown) indicate that the proteins are homogeneously distributed over the surface.

Protein	Thickness$_{QCM}$ (nm)	Thickness$_{AFM}$ (nm)
BSA	3.8 ± 0.4	6
β-lactoglobulin	2.1 ± 0.2	1.5
β-casein	6.1 ± 0.7	7–8

Table 7.4: Thickness of the protein film estimated by QCM (liquid) and AFM (air). The values obtained for the three proteins are comparable with both techniques. The Sauerbrey equation (eq. 2.8) is a good method to obtain the thickness for this kind of adsorption. The AFM micrographs (not shown) indicate that the proteins are homogeneously distributed over the surface.

7.3.2 Adsorption isotherms

Adsorption isotherms of the proteins were obtained under the same conditions. Increasing protein concentrations were progressively injected into the QCM cell in contact with the PS surface. The adsorbed areal mass as a function of the protein concentration was calculated by the Sauerbrey equation (eq. 2.8). The values are shown in Figure 7.10.

At first sight, different behaviors can be observed. The adsorption of the globular proteins (BSA and β-lactoglobulin) starts around $2{\cdot}10^{-5}$ mM reaching a constant value of 2 and 1.5 mg/m^2, respectively. After the rinsing with protein-free buffer solutions, there was no desorption indicating that the proteins are well attached to the surface. In contrast, the β-casein protein needs a minimum concentration of $2{\cdot}10^{-4}$ mM to produce a significant deposition onto the surface. In this case, the amount of adsorbed protein increases more and more with the molecule concentration and the plateau is not found. This is in agreement with the multilayer formation, as we saw above. After one rinse cycle, loosely adsorbed protein molecules leave the surface and the adsorbed mass decreases.

The highest protein concentration injected during the isotherm experiments, corresponds with the concentration used in the direct adsorption (10^{-3} g/cm^3). However, we can see in Table 7.3 and Figure 7.10 that the total amount of protein in a direct adsorption is higher than that obtained in a progressive adsorption. The explanation of this phenomenon is as follows. When a protein molecule is adsorbed, this is spread and maximizes the contact area with the surface [10]. However, at high protein concentration, the molecules are cooperatively adsorbed and improve packaging with neighboring proteins. Therefore, the individually deposited proteins cover a higher area and the adsorbed amount is lower than the collectively adsorbed proteins. This phenomenon indicates that the protein-protein interaction plays an important role in the final arrangement of the adsorbed layer.

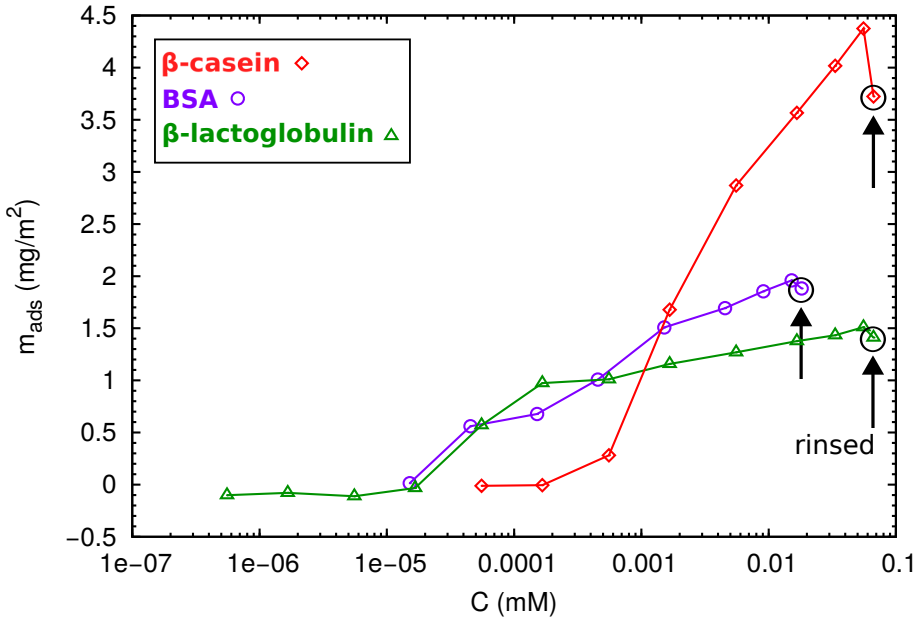

Figure 7.10: Adsorption isotherms of the proteins onto PS hydrophobic surface. The globular proteins (BSA and β-lactoglobulin) reach a constant value at high molecule concentration. While the β-casein adsorbed mass increases progressively with the amount of protein injected. This disordered protein forms a multilayer under the pH adsorption conditions.

7.4 Protein adsorption onto latex microparticles: electrokinetic results

We have performed the physical adsorption of the three proteins over polystyrene (PS) microspheres. We analyze here the main characteristics of the complexes formed. Both, anionic and cationic PS latexes have been used in this experimental work. The conditions of the adsorption process were suitable to ensure a high degree of coverage of the latex surface (see Methods section 2.4). The electrostatic state of the complexes has been studied by electrophoretic mobility (μ_e) measurements as a function of the pH. The results corresponding to the anionic and cationic latex are presented in Figure 7.11 (a) and (b), respectively.

At first sight, we can appreciate that the μ_e of the complexes presents positive values at acid pHs and negative values at alkaline pHs. The μ_e in absolute value of the protein-coated PS particles, always decreases with respect to the mobility of the bare latex. A previous study investigated that this difference is increased at higher protein coverages [44]. Another noteworthy factor is that the pI of the complexes seems to be close to the pI of the proteins in solution (Table 7.1).

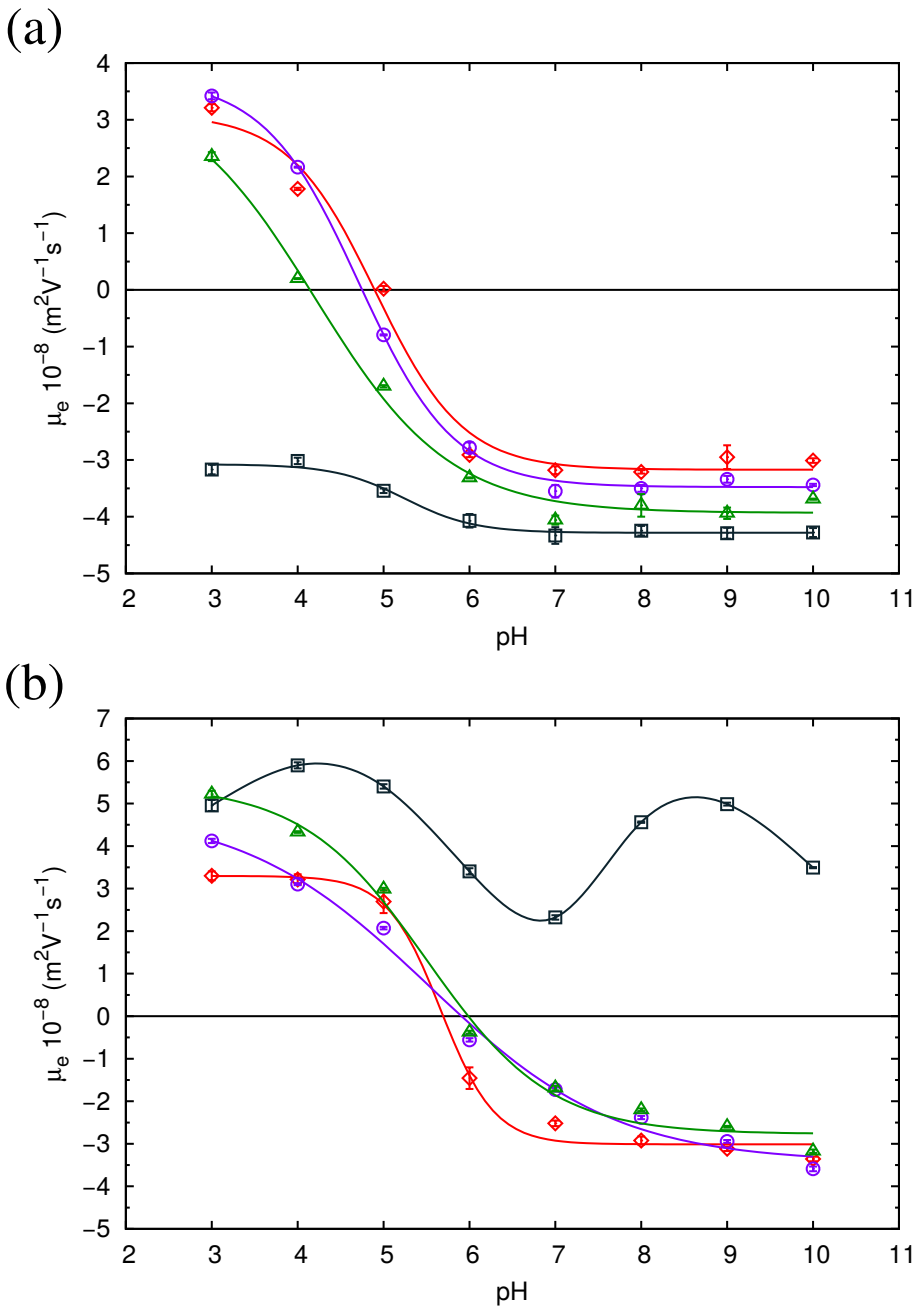

Figure 7.11: Electrophoretic mobility (μ_e) measurements of the colloidal particles as a function of pH for (a) anionic and (b) cationic latexes. For the bare latex (□) and the latex-protein complexes: BSA (○), β-lactoglobulin (△) and β-casein (◇). The solid lines are used for guiding the eye.

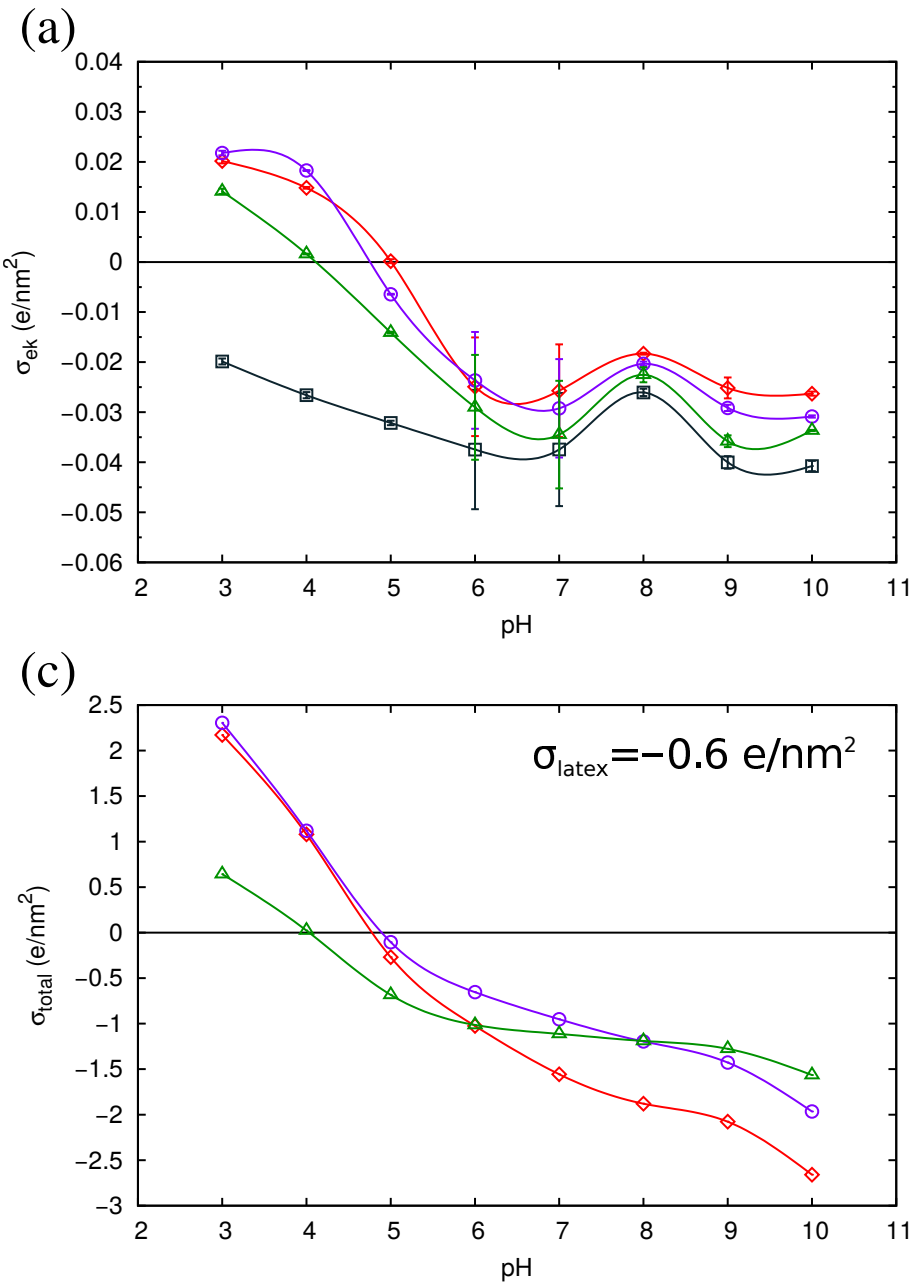

Figure 7.12: Electrokinetic charge (σ_{ek}) of the protein-coated anionic (a) and cationic (b) latexes, obtained by the Grahame equation (eq. 2.4). The total charge of the complexes as sum of the bare latex charge and the protein coverage charge as a function of the pH, are shown in images (c) and (d). The experimental pI of the complexes for the anionic latex (a) matches with the pI expected by the $\longrightarrow$

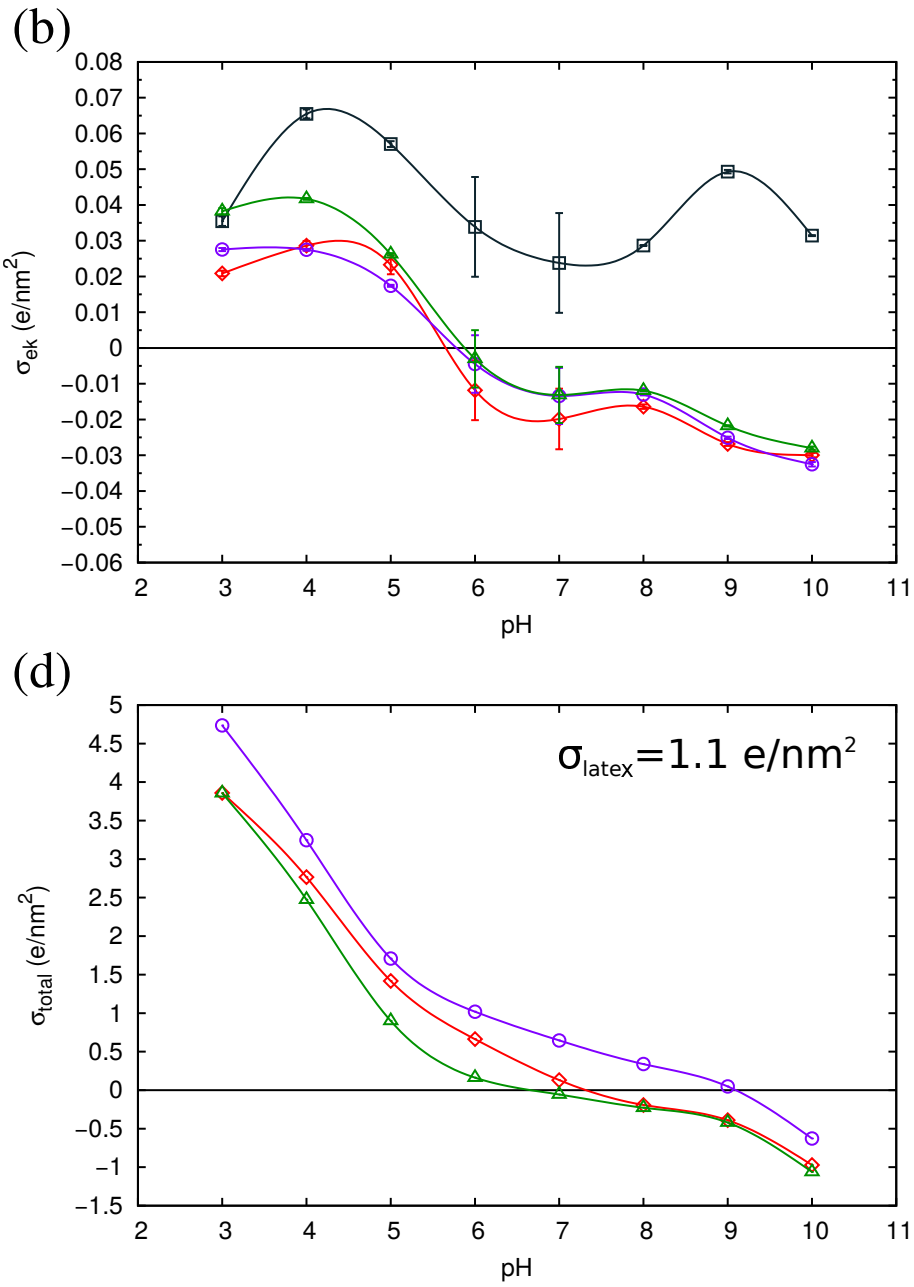

sum of charges (c). However, for the cationic latex, the predicted pI of the complexes (d) is more displaced to alkaline pH with respect to the experimental results (b). The symbols correspond to the bare latex (□) and the latex-protein complexes: BSA (○), β-lactoglobulin (△) and β-casein (◇). The solid lines are used for guiding the eye.

However, the pI of the complex could be displaced by the surface charge of the bare latex. In the case of anionic latex, the pI is displaced to more acid pH. In contrast, with cationic latex the pI values of the complex are more alkaline than the pI of the proteins in solution. Electrokinetic studies [45–47] have demonstrated that at larger amount of protein adsorbed, the pI values of the complex are closer to the pI of the protein molecules.

It has to be taken into consideration that the kind of electrolyte in solution can affect to the μ_e values of the colloids. In our experiments, each buffer solution was prepared with different salts and ion concentrations (ionic strengths lower than 2 mM). For this reason, we have calculated the electrokinetic charge (σ_{ek}) of the complexes to estimate the electrostatic charge responsible for the electrophoretic motion. The results are included in Figure 7.12 (a) and (b) for the anionic and cationic latex, respectively. We can observe that the shapes and the general behavior of the curves follow the same tendency that the μ_e results (Figure 7.11).

It would be reasonable to expect that the total charge of the complexes will be the sum of the bare latex charge plus the protein coverage charge. In Figure 7.12 (c) and (d) we present the estimated total charge of the complexes as a function of pH. The value used for the charge of the bare latex was obtained experimentally by titration (see Methods section 2.1.3). While the protein charge was calculated from the individual charge of the proteins (Figure 7.2) and the degree of coverage in each case.

In the case of the anionic latex, the pI values of the complexes are in agreement with those estimated (Figure 7.12 (a) and (c)). In contrast, the estimated pI values for the cationic latex complexes are more displaced to alkaline pHs than the experimental one (Figure 7.12 (b) and (d)). A possible explanation is that the effective charge of the bare latex will be lower due to the ionic conditions. We can see that the electrokinetic charge of the cationic latex is significantly reduced at neutral pH, at the protein adsorption conditions (Figure 7.12 (b)). This oscilation of σ_{ek} with the pH change is caused by the nature of the buffer solution. We tested that the mobility of the latex is almost constant as a function of the pH with other type of buffer solutions.

Furthermore, out of the pI, the values of the total charge are two order of magnitude higher than the electrokinetic charge. We attribute this discrepancy to counterion condensation. This is a strong accumulation of counterions in the vicinity of the charged particles, which is a very common phenomenon for highly charged colloidal suspensions [48–50]. In the next subsection we analyze the counterion condensation for our systems.

7.4.1 Counterion condensation on latex-protein complexes

The colloidal particles treated here have a high surface charge. The anionic latex possesses a surface charge density of –9.6 μC/cm^2 = –0.6 e/nm^2 and the cationic

latex 17.4 μC/cm^2 = 1.1 e/nm^2. In addition, when protein adsorption is produced, the protein molecules can enhance the charge of the final complexes depending on the pH. At alkaline pH, the protein molecules are negatively charged, thus the complex increases its net charge for the anionic latex. The same occurs at acid pH and the cationic latex. Nevertheless, these high surface charges are not reflected in the electrokinetic charges calculated from the μ_e results, the values are very much lower (Figure 7.12). A possible explanation is the ion condensation. In spite of the ionic strength of the buffered solutions is lower than 2 mM, counterions are adsorbed over the colloids. This ion-association contributes to the electrokinetic motion of the microparticles, reducing their effective charges. In order to corroborate this hypothesis, two theoretical models of counterion condensation were applicated to our systems.

The first model was developed by Manning [51]. This reference includes equations of counterion condensation on charged spheres, cylinders and planes. Our experimental microparticles meet the requirements to a planar wall. This model, based on experimental observations, proposes that the charge of a polyelectrolyte system is unvariable once a critical charge load is reached due to counterion condensation. The electrostatic surface free energy is obtained by applying a standard charging procedure of the Poisson-Boltzmann equation. The free energies ascribe any departure, from linear Debye–Hückel electrostatics, to collapse of counterions from the diffuse ion atmosphere onto the surface of the polyelectrolyte. An entropic term is added because of this ion migration. For a charged plane wall, the critical value of the surface charge density becomes:

$$\sigma_{crit} = -\frac{e\kappa \ln(\kappa\lambda_B)}{2\pi z\lambda_B} \tag{7.1}$$

where e is the electronic charge, z the unsigned valence of the counterion, κ is the Debye constant and $\lambda_B = e^2/4\pi\varepsilon_0\varepsilon_r k_B T$ is the Bjerrum length (ε_0 is the vacuum permittivity, ε_r is the dielectric constant of water, k_B is the Boltzmann's constant and T the temperature). For higher surface charge density than this critic value, the effective surface charge density yields:

$$\sigma_{eff} = -\frac{e\kappa \ln(c_0)}{4\pi z\lambda_B} \tag{7.2}$$

where c_0 is the bulk concentration of the counterions. As we have mentioned and we can see in the last equation, the effective charge is independent of the bare surface charge of the particle.

The second model was developed by Hansen and McDonald [52]. This model consider a charged planar surface immersed in a symmetric electrolyte. An explicit relation between the bare surface charge density σ and the effective surface charge density is derived within Poisson–Boltzmann theory. This relation is:

$$\sigma_{eff} = \sigma_{sat}\left[\sqrt{1+(\sigma_{sat}/2\sigma)^2} - \sigma_{sat}/2\sigma\right] \tag{7.3}$$

where σ_{sat} is the saturation charge density:

$$\sigma_{sat} = \frac{e\kappa}{\pi\lambda_B} \tag{7.4}$$

For high surface charge, the counterion condensation strongly reduces the absolute value of the bare charge. In this case the effective value reaches its maximum value σ_{sat}, which is independent of σ.

We have applied these equations to our colloidal systems (bare latex and complexes) immersed in the different buffered solutions depending on the pH (see Methods section 2.1.2). In Figure 7.13 we show the values of the effective charges obtained with both models for the bare anionic (a) and cationic (b) latexes. It is noticeable that the effective charges match pretty good with the electrokinetic charges (from μ_e measurements), especially the proposed model by Hansen and McDonald. Therefore, the counterion condensation seems the responsible for the low surface charges reflected in the experimental results.

Regarding the results for the different latex-protein complexes (Figures 7.14–7.16), the theoretical values are broadly in line with the experimental results. Again, the Hansen and McDonald model seems more suitable than the Manning model. In the case of the protein-coated anionic latex (a), the pI resulting from the theoretical models is in good agreement with the experimental values. However, for the protein-coated cationic latex (b), the calculated pI is very displaced to alkaline pHs, mainly for the BSA complex (Figure 7.16 (b)).

It is important to keep in mind that counterion condensation is not produced in the proximities of the pI of the complexes, since the total charge is very low. Therefore, the σ_{ek} (close to the pI) should be identical to the sum of the charges of the latex-protein complex at this pH. Nevertheless, this point is strongly depending on the latex charge and the protein coverage. Therefore, little variations in these estimated values can produce important changes in the calculated pI, which does not match with the experimental pI. For instance, we do not take into account the possibility of counterions trapped in the contact region between the latex surface and proteins, as other authors suggest [44, 47, 53]. This would result in a considerable reduction in the bare latex charge.

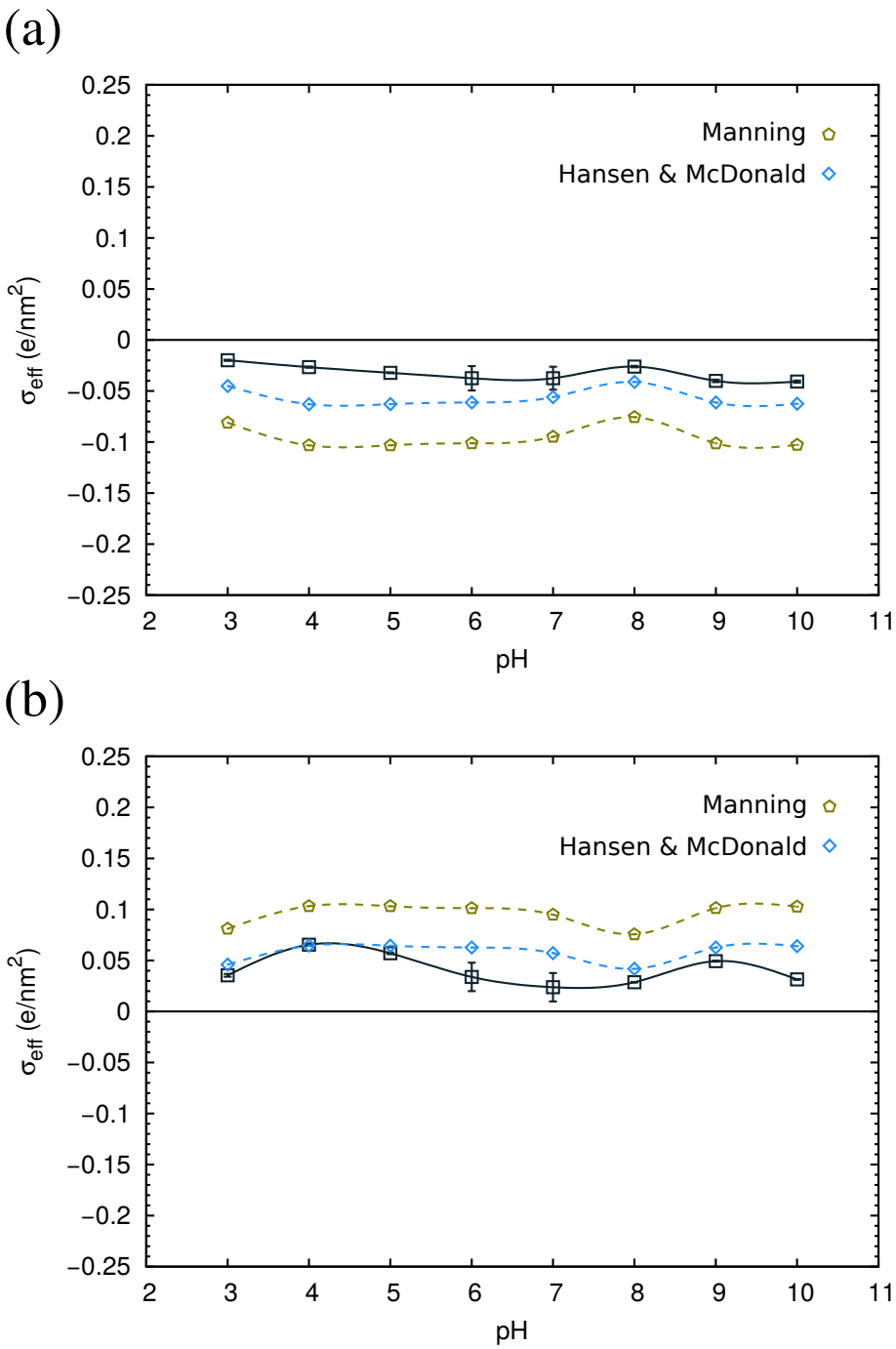

Figure 7.13: Electrokinetic charge (□) of the bare anionic (a) and cationic (b) latexes. The effective charges calculated by the counterion condensation models: Manning (⬠) and Hansen & McDonald (◇) are shown. The lines are used for guiding the eye.

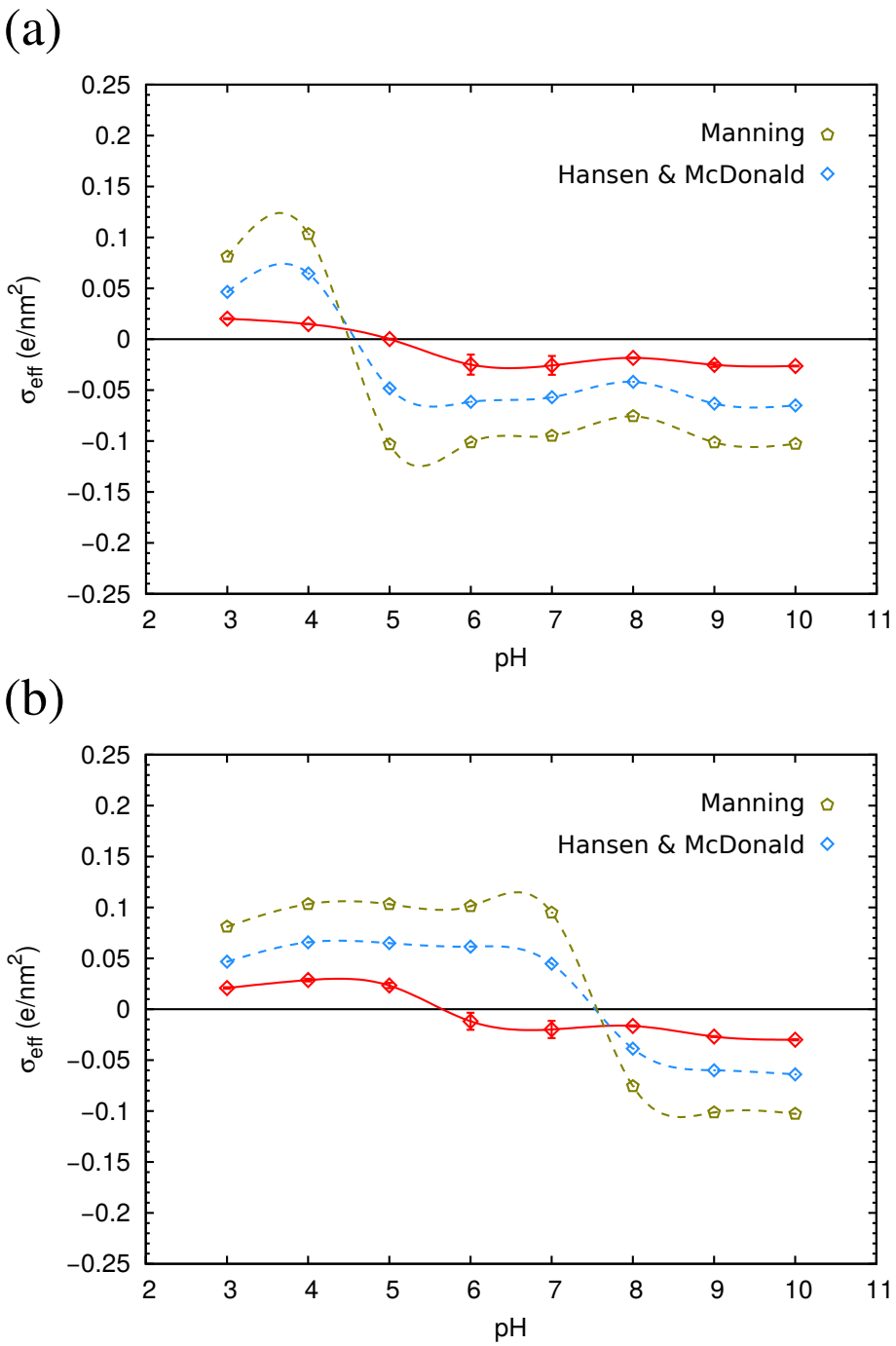

Figure 7.14: Electrokinetic charge (◇) of the β-casein protein-coated anionic (a) and cationic (b) latexes. The effective charges calculated by the counterion condensation models: Manning (⬠) and Hansen & McDonald (◇) are shown. The lines are used for guiding the eye.

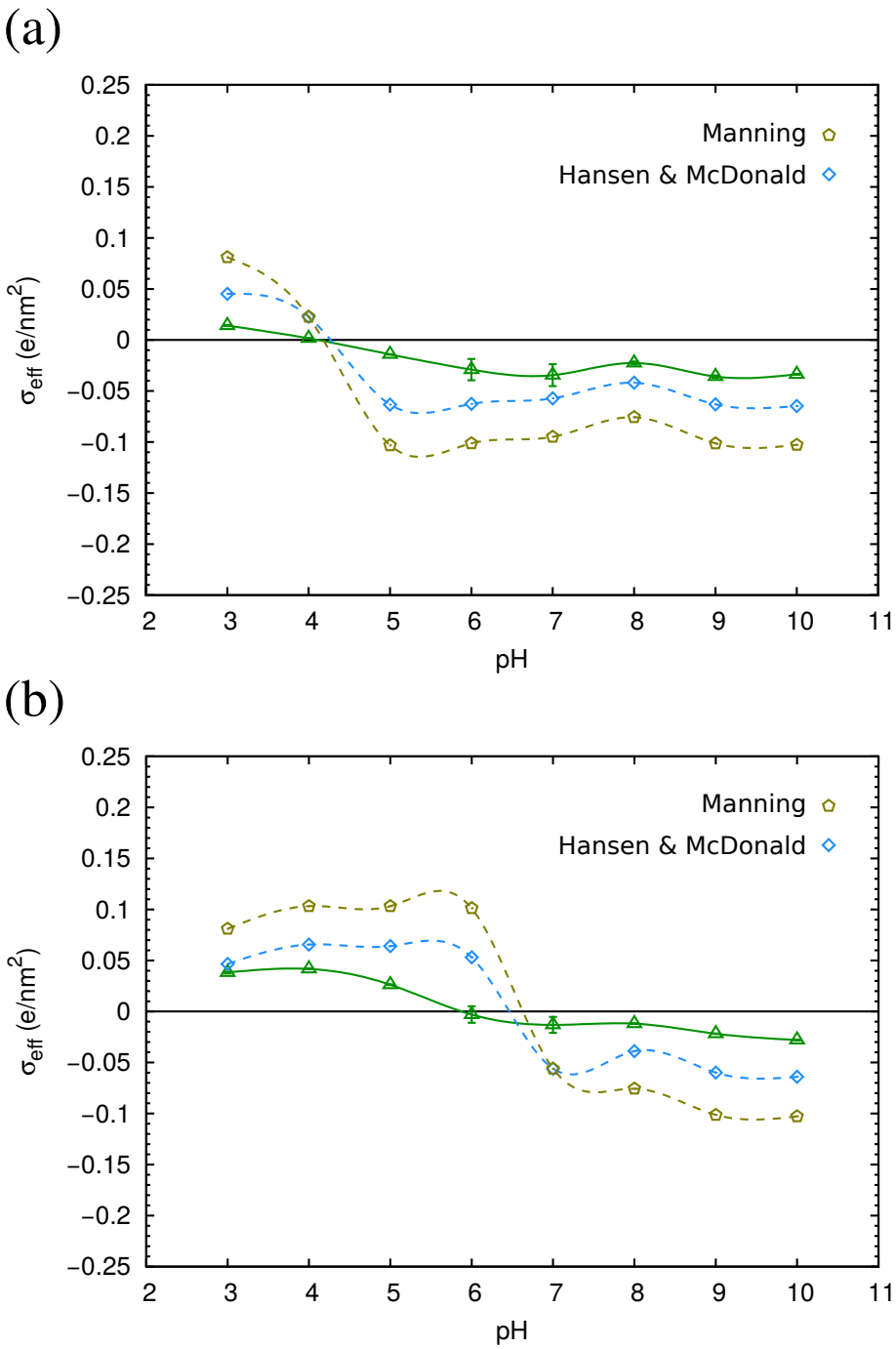

Figure 7.15: Electrokinetic charge (△) of the β-lactoglobulin protein-coated anionic (a) and cationic (b) latexes. The effective charges calculated by the counterion condensation models: Manning (⬠) and Hansen & McDonald (◇) are shown. The lines are used for guiding the eye.

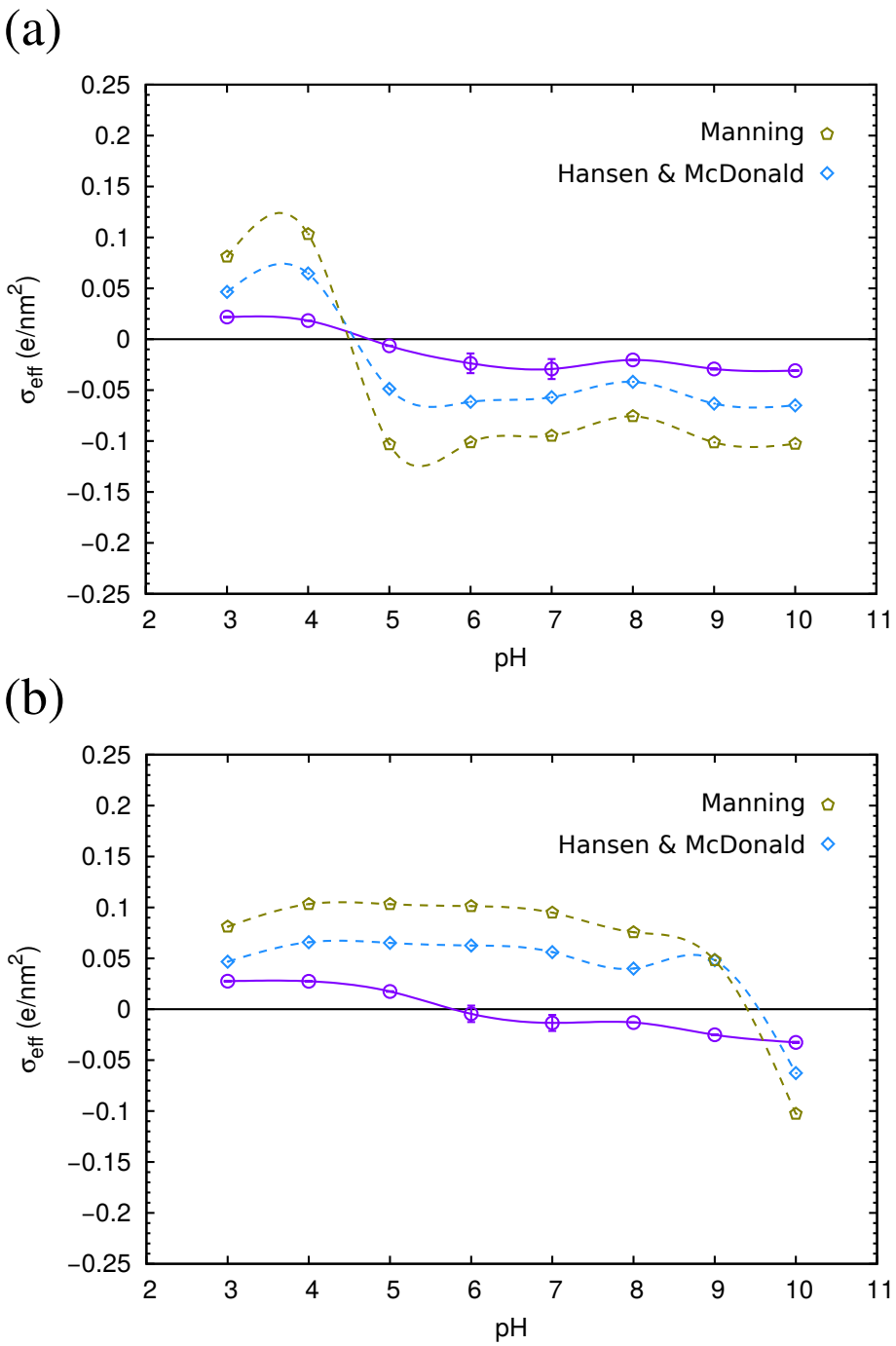

Figure 7.16: Electrokinetic charge (○) of the BSA protein-coated anionic (a) and cationic (b) latexes. The effective charges calculated by the counterion condensation models: Manning (⬠) and Hansen & McDonald (◇) are shown. The lines are used for guiding the eye.

7.5 Conclusions

In this chapter, we have investigated three proteins of different characteristics. The globular proteins: β-lactoglobulin and BSA, and a flexible and disordered protein: β-casein. Adsorption studies of the three proteins have been performed onto either PS flat substrates (negatively charged) and PS latex microspheres (with negative and positive charges). The properties of the protein films have been studied by QCM. These proteins form rigid and homogeneous layers onto the sorbent surface. On one hand, the globular proteins are adsorbed forming a monolayer, while the β-casein molecules are arranged in a multilayer, in concordance with previous studies [9, 23, 37–41]. In the case of β-casein, the loosely protein adsorbed are easily removed by rinse cycles.

In addition, the adsorption kinetic was analyzed for the three proteins. A progressive adsorption results in higher area occupied per molecule. Therefore, the adsorbed mass is lower than for a direct adsorption. In this last case, the adsorbed molecules are better packaged with their neighbors.

Another important difference between the globular proteins and the β-casein is the final state of the film. When the β-casein proteins are deposited onto the surface, these undergo a rearrangement until reaching the final configuration. This phenomenon was not observed for the globular proteins. The β-casein rearrangement has been also confirmed by MD simulations. From this simulation, the thickness obtained for a β-casein monolayer matches with typical experimental values [12, 42, 43].

Protein-coated PS microspheres have been characterized by electrophoretic mobility (μ_e) as a function of pH. From this data, the electrokinetic charge (σ_{ek}) of the complexes has been obtained by the Grahame equation (eq. 2.4). This parameter shows the electrostatic charge responsible for the electrokinetic motion of the particles. In addition, we have calculated the total charge of the complexes from the sum of the bare latex charge and the protein coverage charge. We could see for the protein-coated anionic latex, that the estimated pI values are in good agreement with those experimental values. However, in the case of the cationic latex, the estimated pI of the complexes is displaced to more alkaline pHs with respect to the experimental pI. We attributed this discrepancy to an overestimation of the cationic latex charge under the pH-adsorption conditions.

On the other hand, out of the pI, the σ_{total} is around two order of magnitude higher than the σ_{ek}. It seems that this difference is well explained by counterion condensation. In spite of the buffered solutions used have a low ionic strength (< 2 mM), an ion accumulation over the colloids produces a reduction in their effective charge. This is due to our systems possess high surface charges.

The physico-chemical characterization of the complexes will be very useful in the next chapter, where we will study the interaction of these interfaces with big hydrophobic ions.

References

[1] Norde, W.; Lyklema, J. Why proteins prefer interfaces. *J. Biomater. Sci.* **1991**, *2*, 183–202.

[2] Monopoli, M. P.; Åberg, C.; Salvati, A.; Dawson, K. A. Biomolecular coronas provide the biological identity of nanosized materials. *Nature Nanotech.* **2012**, *7*, 779–786.

[3] Wee, K. W.; Kang, G. Y.; Park, J.; Kang, J. Y.; Yoon, D. S.; Park, J. H.; Kim, T. S. Novel electrical detection of label-free disease marker proteins using piezoresistive self-sensing micro-cantilevers. *Biosens. Bioelectron.* **2005**, *20*, 1932–1938.

[4] Vollmer, F.; Arnold, S. Whispering-gallery-mode biosensing: label-free detection down to single molecules. *Nature methods* **2008**, *5*, 591–596.

[5] Cai, K.; Bossert, J.; Jandt, K. D. Does the nanometre scale topography of titanium influence protein adsorption and cell proliferation? *Colloid. Surf. B* **2006**, *49*, 136–144.

[6] Ellingsen, J. E. A study on the mechanism of protein adsorption to TiO 2. *Biomaterials* **1991**, *12*, 593–596.

[7] Pavithra, D.; Doble, M. Biofilm formation, bacterial adhesion and host response on polymeric implants—issues and prevention. *Biomed. Mater.* **2008**, *3*, 034003.

[8] Hucknall, A.; Rangarajan, S.; Chilkoti, A. In pursuit of zero: polymer brushes that resist the adsorption of proteins. *Adv. Mater.* **2009**, *21*, 2441–2446.

[9] Nakanishi, K.; Sakiyama, T.; Imamura, K. On the adsorption of proteins on solid surfaces, a common but very complicated phenomenon. *J. Biosci. Bioeng.* **2001**, *91*, 233–244.

[10] Rabe, M.; Verdes, D.; Seeger, S. Understanding protein adsorption phenomena at solid surfaces. *Adv. Colloid Interface Sci.* **2011**, *162*, 87–106.

[11] Haynes, C. A.; Norde, W. Structures and stabilities of adsorbed proteins. *J. Colloid Interface Sci.* **1995**, *169*, 313–328.

[12] Mackie, A. R.; Mingins, J.; North, A. N. Characterisation of adsorbed layers of a disordered coil protein on polystyrene latex. *J. Chem. Soc., Faraday Trans.* **1991**, *87*, 3043–3049.

[13] Docena, G.; Fernandez, R.; Chirdo, F.; Fossati, C. Identification of casein as the major allergenic and antigenic protein of cow's milk. *Allergy* **1996**, *51*, 412–416.

[14] Goldman, A.; Anderson, D.; Sellers, W.; Saperstein, S.; Kniker, W.; Halpern, S. Milk allergy I. Oral challenge with milk and isolated milk proteins in allergic children. *Pediatrics* **1963**, *32*, 425–443.

[15] Wright, A.; Thompson, M. Hydrodynamic structure of bovine serum albumin determined by transient electric birefringence. *Biophys. J.* **1975**, *15*, 137.

[16] Demanèche, S.; Chapel, J.-P.; Monrozier, L. J.; Quiquampoix, H. Dissimilar pH-dependent adsorption features of bovine serum albumin and α-chymotrypsin on mica probed by AFM. *Colloid Surf. B* **2009**, *70*, 226–231.

[17] Barbosa, L. R.; Ortore, M. G.; Spinozzi, F.; Mariani, P.; Bernstorff, S.; Itri, R. The importance of protein-protein interactions on the pH-induced conformational changes of bovine serum albumin: a small-angle X-ray scattering study. *Biophys. J.* **2010**, *98*, 147–157.

[18] Bujacz, A.; Zielinski, K.; Sekula, B. Structural studies of bovine, equine, and leporine serum albumin complexes with naproxen. *Proteins* **2014**, *82*, 2199–2208.

[19] Humphrey, W.; Dalke, A.; Schulten, K. VMD: visual molecular dynamics. *J. Mol. Graphics* **1996**, *14*, 33–38.

[20] Marinova, K. G.; Basheva, E. S.; Nenova, B.; Temelska, M.; Mirarefi, A. Y.; Campbell, B.; Ivanov, I. B. Physico-chemical factors controlling the foamability and foam stability of milk proteins: Sodium caseinate and whey protein concentrates. *Food Hydrocolloids* **2009**, *23*, 1864–1876.

[21] Caldwell, K. D.; Li, J.; Li, J.-T.; Dalgleish, D. G. Adsorption behavior of milk proteins on polystyrene latex: a study based on sedimentation field-flow fractionation and dynamic light scattering. *J. Chromatogr.* **1992**, *604*, 63–71.

[22] Maldonado-Valderrama, J.; Terriza, J. H.; Torcello-Gomez, A.; Cabrerizo-Vilchez, M. In vitro digestion of interfacial protein structures. *Soft Matter* **2013**, *9*, 1043–1053.

[23] Graham, D.; Phillips, M. Proteins at liquid interfaces. *J. Colloid Interface Sci.* **1979**, *70*, 403–439.

[24] Loch, J.; Polit, A.; Gorecki, A.; Bonarek, P.; Kurpiewska, K.; Dziedzicka-Wasylewska, M.; Lewiński, K. Two modes of fatty acid binding to bovine β-lactoglobulin—crystallographic and spectroscopic studies. *J. Mol. Recognit.* **2011**, *24*, 341–349.

[25] Protein Data Bank: An Information Portal to Biological Macromolecular Structures., http://www.rcsb.org/, Accessed: 2015-11-27.

[26] Pieper, U.; Webb, B. M.; Dong, G. Q.; Schneidman-Duhovny, D.; Fan, H.; Kim, S. J.; Khuri, N.; Spill, Y. G.; Weinkam, P.; Hammel, M. et al. ModBase, a database of annotated comparative protein structure models and associated resources. *Nucl. Acids Res.* **2014**, *42*, D336–D346.

[27] Li, H.; Robertson, A. D.; Jensen, J. H. Very fast empirical prediction and rationalization of protein pKa values. *Proteins* **2005**, *61*, 704–721.

[28] Pace, C. N.; Vajdos, F.; Fee, L.; Grimsley, G.; Gray, T. How to measure and predict the molar absorption coefficient of a protein. *Protein Sci.* **1995**, *4*, 2411.

[29] Farrell, H.; Jimenez-Flores, R.; Bleck, G.; Brown, E.; Butler, J.; Creamer, L.; Hicks, C.; Hollar, C.; Ng-Kwai-Hang, K.; Swaisgood, H. Nomenclature of the proteins of cows' milk—sixth revision. *J. Dairy Sci.* **2004**, *87*, 1641–1674.

[30] Lomize, M. A.; Lomize, A. L.; Pogozheva, I. D.; Mosberg, H. I. OPM: orientations of proteins in membranes database. *Bioinformatics* **2006**, *22*, 623–625.

[31] Huang, D. M.; Cottin-Bizonne, C.; Ybert, C.; Bocquet, L. Aqueous electrolytes near hydrophobic surfaces: Dynamic effects of ion specificity and hydrodynamic slip. *Langmuir* **2008**, *24*, 1442–1450.

[32] Werder, T.; Walther, J. H.; Jaffe, R.; Halicioglu, T.; Koumoutsakos, P. On the water-carbon interaction for use in molecular dynamics simulations of graphite and carbon nanotubes. *J. Phys. Chem. B* **2003**, *107*, 1345–1352.

[33] Calero, C.; Faraudo, J.; Bastos-González, D. Interaction of monovalent ions with hydrophobic and hydrophilic colloids: Charge inversion and ionic specificity. *J. Am. Chem. Soc.* **2011**, *133*, 15025–15035.

[34] Giorgino, T. Computing 1-D atomic densities in macromolecular simulations: the density profile tool for VMD. *Comp. Phys. Comm.* **2014**, *185*, 317–322.

[35] Siretanu, I. Nanostructuration contrôlée de films de polymères., Ph.D. Thesis, Bordeaux 1, 2011.

[36] Reviakine, I.; Johannsmann, D.; Richter, R. P. Hearing what you cannot see and visualizing what you hear: interpreting quartz crystal microbalance data from solvated interfaces. *Anal. Chem.* **2011**, *83*, 8838–8848.

[37] Pandey, L. M.; Pattanayek, S. K.; Delabouglise, D. Properties of adsorbed bovine serum albumin and fibrinogen on self-assembled monolayers. *J. Phys. Chem. C* **2013**, *117*, 6151–6160.

[38] Atkinson, P. J.; Dickinson, E.; Horne, D. S.; Richardson, R. M. Neutron reflectivity of adsorbed β-casein and β-lactoglobulin at the air/water interface. *J. Chem. Soc., Faraday Trans.* **1995**, *91*, 2847–2854.

[39] Lebec, V.; Landoulsi, J.; Boujday, S.; Poleunis, C.; Pradier, C.-M.; Delcorte, A. Probing the orientation of β-lactoglobulin on gold surfaces modified by alkyl thiol self-assembled monolayers. *J. Phys. Chem. C* **2013**, *117*, 11569–11577.

[40] Lee, M.; Park, S. K.; Chung, C.; Kim, H. QCM study of β-casein adsorption on the hydrophobic surface: Effect of ionic strength and cations. *Bull. Korean Chem. Soc.* **2004**, *25*, 1031–1035.

[41] Murray, B. S.; Cros, L. Adsorption of β-lactoglobulin and β-casein to metal surfaces and their removal by a non-ionic surfactant, as monitored via a quartz crystal microbalance. *Colloid Surf. B* **1998**, *10*, 227–241.

[42] Brooksbank, D. V.; Davidson, C. M.; Horne, D. S.; Leaver, J. Influence of electrostatic interactions on β-casein layers adsorbed on polystyrene latices. *J. Chem. Soc., Faraday Trans.* **1993**, *89*, 3419–3425.

[43] Nylander, T.; Wahlgren, N. M. Competitive and sequential adsorption of β-casein and β-lactoglobulin on hydrophobic surfaces and the interfacial structure of β-casein. *J. Colloid Interface Sci.* **1994**, *162*, 151–162.

[44] Martín, A.; Puig, J.; Galisteo, F.; Serra, J.; Hidalgo-Álvarez, R. On some aspects of the adsorption of immunoglobulin-G molecules on polystyrene microspheres. *J. Dispers. Sci. Technol.* **1992**, *13*, 399–416.

[45] Shirahama, H.; Ohno, H.; Suzawa, T. Preparation, characterization, and albumin adsorption of amphoteric polymer latices. *Colloids Surf.* **1991**, *60*, 1–17.

[46] Galisteo-González, F.; Martín-Rodríguez, A.; Hidalgo-Alvarez, R. Adsorption of monoclonal IgG on polystyrene microspheres. *Colloid Polym. Sci.* **1994**, *272*, 352–358.

[47] Delgado, Á. V., *Interfacial electrokinetics and electrophoresis*; CRC Press: 2001; Vol. 106.

[48] Oosawa, F., *Polyelectrolytes*; Dekker, New York: 1971.

[49] Manning, G. S. Limiting laws and counterion condensation in polyelectrolyte solutions. *J. Chem. Phys.* **1969**, *51*, 924–933.

[50] Belloni, L. Ionic condensation and charge renormalization in colloidal suspensions. *Colloid Surf. A* **1998**, *140*, 227–243.

[51] Manning, G. S. Counterion condensation on charged spheres, cylinders, and planes. *J. Phys. Chem. B* **2007**, *111*, 8554–8559.

[52] Hansen, J.-P.; McDonald, I. R., *Theory of Simple Liquids: With Applications to Soft Matter (Chapter 12)*; Academic Press: 2013.

[53] Elgersma, A. V.; Zsom, R. L.; Norde, W.; Lyklema, J. The adsorption of bovine serum albumin on positively and negatively charged polystyrene latices. *J. Colloid Interface Sci.* **1990**, *138*, 145–156.

8 Interaction of organic ions with proteins

8.1 Background

Proteins are made up of amino acids, which form complex structures and lead to complicated interactions with their environment. In general, the biological function of proteins is performed in aqueous solution, where they interact with different kind of electrolytes [1]. Specific ion-protein interactions can influence in the internal structure of proteins and the protein-protein interactions (stabilization or denaturation) [2, 3]. Thus, protein-ion interaction is relevant for the understanding of the whole system, as well as in the development of applications. For instance, proteins are widely used in the food industry (formation and stabilization of emulsions) [4] or for biosensor applications [5], among others; ions are typically involved in those applications.

In general, proteins tend to accumulate at interfaces [6]. Importantly, protein adsorption modifies the properties of the sorbent, in particular its electrostatic charge and hydrophobicity. The final properties will depend on the nature of the protein and the degree of coverage. Therefore, protein adsorption allows to generate soft interfaces with different degree of hydrophobicity. It is worth noting that colloidal surfaces with different degree of hydrophobicity can produce interesting interactions with ions. It is widely recognized, that the hydrophobic/hydrophilic nature of surfaces plays a fundamental role in the water-mediated interactions with ions [7–9]. Big hydrophobic ions, in particular, are able to cause huge effects over hydrophobic surfaces [9–11].

For this kind of ions, like tetraphenylarsonium cation (Ph_4As^+) and tetraphenylborate anion (Ph_4B^-), the ion-surface interactions are not always dominated by the electrostatic charge. Often, the most relevant factor is the nature of the surface. The hydrophobic ions tend to adsorb onto hydrophobic surfaces, while they are repelled by the hydrophilic ones [9, 10]. In the case of highly hydrophobic surfaces, ion accumulation can produce giant charge inversions at low concentrations [9, 12]. These type of interactions can provide relevant informa-

tion concerning ionic specificity.

Additionally, as shown in previous chapters, the Ph_4B^- anion usually shows more significative effects at lower concentrations than the Ph_4As^+ cation, in spite of their similarities. This fact is related with the different behavior of anions and cations due to the asymmetrical interactions with water molecules [7, 13–15]. The charge of these ions is located at their center, whereas neutral and hydrophobic rings interact with the environment. Nevertheless, even for large ions, the hydration of the anion and the cation is unequal, as previous experimental [16] and simulation studies [17, 18] have demonstrated. This can result in interactions of different magnitude [9]. Interestingly, the different behavior of anions and cations, is increased when the tetraphenyl ions interact with a soft matter system [11].

In this chapter we have investigated the interactions taking place between the tetraphenyl ions and colloidal particles coated by proteins of different hydrophobicity. The complexes used, of β-casein, β-lactoglobulin and BSA, were characterized in Chapter 7. The affinity of the tetraphenyl ions to the complexes has been investigated by electrophoresis and colloidal stability. The tetraphenyl ions interact so strongly with proteins that they may able to modify their structure. This is why we have monitored their conformational changes with the Quartz Crystal Microbalance (QCM) technique. This chapter aims to inquire into the following aspects. First, we explore the role of the hydrophobic nature of a surface in the ion-surface interactions, in particular for big hydrophobic ions (tetraphenyl ions), which produce more intense effects than inorganic ions. Second, we study the effects caused by these ions, as great charge inversions and conformational changes induced in soft interfaces. Finally, we seek to confirm the different behavior of Ph_4B^- and Ph_4As^+ when interacting with this kind of systems.

8.2 Results and discussion

8.2.1 Hydrophobic degree of the β-casein, BSA and β-lactoglobulin proteins

We have performed a thermodynamic calculation at neutral pH, by OPM (see Methods section 3.3) to determine the degree of hydrophobicity of the proteins. The results are shown in Figure 8.1. We obtained the Gibbs free energy or transfer energy of the proteins from water to a nonpolar solvent. From these values the proteins have been ordered in a hydrophobic scale. In every case the transfer of the protein is energetically favorable, as indicates the negative sign. However, we can see that the magnitude of the energy is different for each protein (Figure 8.1). The β-casein presents the higher value for the transfer energy (–9.5 kcal/mol), followed by the BSA (–5.1 kcal/mol) and finally the β-lactoglobulin

(–1.7 kcal/mol). This means that the β-casein protein is more hydrophobic than the globular proteins. On the other hand, the BSA shows a middle behavior and the β-lactoglobulin seems the less hydrophobic.

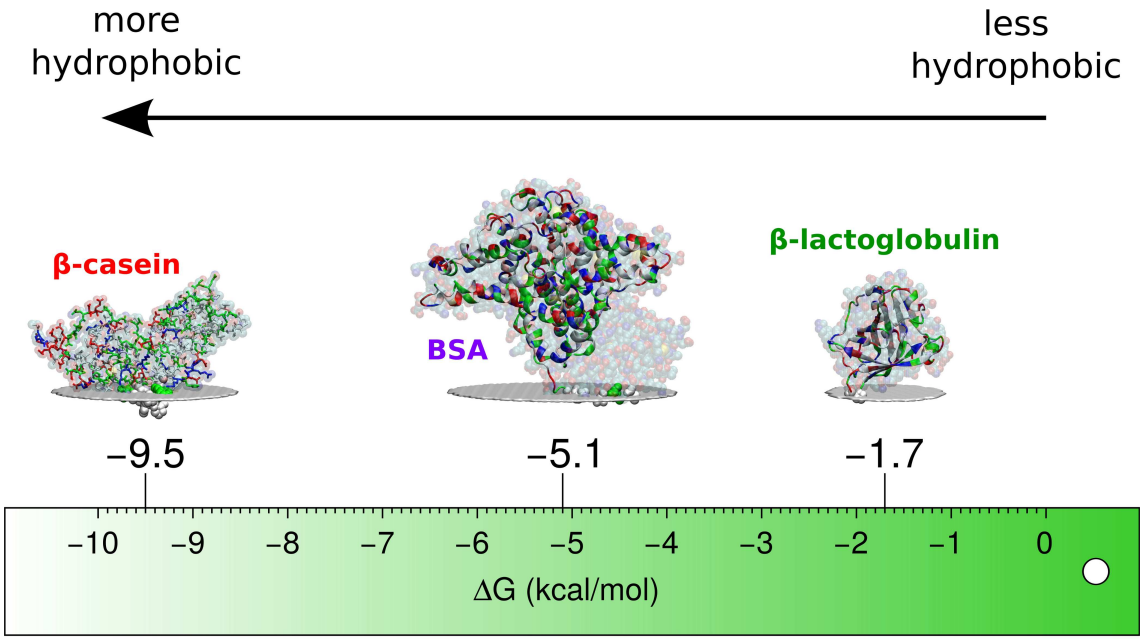

Figure 8.1: Proteins ordered in a standard hydrophobic scale. The images of the proteins were made with VMD [19]. The protein structures are represented in NewCartoon visualization, except β-casein that is shown in Bond visualization. The protein residues are colored depending on their nature: hydrophobic (white), hydrophilic (green), positively charged (blue) and negatively charged (red). The white slab separates the most hydrophobic part of the protein (van der Waals spheres) from the rest of the residues of both nature.

8.2.2 Electrokinetic and stability studies of latex-protein complexes in presence of the tetraphenyl salts

We have studied the interactions of PS latex microspheres and the complexes with the tetraphenyl ions. Previous studies [9–11] showed that the tetraphenyl ions feel a great affinity for hydrophobic interfaces. The degree of hydrophobicity of our experimental systems can be ranked as:

PS bare latex > **β-casein** > **BSA** > **β-lactoglobulin**

Therefore, we anticipate a different degree of ion-interaction with each interface in the mentioned order.

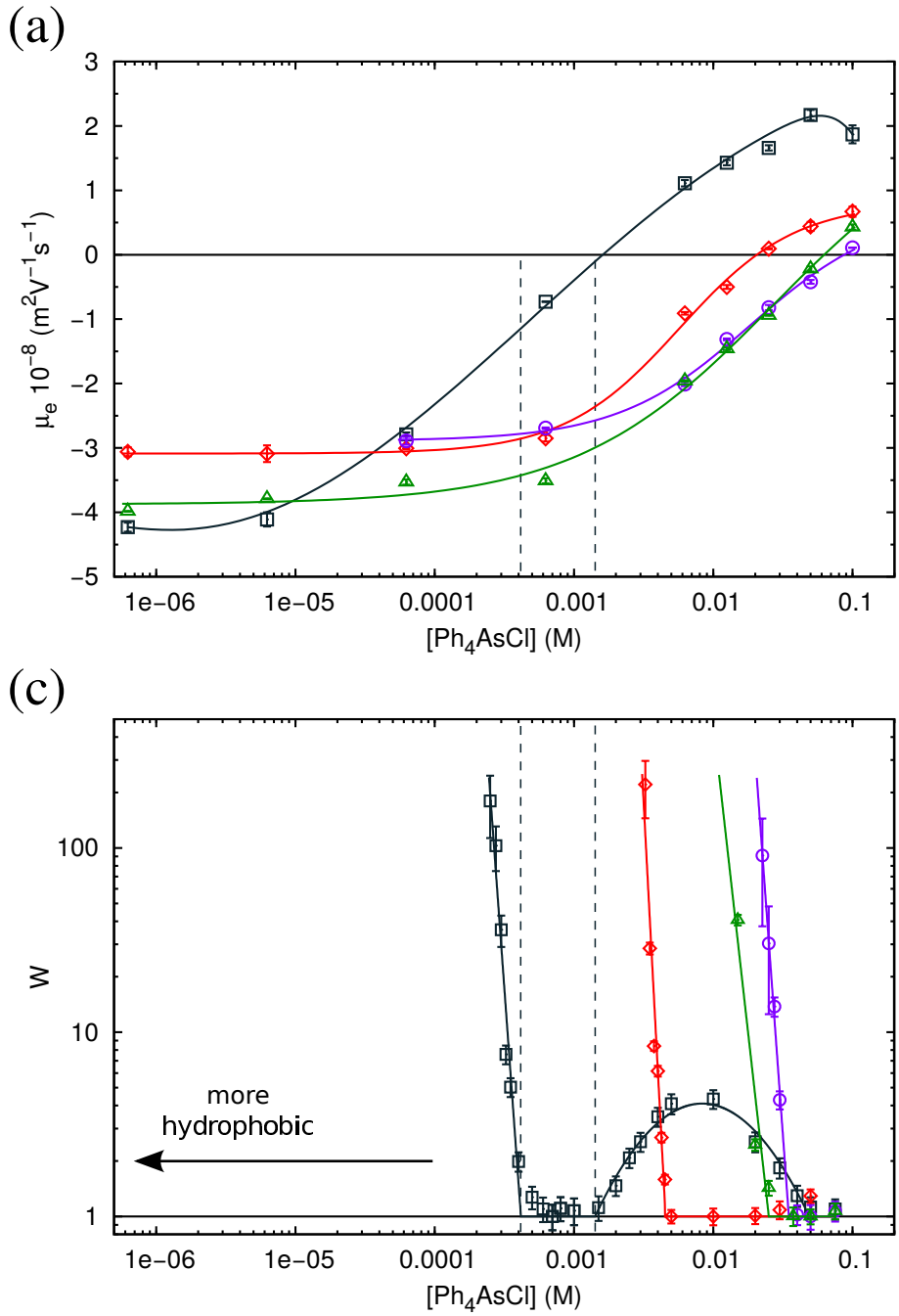

Figure 8.2: Electrophoretic mobility (a),(b) and stability (c),(d) measurements of the anionic PS latex (□) and their latex-protein complexes: β-casein (◇), BSA (○) and β-lactoglobulin (△) against the tetraphenyl ion concentration.
(a), (c) results correspond to $Ph_4As^+Cl^-$ salt at pH 10, and (b), (d) to $Na^+Ph_4B^-$ salt at pH 4 (except for the β-lactoglobulin complex that was measured at $\longrightarrow$

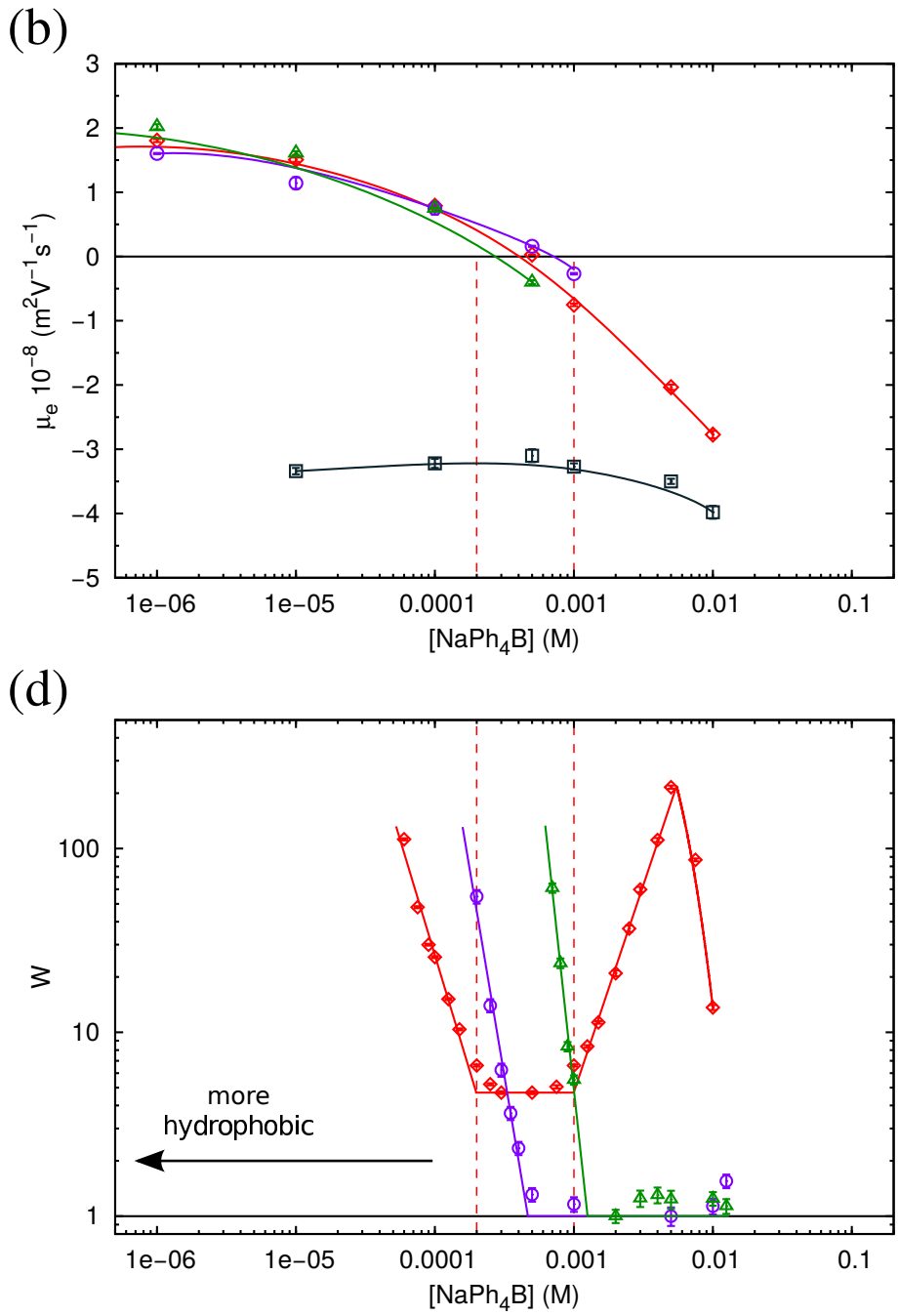

pH 3). The solid lines of the μ_e curves are used for guiding the eye. On the other hand, the solid lines of the stability plots are linear fits to obtain the CCC values. The vertical discontinuous lines indicate the unstability zone for the anionic latex in presence of $Ph_4As^+Cl^-$ and for the β-casein complex in presence of $Na^+Ph_4B^-$.

First, we measured the μ_e of the colloids as a function of the tetraphenyl ion concentration. Both, the Ph_4As^+ cation and the Ph_4B^- anion acted as counterions for the protein-coated particles. The experiments were carried out at pH 10 (negatively charged complexes) with the Ph_4AsCl salt and at pH 4 (positively charged complexes) with the $NaPh_4B$. The μ_e curves of the complexes are shown in Chapter 7. As the β-lactoglobulin complex showed a μ_e value close to zero at pH 4 (Figure 7.11 (a)), the measurements with this protein were performed at pH 3. The results for the protein-coated anionic microspheres are shown in Figure 8.2 (a) for the Ph_4As^+ cation and (b) for the Ph_4B^- anion. In addition, the stability of the colloidal particles in presence of the organic salts was studied. The results are presented in Figure 8.2 (c) for Ph_4AsCl salt and (d) for the $NaPh_4B$ salt.

Mobility curves (Figures 8.2 (a) and (b)) show that for both ions the μ_e decreases as the concentration of tetraphenyl increases. These results reflect the screening of the surface charge as a function of the concentration. However, a different behavior between $Na^+Ph_4B^-$ and the $Ph_4As^+Cl^-$ is observed. The μ_e curves for the Ph_4As^+ are different for each system (8.2 (a)) while in the case of the Ph_4B^- the μ_e values for the three complexes are very similar.

Figure 8.2 (a) shows that μ_e is close to zero for the anionic PS latex at 1 mM of $Ph_4As^+Cl^-$, at 10 mM for the β-casein complex and almost at 100 mM for the globular protein complexes. The same order is followed in the stability results (Figure 8.2 (c)) which is reflected in the values of the critical coagulation concentration (CCC) summarized in Table 8.1. Because this order follows the same sequence given by the hydrophobicity of our systems, we can conclude that the Ph_4As^+ cation accumulates in a higher extension as the interface is more hydrophobic.

more hydrophobic ↓

System	$CCC_{Ph_4AsCl} \cdot 10^{-3}$ (M)	$CCC_{Ph_4BNa} \cdot 10^{-3}$ (M)
β-lactoglobulin	25 ± 3	1.25 ± 0.05
BSA	34.9 ± 0.7	0.47 ± 0.02
β-casein	4.5 ± 0.1	0.20 ± 0.04
Anionic latex	0.42 ± 0.01	Stable

Table 8.1: Critical coagulation concentration (CCC) of the anionic PS microparticles and the latex-protein complexes with the tetraphenyl salts.

In contrast, we did not observe any apreciable difference in the $NaPh_4B$ concentrations to get $\mu_e \sim 0$ for the different complexes (Figure 8.2 (b)). Nevertheless, the stability results (Figure 8.2 (d)) reflect such differences in the CCC values for the three complexes. In our opinion, the CCC values are so small that could not be discriminated by electrophoretic mobility measurements. On the other hand, these small values reflect the high affinity of the Ph_4B^- anion, acting as counterion, for the interface of the proteins. By comparing the CCC values obtained with both

tetraphenyl ions, we see that they are typically 20 to 100 times lower for Ph_4B^- than for Ph_4As^+, in spite of the complexes have similar electrokinetic charges (in absolute value), around 0.02 and –0.02 e/nm^2, respectively. It is clear that the interaction of the Ph_4B^- anion is stronger than that of the Ph_4As^+ cation. These results are in line with those obtained in previous chapters with the PNIPAM systems. In addition, the CCC values corresponding to the $NaPh_4B$ electrolyte, shown in Table 8.1, follow the hydrophobic order established by the thermodynamic calculation: β-casein $>$ BSA $>$ β-lactoglobulin (Figure 8.1). Thus, the Ph_4B^- anion is accumulated to a greater extent on increasingly hidrophobic interfaces. In the case of the bare anionic latex, the organic anion acts as coion, consequently the ion-adsorption increases the net charge of the colloid which stays stable in all the ion concentration range.

Another implication of the strong interaction of these ions with the interfaces is that they are able to produce charge inversion of hydrophobic surfaces at low salt concentrations [9], as we have also observed with the PNIPAM microgels (Chapter 4). In the present case, we have found an important charge reversal of the anionic latex in presence of the organic cation (Figure 8.2 (a)). This charge inversion is also reflected in the stability curves (Figure 8.2 (c)). At concentrations where the mobility values were close to zero, the latex became unstable (W=1; aggregate state). However, when the mobility sign changed, the latex particles showed again stabilization. This re-stabilization is generated by the charge reversal; as the concentration of $Ph_4As^+Cl^-$ is further increased the latex aggregated again due to the screening of the surface charge. Charge reversal was also observed for the β-casein complex (Figure 8.2 (a)), although it was not important enough to re-stabilize the system. In addition, a great charge reversal was observed with the most hydrophobic complex (β-casein) in presence of the Ph_4B^- anion (Figure 8.2 (b)). This inversion produced a re-stabilization of the complex followed by aggregation at higher concentrations (see Figure 8.2 (d)). Re-stabilization processes mediated by hydration forces observed with hydrophilic interfaces are known [8, 14, 20–25] but to best of our knowledge, this is the first time that a re-stabilization generated by charge inversion has been reported.

We also performed several experiments with the proteins adsorbed on cationic PS latexes. Results on μ_e with the adsorbed proteins show a similar behavior than that for the anionic particles (see Figure 8.3), indicating that the interfaces of the complexes are similar in both cases. Moreover, the cationic latex shows the same behavior than anionic latex, but changing the counterion/coion role for the tetraphenyl ions. This is, μ_e remained positive in the range of concentrations studied for the Ph_4As^+ acting as coin, while a great charge reversal was observed at $5{\cdot}10^{-4}$ M when the Ph_4B^- acted as counterion.

From all these results we can conclude that the interaction of the tetraphenyl ions with the proteins is strong enough to expect structural changes in the protein conformation. These modifications have been monitored by QCM.

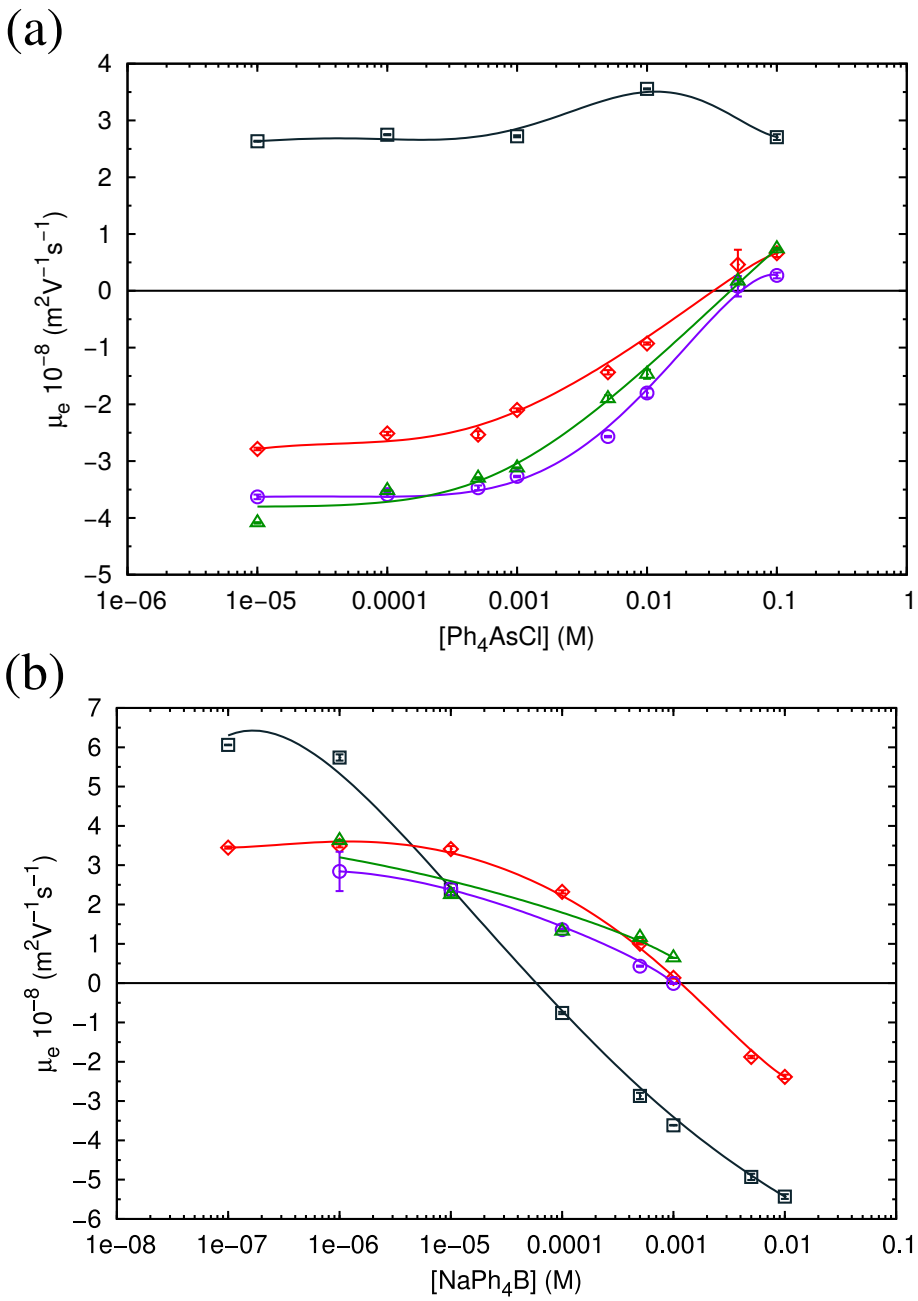

Figure 8.3: Electrophoretic mobility measurements of the cationic PS latex (□) and their latex-protein complexes: β-casein (◇), BSA (○) and β-lactoglobulin (△) against the $Ph_4As^+Cl^-$ concentration at pH 10 (a) and against the $Na^+Ph_4B^-$ concentration at pH 4 (b).

8.2.3 Conformational changes in protein structure induced by tetraphenyl salts (QCM study)

We have used the QCM-D to explore in more detail the interaction of the different proteins with the hydrophobic tetraphenyl ions. The proteins were adsorbed at the same medium conditions that in the previous QCM experiments (section 7.3). The adsorption was performed onto a gold surface coated with a methyl-terminated SAM (–CH_3), instead of the PS surface, since the tetraphenyl ions modify the PS structure (see Methods section 2.8.2). After 30 min of protein adsorption the solution in the QCM device was exchanged by protein-free buffer solutions at the same pH. Subsequently, the adsorbed protein layers were exposed to basic or acid buffers, solutions of NaCl 1 mM, and sequentially increasing concentrations of the tetraphenyl salts. Finally, the protein layers were exposed again to buffer solutions to verify the reversibility of the process.

After protein adsorption, we explored the conformational changes induced by changing pH, and by the interaction between the proteins and the tetraphenyl ions. Two scenarios were explored, with the hydrophobic ions acting either as counterions (Figures 8.4–8.6; Ph_4B^- at acid pH or Ph_4As^+ at basic pH) or as coion (Figures 8.7–8.9; Ph_4As^+ at acid pH or Ph_4B^- at basic pH). A similar general trend was observed for the three proteins. Substantial protein swelling was observed when rinsing at pH10, as evidenced by the increment in ΔD_n (Figures 8.4 (a), 8.5 (a) and 8.6 (a)). However, rinsing with acid buffer slightly changed the protein conformation (other than inducing some β-casein desorption, as discussed above in section 7.3), as it is reflected in the small swelling of the proteins (Figures 8.4 (b), 8.5 (b) and 8.6 (b)). The influence of the tetraphenyl salts on protein conformation is very revealing. When the hydrophobic ions act as counterions of the adsorbed proteins, progressively increasing the salt concentration induces first the decreasing and then the increasing of absolute values of ΔD_n and Δf_n, and of $\Delta f_n/n$ dispersion. As discussed below, we associate this non-monotonic behavior to continuously increasing association of the hydrophobic ions to the adsorbed protein films. Thus, the first stage points to protein dehydration (due to decreasing the effective charge on the proteins) and film densification due to greater screening of intermolecular repulsive electrostatic interaction at larger salt concentrations. The second stage suggests the re-swelling of the films; charge inversion is probably responsible for this behavior. On the other hand, when the hydrophobic ions act as coions, a progressive but less marked protein layer swelling was observed with increasing salt concentration. It is truly remarkable that the hydrophobic coions appear to get associated to the protein films overcoming the electrostatic repulsion, evidencing the determinant role of the hydrophobic interaction (Figures 8.7–8.9).

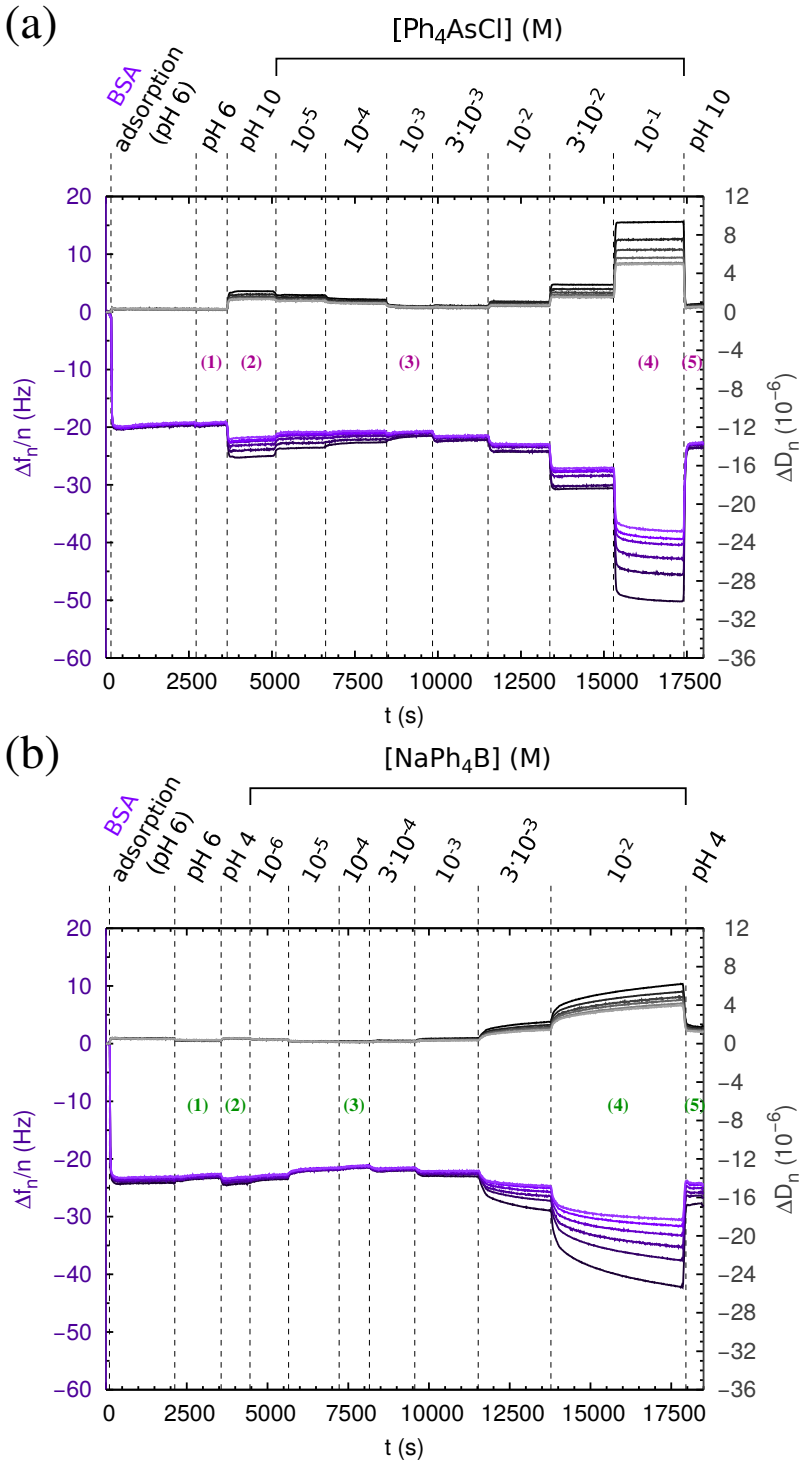

Figure 8.4: QCM-D measurements of BSA film in presence of (a) $Ph_4As^+Cl^-$ at pH 10 and (b) $Na^+Ph_4B^-$ at pH 4 (organic ions as counterions). Changes in frequency, $\Delta f_n/n$ (negative part) and changes in energy dissipation, ΔD_n (positive part) are represented. Each overtone from 3 to 13 is shown in a different tonality, from dark to pale color.

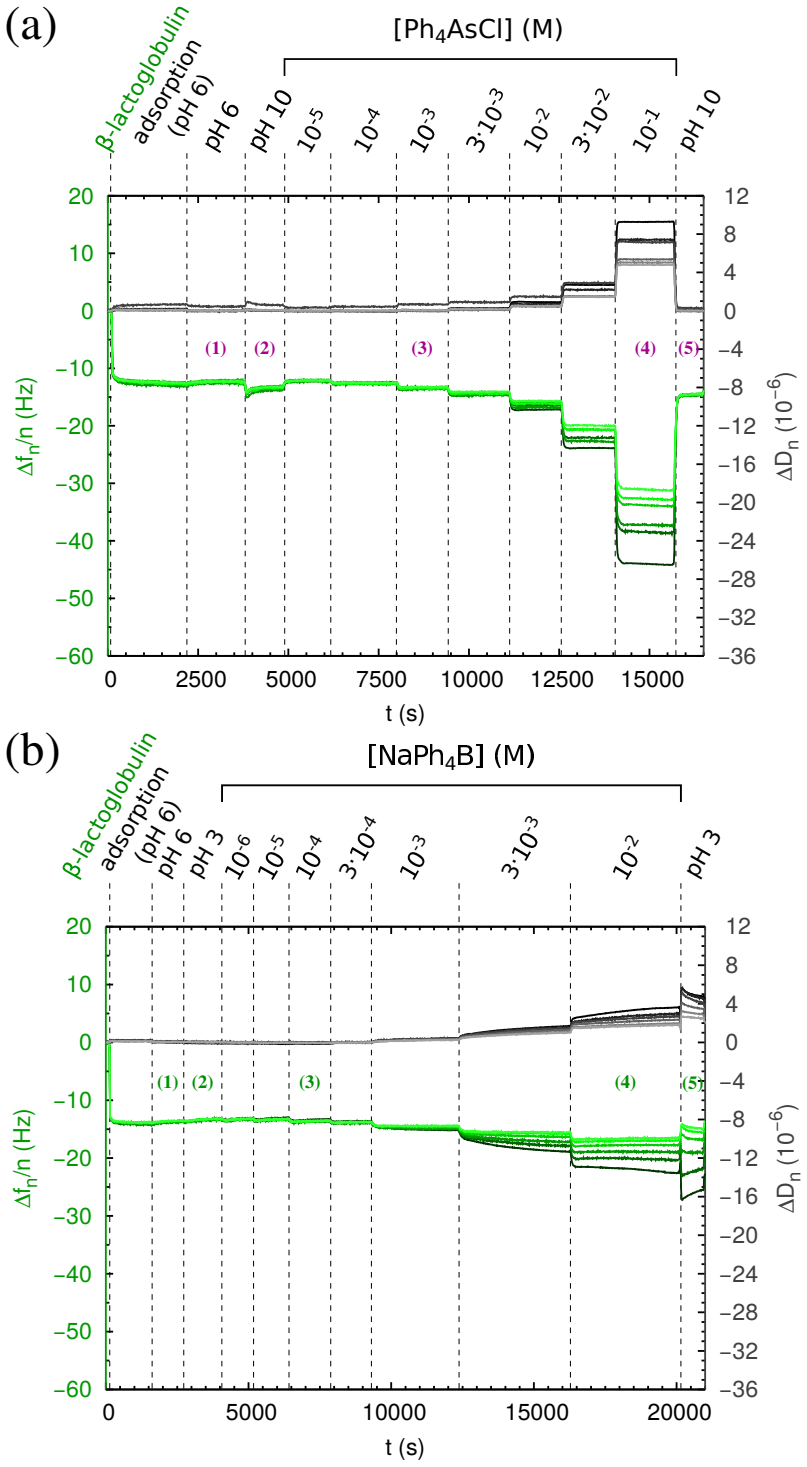

Figure 8.5: QCM-D measurements of β-lactoglobulin film in presence of (a) $Ph_4As^+Cl^-$ at pH 10 and (b) $Na^+Ph_4B^-$ at pH 3 (organic ions as counterions). Changes in frequency, $\Delta f_n/n$ (negative part) and changes in energy dissipation, ΔD_n (positive part) are represented. Each overtone from 3 to 13 is shown in a different tonality, from dark to pale color.

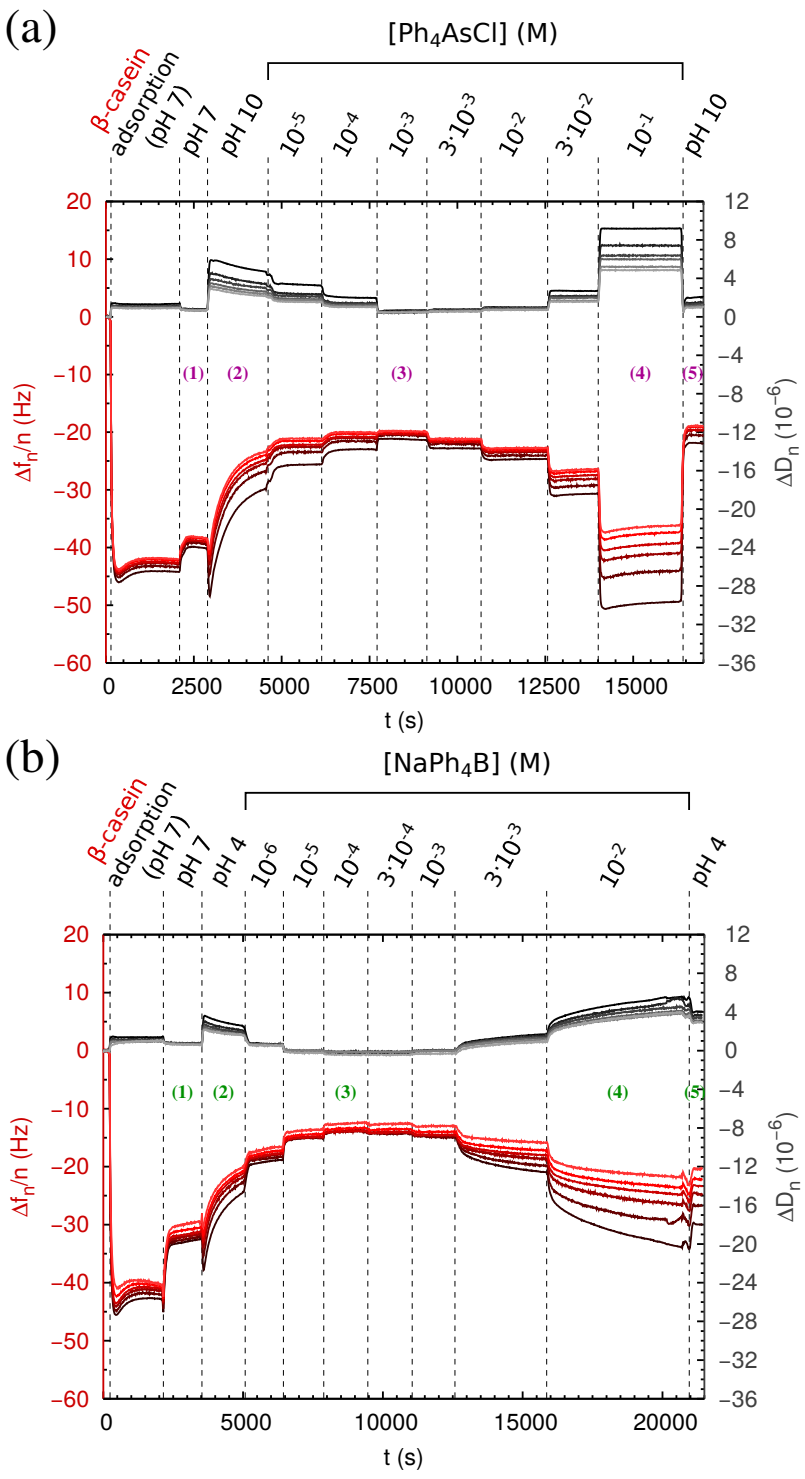

Figure 8.6: QCM-D measurements of β-casein film in the presence of (a) $Ph_4As^+Cl^-$ at pH 10 and (b) $Na^+Ph_4B^-$ at pH 4 (organic ions as counterions). Changes in frequency, $\Delta f_n/n$ (negative part) and changes in energy dissipation, ΔD_n (positive part) are represented. Each overtone from 3 to 13 is shown in a different tonality, from dark to pale color.

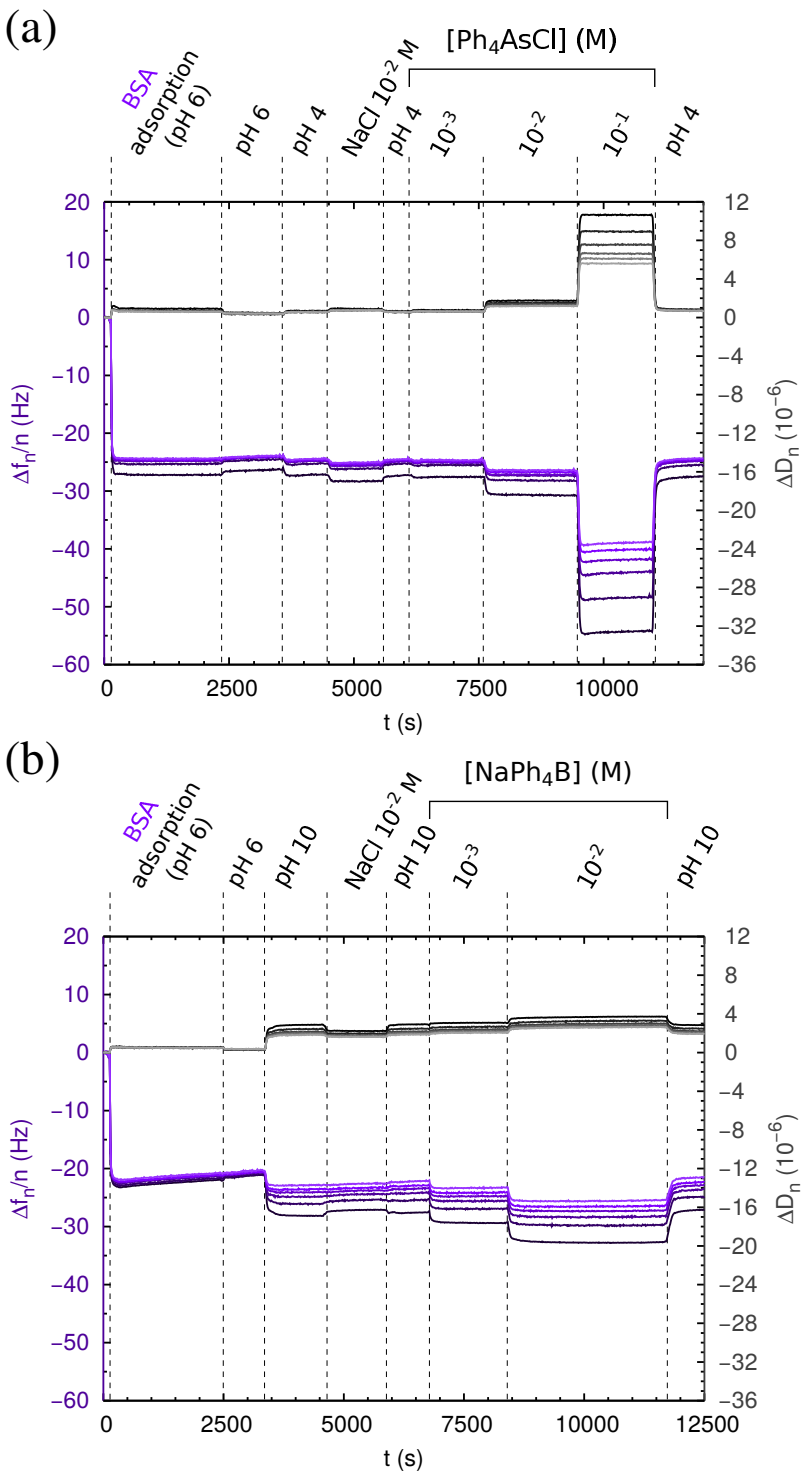

Figure 8.7: QCM-D measurements of BSA film in presence of (a) $Ph_4As^+Cl^-$ at pH 4 and (b) $Na^+Ph_4B^-$ at pH 10 (organic ions as coions). Changes in frequency, $\Delta f_n/n$ (negative part) and changes in energy dissipation, ΔD_n (positive part) are represented. Each overtone from 3 to 13 is shown in a different tonality, from dark to pale color.

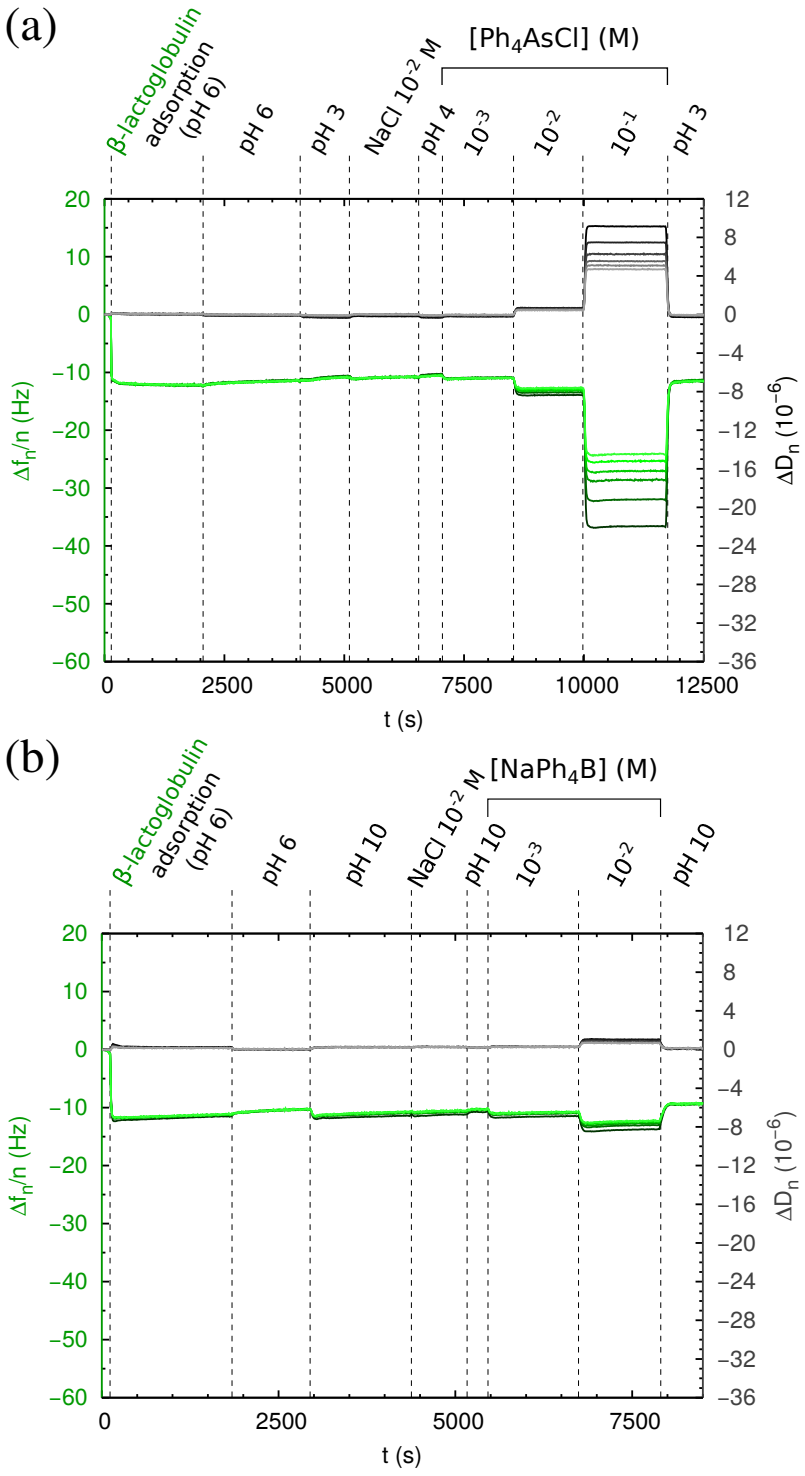

Figure 8.8: QCM-D measurements of β-lactoglobulin film in presence of (a) $Ph_4As^+Cl^-$ at pH 3 and (b) $Na^+Ph_4B^-$ at pH 10 (organic ions as coions). Changes in frequency, $\Delta f_n/n$ (negative part) and changes in energy dissipation, ΔD_n (positive part) are represented. Each overtone from 3 to 13 is shown in a different tonality, from dark to pale color.

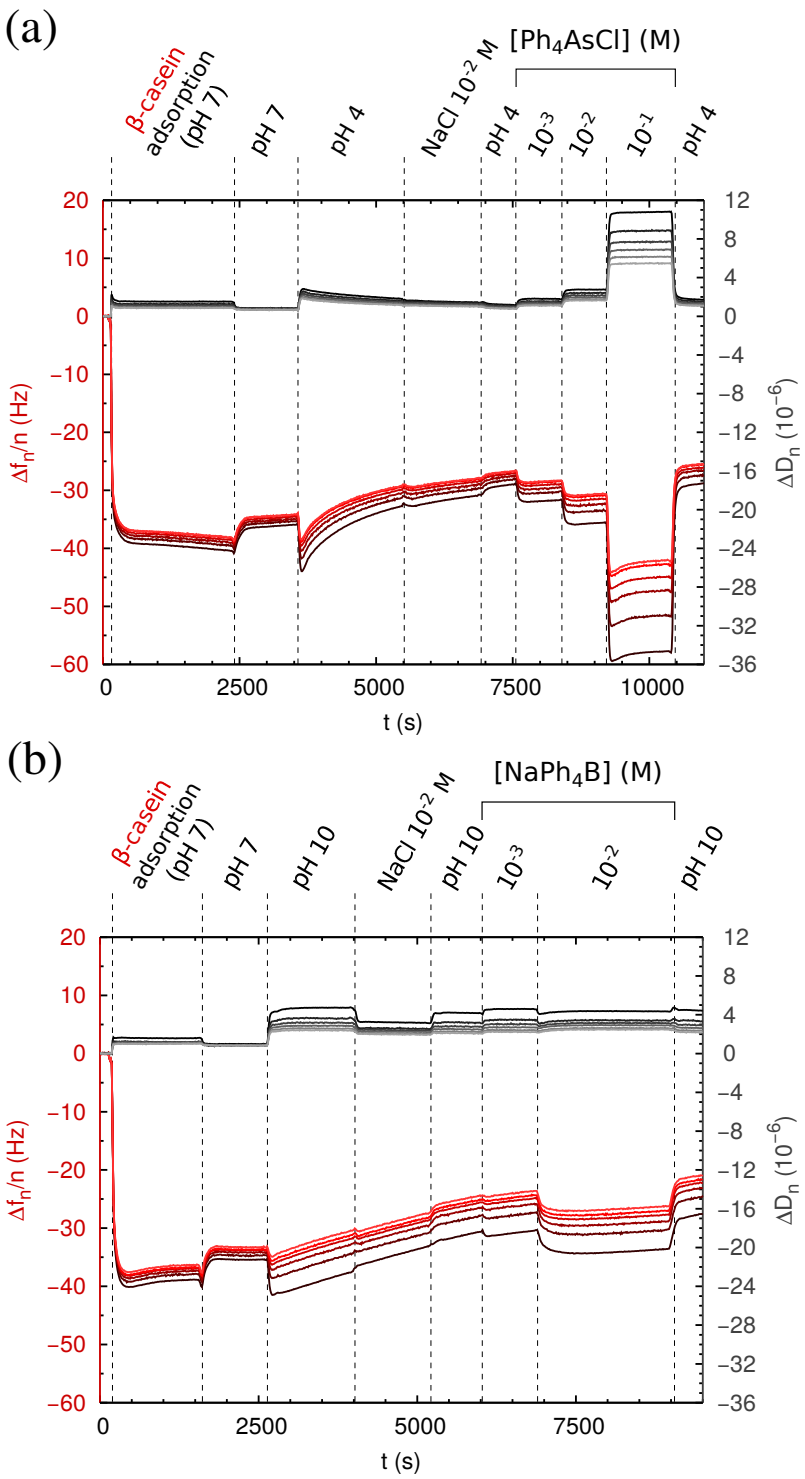

Figure 8.9: QCM-D measurements of β-casein film in presence of (a) $Ph_4As^+Cl^-$ at pH 4 and (b) $Na^+Ph_4B^-$ at pH 10 (organic ions as coions). Changes in frequency, $\Delta f_n/n$ (negative part) and changes in energy dissipation, ΔD_n (positive part) are represented. Each overtone from 3 to 13 is shown in a different tonality, from dark to pale color.

It appears that some irreversible ion adsorption occurs when the Ph_4B^- anion acts as counterion of the proteins. As it can be observed in Figures 8.4–8.6, after the treatment with hydrophobic salts the measured f and D only returned to their original values (before exposure to salt) upon rinsing with salt-free buffer solutions with the Ph_4As^+. For the three proteins investigated greater (lower) $\Delta f_n/n$ dispersion was observed for the acid (basic) conditions after exposure to the salt-free buffer for the Ph_4B^-. This indicates a certain degree of irreversibility of ionic co-adsorption on the protein layer probably due to the higher capacity of the Ph_4B^- to penetrate into it, further enhanced by the electrostatic attraction. It is also remarkable that the increase, in absolute value, of f and D was easily reached for the Ph_4As^+ as the concentration increased while for the Ph_4B^- this increment was much slower. This suggests that the anions are being adsorbed deeper in the protein layers. In contrast, when the hydrophobic ions acted as coions (or after treatment with NaCl; Figures 8.7–8.9), similar f and D values were obtained before and after salt treatment, suggesting the efficient removal of the co-adsorbed hydrophobic ions.

A compilation of the ΔD_3 and Δf_3 results measured at different salt concentrations is presented in Figure 8.10 (in all cases, the experiments with the Ph_4B^- anion were limited to lower salt concentrations due to its low solubility). The general trends (dehydration or swelling) are observed at roughly the same salt concentration for the different proteins. Nevertheless, clear differences were observed in electrokinetic/stability measurements (cf. Figure 8.2). It is interesting to compare the effect of the different tetraphenyl salts. When acting as counterions of the proteins, it is apparent that Ph_4B^- induces similar effects than Ph_4As^+ at much lower concentrations (roughly a 10-fold reduction in concentration for similar f or D changes), in agreement with electrokinetic and stability experiments (cf. Figure 8.2). A much slower temporal evolution of f and D was also observed for the proteins in contact with Ph_4B^- as counterion (cf. Figures 8.4–8.6). On the contrary, no marked difference on the effect of both salts (in f and D shifts or their temporal evolution) was observed when the hydrophobic ions were acting as coions of the adsorbed protein.

Schematic illustrations of the different regimes of protein adsorption and ion-protein interaction when ions act as counterions observed in this chapter are presented in Figure 8.11. We have drawn a cartoon for each organic ion because of the different swelling of the protein layers at basic and acid pH and the different final states reached with the Ph_4As^+ (Figure 8.11 (a)) and the Ph_4B^- (Figure 8.11 (b)) when rinsing with buffers. First, the proteins are densely adsorbed at pH closed to pI; the formation of a compact layer is favored due to the reduced intermolecular electrostatic interaction at this close-to-neutrality condition (part (1)). Changing the pH to basic or acid conditions increases the net molecular charge, increasing intermolecular repulsion and favoring protein swelling (slightly for acid pH and more significant for basic pH) (part (2)). For the case of β-casein this pro-

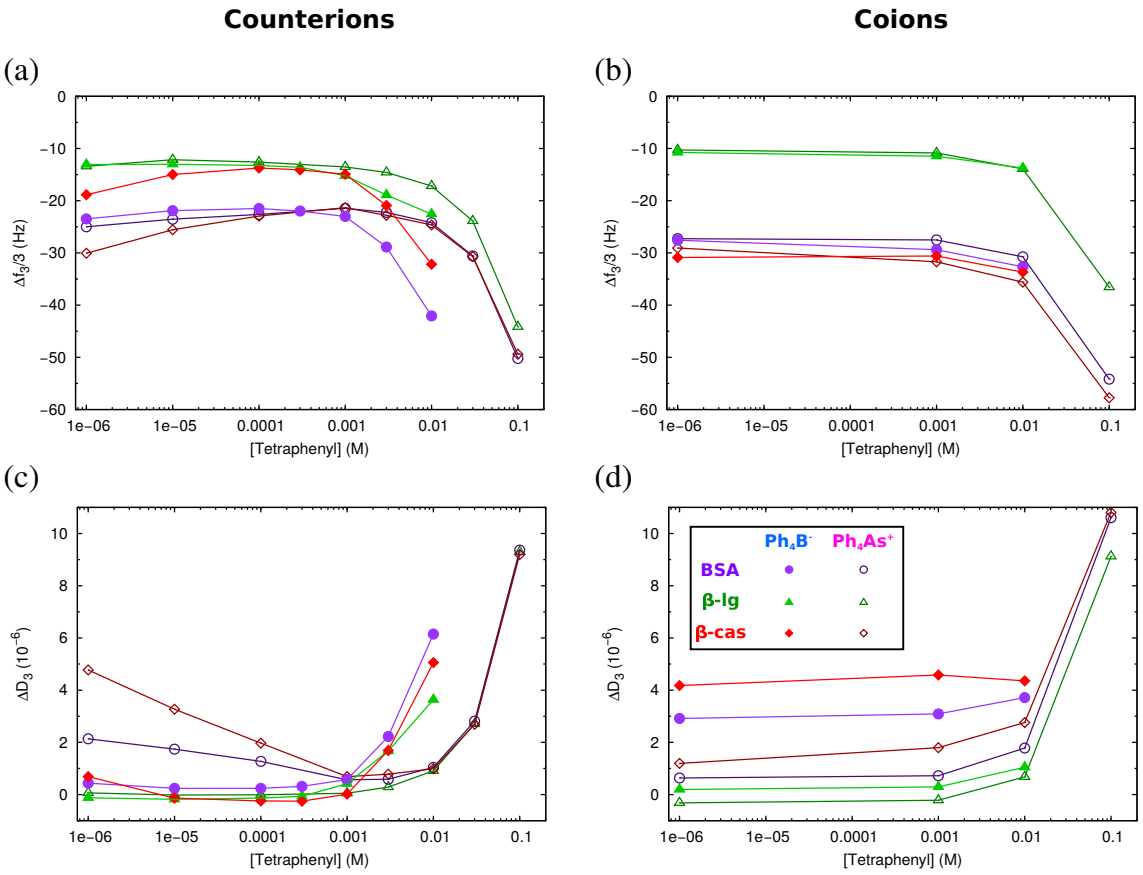

Figure 8.10: Changes in frequency and dissipation of the third overtone measured at different salt concentrations. Δf_3 and ΔD_3 of the protein films in presence of the tetraphenyl ions acting as counterions (left) and coions (right). Conformational changes of the three proteins are detected at roughly the same salt concentrations. However, for Ph_4B^- in comparison with Ph_4As^+ a 10-fold reduction in concentration for similar f or D changes is observed.

motes desorption of loosely adsorbed macromolecules. Addition of salt has several effects. On one hand, the extension of the electrostatic repulsion is reduced (screened) by adding NaCl or tetraphenyl salts. On the other hand, adsorption of hydrophobic ions reduces the charge density when they act as counterions of the preadsorbed protein layer. Progressively increasing concentration of hydrophobic counterions first neutralizes (part (3)) and then reverses the charge promoting reswelling (part (4)) of the adsorbed layer. These results can be related with mobility and stability measurements (Figure 8.2). Upon counterion adsorption the protein layer is compacted, μ_e goes to zero reducing the stability of the system. The regime of charge reversal was not accessible in electrokinetic/stability measurements (except for the case of β-casein) due to the aggregation of the protein-coated latexes.

However, it is clearly evidenced in the QCM-D results. Finally, rinsing with salt-free buffer solutions, reversibility is reached with the Ph_4As^+ cation but not with the Ph_4B^- anion (part (5)).

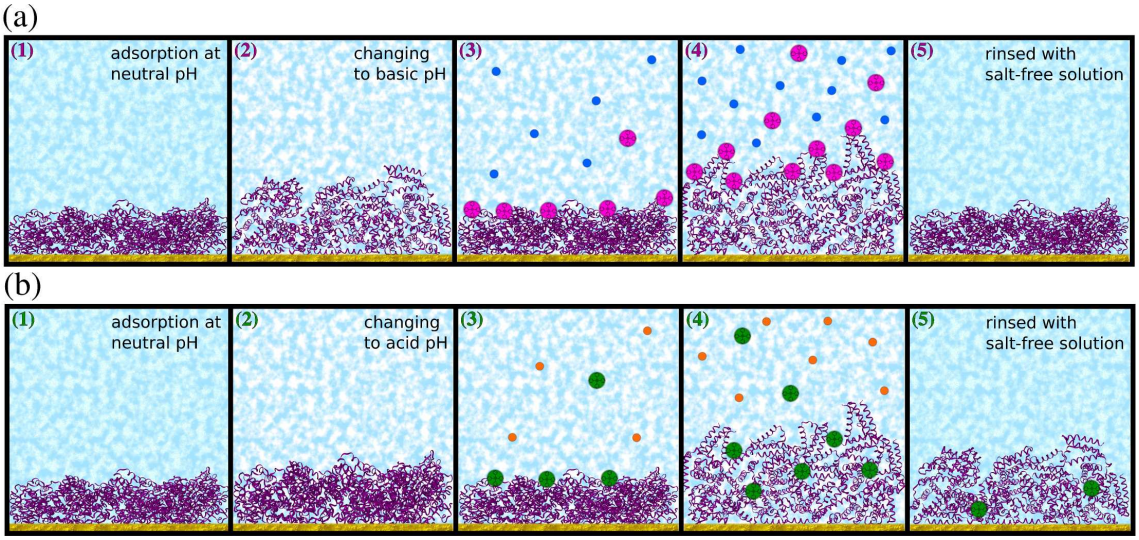

Figure 8.11: Schematic cartoon of the proposed conformational changes undergo by the protein films adsorbed onto a flat substrate. In presence of $Ph_4As^+Cl^-$ salt (a) and for $Na^+Ph_4B^-$ (b), tetraphenyl ions acting as counterions. (1) Proteins are densely adsorbed at pH closed to pI. (2) Changing the pH to basic or acid conditions increases the net molecular charge, increasing intermolecular repulsion and favoring protein swelling (slightly for acid pH and more significant for basic pH). (3) The tetraphenyl ions, Ph_4As^+ (fuchsia circles) or Ph_4B^- (green circles), are adsorbed onto the protein layer reducing the charge density when they act as counterions. The protein film is compacted again. (4) At higher ionic concentrations, the ion adsorption reverses the charge of the protein interface. The protein layer is swollen more and more as the ionic concentration is increased. (5) After rinsing with salt-free buffer solutions, reversibility is reached with the Ph_4As^+ cation but not with the Ph_4B^- anion. The Cl^- ions are represented as blue circles, whereas the Na^+ as orange circles.

Several aspects deserve to be highlighted. First, the different behavior observed in presence of hydrophobic ions acting as coions or counterions is noteworthy. When acting as coions, the effect of the hydrophobic ions seems to be completely reversible. The opposite is true when Ph_4B^- acts as counterion, suggesting partially irreversible coadsorption. In addition, there is a more important but slower influence of the hydrophobic anion acting as counterion. We have reported in the past that this anion is able to strongly disrupt and even penetrate in soft-matter systems, a behavior which we fail to observe for the case of the hydrophobic cation

[11]. A similar scenario could explain the differences between both counterions observed in the present study. On the contrary, both hydrophobic ions (anion or cation) appear to be similarly effective adsorbing on equally charged proteins, i.e., when acting as coions. Finally, the charge reversal of the proteins in presence of monovalent ions is truly remarkable. Charge inversion, associated to particular phase transitions in biological or colloidal systems, has often been reported to be a consequence of correlated adsorption of multivalent counterion or polyions, when the concentration of adsorbed ions is large enough to overcompensate the original charge. On the contrary, the charge reversal observed in this work is due to different ("chemical") reasons, related to the combined effect of electrostatic and hydrophobic interaction leading to protein charge reversal, which appears at very low concentrations of adsorbing hydrophobic ions.

8.3 Conclusions

In this chapter, we have studied how three proteins of different characteristics interact with big hydrophobic ions. The proteins chosen are the two major allergenic proteins of the cow's milk: β-lactoglobulin and β-casein. Additionally, we have studied the BSA as reference protein. Protein-coated PS microspheres (complexes) were prepared by physical adsorption with the objective of obtaining interfaces of different degree of hydrophobicity. Firstly, a quantitative study to determine the hydrophobic degree of the proteins was performed. From these results, the different systems were ordered in a standard hydrophobic scale as: PS bare latex $>$ β-casein $>$ BSA $>$ β-lactoglobulin.

The interactions of the tetraphenyl ions with other interfaces are dominated by the hydrophobic effect [9, 11]. The accumulation of these organic ions onto an interface depends directly on its degree of hydrophobicity. In addition, the Ph_4B^- anion always shows a more hydrophobic behavior than the Ph_4As^+ cation, in spite of their similarities (size and chemical structure). In this study, we have checked that the tetraphenyl ions interact strongly with the proteins mentioned in function of their hydrophobicity.

The electrophoretic mobility and the stability of the complexes were investigated as a function of the tetraphenyl ion concentration. The results indicate that the tetraphenyl ions are accumulated in the interface reducing the electrostatic repulsion between the particles and causing their aggregation when the ions act as counterions. However, the affinity of the organic ions depends on the hydrophobicity of the interface. Thus, the ion concentration needed to screen the surface charge is lower at higher hydrophobic interfaces. In addition, for the most hydrophobic interfaces (bare latex and β-casein complex) the accumulation of the ions was such that huge charge inversions occurred. This phenomenon was accompanied by the re-stabilization of the system. This is, at ionic concentrations

higher than the critical coagulation concentration (CCC) the system is stable. In contrast, the BSA and β-lactoglobulin complexes aggregate irreversibly at higher concentrations. Another interesting factor observed was that the ionic concentrations needed to destabilize these colloidal systems is roughly one order of magnitude lower for the anion than for the cation.

The interaction of the tetraphenyl ions with soft systems is so strong that we have monitored conformational changes undergoing by the proteins with a Quartz Crystal Microbalance device. Each one of the three proteins was adsorbed onto a hydrophobic flat substrate and then were exposed to the tetraphenyl ions. The protein films are capable of swelling or compacting in function of the individual charge of the proteins. The tetraphenyl ions are accumulated onto the protein film. When acting as counterions, they reduce the protein electrostatic charge and the layer is compressed. However, at higher ionic concentration, charge reversal causes repulsion between the protein molecules and the film is hydrated again. On the other hand, when the ions act as coions the charge of the proteins increases and the films are swollen with increasing ionic concentration. From these results, we could infer that the charge inversion concentration is one order of magnitude higher for the cation than for the anion, as in the electrokinetic/stability studies.

It is worth noting that, in all cases, the swelling process was instantaneous in presence of the $Ph_4As^+Cl^-$, whereas this process occurred in a slow and progressive way with the $Na^+Ph_4B^-$. This fact could be related with the ability of the anion to penetrate deeper into the protein film and interact more strongly than the cation. Interestingly, this difference dissapears when the ions act as coions.

From all these results, we can conclude that the interaction between ions and interfaces depend directly on the hydrophobic degree of both, ions and interfaces. The tetraphenyl ions feel higher affinity to the β-casein than to the less hydrophobic proteins: BSA and β-lactoglobulin. On the other hand, we have observed that the anion and the cation interact differently with these interfaces. This is related with the dissimilar hydration of cations and anions [16, 18]. The anion shows a more hydrophobic behavior. Thus, the ionic concentration needed to modify the state of a protein is always lower for the Ph_4B^- than for the Ph_4As^+. In addition, it seems that the anion is able to penetrate deeper in soft systems than the cation.

References

[1] Honig, B.; Nicholls, A. Classical electrostatics in biology and chemistry. *Science* **1995**, *268*, 1144–1149.

[2] Baldwin, R. L. How Hofmeister ion interactions affect protein stability. *Biophys. J.* **1996**, *71*, 2056.

[3] Jungwirth, P.; Winter, B. Ions at aqueous interfaces: From water surface to hydrated proteins. *Annu. Rev. Phys. Chem.* **2008**, *59*, 343–366.

[4] Hunt, J. A.; Dalgleish, D. G. Heat Stability of Oil-in-Water Emulsions Containing Milk Proteins: Effect of Ionic Strength and pH. *J. Food Sci.* **1995**, *60*, 1120–1123.

[5] Dancil, K.-P. S.; Greiner, D. P.; Sailor, M. J. A porous silicon optical biosensor: detection of reversible binding of IgG to a protein A-modified surface. *J. Am. Chem. Soc.* **1999**, *121*, 7925–7930.

[6] Norde, W.; Lyklema, J. Why proteins prefer interfaces. *J. Biomater. Sci.* **1991**, *2*, 183–202.

[7] Lyklema, J. Simple Hofmeister series. *Chem. Phys. Lett.* **2009**, *467*, 217–222.

[8] López-León, T.; Santander-Ortega, M. J.; Ortega-Vinuesa, J. L.; Bastos-González, D. Hofmeister effects in colloidal systems: influence of the surface nature. *J. Phys. Chem. C* **2008**, *112*, 16060–16069.

[9] Calero, C.; Faraudo, J.; Bastos-González, D. Interaction of monovalent ions with hydrophobic and hydrophilic colloids: Charge inversion and ionic specificity. *J. Am. Chem. Soc.* **2011**, *133*, 15025–15035.

[10] Martín-Molina, A.; Calero, C.; Faraudo, J.; Quesada-Pérez, M.; Travesset, A.; Hidalgo-Álvarez, R. The hydrophobic effect as a driving force for charge inversion in colloids. *Soft Matter* **2009**, *5*, 1350–1353.

[11] Pérez-Fuentes, L.; Drummond, C.; Faraudo, J.; Bastos-González, D. Anions make the difference: insights from the interaction of big cations and anions with poly (N-isopropylacrylamide) chains and microgels. *Soft Matter* **2015**, *11*, 5077–5086.

[12] Pérez-Fuentes, L.; Bastos-González, D.; Drummond, C.; Faraudo, J. Re-estabilizing forces in colloids induced by hydrophobic ions. *Materials (in preparation)*,

[13] Lyklema, J. Lyotropic sequences in colloid stability revisited. *Adv. Colloid Interface Sci.* **2003**, *100*, 1–12.

[14] López-León, T.; Jódar-Reyes, A. B.; Bastos-González, D.; Ortega-Vinuesa, J. L. Hofmeister effects in the stability and electrophoretic mobility of polystyrene latex particles. *J. Phys. Chem. B* **2003**, *107*, 5696–5708.

[15] López-León, T.; Jódar-Reyes, A.; Ortega-Vinuesa, J.; Bastos-González, D. Hofmeister effects on the colloidal stability of an IgG-coated polystyrene latex. *J. Colloid Interface Sci.* **2005**, *284*, 139–148.

[16] Scheu, R.; Rankin, B. M.; Chen, Y.; Jena, K. C.; Ben-Amotz, D.; Roke, S. Charge asymmetry at aqueous hydrophobic interfaces and hydration shells. *Angew. Chem.* **2014**, *126*, 9714–9717.

[17] Schurhammer, R.; Wipff, G. About the TATB hypothesis: solvation of the $As\varphi_4^+$ and $B\varphi_4^-$ ions and their tetrahedral and spherical analogues in aqueous/nonaqueous solvents and at a water–chloroform interface. *New J. Chem.* **1999**, *23*, 381–392.

[18] Schurhammer, R.; Wipff, G. Are the hydrophobic $AsPh_4^+$ and BPh_4^- ions equally solvated? A theoretical investigation in aqueous and nonaqueous solutions using different charge distributions. *J. Phys. Chem. A* **2000**, *104*, 11159–11168.

[19] Humphrey, W.; Dalke, A.; Schulten, K. VMD: visual molecular dynamics. *J. Mol. Graphics* **1996**, *14*, 33–38.

[20] Peula-García, J. M.; Ortega-Vinuesa, J. L.; Bastos-González, D. Inversion of Hofmeister series by changing the surface of colloidal particles from hydrophobic to hydrophilic. *J. Phys. Chem. C* **2010**, *114*, 11133–11139.

[21] Santander-Ortega, M.; Peula-García, J.; Goycoolea, F.; Ortega-Vinuesa, J. Chitosan nanocapsules: effect of chitosan molecular weight and acetylation degree on electrokinetic behaviour and colloidal stability. *Colloids Surf. B* **2011**, *82*, 571–580.

[22] Valle-Delgado, J.; Molina-Bolívar, J.; Galisteo-González, F.; Gálvez-Ruiz, M. Evidence of hydration forces between proteins. *Curr. Opin. Colloid Interface Sci.* **2011**, *16*, 572–578.

[23] Chik, J.; Mizrahi, S.; Chi, S.; Parsegian, V. A.; Rau, D. C. Hydration forces underlie the exclusion of salts and of neutral polar solutes from hydroxypropylcellulose. *J. Phys. Chem. B* **2005**, *109*, 9111–9118.

[24] Guo, F.; Friedman, J. M. Charge density-dependent modifications of hydration shell waters by Hofmeister ions. *J. Am. Chem. Soc.* **2009**, *131*, 11010–11018.

[25] Merk, V.; Rehbock, C.; Becker, F.; Hagemann, U.; Nienhaus, H.; Barcikowski, S. In situ non-DLVO stabilization of surfactant-free, plasmonic gold nanoparticles: Effect of Hofmeister's anions. *Langmuir* **2014**, *30*, 4213–4222.

9 Computer simulations of organic ions with model surfaces

9.1 Background

Big ions such as the Ph_4B^- anion and the Ph_4As^+ cation are particularly interesting for the theory of electrolytes in solution because they are very similar in all aspects (size, chemistry...) differing only in the anionic or cationic character. Nevertheless, it is not clear whether the Ph_4B^- anion and the Ph_4As^+ cation have identical or different solvation and hydrogen bonding properties, which should have an impact on the interaction of these ions with surfaces and interfaces. As we have seen in this dissertation, simulation and experimental results have shown dramatic differences between the interaction of the Ph_4B^- anion and the Ph_4As^+ cation with soft matter (PNIPAM and proteins), being the interaction of the anion much stronger.

It is not obvious, however, whether this difference shall be maintained when these ions interact with a solid surface. For this reason, in this chapter we will analyze the interaction of the Ph_4B^- anion and the Ph_4As^+ cation with hydrophobic/hydrophilic solid interfaces. This study is an extension of a previous work where the interaction of the Ph_4B^- anion with hydrophilic and hydrophobic solid surfaces was considered [1].

9.2 Technical details for MD simulations

9.2.1 Ions in bulk water (no surface)

In order to study the hydration of the tetraphenyl ions, we performed NPT simulations of the Ph_4B^- anion and the Ph_4As^+ cation with its corresponding counter-ion (Na^+ or Cl^-) immersed in water. The size of the simulation box was of 40 Å $\times$ 40 Å $\times$ 40 Å (1943 and 1945 water molecules for the anion and the cation, respectively). After 20 ns of simulation, we calculated the g(r) functions between

the central atom of the tetraphenyl ions (B or As) and both hydrogen and oxygen atoms of water molecules.

9.2.2 Ions and neutral surfaces

To quantify the interactions of tetraphenyl ions with both hydrophobic and hydrophilic neutral surfaces, we have carried out simulations with these ions and the surfaces mentioned. The force field employed for both surfaces is based on a generic model previously developed [2]. The hydrophilic or hydrophobic character of the surface is obtained by using different values for the ϵ Lennard-Jones parameter for the atoms of the solid. A hydrophobic surface with a contact angle of about 140º is obtained using ϵ=0.164 kcal/mol. A hydrophilic surface with a contact angle of 55º is obtained employing ϵ=2.084 kcal/mol. For both surfaces σ=3.374 Å. In our simulations, the surface was made of 400 atoms arranged in four equal layers (of 100 atoms each one) of dimensions 33.74 $\times$ 33.74 Å aligned one above the other one forming a primitive cubic structure. The atoms of the surface were maintained fixed during the whole simulation, as in previous studies [1, 2].

On top of the surface, we placed a water slab containing 1640 water molecules, a Ph_4As^+ cation and a Cl^- anion. The simulated system is shown in Figure 9.1.

The configurations obtained after 5-10 ns of NPT simulations were employed as the starting point for free energy calculations of the water-mediated interaction between the Ph_4As^+ and the surface. The potential of mean force (PMF) of the Ph_4As^+ as a function of the separation of the surface (hydrophobic or hydrophilic) was obtained performing biased MD simulations (10-20 ns) using the adaptive biasing force technique (MD-ABF) [3], as described in the section 3.2.2 of Materials and Methods. In the case of the hydrophobic surface we employed a force constant of 5 kcal/(mol $\cdot$ Å^2). In the case of the hydrophilic surface we used a larger force constant of 10 kcal/(mol $\cdot$ Å^2). We obtained the PMF from the closest approach to the surface until the interaction vanished, with 0.1 Å resolution.

The data corresponding to the Ph_4B^- anion was taken from ref [1].

9.2.3 Interaction between ions and charged surfaces

The data previously obtained from MD-ABF simulations has been used to predict the interaction between the organic ions and planar charged surfaces. We have followed the methodology proposed in reference [4]. We have solved the Poisson-Boltzmann equation for a flat surface including the specific potential (V^{PMF}) generated by the tetraphenyl ion, which has been calculated from simulations with full atomistic detail. It is assumed that the density profile $\rho_i(z)$ of each ion i is given by:

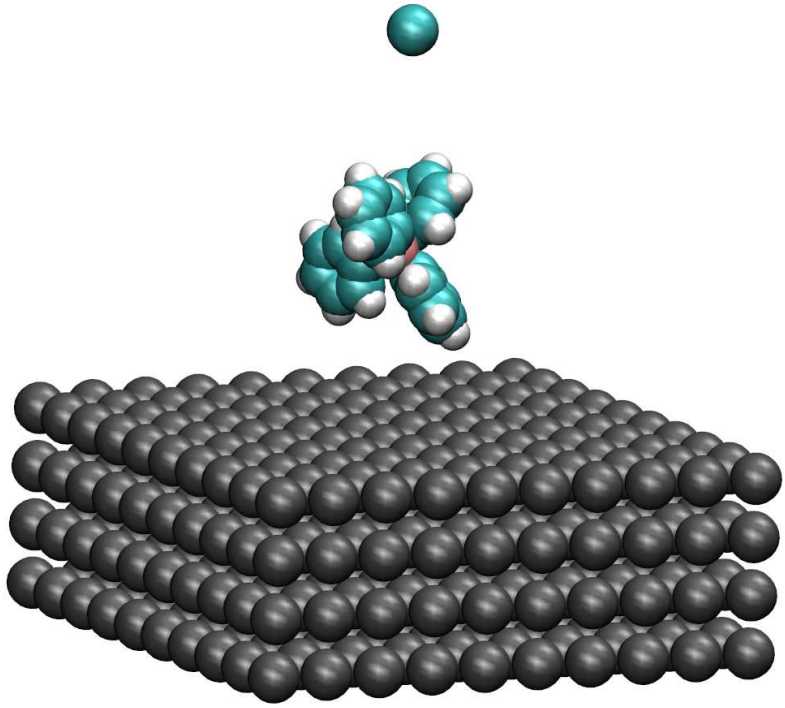

Figure 9.1: Representative snapshot of the simulation system with the Ph_4As^+ cation. All atoms are represented with Van der Waals radius. Cl^- ion is shown as a cyan sphere, the Ph_4As^+ is compound by an arsenic atom (pink), carbon atoms (cyan) and hydrogen atoms (white). Atoms of the generic hydrophobic or hydrophilic surfaces are shown in gray. Water molecules have been omitted for clarity.

$$\rho_i(z) = \rho_0 \exp(-\beta V_i^{PMF}(z) - \beta q_i \phi(z)) \tag{9.1}$$

where $\beta = 1/k_B T$, ρ_0 is the ionic density (number of ions per unit volume) at bulk, q_i is the electrostatic charge of the ion and $\phi(z)$ the average electrostatic potential. In equation 9.1, it is assumed that the specific potential and the electrostatic potential are additives. The $\phi(z)$ is obtained from the Poisson-Boltzmann equation:

$$-\varepsilon_0 \varepsilon_r \frac{d^2}{dz^2}\phi(z) = \sum_i q_i \rho_i(z) \tag{9.2}$$

where ε_0 is the vacuum permittivity and ε_r is the dielectric constant of water. This equation is subject to the boundary condition of bare charge density σ_0 at the surface at z=0:

$$\varepsilon_0 \varepsilon_r \left. \frac{d\phi}{dz} \right|_{z=0} = -\sigma_0 \tag{9.3}$$

The equations 9.1–9.3 have been solved numerically using a program available in the Supporting Information of reference [1]. In this numerical solution, instead of using the values of the V^{PMF} obtained from the simulations, we have used a fitting function to the PMF data. We employed the functions proposed in the reference [1]:

$$V^{PMF}(z - z_0) = A\,(z - z_0)^2\,\exp\left[B\,(z - z_0)\right] \tag{9.4}$$

$$V^{PMF}(z - z_0) = A\,\exp\left[B\,(z - z_0 + C)^2\right] + D\,\exp\left[E\,(z - z_0)\right] \tag{9.5}$$

with A, B, C, D and E as free parameters and z_0 corresponding to the distance of maximum approach between the ion and the surface. The first function has a minimum, so it is suitable for surfaces with adsorbed ions, whereas the latter function represents a monotonic repulsion, being appropriate for reproducing a surface-ion repulsion.

From the numerical solution of eqs. 9.1–9.3 we can obtain the density profiles of ions and the electrostatic potential of the surface. In this way, it is possible to determine if there is ionic adsorption or charge inversion of the surface.

9.3 Results and Discussion

9.3.1 Ions immersed in water and their interaction with neutral surfaces

We have performed all-atomic molecular dynamics (MD) simulations of the Ph_4As^+ cation and the Ph_4B^- anion as described above. As mentioned before, these hydrophobic ions have the same chemical structure, valence and similar size, thus the main difference is their global charge. In the simulation model used here [5], the vast majority of the charge is in the central atom, whereas the partial charges of the phenyl rings are small and similar between the anion and the cation (see section 3.2.4 of Materials and Methods).

First, we present the analysis of the simulations carried out with the tetraphenyl ions and both hydrophobic and hydrophilic neutral surfaces. During the NPT simulations we could observe that the tetraphenyl ions showed opposite behaviors in presence of each type of surface. Both hydrophobic ions (Ph_4B^- and Ph_4As^+) adsorb onto the hydrophobic surface but they remain away from the hydrophilic surface. Hydrophobic ions feel a great attraction to the hydrophobic surface, while no attraction was found for the hydrophilic surface.

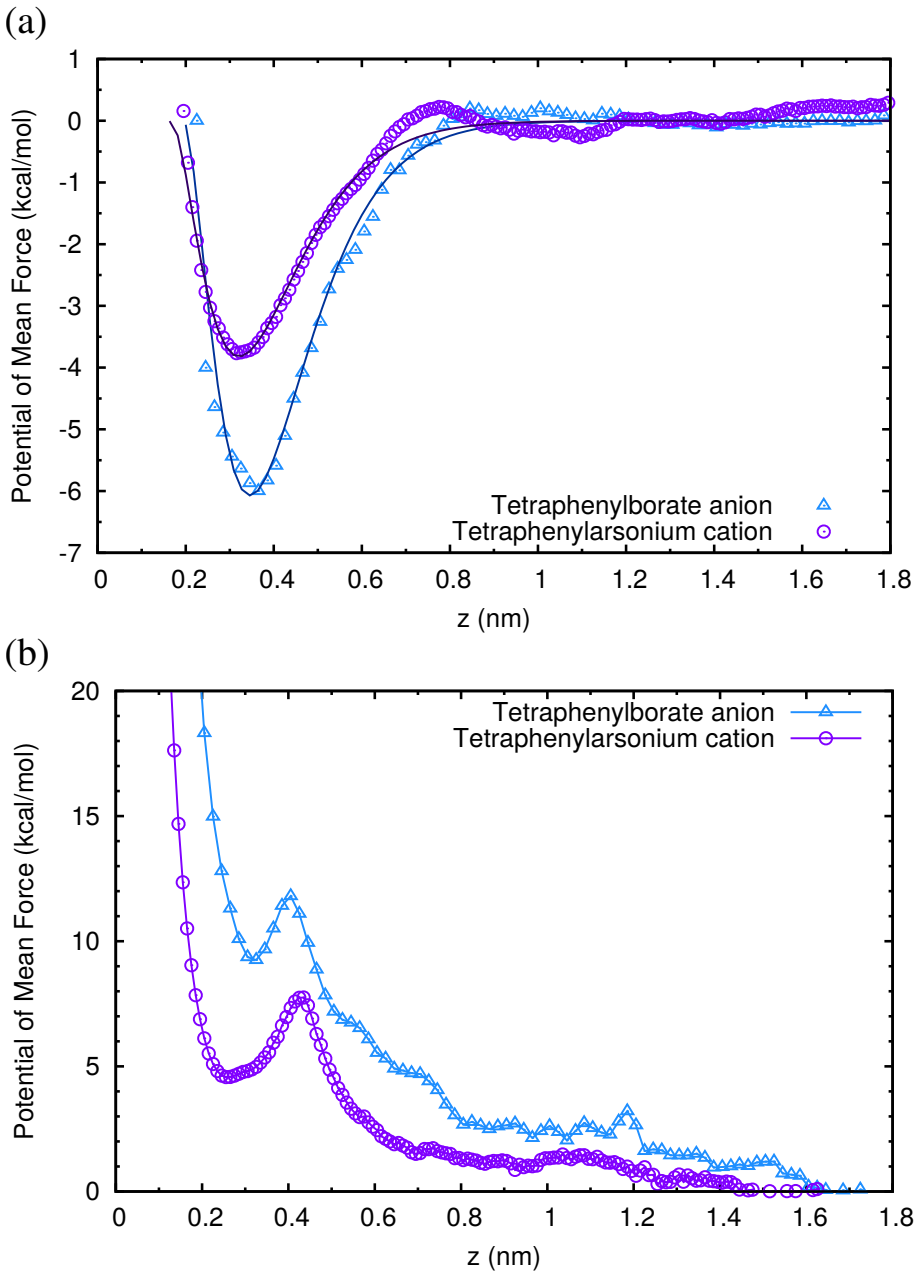

Figure 9.2: Potential of mean force for the Ph_4B^- anion (△) and the Ph_4As^+ cation (○) with hydrophobic (a) and hydrophilic (b) generic surfaces. In both cases the PMF has been obtained by MD-ABF simulations. In the panel (a), solid lines represent the fit to the simulation results in order to use it for theoretical calculations, whereas in (b), solid lines are used for guiding the eye. The abscissa coordinate (z) represents the distance between the central atom of the ion (B or As) and the top part of the surface, which is located at the origin (z=0). The data of the Ph_4B^- anion has been obtained from a previous work [1].

In order to quantify these interactions, we have conducted MD-ABF biased simulations to obtain the potentials of mean force (PMF) as described above. The results are shown in Figure 9.2. The PMF is represented as a function of z, which is the distance between the central atom of the ion (B or As) and the top part of the surface. It can be observed that the interaction of tetraphenyl ions with hydrophobic (Figure 9.2 (a)) or hydrophilic surfaces (Figure 9.2 (b)) is completely different. In the case of the hydrophobic surface, the PMF has a clear adsorption minimum at z =3.4 Å for the Ph_4B^- anion and 3.2 Å for the Ph_4As^+ cation, with a free energy of –6.00 kcal/mol and –3.64 kcal/mol, respectively. The depth of the adsorption minimum indicates the magnitude of the interaction energy, which is higher in the case of the anion (see Figure 9.2 (a)). It is interesting to compare these results with those obtained for soft hydrophobic interfaces (PNIPAM chains) in Chapter 4. We obtained a free energy of interaction of –37.7 kcal/mol for the Ph_4B^- anion and –8.5 kcal/mol for the Ph_4As^+ cation with this polymer. Therefore, the anion interacts more strongly with hydrophobic interfaces than the cation. However, this difference between the anion and the cation is smaller in the case of hard surfaces than in the case of soft interfaces. This is reasonable, since soft interfaces are easily deformable and ions can penetrate inside them increasing the hydrophobic interactions, which is not possible with hard surfaces.

In the case of the hydrophilic surface (Figure 9.2 (b)), the interaction is always repulsive with a peak at $z \simeq 4$ Å for both ions, corresponding to the first hydration layer of the surface. The hydrophilic surface prefers to interact with water molecules instead of interacting with these big ions and an extra energy would be required to dehydrate the surface and to allow the contact between the ion and the surface.

These results suggest that hydration seems an important factor to consider in the ion-surface interactions. For both, hydrophobic surface and hydrophobic ions, loosing hydration water molecules is favorable. Therefore, it is interesting to study the possible changes in the hydration of tetraphenyl ions (Ph_4B^- and Ph_4As^+), in solution and when they are adsorbed on a surface.

These ions have a particular cross-like shape, thus the first layers of hydration are not clearly established. For this reason, we define here the ionic radius as the distance between the central atom (B or As) and the most external group –CH of the ion; these values are 5 Å for the anion and 5.25 Å for the cation. From this definition of ionic size, it is possible to find several water molecules inside of the ion.

In Figure 9.3 we show the radial pair distribution functions g(r) between the tetraphenyl ions and water molecules when the ions are immersed in bulk water (Figures 9.3 (a) and (b)) and when they are adsorbed on the hydrophobic surface (Figures 9.3 (c) and (d)). The g(r) functions were calculated between the central atom of the ion (B or As), and hydrogen or oxygen atoms belonging to water molecules. The g(r) functions for both ions in solution look similar (see Figures

9.3 (a) and (b)) due to their analogous structure, although there are significant differences caused by their opposite charge.

Snapshots from the MD simulations of the tetraphenyl ions immersed in water are represented in Figures 9.3 (e), (f) and (g). We can see the typical positions of water molecules around the ions, which are consistent with earlier reports [5].

Let us consider first the results for the Ph_4B^- anion. In Figure 9.3 (e) we can observe two characteristic positions of water molecules around the anion. In the first position (bottom of Figure 9.3 (e)) both hydrogen atoms of the water molecule are oriented to two separate phenyl rings belonging to Ph_4B^-, whereas in the second one (right in Figure 9.3 (e)) only one hydrogen atom is oriented to a phenyl ring. These positions are responsible for the main peak of the g(r) function to a distance of less than 4 Å (Figure 9.3 (a)). As a consequence of these preferred positions, the oxygen atom of the same water molecule is placed at 4.5–5 Å from the central atom (see Figure 9.3 (f)). This is reflected in the first peak of g(r) (Figure 9.3 (a)). These water molecules are within the limit of the ionic radius, 5 Å (blue arrow in the plots). This first peak caused by the inner molecules has a value lower than 1, indicating that water molecules would rather being in bulk instead of hydrating the anion. If we compare now the hydration of the anion in solution and adsorbed on a surface (Figures 9.3 (a) and (c)), we can note that the g(r) functions are a little different. The main peaks for both hydrogen and oxygen atoms (water molecules) are approximately in the same positions. However, when the anion is adsorbed the peaks appear more pronounced and in this case their maximum values are greater than 1 (the reference value for bulk water). Therefore, the structure of liquid water around the anion, changes when it is adsorbed over the surface. At this state, the anion does not disturb the liquid water structure as much as it does when it is completely surrounded by water.

In addition, we have calculated the average number of inner water molecules to the ion over the simulation time. The anion has a total of 5.5 inner water molecules in solution (1–12 molecules), whereas for the adsorbed anion, this value is reduced to 4.6. On average the anion lost 1 inner water molecule in the adsorption process.

The situation is different for the hydrophobic cation, as can be observed in Figure 9.3 (b). The g(r) function of the Ph_4As^+ cation and the hydrogen atoms (water molecules) does not show a first peak. This implies that there is no direct interaction, as in the case of the anion. Although both tetraphenyl ions have a similar structure (one central atom and four phenyl rings), the hydrogen atoms of water molecules interact more strongly with the anion. Therefore, the sign of the charge of the ions plays an important role in the orientation of water molecules around them, even for big hydrophobic ions like those studied here.

Regarding the oxygen atoms, g(r) functions in Figures 9.3 (a) and (b) show a similar shape. For the cation, the distance between the As atom and the oxygen atoms is around 5.5 Å (Figure 9.3 (g)), larger than that obtained for the an-

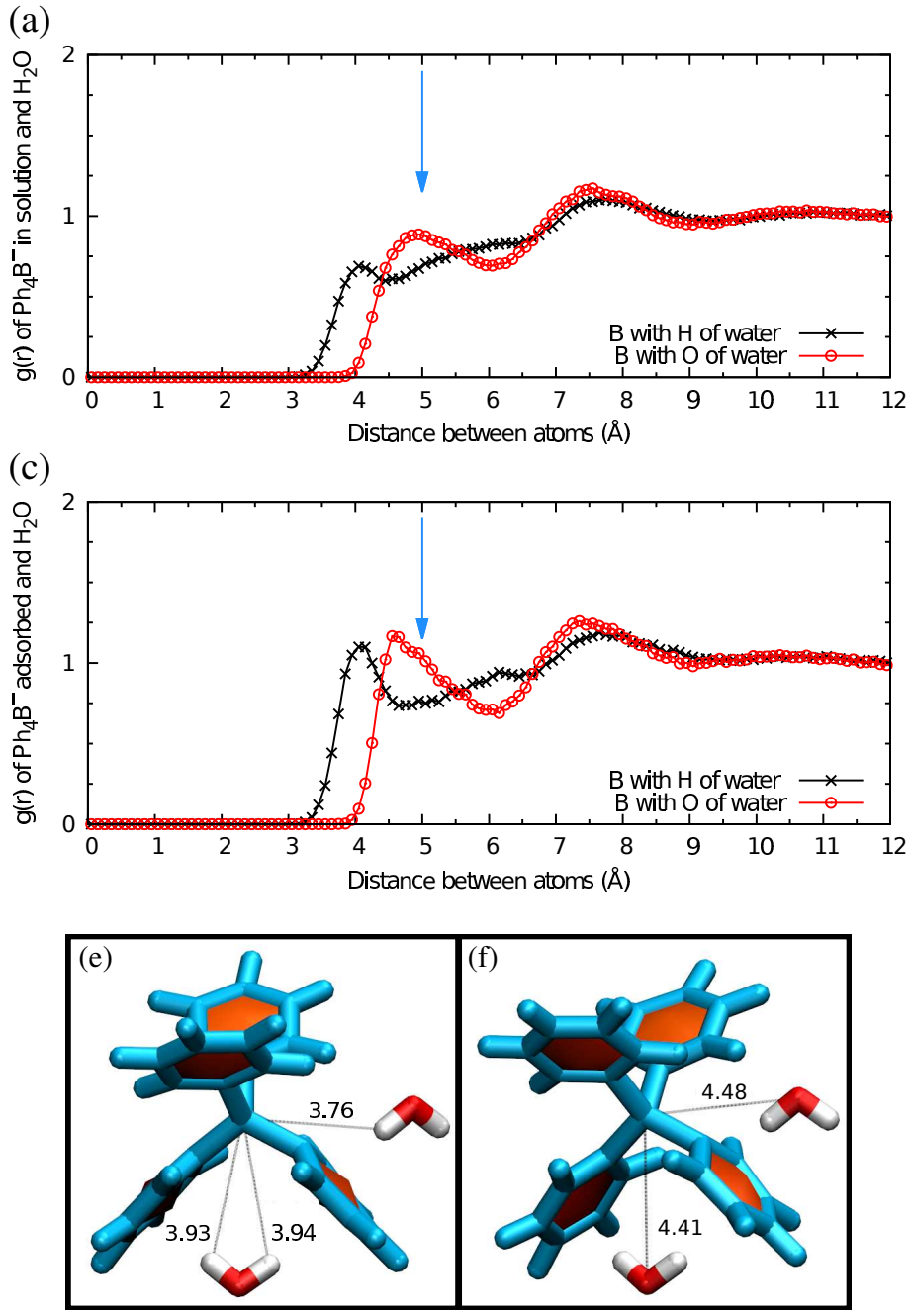

Figure 9.3: Radial pair distribution functions g(r) between the tetraphenyl ions and water molecules. The abscissa represents the distance between the central atom of the ions, the boron atom in the case of Ph_4B^- (blue ion) or the arsenic atom in the case of Ph_4As^+ (purple ion), and both hydrogen (×) or oxygen (○) atoms of the water molecules. The figures (a) and (b) represent the g(r) functions of the tetraphenyl ions in solution, whereas the figures (c) and (d) contain ⟶

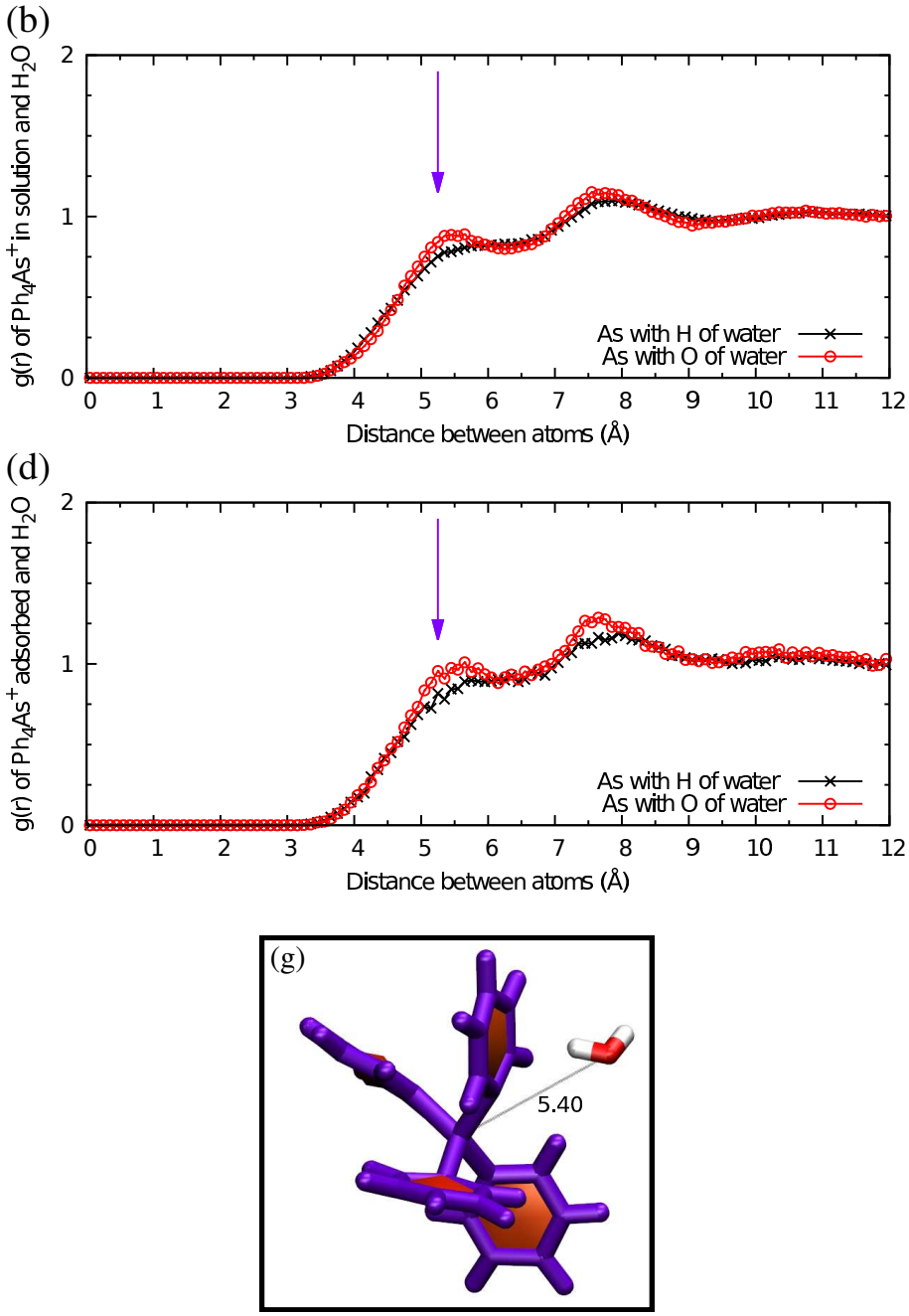

the g(r) functions of the ions adsorbed over the hydrophobic surface. The arrows indicate the radius of each ion, Ph_4B^- (blue) or Ph_4As^+ (purple), defined as the distance from the central atom to the most external –CH group of the tetraphenyl ion. Snapshots of the anion (e and f) and of the cation (g) are shown together with typical orientations of water molecules around the ions. Labels of the distances between the atoms from MD simulations are indicated in Å.

ion (∼4.5 Å). In general, oxygen atoms interact more strongly with cations than with anions. However, in water molecules, oxygen atoms are bonded to hydrogen atoms which are placed in a favorable position around the anion. This makes that the oxygen atom (in the same molecule) is placed at a certain distance from the anion. Therefore, in the case of the tetraphenyl ions, the oxygen atoms are situated closer to the anion than to the cation.

As can be observed in Figure 9.3 (b) water molecules around the cation, corresponding to the first peak in g(r), are located at 5.5 Å, farther than the ionic radius, which is 5.25 Å (indicated by the purple arrow). As we have done for the anion, we compare now the hydration of the cation in solution and adsorbed on the hydrophobic surface. We can observe that the g(r) functions shown in Figure 9.3 (b) and (d) are essentially identical. Therefore the structure of liquid water around the cation remains unchanged when this ion is adsorbed on the surface. Again, we have determined the average number of inner water molecules. The cation has 6.1 molecules in solution (1–12 molecules) and 4.0 when it is adsorbed. This means that in the adsorption process, the cation loses an average of 2 inner water molecules.

9.3.2 Interactions between ions and charged surfaces

In the previous subsection we have obtained the PMF profiles by MD-ABF simulations for the tetraphenyl ions and the generic neutral surfaces. The data shown in Figure 9.2 (a) is now used to predict the interaction of the ions with hydrophobic charged surfaces by numerical resolution of equations 9.1–9.3.

We have fitted the PMF data with the equation 9.4. The fit parameters are $A = -1942.97$ and $B = -13.1621$ for the Ph_4B^- anion [1], and $A = -1172.58$ and $B = -12.8921$ for the Ph_4As^+ cation, such that z is given in nm and energy in kcal/mol. We take $z_0 = 0.194$ nm for the anion and $z_0 = 0.166$ nm for the cation (the closest approach between the ion and the surface). The fitting functions are only valid for $z \geq z_0$ (z is the distance between the central atom of the ion (B or As) and the top part of the surface, which is situated at $z = 0$). In Figure 9.2 (a), the fitting functions are represented.

The numerical solutions of eqs. 9.1–9.3 (results not shown) reveal that the tetraphenyl ions are adsorbed over hydrophobic charged surfaces of opposite sign (positively charged surfaces for the anion and negatively charged surfaces for the cation). The analysis of ion distribution and electrostatic potential shows that from a certain ionic concentration, the ions adsorb to a greater extent than the surface charge density, then charge inversion of the surfaces is produced.

These numerical solutions have been used to calculate the minimum concentration of tetraphenyl ions required to cause charge inversion of surfaces with bare charge density σ_0. The results are shown in the Figure 9.4. The linear behavior of the numerical solution is consistent with the thermodynamic model which has

been proposed in previous works [6, 7] with an adsorption free energy per ion $\Delta\mu_0$:

$$c_I = \frac{\sigma_0}{qH} \exp(\Delta\mu_0 / k_B T) \tag{9.6}$$

where q is the charge of the counterion (regarding the charge of the surface) and H is the thickness of the layer formed by the adsorbed ions, which can be interpretated as the ion size. In the Figure 9.2 (a) we note that the decay of the PMF is roughly 0.5 nm for both ions. This amount is close to the radius of the tetraphenyl ions (Figure 1.1) and to the ionic radius defined in this chapter (5 Å for the anion and 5.25 Å for the cation). Thus, we have performed a linear fit to the data with $H = 0.5$ nm (Figure 9.4) and we have obtained the adsorption free energy per ion $\Delta\mu_0$. The values are $\Delta\mu_0 = -8.5 k_B T$ for the Ph_4B^- anion and $\Delta\mu_0 = -5.0 k_B T$ for the Ph_4As^+ cation.

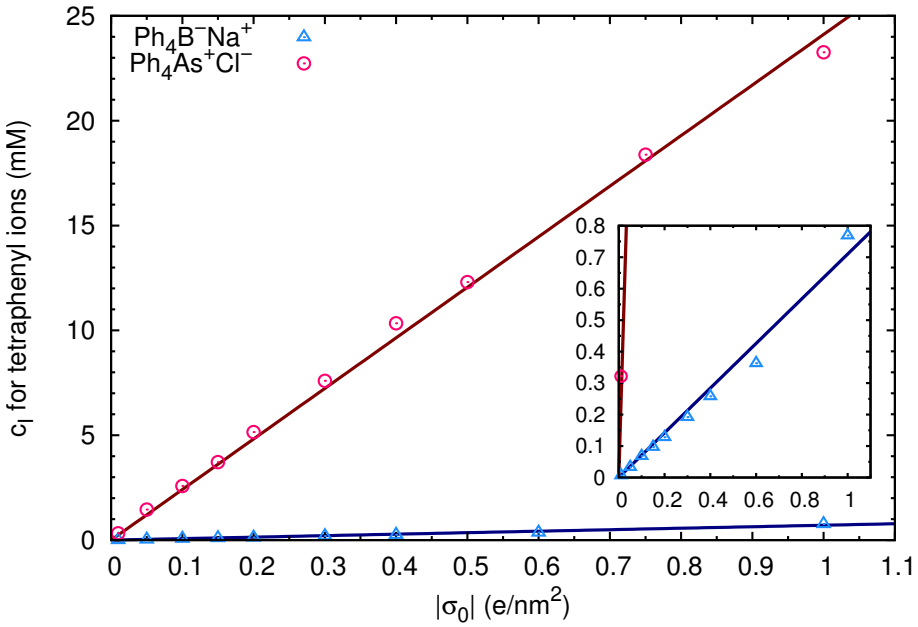

Figure 9.4: Minimum ionic concentration of $Ph_4B^-Na^+$ (△) and $Ph_4As^+Cl^-$ (○) required to induce charge inversion in hydrophobic surfaces with charge density $+|\sigma_0|$ and $-|\sigma_0|$, respectively. Solid lines represent the linear fit applied to these data, which was used to calculate the adsorption free energy per ion $\Delta\mu_0$ from a theoretical model (eq 6). The results obtained are $\Delta\mu_0 = -8.5 k_B T$ for the anion and $\Delta\mu_0 = -5.0 k_B T$ for the cation, with $H = 0.5$ nm for both ions. The data of $Ph_4B^-Na^+$ has been extracted from the reference [1].

Regarding the inorganic ions, in the previous work [1], the PMF of Na^+ with neutral surfaces, show that the interaction energy was very small in comparison

with that obtained for the Ph_4B^- anion. For this reason, we have not performed the corresponding simulations for Cl^-.

The results for the tetraphenyl ions show that these monovalent ions produce charge reversal at very low ionic concentrations, especially the anion (see Figure 9.4). This is consistent with experimental results; for a typical colloid the charge inversion takes place around 0.01–0.1 mM with the Ph_4B^- ([1] and Chapter 8) and around 0.1–1 mM with the Ph_4As^+ ([6] and Chapter 8), when the ions act as counterions. Therefore, it seems that planar surfaces are a good approximation to model colloids.

In conclusion, both organic ions feel a great attraction to hydrophobic interfaces. However the anion is more hydrophobic, showing a higher adsorption free energy. Therefore, the minimum ionic concentration required to produce charge inversion is much lower for the anion than for the cation. In spite of the fact that both ions have a similar size, same chemical structure and net electrostatic charge, their water-mediated interactions with planar surfaces are intrinsically different.

9.4 Conclusions

In this chapter, we have studied the behavior of big hydrophobic ions in presence of generic planar surfaces; the different interactions have quantified by MD simulations. We have dealt with the Ph_4B^- anion and the Ph_4As^+ cation. These ions are very similar in size, shape and chemical structure, but with opposite sign of their electrostatic charges. During the simulations we have observed that these ions are attracted and adsorbed on hydrophobic neutral surfaces and repelled by hydrophilic neutral surfaces. We have verified that the favorable interaction of both ions with the hydrophobic surface is represented by an adsorption minimum in the Potential of Mean Force (PMF), and that the adsorption free energy is larger for the anion (–6.00 kcal/mol) than for the cation (–3.64 kcal/mol). The interactions between ions and surfaces are mediated by the water structure around both, which is determined by the nature of the surface and the character of the ions. In solution, the anion breaks the bulk water arrangement to a greater extent than the cation, thus the anion shows a more hydrophobic character and its interaction with the hydrophobic surface is stronger, than in the case of the cation. This fact is reflected in the hydration changes of the anion when is adsorbed on the surface. In contrast, no changes in hydration were observed when the cation is adsorbed. In Chapter 4, we have seen that the different behavior of the anion and the cation is enlarged when they interact with a hydrophobic deformable interface, since the ions can penetrate inside it increasing the magnitude of the hydrophobic interaction.

In addition, we have solved numerically a generalized Poisson-Boltzmann equation taking into account the simulation results for the interactions between the

ions and the hydrophobic neutral surfaces, in order to determine their interactions with hydrophobic charged surfaces. We have found that the amount of adsorbed ions overtakes the bare charge of the surface, producing charge inversion. This fact is in agreement with experimental measurements ([1, 6] and Chapter 8); these monovalent and hydrophobic ions produce charge reversal on hydrophobic colloids at low ionic concentrations. In each case, we have obtained the minimum ion concentration needed to cause charge inversion depending on the bare charge of the surface. From these data we have estimated the adsorption free energy per ion, being –8.5 k_BT (–5.07 kcal/mol) for the anion and –5.0 k_BT (–2.98 kcal/mol) for the cation. This means that the required ion concentration to produce charge reversal is much lower in the case of the anion. Similar tendencies are observed in experimental systems, thus we can conclude that planar surfaces are a good approximation for modeling real colloids.

Our simulation results allow the understanding of the interactions between ions and surfaces at the atomic level. We have corroborated that the hydrophobic effect is the driving force in the organic ion adsorption on surfaces. As a consequence, charge inversion is observed in the case of hydrophobic surfaces, but not for interfaces of hydrophilic character.

Therefore, even for big hydrophobic anions and cations with very similar properties, the water-mediated interactions with interfaces are intrinsically different. The hydrogen atom is smaller than oxygen, thus the water molecule can aproach closer to anions than to cations. This results on different hydrogen bonding capabilities for anions and cations, which makes an anion more hydrophobic than a cation of equal size.

References

[1] Calero, C.; Faraudo, J.; Bastos-González, D. Interaction of monovalent ions with hydrophobic and hydrophilic colloids: Charge inversion and ionic specificity. *J. Am. Chem. Soc.* **2011**, *133*, 15025–15035.

[2] Huang, D. M.; Cottin-Bizonne, C.; Ybert, C.; Bocquet, L. Aqueous electrolytes near hydrophobic surfaces: Dynamic effects of ion specificity and hydrodynamic slip. *Langmuir* **2008**, *24*, 1442–1450.

[3] Hénin, J.; Fiorin, G.; Chipot, C.; Klein, M. L. Exploring multidimensional free energy landscapes using time-dependent biases on collective variables. *J. Chem. Theory Comput.* **2009**, *6*, 35–47.

[4] Schwierz, N.; Horinek, D.; Netz, R. R. Reversed anionic Hofmeister series: the interplay of surface charge and surface polarity. *Langmuir* **2010**, *26*, 7370–7379.

[5] Schurhammer, R.; Wipff, G. Are the hydrophobic $AsPh_4^+$ and BPh_4^- ions equally solvated? A theoretical investigation in aqueous and nonaqueous solutions using different charge distributions. *J. Phys. Chem. A* **2000**, *104*, 11159–11168.

[6] Martín-Molina, A.; Calero, C.; Faraudo, J.; Quesada-Pérez, M.; Travesset, A.; Hidalgo-Álvarez, R. The hydrophobic effect as a driving force for charge inversion in colloids. *Soft Matter* **2009**, *5*, 1350–1353.

[7] Besteman, K.; Zevenbergen, M.; Lemay, S. Charge inversion by multivalent ions: Dependence on dielectric constant and surface-charge density. *Phys. Rev. E* **2005**, *72*, 061501.

IV Conclusions

10 Conclusions

In this dissertation ionic specific effects have been investigated with both, inorganic (classical Hofmeister) and organic ions. The main conclusions for the different parts are enumerated below.

First part. PNIPAM chains and microgels:

1. Organic ions interact strongly with hydrophobic soft interfaces (PNIPAM chains and microgels). The interaction of the tetraphenyl ions with PNIPAM neutral chains has been quantified by MD simulations, being the adsorption of Ph_4B^- four times more favorable than that of Ph_4As^+. The anion is able to penetrate deeper and surround itself with polymer groups, while the cation interacts with the surface groups.

2. The hydrophobic effect appears to be the driving force for this strong accumulation that results in great charge inversions (overcharging) when the tetraphenyl ions act as counterions (coions), as we have observed experimentally by electrokinetic studies and AFM.

3. QCM has shown to be a powerful tool to characterize the viscoelastic properties of adsorbed PNIPAM microgels, allowing a reliable determination of the T_{LCS}, which is very sensitive to the ionic environment.

4. Calorimetric data confirm that the tetraphenyl anion has a stronger affinity to the hydrophobic PNIPAM interface than the tetraphenyl cation. This difference has been reflected in the displacement of T_{LCS} for both salts: while Ph_4B^- significantly reduced the T_{LCS} at low concentrations, Ph_4As^+ slightly increased this temperature in the range of concentrations studied. In addition, the shapes of the endothermic peaks were also different, being those of the Ph_4B^- much shorter and wider than those of the Ph_4As^+. And, more important, the formation of long-lasting small particles with very narrow size

distributions at temperatures higher than T_{LCS} was observed for the Ph_4B^- anion, but not for the Ph_4As^+ cation.

5. QCM and DSC measurements have shown that, in the case of inorganic anions, strongly hydrated ions and weakly hydrated ions provide different results in the PNIPAM transition. The T_{LCS} values obtained for the different salts varied according to the Hofmeister series. This indicates that more hydrated anions can easily dehydrated PNIPAM chains reducing the T_{LCS} in a higher extension than less hydrated anions. Therefore, we can say that the solvation degree of ions plays a fundamental role in ionic specificity.

Second part. Proteins:

1. The main characteristics of the well-structured globular proteins (BSA and β-lactoglobulin) and the more disordered and flexible protein (β-casein), have been determined by simulations and theoretical calculations. Using QCM we have shown that the globular proteins are adsorbed rigidly as monolayers. In contrast, β-casein forms a loosely adsorbed multilayer. MD simulations with β-casein indicate that the protein adsorption barely depends on the charge of the surface, since is driven by hydrophobic interactions.

2. Protein-coated latex microspheres have been prepared and characterized by electrophoretic mobility (μ_e) measurements. Our experimental μ_e results have been interpreted in terms of theoretical models of counterion condensation. The theoretical models used are based on the reduction of the charge of highly charged surfaces by counterion adsorption. The effective charge depends on the Debye length, related with the ionic concentration in the medium.

3. From thermodynamic calculations we have determined that β-casein is the most hydrophobic of the proteins studied, followed by BSA and β-lactoglobulin. Interfaces of different hydrophobic degree were obtained adsorbing the proteins on latex microparticles. We have corroborated, with μ_e and colloidal stability measurements, that the interaction of the tetraphenyl ions is directly related with the hydrophobic degree of the interface. The ion adsorption increases and the ionic concentration needed to screen the surface charge decreases with surface hydrophobicity.

4. Tetraphenyl ions strongly interact with proteins, producing conformational changes, which have been monitored by the QCM technique. These changes depend on the ions acting as coions or counterions and on their concentrations. At low counterion concentrations, rigid proteins films are formed when the ions screen electrostatic repulsive interactions between the proteins. In contrast, at higher concentrations, swollen protein films are obtained when the adsorption of the ions enhance the total electric charge of

the film. This happens when the organic ions act as coions or when charge reversal was observed (ions as counterions). In general, the same protein state can be achieved with Ph_4B^- and Ph_4As^+, although larger cation concentrations (ca. 10 times) are necessary to achieve similar effects.

Third part. Model surfaces:

1. MD simulations have shown that tetraphenyl ions are attracted and adsorbed over hard hydrophobic neutral surfaces and repelled by hydrophilic ones. In the case of the hydrophobic surface, the favorable interaction is nearly two times larger for the anion than that for the cation.

2. From the simulation results, a theoretical model is proposed to estimate the minimum ionic concentration needed to produce charge reversal on hydrophobic charged surfaces. This concentration is lower for the anion than for the cation, as we expected from the more favorable interaction of the anion with this kind of interfaces. In addition, this is consistent with experimental results obtained with latex microparticles.

To sum up, we can conclude that the studies performed in this dissertation support a mechanism of accumulation of chaotropic (kosmotropic) ions onto hydrophobic (hydrophilic) interfaces and exclusion from hydrophilic (hydrophobic) surfaces. We have observed, in particular with organic ions, a strong ion-adsorption onto hydrophobic and soft interfaces. This interaction has been quantified with the tetraphenyl ions (classified as super-chaotropes) by simulation and theoretical results in good agreement with the experiments. On the other hand, it has been also manifested the difference between anions and cations. In spite of their structural similarities, the tetraphenyl anion and cation clearly show different behavior in both situations, in solution and interacting with other interfaces, as is shown by experiments, theoretical calculations and simulations. It seems that anions disrupt the bulk water structure beyond that cations of similar characteristic, showing a more hydrophobic character. In addition, the different behavior is enhanced when ions interact with soft systems instead of hard surfaces, since the ions can penetrate inside them increasing the hydrophobic interactions.

The work performed during this doctoral thesis open new questions about ionic specificity that could be explored with more different studies. It would be interesting to delve into the study of the interaction between the tetraphenyl ions and proteins by MD simulations. This kind of studies will allow us to quantify this favorable interaction and to detect the protein groups involved in the process. In this way, we will obtain some information about the origin of the ion-protein interaction and the role that water plays on it, as we have studied for the tetraphenyl ions with PNIPAM. A deeper study of the re-stabilization mechanisms in colloids produced by charge inversion and hydration forces should be very valuable. This last issue has not been explored in this thesis, however it is an interesting mechanism observed with several experimental systems which has shown to be very sensitive to ionic specificity. The suitable combination of experiments and simulations may provide us some clues about the microscopic causes that result in these macroscopic behaviors.

List of Figures

List of Tables